

**NOVEL DESIGN AND MANUFACTURING OF ADVANCED  
MULTIFUNCTIONAL STRUCTURAL NANOCOMPOSITES  
CONTAINING SELF-HEALING FIBERS AND GRAPHENE SHEETS  
WITH STRUCTURAL HEALTH MONITORING CAPABILITIES**

**by**

**JAMAL SEYYED MONFARED ZANJANI**

**Submitted to the Graduate School of Engineering and Natural Sciences**

**in partial fulfillment of the requirements for the degree of**

**Doctor of Philosophy**

**Sabanci University**

**Spring 2016**

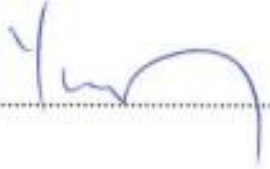
NOVEL DESIGN AND MANUFACTURING OF ADVANCED  
MULTIFUNCTIONAL STRUCTURAL NANOCOMPOSITES  
CONTAINING SELF-HEALING FIBERS AND GRAPHENE SHEETS  
WITH STRUCTURAL HEALTH MONITORING CAPABILITIES

APPROVED BY:

Assoc. Prof. Dr. Mehmet Yildiz  
(Thesis Supervisor)

  
.....

Prof. Dr. Yusuf Menciloglu

  
.....

Assoc. Prof. Dr. Burç Mısırlıoğlu

  
.....

Prof. Dr. Halit Suleyman Turkmen

  
.....

Prof. Dr. Afzal Suleman

  
.....

DATE OF APPROVAL: 01/08/2016

© Jamal Seyyed Monfared Zanjani 2016

All Rights Reserved

*To my loved ones.*

Novel Design and Manufacturing of Advanced Multifunctional Structural  
Nanocomposites Containing Self-Healing Fibers and Graphene Sheets with  
Structural Health Monitoring Capabilities

Jamal SEYYED MONFARED ZANJANI

Materials Science and Engineering, Ph.D. Dissertation, 2016

Thesis Supervisor: Assoc. Prof. Dr. Mehmet Yildiz

Co-Advisor: Asst. Prof. Dr. Burcu Saner Okan

Keywords: Multi-Functional Nanocomposites, Self-Healing, Graphene,  
Multiscale Reinforcement, Tri-axial electrospinning, Structural Health Monitoring

**ABSTRACT**

In the first part of this thesis, a direct, one-step tri-axial electrospinning process was used to fabricate multi-walled fibers with a novel architecture. Different healing agents were encapsulated inside the fibers with two separate protective walls. Presence of an extra layer in the fiber structure facilitated the encapsulation of healing agents and extended the efficiency of the healing functionality. We first took a systematical optimization approach to produce tri-axial hollow electrospun fibers with tunable fiber

diameters and surface morphology. Next, the effect of tri-axial hollow fibers as a primary reinforcement and co-reinforcement in the presence of glass fibers was scrutinized from a material selection point of view. Furthermore, multi-walled fibers were utilized to encapsulate different healing agents inside the fibers and successful and recurring self-healing ability were achieved while preserving the mechanical properties of the composites.

In the second part of this study, three different architectural designs were developed for manufacturing advanced multi-scale reinforced epoxy based composites in which graphene sheets and carbon fibers were utilized as nano- and micro-scale reinforcements, respectively. Graphene/carbon fiber/epoxy composites in various graphene sheet arrangements showed enhancements in in-plane and out of plane mechanical performances. In the hybrid composites, remarkable improvements were observed in the work of fracture by ~55% and the flexural strength by ~51% as well as a notable enhancement on other mechanical properties. In addition, integration of conductive reinforcement in the epoxy matrix enabled us to develop composite structures with high electrical and thermal conductivity, self-heating and de-icing functionalities.

YAPISAL SAĞLIK GÖRÜNTÜLEME KABİLİYETLERİ İLE KENDİ  
KENDİNİ ONARABİLEN FİBERLER VE GRAFEN TABAKALAR İÇEREN  
İLERİ, ÇOK FONKSİYONEL YAPISAL NANOKOMPOZİTLERİN ORJİNAL  
TASARIMI VE ÜRETİMİ

Jamal SEYYED MONFARED ZANJANI

Malzeme Bilimi ve Mühendisliği, Doktora Tezi, 2016

Tez Danışmanı: Doç. Dr. Mehmet Yıldız

İkincil Danışman : Yrd. Doç. Dr. Burcu Saner Okan

Anahtar kelimeler: Çok Fonksiyonel Nanokompozitler, Kendi kendini onarabilme,  
Grafen, Çok Ölçekli Güçlendirme, Üç eksenli elektrodokuma, Yapısal Sağlık  
Görüntüleme

**ÖZET**

Tezin ilk bölümünde, özgün yapıda çok cidarlı fiber üretmek için direkt tek aşamalı üçeksenli elektrodokuma yöntemi kullanılmıştır. Farklı onarım ajanları iki farklı koruma duvarına sahip fiber içerisine yerleştirilmiştir. Fiber yapısı içerisindeki ilave duvar katmanı, onarım ajanlarının fiber içerisine giydirilmesini kolaylaştırmıştır ve onarım fonksiyonunun verimini arttırmıştır. İlk olarak, sistematik optimizasyon yaklaşımı ile üçeksenli içi boş elektropun fiberleri çaplarını ve yüzey morfolojilerini

kontrol ederek ürettik. Daha sonra, içi boş üçeksenli fiberlerin epoksi reçine içindeki güçlendirici etkileri ve yine epoksi reçine içerisinde cam elyafa ek olarak yanıl güçlendirici etkileri malzeme seçimi bakış açısından incelenmiştir. Ayrıca, çok duvarlı fiberler içerilerine çeşitli onarım ajanlarını yüklemek için kullanılmıştır ve onarım ajanı içeren çok duvarlı fiberler ile kompozitin mekanik özelliklerini koruyarak başarılı bir şekilde tekrarlanabilir kendi kendini onarabilme özelliği sağlanmıştır.

Tezin ikinci bölümünde, grafen tabakalarının nano güçlendirici ve karbon fiberlerin mikro güçlendirici olarak kullanıldığı ileri çok ölçekli güçlendirilmiş epoksi tabanlı kompozitleri üretmek için üç farklı yapısal tasarım geliştirilmiştir. Grafen tabakaların farklı düzenlerde yerleştirildiği grafen/karbon fiber/epoksi kompozitlerin düzlem içi ve düzlem dışı mekanik performanslarında iyileşmeler gösterilmiştir. Hibrid kompozitlerde kırılmada yaklaşık %55 ve eğilme mukavemetinde %51 oranında önemli iyileşmeler gözlenirken aynı zamanda diğer mekanik özelliklerde kayda değer iyileşme sağlanmıştır. Bunlara ek olarak, iletken güçlendiricinin epoksi matrisine yüklenmesi yüksek elektrik ve ısı iletkenliği, kendi kendini ısıtma ve buz giderici özellikleri bulunan kompozit yapıların geliştirilmesine olanak sağlamıştır.

## ACKNOWLEDGEMENTS

I would like to express my gratitude to all the people who gave me the possibility to complete this thesis.

First and foremost, I would like to acknowledge and thank my supervisor, Assoc. Prof. Dr. Mehmet Yildiz for his excellent advises throughout the research and for allowing me to explore various aspects of this field while applauding my successes and helping me fix my failures.

Very special thanks go out to my co-supervisor Asst. Prof. Dr. Burcu Saner Okan for her patient guidance, encouragement and excellent advises throughout the research. It would never have been possible for me to take this work to completion without her incredible support.

My sincere appreciation goes to Prof. Dr. Yusuf Menciloglu for his encouragement and his valuable comments and suggestions.

I would also like to thank to our lab specialist Turgay Gonul for his help and effort in solving my technical problems.

Many thanks go in particular to my dear research colleagues Cagatay Yilmaz, and Leila Haghghi Poudeh.

I am truly grateful to my parents for their immeasurable love and care. They have always encouraged me to explore my potential and pursue my dreams. They helped me a lot to reach this stage in my life.

I owe my loving thanks to my dearest friend Haleh Abdizadeh for her constant support, patient help, keeping me motivated and inspiring scientific conversations.

Finally, I would like to gratefully acknowledge financial support from the Scientific and Technical Research Council of Turkey (TUBITAK) with the project numbers of 112M312/COST MP1202.

## TABLE OF CONTENTS

ABSTRACT .....	V
ÖZET .....	VII
ACKNOWLEDGEMENTS .....	IX
TABLE OF CONTENTS .....	X
LIST OF FIGURES .....	XV
LIST OF TABLES .....	XXIII
CHAPTER 1. STATE-OF-THE-ART .....	1
CHAPTER 2. RATIONAL DESIGN AND DIRECT FABRICATION OF MULTI- WALLED HOLLOW ELECTROSPUN FIBERS WITH CONTROLLABLE STRUCTURE AND SURFACE PROPERTIES .....	5
2.1. INTRODUCTION .....	5
2.2. EXPERIMENTAL .....	8
2.2.1. MATERIALS .....	8
2.2.2. LAYER MATERIAL SYNTHESIS .....	8
2.2.3. SOLVENT SELECTION AND DESIGN .....	9
2.2.4. SINGLE AND MULTI-AXIAL ELECTROSPINNING .....	10
2.2.5. CHARACTERIZATION .....	10
2.3. RESULTS AND DISCUSSION .....	11
2.3.1. LAYER MATERIALS OF MULTI-WALLED HOLLOW ELECTROSPUN FIBERS .....	11
2.3.1.1. OUTER LAYER MATERIALS .....	11
2.3.1.2. INNER LAYER MATERIALS .....	12
2.3.2. STUDY OF LAYER MATERIALS BY SINGLE ELECTROSPINNING .....	12
2.3.2.1. THE EFFECT OF SOLVENT ON THE FORMATION OF MULTI-WALLED HOLLOW FIBERS .....	13
2.3.2.2. THE EFFECT OF APPLIED VOLTAGE ON THE FORMATION OF MULTI-WALLED HOLLOW FIBERS .....	17
2.3.2.3. THE EFFECT OF OUTER LAYER POLYMER ON FIBER FORMATION AND HOLLOWNESS .....	19
2.3.3. STRUCTURAL AND THERMAL ANALYSES OF MULTI-WALLED HOLLOW FIBERS .....	21

2.4.	CONCLUSIONS.....	23
CHAPTER 3.	DESIGN AND FABRICATION OF MULTI-WALLED HOLLOW NANOFIBERS BY TRIAXIAL ELECTROSPINNING AS REINFORCING AGENTS IN NANOCOMPOSITES.....	24
3.1.	INTRODUCTION .....	24
3.2.	EXPERIMENTAL.....	26
3.2.1.	MATERIALS.....	26
3.2.2.	FABRICATION OF ELECTROSPUN TRI-AXIAL HOLLOW FIBERS.....	27
3.2.3.	FABRICATION AND CHARACTERIZATION OF FIBER REINFORCED EPOXY COMPOSITES.....	28
3.3.	RESULTS AND DISCUSSION .....	31
3.3.1.	SURFACE MORPHOLOGIES OF TRI-AXIAL HOLLOW FIBERS .....	31
3.3.2.	FLEXURAL PROPERTIES OF TRI-AXIAL HOLLOW FIBER REINFORCED COMPOSITES.....	33
3.3.2.1.	THE EFFECT OF OUTER WALL MATERIAL OF TRI-AXIAL HOLLOW FIBER .....	33
3.3.2.2.	THE EFFECT OF FIBER DIAMETER.....	34
3.3.2.3.	THE EFFECT OF FIBER CONTENT .....	35
3.3.3.	FRACTURE SURFACE ANALYSIS OF HOLLOW FIBER REINFORCED COMPOSITES.....	36
3.3.4.	LAMINATED GLASS FIBER REINFORCED COMPOSITES BY HOLLOW FIBERS ....	37
3.3.5.	DYNAMIC MECHANICAL PROPERTIES OF GLASS FIBER REINFORCED COMPOSITES.....	39
3.3.6.	MICROSCOPIC OBSERVATION AND FAILURE MECHANISMS .....	40
3.4.	CONCLUSIONS.....	42
CHAPTER 4.	REPEATED SELF-HEALING OF NANO AND MICRON SCALE CRACKS IN EPOXY BASED COMPOSITES BY TRI-AXIAL ELECTROSPUN FIBERS INCLUDING DIFFERENT HEALING AGENTS.....	44
4.1.	INTRODUCTION .....	44
4.2.	EXPERIMENTAL.....	48
4.2.1.	MATERIALS.....	48
4.2.2.	SYNTHESIS OF LAYER MATERIALS.....	48
4.2.3.	MULTI-AXIAL ELECTROSPINNING.....	49

4.2.4.	FABRICATION OF FIBER REINFORCED EPOXY COMPOSITES .....	49
4.2.5.	CHARACTERIZATION .....	50
4.3.	RESULTS AND DISCUSSION .....	50
4.3.1.	FABRICATION OF MULTI-WALLED HEALING FIBER .....	50
4.3.2.	FABRICATION OF SELF-HEALING MULTI-WALLED FIBERS BASED ON ROMP.....	51
4.3.3.	FABRICATION OF SELF-HEALING MULTI-WALLED FIBERS BASED ON AMINE–EPOXY REACTION .....	57
4.3.4.	DETERMINATION OF THE CURING STATE OF MATRIX .....	61
4.3.5.	EVALUATION OF SELF-HEALING EFFICIENCY .....	62
4.3.6.	FRACTURE SURFACE CHARACTERIZATION.....	67
4.4.	CONCLUSIONS.....	68
CHAPTER 5.	ACOUSTIC EMISSION AND FIBER BRAGG GRATING AS A NOVEL TECHNIQUE FOR MEASURING SELF-HEALING EFFICIENCY OF TRI-AXIAL ELECTROSPUN FIBERS/ GLASS FIBER/ EPOXY COMPOSITES.....	70
5.1.	INTRODUCTION .....	70
5.2.	EXPERIMENTAL.....	74
5.2.1.	MATERIALS.....	74
5.2.2.	TRI-AXIAL ELECTROSPINNING.....	74
5.2.3.	FABRICATION OF SELF-HEALING FIBER REINFORCED EPOXY COMPOSITES .	75
5.2.4.	CHARACTERIZATION .....	76
5.2.5.	FIBER BRAGG GRATING SENSORS (FBG).....	77
5.3.	RESULTS AND DISCUSSIONS.....	78
5.3.1.	FABRICATION OF TRI-WALLED HEALING FIBER .....	78
5.3.2.	STRUCTURAL CHARACTERIZATION OF TRI-AXIAL HOLLOW AND HEALING FIBERS.....	79
5.3.3.	TRI-AXIAL SELF-HEALING FIBER REINFORCED COMPOSITE WITH FBG SENSORS .....	81
5.3.4.	FRACTURE SURFACE CHARACTERIZATION.....	85
5.3.5.	SELF-HEALING OF EPOXY/GLASS FIBERS INTERFACES .....	86
5.3.5.1.	EVALUATION OF SELF-HEALING BY FLEXURAL TEST AND FBG SENSORS.....	86
5.3.5.2.	EVALUATION OF SELF-HEALING BY TENSILE TEST, POISSON’S RATIO AND	

ACOUSTIC EMISSION.....	88
5.3.6. FRACTURE SURFACE CHARACTERIZATION.....	92
5.4. CONCLUSIONS.....	92
<b>CHAPTER 6. NANO-ENGINEERED DESIGN AND MANUFACTURING OF HIGH-PERFORMANCE EPOXY MATRIX COMPOSITES WITH CARBON FIBER/SELECTIVELY INTEGRATED GRAPHENE AS MULTI-SCALE REINFORCEMENTS.....</b>	<b>94</b>
6.1. INTRODUCTION .....	94
6.2. EXPERIMENTAL.....	97
6.2.1. MATERIALS.....	97
6.2.2. SELECTIVE DISPERSION OF TEGO AS MATRIX AND INTERFACE REINFORCING AGENTS.....	98
6.2.3. FABRICATION OF MULTI-SCALE REINFORCED EPOXY COMPOSITES .....	99
6.2.4. CHARACTERIZATION .....	100
6.3. RESULTS AND DISCUSSION .....	101
6.3.1. MORPHOLOGIES AND PROPERTIES OF TEGO .....	101
6.3.2. TEGO AS A PRIMARY REINFORCEMENT .....	102
6.3.2.1. MECHANICAL PERFORMANCE OF EPOXY/TEGO NANOCOMPOSITES .....	102
6.3.2.2. FRACTURE SURFACE ANALYSIS OF NEAT SPECIMEN AND TEGO/EPOXY COMPOSITE .....	104
6.3.3. MODIFICATION CARBON FIBER-EPOXY MATRIX INTERFACE BY ELECTROSPRAY DEPOSITION OF TEGO .....	105
6.3.4. MECHANICAL PERFORMANCE OF MULTI-SCALE REINFORCED COMPOSITES	110
6.3.4.1. FLEXURAL PROPERTIES .....	111
6.3.4.2. TENSILE PROPERTIES.....	112
6.3.4.3. CHARPY IMPACT TEST .....	113
6.3.5. MICROSCOPIC OBSERVATION AND FAILURE MECHANISMS .....	115
6.4. CONCLUSIONS.....	117
<b>CHAPTER 7. TAILORING VISCOELASTIC RESPONSE, SELF-HEATING AND DEICING PROPERTIES OF HIGH-PERFORMANCE CARBON FIBER REINFORCED EPOXY COMPOSITES WITH SELECTIVELY DISPERSED GRAPHENE AS INTERFACE AND MATRIX REINFORCEMENTS.....</b>	<b>119</b>

7.1.	INTRODUCTION .....	120
7.2.	EXPERIMENTAL.....	123
7.2.1.	MATERIALS.....	123
7.2.2.	FABRICATION OF MULTI-SCALE REINFORCED EPOXY COMPOSITES.....	123
7.2.3.	DYNAMIC MECHANICAL ANALYSES (DMA) .....	124
7.2.4.	ELECTRICAL CONDUCTIVITY MEASUREMENTS .....	124
7.2.5.	THERMAL DIFFUSIVITY ANALYSIS BY PULSE THERMOGRAPHY.....	124
7.2.6.	SELF-HEATING AND ANTI-ICING CHARACTERIZATION .....	125
7.3.	RESULTS AND DISCUSSIONS .....	125
7.3.1.	DYNAMIC MECHANICAL ANALYSIS (DMA).....	125
7.3.2.	DYNAMICAL-MECHANICAL BEHAVIOR OF SPECIMENS UNDER TEMPERATURE SWEEP.....	126
7.3.3.	FREQUENCY DEPENDENCY OF DYNAMICAL-MECHANICAL PROPERTIES AND VISCOELASTIC ACTIVATION ENERGY .....	127
7.3.4.	MASTER CURVES BY TIME-TEMPERATURE SUPERPOSITION.....	130
7.3.5.	ELECTRICAL CONDUCTIVITY .....	131
7.3.6.	SELF- HEATING PERFORMANCE .....	132
7.3.7.	THERMAL-DIFFUSIVITY CHARACTERISTICS OF COMPOSITE SPECIMENS ....	134
7.3.8.	SELF-HEATING APPLICATION IN DE-ICING .....	135
7.4.	CONCLUSIONS.....	136
CHAPTER 8.	CONCLUSIONS .....	138
REFERENCES:	.....	141

## LIST OF FIGURES

Figure 2.1 The chemical representations of outer and inner layer materials (a) PMMA (b) poly(methyl methacrylate-co-styrene) (c) PS and (d) PAAm.....	9
Figure 2.2 (a) Schematic representation of tri-axial electrospinning set-up (b) the high-speed camera image of Taylor cone composed of PMMA as an outer layer and PAAm as a middle layer.....	10
Figure 2.3 2-dimensional solubility diagram of PMMA. ....	12
Figure 2.4 SEM images of single axial electrospun fibers (a) PMMA and (b) PAAm. (The concentration of each polymeric solution is 30 wt. %). ....	13
Figure 2.5 SEM images of electrospun multi-walled hollow PMMA/PAAm fibers fabricated by different outer wall solvents (a) DMF, (b) EA and (c) THF.....	15
Figure 2.6 The graph of distance of inner layer solvent and outer layer solvent calculated by Hansen solubility space as an index of their affinity. ....	16
Figure 2.7 SEM images of multi-walled hollow electrospun fibers of PS/PAAm synthesized with the outer layer solvent of DMF by changing inner layer solvent of (a) water and (b) mixture of water/DMF (volume ratio 3:2). ....	17
Figure 2.8 SEM images of multi-walled hollow electrospun fibers of PS/PAAm synthesized with solvents of THF and water for the outer and inner layers, respectively: (a) and (b) present images at different magnifications. ....	17
Figure 2.9 Taylor cone formation of PMMA 20 wt.% in EA as outer layer solution and PAAm in water as inner layer solution in different applied voltage (a) no voltage, (b) 10 kV, (c) 20 kV and (d) 30 kV.....	18
Figure 2.10 Changes in the fiber diameter by increasing the applied voltage for fibers with outer layer of PMMA in DMF and inner layer of PAAm in WD32 (water: DMF=3:2 (v/v)). ....	19

Figure 2.11 TEM images of (a) and (b) PMMA/PAAm multi-walled hollow fibers with continuous core structure at different magnifications, and (c) the rupture of middle layer in tri-axial hollow fiber structure (Outer layer solvent: EA, inner layer solvent: water). .....	20
Figure 2.12 TEM images (a) and (b) of PS/PAAm hollow fibers in different regions and at different magnifications (Outer layer solvent: EA, inner layer solvent: water). .....	20
Figure 2.13 SEM images of multi-walled hollow fibers with PAAm as an inner layer and poly(methyl methacrylate-co-styrene) as an outer layer prepared by using solvent of (a) EA, (b) and (c) THF.....	21
Figure 2.14 FTIR spectrum of multi-walled hollow electrospun fiber with PMMA as an outer layer and PAAm as an inner layer. ....	22
Figure 2.15 (a) TGA curves of PMMA, PAAm and multi-walled hollow fibers and (b) differential thermal analyses of PMMA, PAAm and multi-walled hollow fibers.....	23
Figure 3.1 Schematic representation of tri-axial electrospinning set-up. ....	28
Figure 3.2 A schematic representation of composite manufacturing by vacuum infusion, a) stacking sequence and the placement of the interlayer where the yellow region indicates the cut specimen for flexural and tensile tests, and b), the vacuum infusion system. ....	29
Figure 3.3 Step by step procedure followed for sample preparation for failure mechanisms analysis.....	30
Figure 3.4 SEM images of tri-axial hollow electrospun fibers of (a) PMMA/PAAm fibers fabricated by outer wall solvent of DMF (b) PMMA/PAAm fibers fabricated by outer wall solvent of EA and (c) PS/PAAm fibers fabricated by outer wall solvent of EA. ...	32
Figure 3.5 Flexural stress-strain curves of samples for neat epoxy and samples reinforced by 0.2 wt.% PS-PAAm and 0.2 wt.% PMMA-PAAm tri-axial hollow fibers. Both fibers are produced with the outer layer solvent of EA and inner layer solvent of water. ....	34
Figure 3.6 Schematic representation of semi-IPN structure formation in PMMA-PAAm tri-axial hollow fiber reinforced composite: (a) PMMA-PAAm tri-axial hollow fiber, (b)	

partial dissolution of PMMA shell into the resin and hardener mixture and (c) semi-IPN structure. ....	34
Figure 3.7 Flexural stress-strain curves of neat epoxy sample and samples reinforced by PMMA-PAAm tri-axial hollow fibers with different fiber diameters. ....	35
Figure 3.8 Flexural stress-strain curves of neat epoxy specimen and specimens reinforced with 0.2 wt.% and 2 wt.% PS-PAAm tri-axial hollow fiber. ....	36
Figure 3.9 SEM images of fracture surface of specimens after 3-point bending tests, (a) Neat epoxy, (b) PMMA/PAAm tri-axial hollow fiber reinforced composite with the outer layer solvent of EA and (c, d) close up view for PMMA/PAAm tri-axial hollow fiber reinforced composite. ....	37
Figure 3.10 Flexural stress-strain curves of glass fiber reinforced epoxy specimen and specimen modified by interlayers of tri-axial hollow fibers of PMMA/PAAm. ....	38
Figure 3.11 Tensile stress vs strain curves of glass fiber reinforced epoxy specimen and specimen modified by interlayers of tri-axial hollow fiber of PMMA/PAAm. ....	39
Figure 3.12 $\tan \delta$ and $E'$ curves of glass fiber reinforced specimens with and without nanofiber interlayers. ....	40
Figure 3.13 SEM images of cross-sectional area of (a, b) glass fiber reinforced epoxy specimen without nanofiber interlayers before applying load, (c, d) glass fiber reinforced epoxy specimen modified by nanofiber interlayers before applying load, (e, f) glass fiber reinforced specimen without nanofiber interlayers after bending, (g, h, i) glass fiber reinforced specimen modified by nanofiber interlayers after bending. ....	41
Figure 4.1 A schematic representation for the multi-axial electrospinning set-up. ....	49
Figure 4.2 (a) and (b) SEM images of as received Grubbs' catalyst at different magnifications. ....	52
Figure 4.3 SEM images of PMMA/PAAm/DCPD tri-axial healing fibers fabricated utilizing different outer wall solvents (a) THF, (b) EA and (c) DMF. ....	53

Figure 4.4 SEM images of (a) PS/PAAm/DCPD and (b) poly(glycidyl methacrylate-co-styrene)/PAAm/DCPD tri-axial healing fibers, which are manufactured using EA as an outer wall solvent.....	53
Figure 4.5 SEM images of PMMA/PAAm tri-axial hollow electrospun fibers fabricated using different outer wall solvents of (a) DMF, and (b) EA.....	55
Figure 4.6 TEM images of (a, b) PMMA/PAAm/DCPD tri-axial healing fibers fabricated using DMF as an outer layer solvent, and (c) PMMA/PAAm tri-axial hollow fiber electrospun through using EA as an outer layer solvent.....	55
Figure 4.7 (a) Cathodoluminescence and (b) secondary electron coupled SEM images of PS/PAAm/DCPD tri-axial electrospun fibers.....	56
Figure 4.8 FTIR spectra of (a) DCPD, PMMA/PAAm tri-axial hollow fiber and PMMA/PAAm/DCPD tri-axial fiber, (b) DCPD, PS/PAAm tri-axial hollow fiber and PS/PAAm/DCPD tri-axial fiber, (c) DCPD, poly(St-co-GMA)/PAAm tri-axial hollow fiber and poly(St-co-GMA)/PAAm/DCP tri-axial fiber. (d) the chemical structure of polymers and DCPD.....	58
Figure 4.9 The change in the viscosity of epoxy resin as a function of volume percentage of acetone.....	59
Figure 4.10 (a, b) SEM images and (e) TEM image of PMMA/PAAm/hardener tri-axial fiber with 20 wt% PMMA in EA solution as an outer wall, 20 wt% PAAm in water as a middle wall and hardener as a core material (c, d) SEM images and (f) TEM image of PMMA/PAAm/epoxy tri-axial fiber with 20 wt% PMMA in EA solution as an outer wall, 20 wt% PAAm in water as a middle wall and epoxy-acetone 8:2 mixture as a core material.....	60
Figure 4.11 FTIR spectra of (a) hardener, PMMA/PAAm tri-axial hollow fiber and PMMA/PAAm/Hardener tri-axial fiber (b) epoxy resin, PMMA/PAAm tri-axial hollow fiber and PMMA/PAAm/epoxy tri-axial fiber.....	61
Figure 4.12 The variation of gel content of neat epoxy specimens as a function of curing time at constant curing temperature of 70°C (obtained by soxhlet extraction). .....	62

Figure 4.13 Schematic representation of self-healing concept, (a) the incorporation of self healing fibers into a polymer matrix, (b) cracks formation within the matrix due to the external load and consequent rupture of healing fibers, (c) the discharge of healing agent into the crack area followed by its polymerization upon getting in contact with either pre-dispersed catalyst in outer layer of fibers or the hardener released along with the healing epoxy, and (d) healing of crack region.....	65
Figure 4.14 Flexural stress-strain curves of specimens reinforced by (a) PMMA/PAAm tri-axial hollow fibers with the average diameter of 200 nm, (b) PMMA/PAAm/DCPD healing fibers with the average diameter of 200 nm, (c) PMMA/PAAm tri-axial hollow fibers with average diameter of 1 $\mu$ m, (d) PMMA/PAAm/DCPD tri-axial healing fibers with the average diameter of 1 $\mu$ m (e) PMMA/PAAm/(hardener, epoxy) tri-axial healing fibers with the average diameter of 1 $\mu$ m and (f) Normalized flexural modulus of composites reinforced by tri-axial hollow and healing fibers with different diameters as a function of healing cycle.....	66
Figure 4.15 SEM images of fracture area of (a) PMMA/PAAm tri-axial hollow fiber reinforced epoxy specimen with the fiber diameter of 1 $\mu$ m, (b) PMMA/PAAm/DCPD tri-axial healing fiber reinforced epoxy specimen with the fiber diameter of 1 $\mu$ m, (c) PMMA/PAAm PMMA/PAAm tri-axial hollow fiber reinforced epoxy specimen with the fiber diameter of 200 nm (d) PMMA/PAAm/DCPD tri-axial healing fiber reinforced epoxy specimen with fiber diameter of below 200 nm.....	68
Figure 5.1 A schematic representation for tri-axial electrospinning set-up.....	75
Figure 5.2 Stacking sequence and the placement of the interlayer in composite structure produced by vacuum infusion (the yellow region indicates the cut specimen for flexural and tensile tests) where an FBG sensor with the initial wavelength of 1550 nm was placed between the fifth and sixth layers. ....	76
Figure 5.3 Schematic representation of working principle of a FBG.....	78
Figure 5.4 SEM images of (a) PMMA/PAAm/epoxy tri-axial healing fibers, (b) PMMA/PAAm tri-axial hollow fiber; TEM images of (c) PMMA/PAAm/hardener tri-axial healing fibers and (d) PMMA/PAAm tri-axial hollow fiber.....	80

Figure 5.5 FTIR spectra of (a) hardener, PMMA/PAAm tri-axial hollow fiber and PMMA/PAAm/hardener tri-axial fiber and (b) epoxy, PMMA/PAAm tri-axial hollow fiber and PMMA/PAAm/Epoxy tri-axial fiber.....	80
Figure 5.6 Flexural stress–strain curves of specimens reinforced by (a) PMMA/PAAm tri-axial hollow fibers, (b) PMMA/PAAm/(epoxy, hardener) tri-axial healing fibers, and (c) normalized flexural modulus of composites reinforced by tri-axial hollow and healing fibers as a function of healing cycle .....	82
Figure 5.7 The variation of damage indicator as a function of healing cycles.....	84
Figure 5.8 SEM images of fracture areas of (a, b) PMMA/PAAm tri-axial hollow fiber reinforced epoxy specimen, (c, d) PMMA/PAAm/(epoxy, hardener) tri-axial healing fibers reinforced epoxy specimen .....	85
Figure 5.9 (a) Normalized flexural modulus of glass fiber reinforced composites as a function of healing cycle and, Bragg wavelength vs. test duration graph for (b) PMMA/PAAm tri-axial hollow fibers reinforced composites and (c) PMMA/PAAm/(epoxy, hardener) tri-axial healing fibers .....	88
Figure 5.10 (a) Normalized tensile modulus of glass fiber reinforced composites as a function of healing cycle, (b-c). Poisson’s ratio vs. axial strain graphs for PMMA/PAAm tri-axial hollow fibers and PMMA/PAAm/(epoxy, hardener) tri-axial healing fibers reinforced composites, respectively, (d-e) acoustic emission clustering patterns for PMMA/PAAm tri-axial hollow fibers and PMMA/PAAm/(epoxy, hardener) tri-axial healing fibers reinforced composites, respectively, where in these scatter-plots, each data point represents an acoustic signal.....	91
Figure 5.11 SEM images of cross-sectional areas of (a) PMMA/PAAm tri-axial hollow fibers reinforced composite and (b) PMMA/PAAm /(epoxy, hardener) tri-axial healing fibers reinforced composite. ....	92
Figure 6.1 Schematic representation of (a) dispersion of TEGO sheets into the epoxy matrix to obtain nano-reinforced matrix and (b) dispersion of TEGO sheets as an interface reinforcement agent by electrospaying process.....	99

Figure 6.2 Schematic representation of composite manufacturing by vacuum infusion, (a) stacking sequence where the yellow region indicates the cut specimen for mechanical tests, and (b) the vacuum infusion system. ....	100
Figure 6.3 SEM micrographs of (a, b) as received TEGO particles at different magnifications and (c) TEGO sheets after the dispersion into DMF by sonication. ....	102
Figure 6.4 (a) Flexural stress–strain curves of neat and TEGO/epoxy composite specimens with different TEGO contents, (b) flexural modulus improvement and (c) flexural strength improvement graphs as a function of TEGO content. ....	103
Figure 6.5 SEM images of the fracture surface of specimens after three-point bending tests (a, b) neat epoxy, and (c, d) 0.05 wt% TEGO/epoxy composite. ....	105
Figure 6.6 SEM images of carbon fabric mat (a, b) as-received, (c, d) after electro spraying of TEGO sheets and (e) low magnification image of carbon fabric with electro sprayed TEGO. ....	106
Figure 6.7 Raman spectra of as received carbon fiber, TEGO sheets, and TEGO sprayed carbon fiber. ....	108
Figure 6.8 XPS survey scan spectra of as received carbon fiber, TEGO, and TEGO sprayed carbon fiber. ....	109
Figure 6.9 (a) Flexural stress-strain curves, (b) tensile stress–strain curves (c) Poisson’s ratio versus axial strain of carbon fiber-reinforced epoxy specimens with different TEGO arrangements and (d) the window of percentage improvement in mechanical performance with respect to the properties of CFRP. ....	115
Figure 6.10 SEM images of cross-sectional area of specimens after flexural failure (a) CFRP, (b) CFRP/INT, (c) CFRP/MTX, and (d) CFRP/INT+MTX. ....	117
Figure 7.1 Schematic representation of electrical conductivity measurement set-up..	124
Figure 7.2 Temperature sweep of $Tan\delta$ and $E'$ curves of CFRP, CFRP/INT, CFRP/MTX and CFRP/INT+MTX at frequency of 1 Hz. ....	127

Figure 7.3 $\text{Tan}\delta$ vs temperature curves depending on different frequencies in the range of 1 to 20 Hz for (a) CFRP, (b) CRFP/INT, (C) CFRP/MTX, (d) CFRP/MTX+INT specimens, and (e) the graph of $\ln(\omega)$ vs. $1000/T_g$ .....	129
Figure 7.4 $\text{Tan}\delta$ vs frequency master curves of (a) CFRP, (b) CRFP/INT, (C) CFRP/MTX and (d) CFRP/MTX+INT at different reference temperatures .....	131
Figure 7.5 (a) I-V curves and (b) electrical conductivity value vs specimen type .....	132
Figure 7.6 Thermograms of (a) CFRP, (b) CFRP/INT, (c) CFRP/MTX, and (d) CFRP/INT+MTX under constant current of 1 A.....	133
Figure 7.7 Surface temperature decay curves calculated for composite specimens regarding different TEGO sheets configurations.....	135
Figure 7.8 (a) The setup of de-icing experiment, and (b) Ice drop time of CFRP, CFRP/INT, CFRP/MTX under constant current of 3 A, and CFRP/INT+MTX under constant current of 4 A.....	136

## LIST OF TABLES

Table 2.1 Mw, PDI and Tg of outer layer polymers of electrospun fibers .....	11
Table 3.1 Mw, PDI and Tg of outer wall polymers of electrospun fibers. *Viscosity averaged molecular weight (Mv) measured by Mark–Houwink method .....	27
Table 3.2 Improvements in the flexural strength and modulus of hollow fibers reinforced composites in % .....	36
Table 4.1 Percent modulus reduction of specimens in each cycle based on initial modulus value .....	67
Table 5.1 Percent modulus reduction of specimens in each cycle based on initial modulus value .....	83
Table 6.1 Flexural strength and modulus values and their improvement percentages of neat and TEGO/epoxy composites. ....	103
Table 6.2 The intensities and peak positions of D and G bands, and ID/IG ratios of pristine carbon fiber, TEGO sprayed carbon fiber and TEGO sheets .....	110
Table 6.3 XPS spectra results of C1s and O1s for TEGO, carbon fiber, and TEGO sprayed carbon fiber .....	110
Table 6.4 Summary of mechanical properties of carbon fiber reinforced specimens ..	115
Table 7.2 Slopes of $\ln\omega$ vs. $1000/T_g$ graphs, R2 values, and activation energies ( $\Delta H$ ) of composite specimens .....	130
Table 7.3 Sample thickness, crossing time ( $\tau_c$ ) and calculated Thermal diffusivity....	135

## CHAPTER 1.STATE-OF-THE-ART

Fiber-reinforced polymeric composites with superior strength and stiffness to weight ratio, relatively easy manufacturing process, and multi-functionality are promising alternative in design and development of structural and functional materials for aerospace, aeronautics, energy and automobile industries [1]. However, growing demand of industries for materials with higher mechanical and physical properties as well as different functionalities leads to development and fabrication of a novel class of materials named nanocomposites. Nanocomposites benefit from unique mechanical properties, large aspect ratio, and various functionality of nano-materials to offer polymeric structures with enhanced mechanical integrity, physical performance and multi-functionalities [2].

Embedment of reinforcing fibers into the polymeric matrix is the most common way to improve the structural performance (i.e., specific strength and stiffness, among others) of polymeric materials [3]. However, the reinforced polymeric materials (composites in general term) are inherently susceptible to crack initiation and subsequent growth under external loads due to their heterogeneous structure, which unavoidably leads to a gradual degradation in mechanical properties of composites as a function of time [4, 5]. In order to circumvent this issue, it would be a prudent approach to use reinforcing fibers with healing/repairing agent(s) in composite materials [6]. Reinforcing fibers with an healing functionality can improve the mechanical properties of composites, prolong their effective lifetime and expand their capabilities for more advance applications [7]. Inspired by autonomous healing of wounds in living biological systems, scientist and engineers have been in constant search of methods to develop smart materials with self healing capability [8]. One practical approach is based on the delivery of encapsulated liquid agent into fractured areas whereby the mechanical properties of the damaged polymeric material can be partially or fully restored by repairing micro cracks.

On the other hand, the performance of fiber-reinforced composites is particularly affected by the properties of the constituent materials and the strength of fiber–matrix

interfaces which influence the efficiency of load transfer from the matrix to the reinforcements [9, 10]. In order to address these issues and achieve the desired performance, there have been several attempts for the enhancement of composite properties which are categorized into two parts: improvement of matrix properties and interface modification [11].

Graphene as a promising reinforcing agent started receiving attention as modifier/reinforcement in polymers and polymeric composites due to being one of the strongest materials ever measured with a theoretical Young's modulus of 1060 GPa and an ultimate strength of 130 GPa [12, 13]. In addition, high specific surface area of graphene sheets results in stronger interfacial interactions and better load transfer between polymeric matrix and reinforcement particles which make them suitable candidate for nanocomposite fabrication [14]. It is known that nanocomposites reinforced by graphene-based materials even at very low loadings have shown great influence on mechanical performance, thermal, electrical conductivity, and flame retardancy in comparison of unmodified polymers [15, 16].

In the first part of this study, we conducted a systematical optimization study to produce tri-axial hollow electrospun fibers with tunable fiber diameters and surface morphologies by using different polymers and changing electrospinning processing parameters [17]. In addition, the effect of tri-axial hollow fibers as primary reinforcement and co-reinforcement in the presence of glass fibers were investigated from material selection to processing optimization [18]. Furthermore, tri-walled healing fibers were utilized to encapsulate different healing agents inside the fibers with two distinct protective walls. The presence of an intermediate layer facilitates ease encapsulation of healing agents and extends the efficiency and life-time of the healing functionality and thus preserve the mechanical properties of the composite by repairing micro and nano scale cracks under test condition [19]. In addition, various structural health monitoring and non-destructive testing techniques such as incorporation of Fiber Bragg Gratings sensors, and monitoring the acoustic emission, and Poisson's ratio reduction coupled with traditional mechanical testing methods are employed to evaluate the self-healing efficiency of composite structures.

In the second part, three different architectural designs are developed for manufacturing advanced multi-scale reinforced epoxy based composites in which graphene sheets and carbon fibers are utilized as nano- and micro-scale reinforcements, respectively. In the first design, electrospraying technique as an efficient and up-scalable method is employed for the selective deposition of graphene sheets onto the surface of carbon fabric mats. Controlled and uniform dispersion of graphene sheets on the surface of carbon fabric mats enhances the interfacial strength between the epoxy matrix and carbon fibers and increases the efficiency of load transfer between matrix and reinforcing fibers. In the second design, graphene sheets are directly dispersed into the hardener-epoxy mixture to produce carbon fiber/epoxy composites with graphene reinforced matrix. In the third design, the combination of the first and the second arrangements is employed to obtain a multi-scale hybrid composite with superior mechanical properties. The effect of graphene sheets as an interface modifier and as a matrix reinforcement as well as the synergetic effect due to the combination of both arrangements are investigated in details by conducting various physical-chemical characterization techniques. Graphene/carbon fiber/epoxy composites in all three different arrangements of graphene sheets show enhancement in in-plane and out of plane mechanical performances. In the hybrid composite structure in which graphene sheets are used as both interface modifier and matrix reinforcing agent, remarkable improvements are observed in the work of fracture by about 55% and the flexural strength by about 51% as well as a notable enhancement on other mechanical properties. In addition, viscoelastic behavior of epoxy/carbon fiber/selectively integrated graphene composites including effect of temperature, frequency, and graphene sheets configuration are studied using dynamical mechanical testing techniques. Incorporation of conductive graphene and carbon fibers as reinforcements into epoxy matrix resulted in electrically conductive structures with self-heating and deicing capabilities. This study brings a new insight into design and fabrication hierarchical multi-scale, self-healing and multi-functional structural materials which can be a stepping-stone for future developments.

Material from this dissertation has been published in the following forms and two addition papers are under preparation or submission processes:

**Jamal Seyyed Monfared Zanjani**, B. Saner Okan, I. Letofsky-Papst, M. Yildiz, Y. Z. Menciloglu, “Rational design and direct fabrication of multi-walled hollow

electrospun fibers with controllable structure and surface properties". **European Polymer Journal** 62, (2015) 66-76.

**Jamal Seyyed Monfared Zanjani**, B. Saner Okan, M. Yildiz, Y. Menciloglu, "Fabrication and morphological investigation of multi-walled electrospun polymeric nanofibers", **MRS Online Proceedings Library** (2014), 1621.

**Jamal Seyyed Monfared Zanjani**, B. Saner Okan, Y. Z. Menciloglu, and M. Yildiz, "Design and fabrication of multi-walled hollow nanofibers by triaxial electrospinning as reinforcing agents in nanocomposites," **J. Reinf. Plast. Compos.**, 34, 16, (2015), 1273-1286.

**Jamal Seyyed Monfared Zanjani**, Burcu Saner Okan, Ilse Letofsky-Papst, Yusuf Menciloglu, Mehmet Yildiz, "Repeated self-healing of nano and micro scale cracks in epoxy based composites by tri-axial electrospun fibers including different healing agents" **RSC Advances**, 5, 89 (2015) 73133-73145.

**Jamal Seyyed Monfared Zanjani**, Burcu Saner Okan, Yusuf Ziya Menciloglu and Mehmet Yildiz, "Nano-Engineered Design and Manufacturing of High Performance Epoxy Matrix Composites with Carbon Fiber/Selectively Integrated Graphene as Multi-Scale Reinforcements". **RSC Advances**, 6, (2016), 9495-9506.

## **CHAPTER 2. RATIONAL DESIGN AND DIRECT FABRICATION OF MULTI-WALLED HOLLOW ELECTROSPUN FIBERS WITH CONTROLLABLE STRUCTURE AND SURFACE PROPERTIES**

Multi-walled hollow fibers with a novel architecture are fabricated through utilizing a direct, one-step tri-axial electrospinning process with a manufacturing methodology which does not require any post-treatments for the removal of core material for creating hollowness in the fiber structure. The hydrophilicity of both inner and outer layers' solution needs to be dissimilar and carefully controlled for creating a two-walled/layered hollow fiber structure with a sharp interface. To this end, Hansen solubility parameters are used as an index of layer solution affinity hence allowing for control of diffusion across the layers and the surface porosity whereby an ideal multi-walled hollow electrospun fiber is shown to be producible by tri-axial electrospinning process. Multi-walled hollow electrospun fibers with different inner and outer diameters and different surface morphology are successfully produced by using dissimilar material combinations for inner and outer layers (i.e., hydrophobic polymers as outer layer and hydrophilic polymer as inner layer). Upon using different material combinations for inner and outer layers, it is shown that one may control both the outer and inner diameters of the fiber. The inner layer not only acts as a barrier and thus provides an ease in the encapsulation of functional core materials of interest with different viscosities but also adds stiffness to the fiber. The structure and the surface morphology of fibers are controlled by changing applied voltage, polymer types, polymer concentration, and the evaporation rate of solvents. It is demonstrated that if the vapor pressure of the solvent for a given outer layer polymer is low, the fiber diameter decreases down to 100 nm whereas solvents with higher vapor pressure result in fibers with the outer diameter of up to 1  $\mu\text{m}$ . The influence of electric field strength on the shape of Taylor cone is also monitored during the production process and the manufactured fibers are structurally investigated by relevant surface characterization techniques.

### **2.1. Introduction**

Hollow structured nanofibers with exceptional properties such as low density, high specific surface area, and tunable surface properties have found considerable

applications in catalysis [20], drug delivery [21], membrane [22], and photonics [23]. Up to now, two different approaches have been developed to fabricate hollow fibers through electrospinning process. The first approach introduced by Bognitzki et al. [24] uses the conventional electrospun polymeric fibers as templates for the fabrication of hollow fibers through coating the templates with wall materials using various deposition techniques, and then removes the template to obtain hollow structures. Similar procedure was utilized in the fabrication of hollow fibers of titanium dioxide [25], silica [26] and alumina [27]. Complexity in coating, template removal processes and type of material are the limiting factors of the method in question for the production of hollow fibers. The second approach employs co-axial electrospinning process to produce core-shell fibers from two different solutions and then hollow structured fibers is fabricated by selective removal of the core material. Li et al. [28, 29] used co-electrospinning of polyvinylpyrrolidone and titanium tetraisopropoxide solution in ethanol as the shell and mineral oil as the core, which is followed by the subsequent extraction of oil and calcination process to fabricate hollow titania fibers. In another study, hollow carbon nanotubes were fabricated by co-electrospinning of poly(methyl methacrylate) (PMMA) solution as fiber's core and polyacrylonitrile (PAN) as fiber's shell with the subsequent degradation of PMMA and then carbonization of PAN [30]. Dror et al. [31] fabricated polymeric bio-microtubes by using co-electrospun biocompatible and biodegradable polymers as core and shell of fibers and transformed the core/shell structure into hollow fibers by controlling the evaporation of the core solution.

In order to increase the strength and functionality of co-axial electrospun fibers, an additional wall in fiber structure is provided by multi-axial electrospinning which is a single-step method to fabricate third generation electrospun nanofibers with a unique architecture and morphology. In the fabrication process of multi-axial electrospun nanofibers, a strong electric field is applied between a nozzle containing concentric tubes allowing for the extrusion of different fluids to tip of the nozzle and grounded metallic plate as a collector. When the electrostatic forces on the surface of polymeric solutions exceed the surface tension of droplets, the jet of polymeric solutions is ejected from the tip of the nozzle and undergoes bending instabilities, whipping motions and diameter reduction in order to form multi-axial fibers with diameter ranging from several nanometers to micrometers [32]. The advantage of these sandwich-structured fibers is in

the insertion of an extra intermediate layer between the inner cavity and outer wall of fibers. This extra layer would provide an inert medium for the core material to be encapsulated thereby reducing the environmental effect and increasing the life time of both core and wall materials.

In literature, one may find a few recent studies which have utilized tri-axial electrospinning technique that focuses on the encapsulation of functional molecules since an extra intermediate layer in electrospun fiber increases the life time of encapsulated materials. Kalra et al. [33] applied tri-axial electrospinning technique to produce fibers with intermediate layer of block-copolymers with self-assembly functionality flanked between the shell layers of thermally stable silica and the core allowing for the post-fabrication annealing of the fibers to obtain equilibrium self-assembly without destroying the fibers morphology. In another study, tri-axial electrospinning technique was utilized to develop nanowire-in-microtube structure by introducing an extra middle fluid as a spacer between the outer and inner layer of fibers and selective removing of middle spacer fluid to achieve hollow cavity between the sheath and the core materials [34]. In another work, biodegradable triaxial nanofibers were produced by using gelatin as middle wall and poly( $\epsilon$ -caprolactone) as inner and outer walls to provide sufficient strength to support developing tissues [35]. Especially these types of multi-axial electrospun fibers have been utilized as drug delivery vehicles since the structure of fiber provides a quick release from the outer sheath layer for short-term treatment and a sustained release from the fiber core for long-term treatment [36].

This study differs from the previous studies in terms of creating hollow and continuous triaxial electrospun fibers in a single step without any post treatments in which hollowness can be tailored. Having a two-walled structure strengthens the electrospun fibers thereby preventing its deformation and in turn leading to continuous fiber structure. Herein, the hollowness of tri-axial electrospun fibers with different outer and inner diameters is controlled by using several solvent-polymer systems and different layer polymers to increase encapsulation efficiency. Hansen solubility parameters are applied to get an index of layer solution miscibility and affinity to control the diffusion of layers through multi-axial electrospinning. To our best knowledge, the current study is the first one for the production of multi-walled hollow fibers by a single-step process without applying any post treatments and inserting any spacer through layers. In this process, two

spinnable polymer solutions as inner and outer layers of fibers with different polarities and viscosities adjusted by changing polymer concentration are chosen to provide composite properties and wider range of applications. In place of multi-axial electrospinning process, single electrospinning methodology is also applied to optimize solution concentration to get well-ordered fiber structure. The diameter, surface morphology and layered structure of multi-walled hollow electrospun fibers are controlled by tailoring the solvent properties, degree of miscibility of solutions, polymer concentration, applied voltage, electrospinning distance, and flow rate.

## **2.2. Experimental**

### **2.2.1. Materials**

The following materials have been used for the experiment: Methyl methacrylate (SAFC, 98.5%), styrene (SAFC, 99%), Azobisisobutyronitrile (AIBN, Fluka, 98%), acrylamide (Sigma, 99%), N, N dimethyl formamide (DMF, Sigma-Aldrich, 99%), methanol (Sigma-Aldrich, 99.7%), tetrahydrofuran (THF, Merck, 99%), ethyl acetate (EA, Sigma-Aldrich, 99.5%).

### **2.2.2. Layer material synthesis**

Polymethyl methacrylate (PMMA), polystyrene (PS) and poly(methyl methacrylate-co-styrene) as hydrophobic polymers and outer layer materials of fibers were synthesized by free radical polymerization of vinyl monomers (30 ml) in presence of AIBN (1 g) as the radical initiator in the medium of THF (50 ml) at 65°C. Polymerization reaction was carried out for 4 h and then the reaction mixture was precipitated in cold methanol and dried for 12 h in a vacuum oven at 50°C. Polyacrylamide (PAAm) as hydrophilic polymer and inner layer material was synthesized by dispersion polymerization of acrylamide monomer (30 g) in methanol (100 ml) by using AIBN (1 g) as an initiator at 65°C. Separation of polymer particles from methanol and monomer mixture was done by vacuum filtration and twice washing the polymer particles with methanol and drying it for 12 h in a vacuum oven at 40°C. Figure 2.1 represents the chemical structures of layer materials chosen for multi-axial electrospinning process.

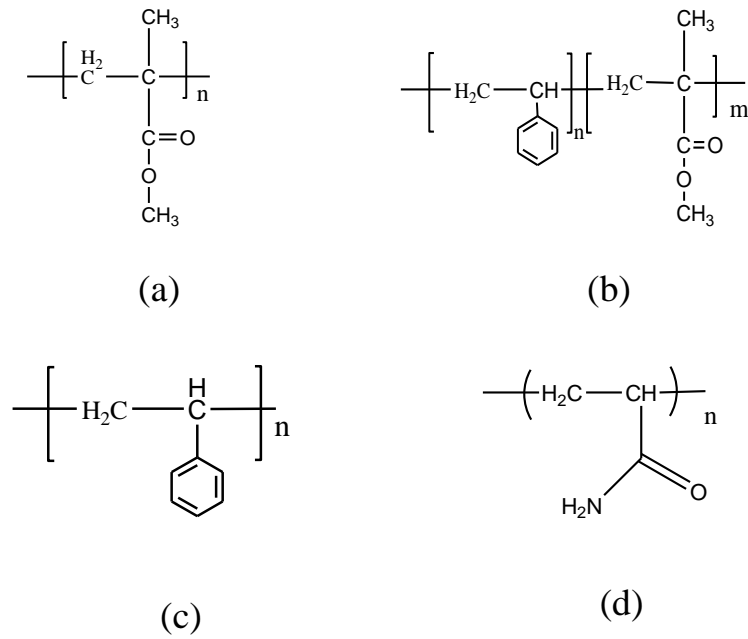


Figure 2.1 The chemical representations of outer and inner layer materials (a) PMMA (b) poly(methyl methacrylate-co-styrene) (c) PS and (d) PAAm

### 2.2.3. Solvent selection and design

Solvents and solvent systems are selected based on Hansen solubility parameters (HSP) using tabulated interactions of molecules in the form of polar ( $\delta_p$ ), dispersive ( $\delta_d$ ), and hydrogen bonding ( $\delta_h$ ) components [37]. Two-dimensional graphical representation of these parameters for our system is produced by combining the polar ( $\delta_p$ ) and dispersive ( $\delta_d$ ) components into a new parameter of  $\delta_v = (\delta_d^2 + \delta_p^2)^{1/2}$  which is plotted against  $\delta_h$ . Solvents for outer layer polymers are selected from among those located inside the solubility circle of each polymer considering the electrospinning properties of the polymeric solutions such as electrical conductivity and vapor pressure since these parameters are known to alter the borders of solubility area. Good and poor solvents for several polymers can be predicted by drawing a solubility circle defined by the Hansen coordinates and the radius of interaction [38]. On the other hand, PAAm as an inner layer material is mainly soluble in water, but different co-solvents with various volume ratios can be utilized to tailor the interaction of outer and inner layer solutions. The Hansen solubility parameter of solvent mixtures is calculated using  $\delta_n^{Mix} = \sum a_i \delta_n^i$  equation where n represents the parameter type (p, d, or h) and  $a_i$  is the volume fraction of solvent i. After the selection of ideal solvents for electrospinning, polymer solutions with the unit

of weight percentages (w/w) are prepared by appropriate amount of polymer and solvent, and stirred for 24 h at ambient temperature and pressure to obtain homogeneous solutions.

#### 2.2.4. Single and multi-axial electrospinning

Electrospinning process is performed at ambient room conditions using multi-axial electrospinning set-up purchased from Yflow Company with a custom-made tri-axial nozzle. Hollow fibers covered by two different polymeric layers are produced by tri-axial electrospinning process given in Figure 2.2a Also, the hollowness of fiber is also monitored by the formation of Taylor cone at the end of the syringe seen in Figure 2.2b.

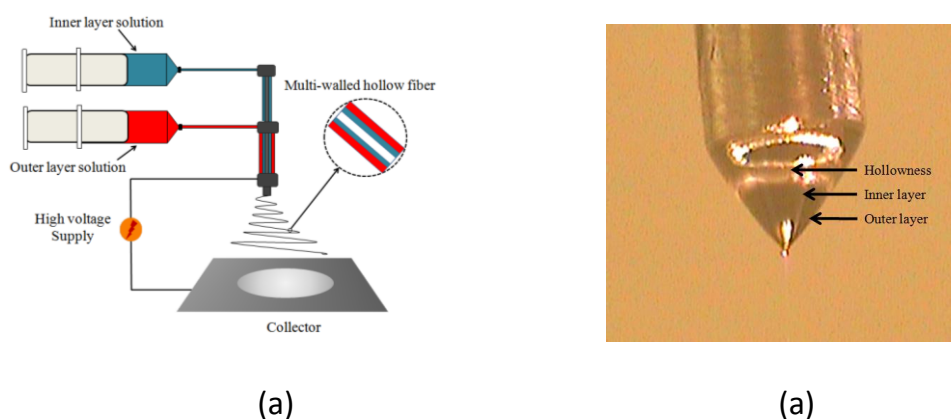


Figure 2.2 (a) Schematic representation of tri-axial electrospinning set-up (b) the high-speed camera image of Taylor cone composed of PMMA as an outer layer and PAAM as a middle layer.

All the fibers were electrospun with a nozzle to collector distance of 7 cm by tuning the applied voltage in the range of 5 kV to 30 kV. The flow rates of outer and inner layer solutions are individually controllable using separate pumps, and are of the values of 20  $\mu\text{l}/\text{min}$  and 15  $\mu\text{l}/\text{min}$ , respectively. Solutions prepared are loaded independently into the syringes which are connected to concentric nozzles, and the flow rate of each layer is controlled by separate pumps.

#### 2.2.5. Characterization

The structure of synthesized polymer was investigated by 500 MHz Varian Inova  $^1\text{H}$ -Nuclear Magnetic Resonance (NMR). The molecular weight and polydispersity index of outer layer polymers were determined by Viscotek-VE2001 gel permeation chromatography (GPC) in DMF. The functional groups of polymers and fibers were

investigated by Netzsch Fourier Transform Infrared Spectroscopy (FTIR). Thermal behaviors of polymers and fibers were examined by Netzsch Thermal Gravimetric Analyzer (TGA) and Differential Scanning Calorimeter (DSC) by a 10°C/min scanning rate under nitrogen atmosphere. The surface morphologies of fibers were analyzed by a Leo Supra 35VP Field Emission Scanning Electron Microscope (SEM) and JEOL 2100 Lab6 High Resolution Transmission Electron Microscopy (TEM). Elemental analysis of fibers was performed by Energy-Dispersive X-Ray (EDX) analyzing system. Taylor cone shape images were taken by high-speed camera.

## 2.3. Results and Discussion

### 2.3.1. Layer materials of multi-walled hollow electrospun fibers

#### 2.3.1.1. Outer layer materials

For the production of composite hollow fibers, as can be recalled the hydrophobic polymers as a protective outer layer of fibers were synthesized through free radical polymerization in solution medium. Here, it should be noted that it is critical to choose the hydrophobic polymers as an outer layer material to prevent the diffusion of layers during electrospinning thus providing the layered structure. In multi-axial electrospinning process, PMMA, PS and poly(methyl methacrylate-co-styrene) are used as outer layer polymers, and molecular weight (Mw), polydispersity index (PDI) and glass transition temperature ( $T_g$ ) of these polymers are given in

Table 2.1. A more detailed description of the experimental procedures can be found in the electronic supplementary information.

Table 2.1 Mw, PDI and  $T_g$  of outer layer polymers of electrospun fibers

Polymer	$T_g$ (°C)	Mw (g/mole)	PDI
PMMA	123	326000	3.2
PS	103	313000	1.7
Poly(methyl methacrylate-co-styrene)	98	185000	1.7

### 2.3.1.2. Inner layer materials

In the inner part of composite hollow fibers, the polymers with the hydrophilic nature are chosen to get the desired fiber structure. PAAm as a water-soluble polymer is synthesized for an inner layer of multi-walled hollow fibers via dispersion polymerization and free radical initiator. Viscosity average molecular weight ( $M_v$ ) of PAAm, measured by Mark–Houwink method, is about 87000 g/mole.  $T_g$  of PAAm is around 189°C.

Figure 2.3 exhibits 2-dimensional solubility diagram of PMMA, and the suitable solvents for complete solubility of PMMA are located within the circled area. As stated previously, PAAm as an inner layer is mainly soluble in water; however, different co-solvents with various volume ratios are utilized to tailor the interaction of inner and outer layer solutions.

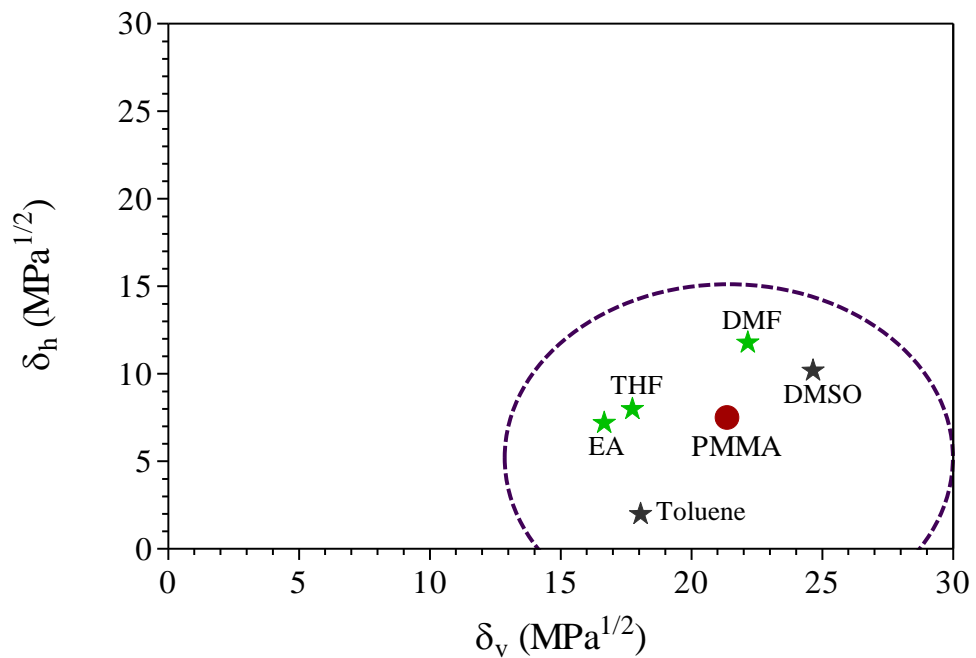


Figure 2.3 2-dimensional solubility diagram of PMMA.

### 2.3.2. Study of layer materials by single electrospinning

Suitable window of processing and material parameters for stable electrospinning process of each polymer is initially determined by performing single-axial

electrospinning. In the case of outer layer materials, polymer concentration in solution plays a critical role in final morphology of fibers. As such, the concentration of PMMA lower than 15 wt % leads to the formation of spherical particles while the concentration higher than 20 wt % results in uniform and brittle electrospun fibers as shown in Figure 2.4a. Such a difference in the form of final electrospun product is attributed to the increase in polymer chains in the solution, which enhances the entanglement density and raises the solution elastic behavior. It was observed that polymer concentration higher than 40 wt. %, is not suitable to produce uniform fibers. Single axial electrospinning conditions are also optimized for PAAm as a middle layer. PAAm nanofibers reveal the continuous, uniform and smooth morphology with an average diameter of 250 nm. Unlike fibers obtained using outer layer polymers, PAAm fibers do not show any brittleness and continuous fiber network is observed. Single axial electrospinning experiments show that optimum electrospinning parameters which render a stable Taylor cone and hence uniform fiber formation are those of solution concentration between 20 to 30 wt. %, deposition distance between 5-10 cm and the applied voltage between 5-20 kV.

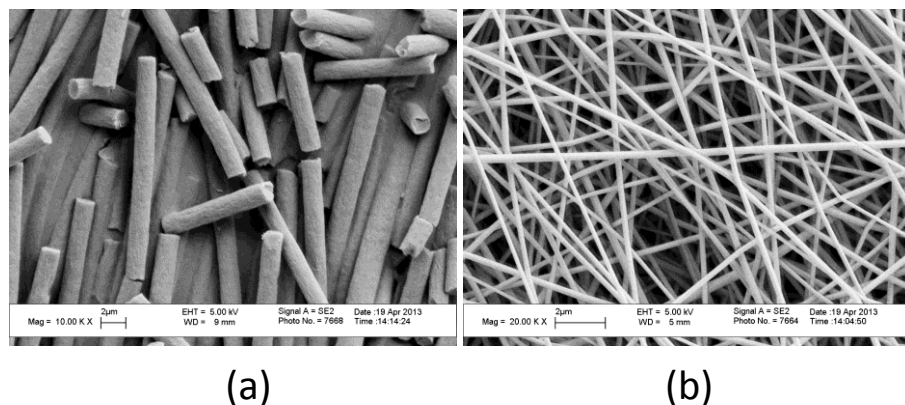


Figure 2.4 SEM images of single axial electrospun fibers (a) PMMA and (b) PAAm. (The concentration of each polymeric solution is 30 wt. %).

### 2.3.2.1. The effect of solvent on the formation of multi-walled hollow fibers

The type of solvent is one of the most important and influential parameters in controlling the morphology and diameter of electrospun polymeric fibers [39]. Multi-axial electrospinning as a newly emerged technique for the fabrication of electrospun

fibers with intricate and advanced morphology requires further considerations for the selection of proper solvent to obtain the desired fiber structures. Figure 5 gives SEM images for multi-walled hollow electrospun fibers with outer layer of PMMA and inner layer of PAAm by using different solvents in outer layer solution. The results show that the fiber diameter increases upon increasing solvent vapor pressure. DMF results in the formation of fiber with the diameter less than 100 nm whereas ethyl acetate (EA) increases the fiber diameter up to 500 nm, and the largest fiber diameter about 1  $\mu\text{m}$  is obtained by THF. The high vapor pressure of THF provides faster drying of outer layer solution during electrospinning process, but solvents with lower vapor pressure like DMF bring about the longer drying time. Thus, polymeric jet with solvents of lower vapor pressure is exposed to instabilities for longer duration and in turn the diameter of fibers is reduced before reaching the surface of the collector. In addition, higher dielectric constant of solvent like DMF provides higher stored electrical energy, ion disassociation and free charge in solution jet. Hence, the polymeric jet is being subjected to higher electrical forces, thereby contributing to further reduction in fibers' diameter [40]. In addition, the inset image in Figure 5b indicates complete breakage of outer layer and the rupture of inner layer that reveals distinct layers and the hollowness of the fiber.

Figure 2.5 also indicates that the solvent type directly affects the surface morphology and porosity of the fibers. In the electrospinning process, rapid acceleration of jet toward the collector surface increases the surface area of the jet hence leading to significantly higher rate of solvent evaporation and rapid evaporation cooling. Thermodynamic instability caused by this cooling leads to phase separation of jet solution into the polymer-rich and solvent rich phase which after drying of the fibers the polymer rich phase remains and the solvent-rich phase forms pores [41]. Heat of vaporization in DMF is higher than THF, but higher rate of evaporation and lower heat capacity of THF made evaporation cooling phenomena stronger resulting in greater phase separation and more porosity within the final fibers. Furthermore, evaporation cooling during the electrospinning caused the condensation of water vapor in the air onto the fiber surface as droplets known as “breath figures” left the pore on the fiber surface after drying of fibers [42].

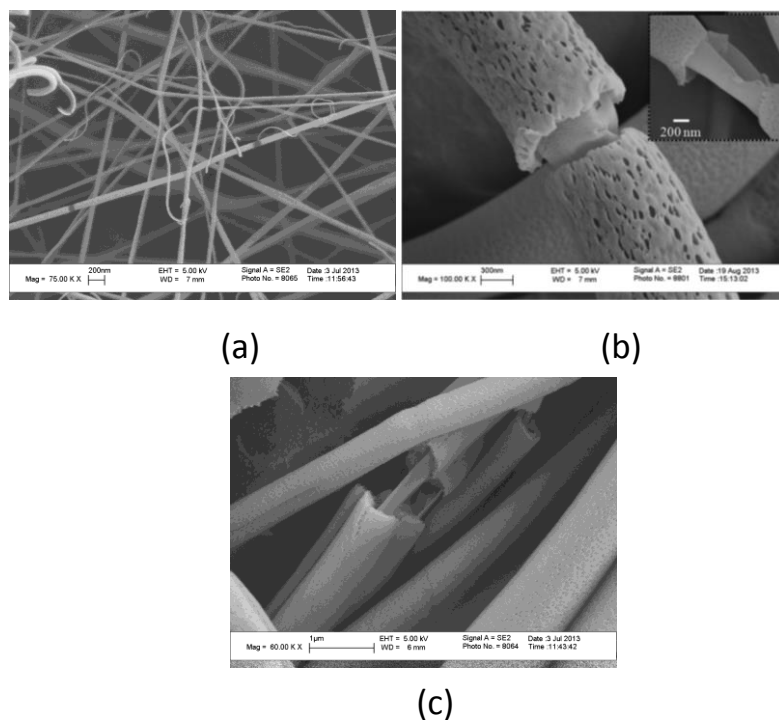


Figure 2.5 SEM images of electrospun multi-walled hollow PMMA/PAAm fibers fabricated by different outer wall solvents (a) DMF, (b) EA and (c) THF.

The miscibility of layer solutions in multi-axial electrospinning process is another parameter influencing the final morphology of fibers. It is expected that solutions with lower affinity with respect to one another form distinct layers with clear interface upon the electrospinning whereas solutions with partial miscibility causes diffusive interface morphology between the layers [38]. For instance, PS as an outer layer is completely soluble in DMF and PAAm is dissolved in water easily. During the process of these materials, water and DMF mixture with volume ratio of 3:2 (WD32) is used to dissolve PAAm inner layer but DMF present in both inner and outer layers increases the affinity of both inner and outer layer solutions whereby layers start to diffuse through each other. To explain the affinity of solutions in question quantitatively, it is prudent to refer to Hansen solubility space. In

Figure 2.6, one can see that the WD32 solvent is located at a distance of  $12.25 \text{ MPa}^{1/2}$  from DMF in Hansen space (high affinity) while water is at a longer distance of  $30.6 \text{ MPa}^{1/2}$  from the WD32, implying less affinity to outer layer solution. SEM images in

Figure 2.7 reveal the formation of electrospun multi-walled hollow fibers produced by different pairs of solutions providing different affinities for layers.

Figure 2.7a shows a sharp and smooth interface between inner and outer layers of the fibers prepared by PAAm in water as an inner layer and PS in DMF as an outer layer. On the other hand, this distinction between layer materials is not observed in

Figure 2.7 7b due to high affinity of layer solvents. One may note that the inner diameter of the severed surface shown in the inset of

Figure 2.7a is larger than the diameter of the stretched inner layer in the corresponding figure, hence pointing to the hollowness of the fiber.

For better visualization of the hollowness in the multi-walled hollow electrospun fibers, in Figure 2.8 are given SEM images of PS/PAAm fiber synthesized with solvents of THF and water for the outer and inner layers, respectively. Recalling that as the vapor pressure of the solvent increases, so does the diameter of the fiber, and hence, the hollowness can be easily noticed through paying attention to the topology of the fractured fiber surfaces.

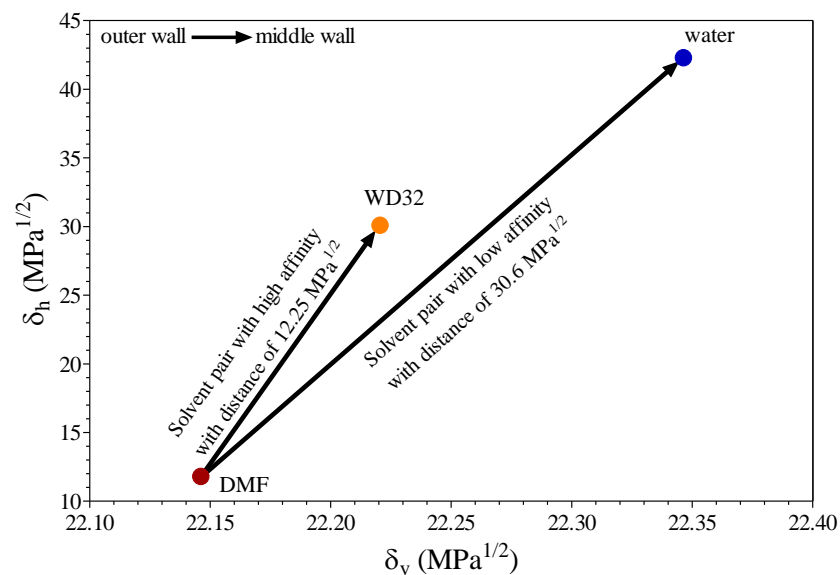


Figure 2.6 The graph of distance of inner layer solvent and outer layer solvent calculated by Hansen solubility space as an index of their affinity.

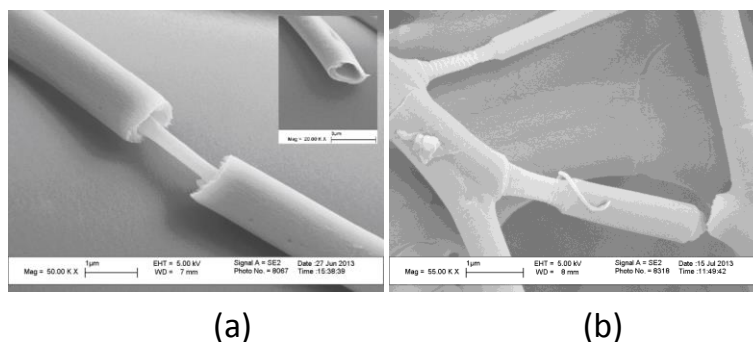


Figure 2.7 SEM images of multi-walled hollow electrospun fibers of PS/PAAm synthesized with the outer layer solvent of DMF by changing inner layer solvent of (a) water and (b) mixture of water/DMF (volume ratio 3:2).

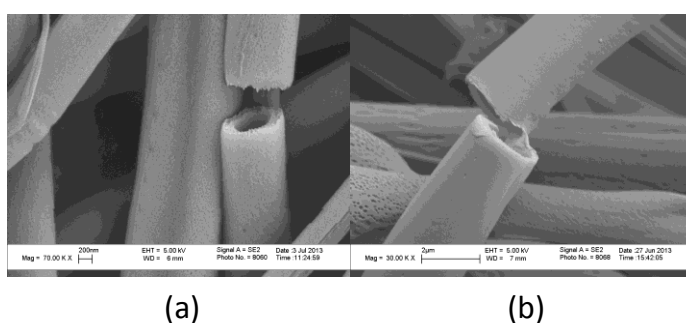


Figure 2.8 SEM images of multi-walled hollow electrospun fibers of PS/PAAm synthesized with solvents of THF and water for the outer and inner layers, respectively: (a) and (b) present images at different magnifications.

### 2.3.2.2. The effect of applied voltage on the formation of multi-walled hollow fibers

Electrical field generated by applied voltage between nozzle and collector is another crucial factor for the production of hollow electrospun fibers. The polymer droplet on the tip of the nozzle needs applied voltage higher than threshold voltage, at which the electric force overcomes the forces associated with the surface tension letting jet to travel toward the collector surface [43]. The balance between the surface and electrical force is also critical in the shape of Taylor cone. Figure 2.9 represents the Taylor cone formations in different applied voltage. Unstable Taylor cone initiates at the applied voltage of 10 kV for PMMA/PAAm hollow fibers jet and then stable Taylor cone is monitored by increasing the voltage up to 20 kV. Moreover, it is observed that further increasing the applied voltage reduces the volume of the cone, and at the 30 kV, multiple

cones are formed resulting in unstable and unpredictable electrospinning process. Figure 2.10 shows the graph of fiber diameter change as a function of applied voltage. As the applied voltage increases from 10 to 20 kV during the fabrication of hollow fibers with outer layer of PMMA solution in DMF and inner layer of PAAm solution in water/DMF mixture, it is observed that the fiber diameter also gradually increases. This can be attributed to the fact that since the applied voltage decreases the travel time of the fiber between the nozzle and collector thereby decreasing bending instabilities, and whipping motions of the fiber experience, the decrease in exposure time to these instabilities leads to increase in the fiber diameter with the increasing applied voltage. Moreover, increasing the applied voltage accelerates the electrospinning process but limits the fiber drying time before reaching the collector whereby wet fibers are gathered on the collector surface.

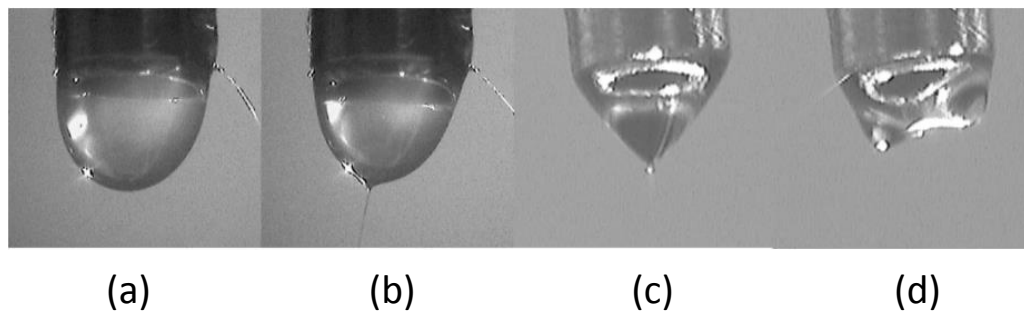


Figure 2.9 Taylor cone formation of PMMA 20 wt.% in EA as outer layer solution and PAAm in water as inner layer solution in different applied voltage (a) no voltage, (b) 10 kV, (c) 20 kV and (d) 30 kV.

Another important parameter affecting the formation of stable cone shape is the flow rate. It is known that if the flow rate of inner and outer layer solutions through the nozzles are insufficient to eject the solutions continuously from the tip of the nozzle, flow instabilities unavoidably occurs hence resulting in bead formation, or defects in the fiber structure [44]. Incompatibility in flow rates for inner and outer fluids can lead to non-uniformities in fiber layers. In course of determining the range of workable flow rates for inner and outer layer solutions, namely 10-50  $\mu\text{l}/\text{min}$ , it is observed the best possible cone shape for core-shell formation is obtained by the flow rates of 20  $\mu\text{l}/\text{min}$  and 15  $\mu\text{l}/\text{min}$  for outer and inner layers, respectively. In the electrospinning of multi-layer fibers, the flow rate of outer layer solution should be always higher than those of inner layer and

core (if exists) solutions to have a complete coverage of these materials and in turn produce structures with uniform layers.

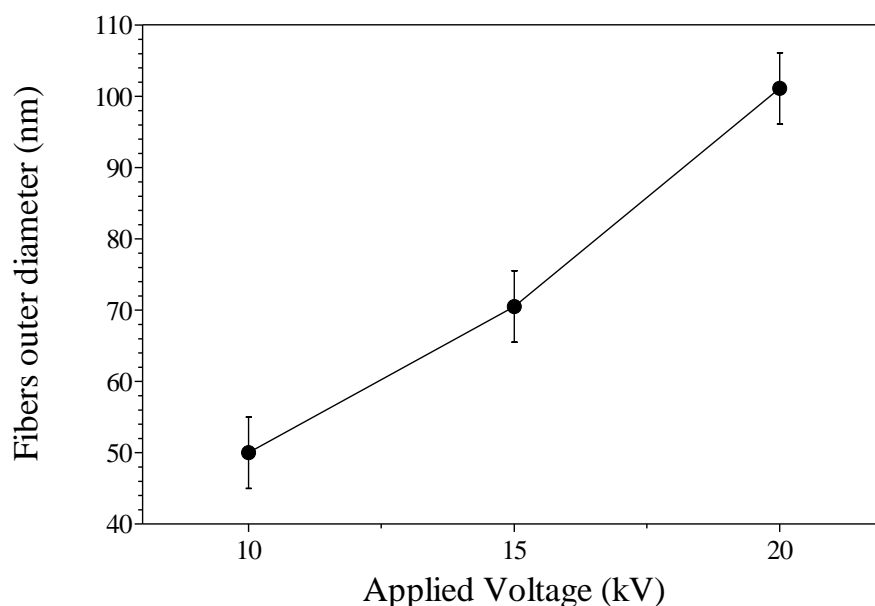


Figure 2.10 Changes in the fiber diameter by increasing the applied voltage for fibers with outer layer of PMMA in DMF and inner layer of PAAM in WD32 (water: DMF=3:2 (v/v)).

### 2.3.2.3. The effect of outer layer polymer on fiber formation and hollowness

In conventional core-shell electrospinning, it is a difficult process to control the hollowness continuously since the instabilities in the course of core formation can occur throughout the spinning process [45]. In this work, we have shown that the utilization of an inner layer, which is readily possible with tri-axial electrospinning process, can overcome these instabilities by acting as a barrier and increasing interconnection between layers. In order to be able to show that the hollowness and structural integrity of the fibers can be controlled, we have electrospun fibers using two different outer layer polymers, namely PMMA and PS while keeping the inner layer material the same, PAAM. Figure 2.11 and 2.11b show TEM images of tri-axial PMMA/PAAM hollow fibers. Bright sections in the central part of fibers with a diameter of about 100–125 nm correspond to hollow core formation. The inner layer of the fiber appears black in color whereas dark gray region belongs to the outer layer of fiber. In Figure 2.11c is given the rupture of inner layer observed in multi-walled hollow fiber structure. Figure 2.12 shows that the usage of PS as an outer layer instead of PMMA leads to an increase in the inner diameter

up to 250 nm. One may reliably conclude from the presented TEM results that the diameter of hollowness can be adjusted by changing the type of polymer in the outer layer. Different polymers have dissimilar affinities with the same solvent, which can influence the drying behavior of solvents during the electrospinning process thereby affecting the wall thickness of the fibers and in turn their hollowness. The controllability of hollowness diameter can provide an easy encapsulation of functional materials with different viscosities if required, and increase the life-time of encapsulated materials through circumventing leakage.

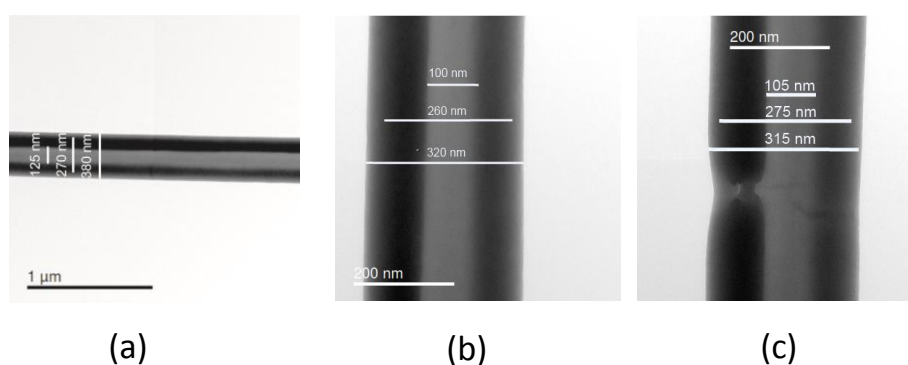


Figure 2.11 TEM images of (a) and (b) PMMA/PAAm multi-walled hollow fibers with continuous core structure at different magnifications, and (c) the rupture of middle layer in tri-axial hollow fiber structure (Outer layer solvent: EA, inner layer solvent: water).

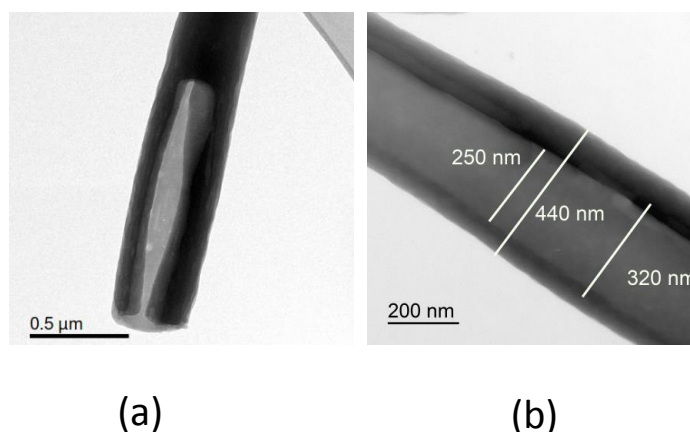


Figure 2.12 TEM images (a) and (b) of PS/PAAm hollow fibers in different regions and at different magnifications (Outer layer solvent: EA, inner layer solvent: water).

In addition to homopolymers, copolymers of styrene and methyl methacrylate are also utilized as an outer layer. Figure 2.13 shows SEM images of tri-axial hollow electrospun fibers fabricated by electrospinning of poly(methyl methacrylate-co-styrene) as an outer layer in different solvents, namely, EA, and THF. The layers of these hollow

fibers produced by EA separate easily from each other and the proper connection is not achieved between inner and outer layers (Figure 2.13a). On the other hand, outer layer processed by THF is not easily separated from the inner layer and fiber elongation can be seen clearly in Figure 2.13b and 2.13c. Consequently, it is possible to fabricate electrospun hollow fibers with different structures and functionalities by using several polymers through tri-axial electrospinning technology.

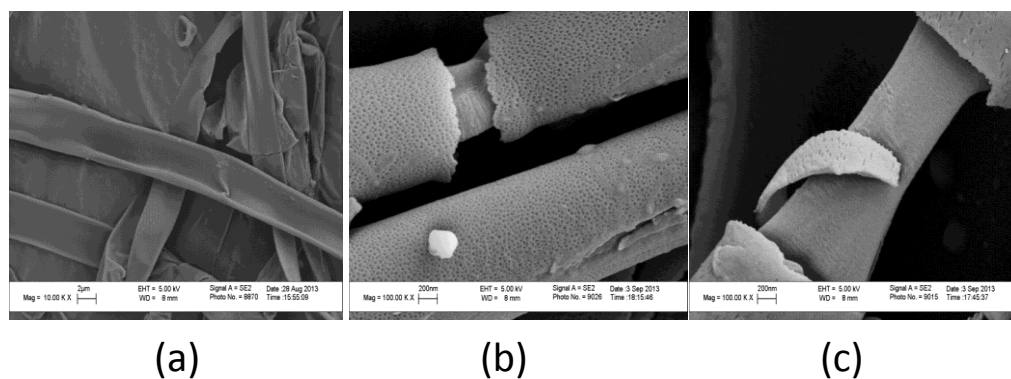


Figure 2.13 SEM images of multi-walled hollow fibers with PAAm as an inner layer and poly(methyl methacrylate-co-styrene) as an outer layer prepared by using solvent of (a) EA, (b) and (c) THF.

### 2.3.3. Structural and thermal analyses of multi-walled hollow fibers

The formation of tri-axial hollow fibers was also investigated by monitoring the functional groups of each layer. Figure 2.14 exhibits FTIR spectrum of multi-walled hollow fiber with PMMA as an outer layer and PAAm as an inner layer. For PMMA polymer, absorption bands at  $2950\text{ cm}^{-1}$  and  $1745\text{ cm}^{-1}$  indicate C-H and C=O stretchings, respectively [46]. For PAAm polymer, asymmetric and symmetric NH stretching of  $\text{NH}_2$  contribute to absorption bands at around  $3300\text{ cm}^{-1}$  [47]. EDX results showed that tri-axial hollow fiber included 56% carbon, 30% oxygen and 14% nitrogen. The nitrogen content in the fiber indicates the presence of PAAm in fiber structure.

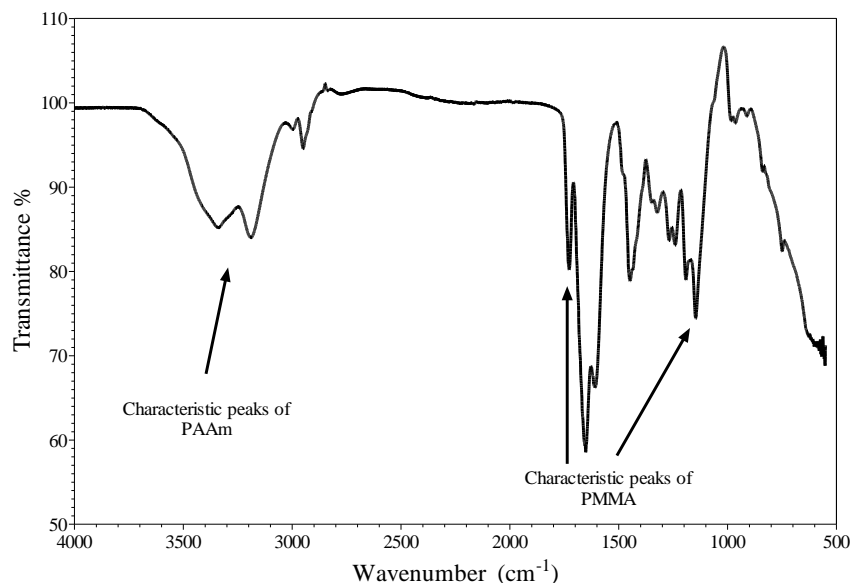


Figure 2.14 FTIR spectrum of multi-walled hollow electrospun fiber with PMMA as an outer layer and PAAm as an inner layer.

The thermal stabilities of PMMA/PAAm multi-walled hollow fibers were evaluated by means of TGA and DTA thermograms. Figure 2.15 exhibits TGA and DTA curves of PMMA and PAAm polymers and multi-walled hollow fiber. Neat radically prepared PMMA shows three steps of weight loss. At first step, PMMA lost 4 % of its weight between 175-225°C due to chain scissioning of head-to-head unstable and sterically hindered linkages [48]. The second stage of degradation with weight loss of 34% was observed between 250-325°C due to scissioning of unsaturated ends (resulting from termination by disproportionation). In the last step, 62% of polymer weight were lost between 325-450°C described by random scissioning within the polymer chain [49]. In the case of neat PAAm, two stages of degradation were observed with 18% weight loss between 225-350°C because of amide side-groups decomposition and, 56% weight loss in the range of 350-500°C due to backbone decomposition [50]. The weight loss curve of multi-walled hollow fibers appeared between PMMA and PAAm (Figure 2.15 15a). As a result, FTIR and TGA analyses proved the successful formation of multi-walled hollow fibers with different layer polymers during tri-axial electrospinning process.

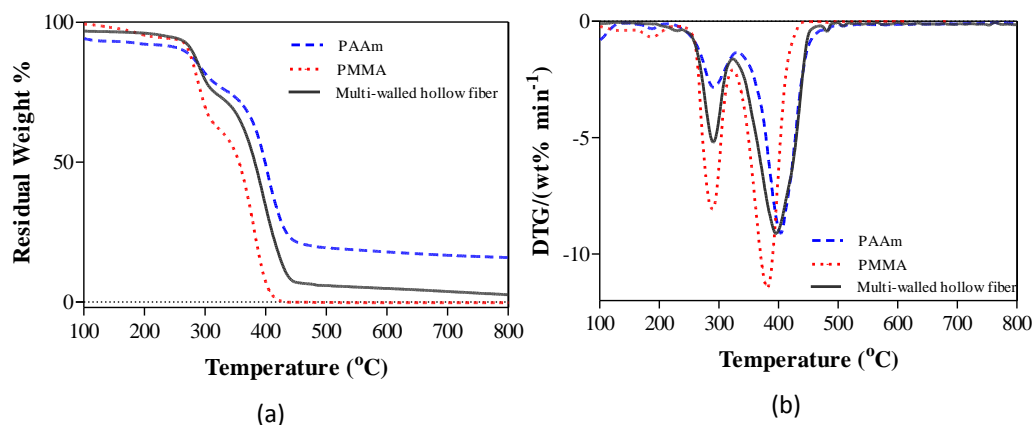


Figure 2.15 (a) TGA curves of PMMA, PAAm and multi-walled hollow fibers and (b) differential thermal analyses of PMMA, PAAm and multi-walled hollow fibers.

## 2.4. Conclusions

In the present work, multi-walled electrospun fibers with controllable hollowness and different polymeric layers were fabricated by a single step process. The inner and outer diameters of fibers and surface morphologies are controlled by changing the solvent type, applied voltage, polymer concentration and polymer type. The suitable window of material and processing parameters for electrospinning of each polymer were determined using single axial electrospinning. This was the first work in the literature to show the production of multi-walled hollow electrospun fibers covered by two different polymeric layers. The system and process parameters of tri-axial electrospinning were optimized to fabricate an ideal hollow structure. The diffusion of layers during electrospinning was controlled by using Hansen solvent selection methods. If the polymer concentration was lower than 15%, the sphere-based structure formation was observed. On the other hand, smooth fibers formation was monitored by increasing the polymer concentration. The porosity of fiber surface and the diameter of hollowness were directly affected by changing outer layer material and the solvent type. In conclusion, these novel fibers with different functionalities can be utilized in water filtration, composites, dialysis membranes, catalysis, drug delivery, membrane, photonics and coatings.

## **CHAPTER 3. DESIGN AND FABRICATION OF MULTI-WALLED HOLLOW NANOFIBERS BY TRIAXIAL ELECTROSPINNING AS REINFORCING AGENTS IN NANOCOMPOSITES**

Multi-walled triaxial hollow fibers with two different outer wall materials are fabricated by core-sheath electrospinning process and integrated into epoxy matrix with or without primary glass fiber reinforcement to produce composites with enhanced mechanical properties. The morphologies of multi-walled hollow fibers are tailored by controlling the materials and processing parameters such as polymer and solvent types. The triaxial hollow fiber fabrication is achieved through using a nozzle containing concentric tubes which allows for the transport of different fluids to tip of the nozzle under the applied high voltage. In comparison to uniaxial electrospun fibers, the hollowness of electrospun fibers enables one to manufacture new reinforcing agents that can improve the specific strength of composites. It is shown that the mechanical properties of epoxy matrix composite incorporated with electrospun fibers as primary fiber reinforcement can be significantly tailored by properly selecting the wall materials, diameters, and the amount of electrospun fibers. We have also presented that triaxial electrospun hollow fibers as co-reinforcement in the glass fiber laminated epoxy matrix composites enhances the flexural modulus by 6.5 %, flexural strength by 14 %, the onset of first layer of glass fabric failure strain by 12.5 % and final failure strain by 20%.

### **3.1. Introduction**

Fiber reinforced advanced composites with thermosetting matrix have emerged as structural materials in applications such as wind turbines, construction, defense, aeronautics and aerospace due to their high strength, rigidity and light weight. The performance of fiber reinforced composites is mainly controlled by the strength of the fiber–matrix interface and the efficiency of load transfer from the matrix to the reinforcement fiber [51]. However, most of the fiber reinforced composites do suffer from inadequate interlaminar strength and low fracture toughness which may cause catastrophic failures without showing any external signs of the damage [52].

Recently, electrospun polymeric fibers with high surface area to volume ratio, tailorable surface functionality and excellent mechanical performance compared to microfibers of the same material have been considered as an efficient reinforcing material in design and fabrication of polymer matrix composites [53]. Electrospun fibers can be utilized as primary reinforcement as well as co-reinforcement in the presence of high performance microfibers such as glass and carbon fabrics [54, 55]. Dzenis et al. [56] pioneered the utilization of electrospun nanofibrous mat for improving the interlaminar fracture resistance, interlaminar toughness, strength and delamination resistance of laminated composite materials. Li et al. [57] used polysulfone electrospun mat interlayers to enhance interlaminar fracture toughness of carbon fiber/epoxy composite and reported that the electrospun fibers improve the fracture toughness more efficiently than films prepared by solvent method. In another work, the electrospun polycarbonate nano-interlayers inserted between the plies of laminated composite shifted the onset of delamination to higher stress level by 8.1 %, and decreased the numbers of microcracks at the delamination stress by 21.6 % and increased the ultimate strength by 9.8 % [58]. Zhang et al. [59] demonstrated interlayer toughening of carbon/epoxy composites by using polyetherketone cardo nanofiber membranes electrospun directly onto carbon fabrics. Their results showed that finer nanofiber stabilized the crack propagation during delamination thereby improving the flexure property. They also reported that the increase in the nanofiber interlayer thickness resulted in enhanced Mode I delamination fracture toughness and reduced flexure strength. Bilge et al. [60, 61] used chemistry tuned compatibility of Poly(styrene-co-glycidyl methacrylate) nanofibers with epoxy matrix and its ability to confine multi-walled carbon nanotube (MWCNTs) to increase both flexural strength and flexural modulus up to 25 % and 29 % respectively as well as enhancing the delamination resistance up to 70 % in carbon/epoxy laminated composite.

On the other hand, several research groups have utilized electrospun fibers as primary reinforcing agents in thermosetting matrix. Gao et al. [62] integrated electrospun glass nano-fibers into dental composites to increase flexural strength, young modulus and fracture energy of specimens. Moreover, Lin et al. [63] utilized core-shell nanofibers with the high strength core and the shell with good adhesion to matrix through shell chains interpenetration and entanglement with the cross-linked matrix to create an in-situ nano-interface in order to reinforce the Bis-GMA dental resin. The strength, Young's modulus,

and work of failure were enhanced by 18.7 %, 14.1 % and 64.8 %, respectively. Ozden et al. [55] studied the reinforcing abilities of three different polymeric electrospun fiber to monitor the effect of glass transition temperature on stiffness of composites. When MWCNT is used as a reinforcing agent in electrospun poly(styrene-co-glycidyl methacrylate), a significant increase in flexural modulus was observed up to 20% compared to neat epoxy [53].

In the present work, tri-axial hollow fibers with two different wall materials and novel architecture are fabricated by using multi-axial electrospinning. Two different polymers, namely, polystyrene and polymethyl methacrylate, both of which are known to have high compatibility with epoxy matrix, are utilized as outer wall of electrospun fibers to improve the strength of the fiber–matrix interface and in turn to increase the efficiency of load transfer from the matrix to the fibers. The middle wall of electrospun fibers is fabricated from polyacrylamide (PAAm) having higher strength than the outer wall material to enhance the mechanical properties of electrospun fibers. Tri-axial hollow fibers with different morphology and diameter are produced by tailoring the materials and processing parameters [64]. Classical molding and vacuum infusion techniques are employed to produce hollow fiber reinforced composites. In classical molding process, the electrospun fiber is used as a primary reinforcement for the epoxy resin. The effect of fiber wall materials, fiber diameter, and fiber content on mechanical performance of epoxy composites is investigated by monitoring flexural properties. In vacuum infusion process, tri-axial electrospun fibers are deposited onto glass fibrous mats to form interlayers and the effect of the interlayers on the mechanical performance of laminated composites is studied extensively.

## **3.2. Experimental**

### **3.2.1. Materials**

Polymethyl methacrylate (PMMA) and Polystyrene (PS) (used as epoxy matrix compatible outer wall materials fibers) were synthesized by free radical polymerization of vinyl monomers (30 ml) in presence of Azobisisobutyronitrile (AIBN, 1 gr) as the radical initiator in the medium of tetrahydrofuran (THF, 50 ml) at 65°C for 4 h and then, the reaction mixture was precipitated in cold methanol and dried for 12 h in a vacuum oven at 50°C. Polyacrylamide (PAAm) as a water-soluble polymer (employed as high

strength inner wall material for fibers) was synthesized by dispersion polymerization of acrylamide monomer (30 g) in methanol (100 ml) by using AIBN (1 g) as an initiator at 65°C. The separation of polymer particles from methanol and monomer mixture was done by vacuum filtration and twice washing the polymer particles with methanol and drying it for 12 h in a vacuum oven at 40°C. Molecular weight (Mw), polydispersity index (PDI), and glass transition temperature (Tg) of these polymers are presented in Table 1. The molecular weight and polydispersity index (PDI) of outer wall polymers were determined by Viscotek-VE2001 gel permeation chromatography (GPC) in DMF and the viscosity average molecular weight of PAAm was measured by Mark–Houwink method. N, N-dimethyl formamide (DMF, Sigma-Aldrich, 99%), THF (Merck, 99%), and ethyl acetate (EA, Sigma-Aldrich, 99.5%) were used as solvents in solution preparation for electrospinning process. Araldite LY 564 resin, Hardener XB 3403 and 0/90 biaxial E-glass stitched fabrics of Metyx company with the average weight of 313 g/m<sup>2</sup> (161 g/m<sup>2</sup> along the (0°) direction, and 142 g/m<sup>2</sup> along the (90°) direction) were used for the production of laminated composite.

Table 3.1 Mw, PDI and Tg of outer wall polymers of electrospun fibers. \*Viscosity averaged molecular weight (Mv) measured by Mark–Houwink method

Polymer	Tg (°C)	Mw (g/mole)	PDI
PMMA	123	326000	3.2
PS	103	313000	1.7
PAAm*	189	87000*	-

### 3.2.2. Fabrication of electrospun tri-axial hollow fibers

Electrospinning process was performed by using custom made tri-axial nozzle and electrospinning set-up purchased from Yflow Company. The outer and inner diameters of the outer and middle nozzles are respectively 2.28/1.7 mm, and 1.4/1.1 mm while a rod with diameter of 0.7 mm is used as inner part of electrospinning nozzle system to provide hollowness to the electrospun fiber. Prepared solutions for each wall were loaded independently into the syringes connected to a nozzle, and the flow rate of each wall material was controlled by separate pumps. The flow rate of outer wall was kept higher than that of middle wall in order to have a complete coverage of middle wall by the outer wall material where the flow rates of the outer and inner walls are respectively 20 µl/min

and 15  $\mu\text{l}/\text{min}$ . Electrospinning process was performed using a fixed nozzle to collector distance of 7 cm and tuned applied voltage in the range of 5 kV to 30 kV to obtain stable Taylor cone. Figure 3.1 shows the schematic representation of tri-axial electrospinning set-up and process.

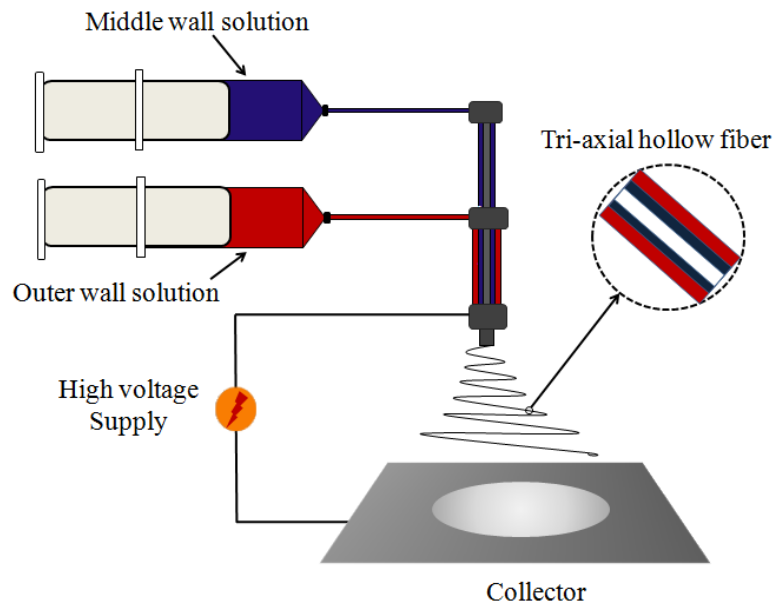


Figure 3.1 Schematic representation of tri-axial electrospinning set-up.

### 3.2.3. Fabrication and characterization of fiber reinforced epoxy composites

Two different composite production methods, namely, classical molding and vacuum infusion processes are utilized to prepare hollow-fiber reinforced composites. In the former method, appropriate amount of electrospun fibers are placed into Teflon moulds in such a way that the mold surface and height is uniformly covered, and then impregnated by the mixture of degassed resin and hardener system. Subsequently, vacuum oven is employed to remove the entrapped air bubbles from the resin and to cure the resin hardener mixture at 50°C for 15 h and post cure at 80°C for 24 h. The electrospun fiber reinforced molded samples have the length, the width, and the thickness of 100 mm, 14 mm, and 3 mm respectively for three point bending tests. In order to investigate the effect of electrospun fiber on the mechanical properties of glass fiber reinforced epoxy matrix composite, tri-axial hollow fibers are initially deposited only on the 0° side of the 90°/0° biaxial E-glass stitched fabrics, which are then stacked to form a laminate of

$[(90^\circ/0^\circ)_3]_s$ . Upon stacking, the electrospun interlayer on the  $0^\circ$  side is shared with the  $90^\circ$  side of the biaxial fabric. The stacked fabrics are impregnated by the epoxy resin after being degassed by vacuum infusion process to manufacture a composite panel with the dimensions of  $30\text{ cm} \times 20\text{ cm} \times 0.25\text{ cm}$ . The stacking sequence of the plies together with the placement of interlayer, and the schematic of the resin infusion process are given in Figure 3.2. The weight fraction of the primary reinforcement is 60 wt % while the weight content of the electrospun fiber is 2 wt %. The volume fractions of glass fiber in the composite laminates were calculated by burning test as nearly 40 % of overall composites. The manufactured composite panel is cut to flexural and tensile test specimens with the dimensions of  $8\text{ cm} \times 1.5\text{ cm} \times 0.25\text{ cm}$ , and  $16\text{ cm} \times 2\text{ cm} \times 0.25\text{ cm}$  (with the gage length of 10 cm) respectively, which are then tested to evaluate their mechanical properties. To avoid the breakage of tensile specimens at grip locations, both ends of specimens are tabbed with an aluminum tab having a dimension of  $3\text{ cm} \times 2\text{ cm} \times 0.1\text{ cm}$  using two-component room temperature curing epoxy system (araldite, 2011). Flexural and tensile tests are repeated three times for each type of specimens.

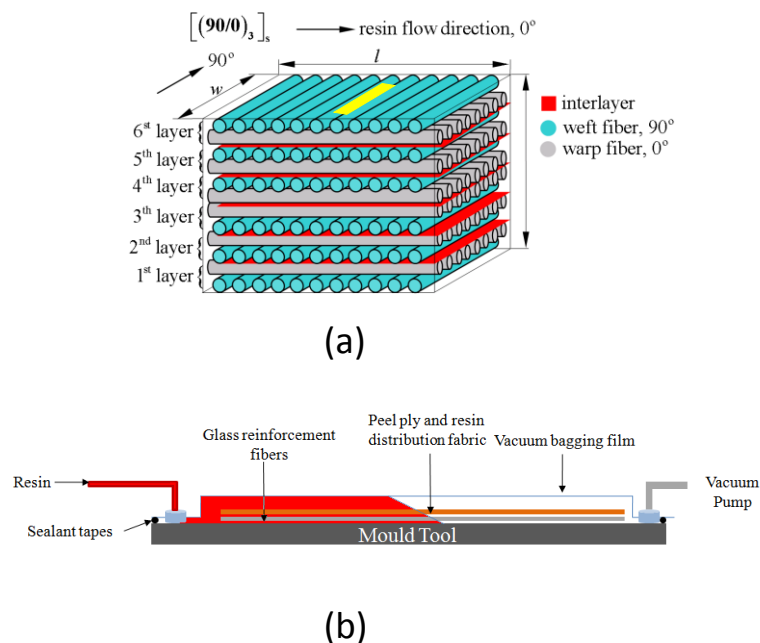


Figure 3.2 A schematic representation of composite manufacturing by vacuum infusion, a) stacking sequence and the placement of the interlayer where the yellow region indicates the cut specimen for flexural and tensile tests, and b), the vacuum infusion system.

A detailed fractographic analysis was carried out in order to identify the failure mechanisms of composites on the cross section along the length of the specimen through

thickness. Both flexural and tensile test specimens are cut such that the length of the specimens is aligned with the direction of weft fibers as shown in Figure 3.2a where the yellow painted region illustrates the cut specimen for flexural and tensile tests. A specific custom-made apparatus is used to stabilize the displacement of composites after 3-point bending test [65] and then these specimens are directly immersed into the fast curing resin/hardener mixture and thus the specimens preserve the displacement after curing. Figure 3.3 represents step by step procedure followed for the preparation of samples for fractographic analysis. Figure 3.3a exhibits the cut specimen of the glass fiber reinforced composite modified by multi-walled hollow polymeric fibers and apparatus which is used in this characterization technique. In Figure 3.3b, specimen is fixed with desired displacement into the apparatus and in Figure 3.3c and 3.3d, the specimen fixed by the apparatus is immersed into the fast curing hardener and epoxy mixture to preserve the displacement after curing. Figure 3.3 e, 3.3f, 3.3g and 3.3h illustrate the specimen after the surrounding epoxy hardener mixture has been cured, and after the specimen is cut into the desired geometry for the next step. The cut specimen containing failure area of 3-point bending specimen is polished and then coated with Au/Pd for SEM characterization (Figure 3.3i).

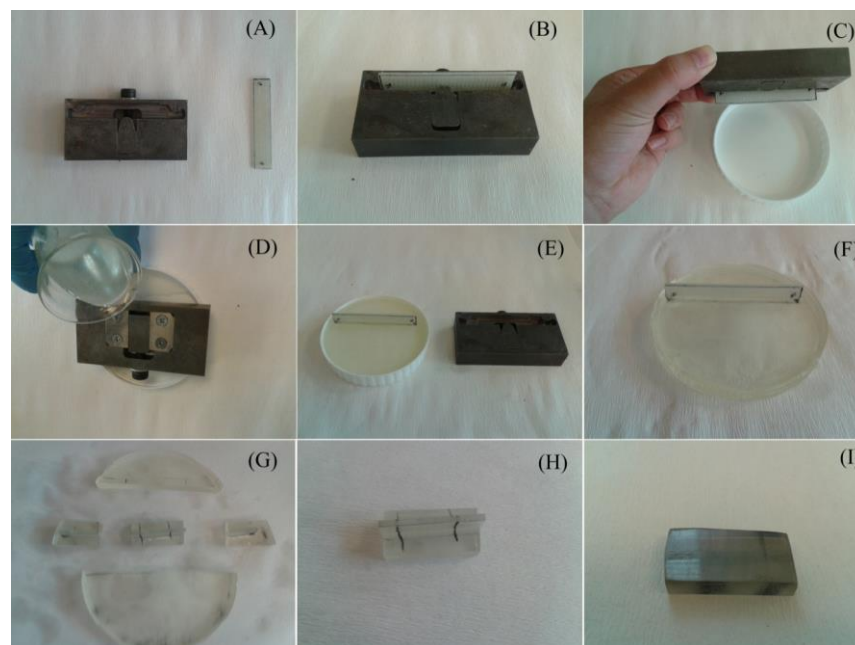


Figure 3.3 Step by step procedure followed for sample preparation for failure mechanisms analysis.

The surface morphologies of fibers and cross sectional area of specimens after breakage were analyzed by a Leo Supra 35VP Field Emission Scanning Electron Microscope (SEM). The mechanical tests were conducted by using ZWICK Proline 100 Universal Test Machine (UTM) with 10 and 100 kN load cells for 3-point bending and tensile tests, respectively using a constant cross-head speed of 2 mm/min. ASTM D790-03 and ASTM D5083 – 02 standards are used for 3-point bending and tensile tests to measure mechanical properties of composite samples, respectively. Dynamic Mechanical Analyzer (Netzsch DMA 242 C) is used to analyze mechanical properties of the composite as a function of temperature, time and frequency.

### **3.3. Results and discussion**

#### **3.3.1. Surface Morphologies of tri-axial hollow fibers**

Three different types of tri-axial hollow electrospun fiber were fabricated to investigate the effect of the type of outer layer polymer, and fibers diameter on the mechanical properties of composites, namely, PMMA/PAAm hollow fibers fabricated by using two different outer wall solvents (i.e., DMF, and EA) and PS/PAAm hollow fibers with the outer wall solvent of EA. Figure 3.4 exhibits the fiber morphology of tri-axial hollow electrospun fibers with outer wall of PMMA and PS and inner wall of PAAm. The effect of solvent type on fiber morphology during electrospinning process is also investigated. When DMF is used as an outer wall solvent in PMMA, the resulting fiber diameter is about 100 nm as shown in Figure 3.4a. On the other hand, higher vapor pressure of ethyl acetate (EA) as outer wall solvent in PMMA leads to the formation of fibers with diameter larger than 500 nm as can be seen in Figure 3.4b. As discussed in details in our previous paper [17], the polymeric jet of the outer wall solution prepared by using low vapor pressure solvent is subjected to the instabilities of electrospinning process at longer time and thus, the diameter of fibers is reduced before reaching the surface of the collector. On the other hand, the utilization of higher vapor pressure solvent results in faster drying of polymeric jet during electrospinning, thereby producing fibers with a larger diameter.

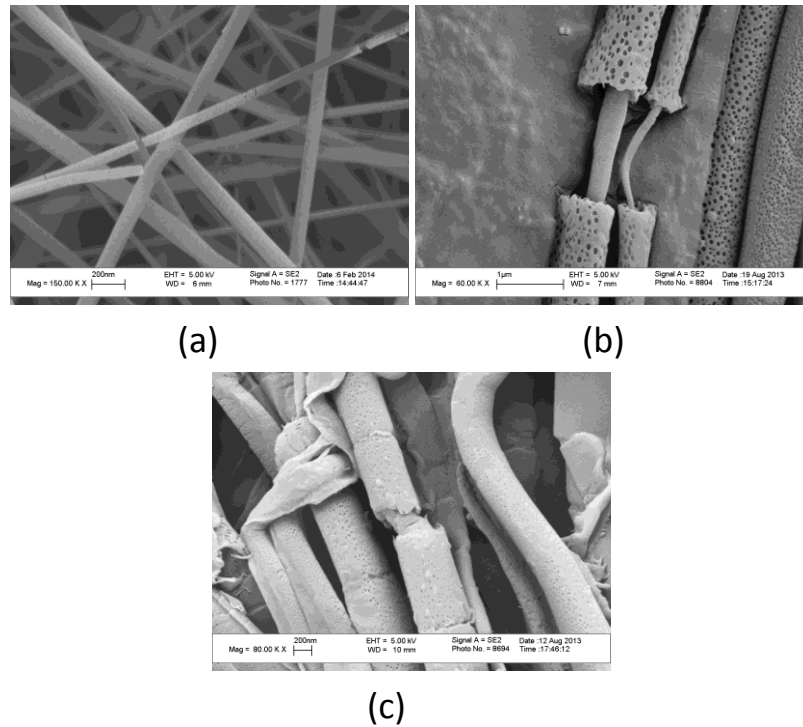


Figure 3.4 SEM images of tri-axial hollow electrospun fibers of (a) PMMA/PAAm fibers fabricated by outer wall solvent of DMF (b) PMMA/PAAm fibers fabricated by outer wall solvent of EA and (c) PS/PAAm fibers fabricated by outer wall solvent of EA.

During the handling of the electrospun fiber mat, it was observed that increasing the solvent pressure makes fibers more brittle. This observation can be substantiated as follows. Note that multi-walled fibers with smaller and larger diameters produced by the same wall materials are expected to have the similar strain values at breakage. Defining the strain as  $\varepsilon = d/r$  where  $d$  is the fiber diameter and  $r$  is the radius of curvature due to the bending, one can readily infer that the fiber having a larger diameter should break with the bigger radius of curvature hence giving rise to more brittle behavior whereas fibers with smaller diameter should be capable of being bent to smaller radius of curvature, thus evoking more bending capabilities. Figure 3.4c represents tri-axial hollow electrospun fiber with outer wall of PS and the diameter of these fibers is almost same as the one having the outer wall polymer of PMMA synthesized by EA solvent shown in Figure 3.4b.

### **3.3.2. Flexural properties of tri-axial hollow fiber reinforced composites**

#### **3.3.2.1. The effect of outer wall material of tri-axial hollow fiber**

The interfacial interactions between outer wall of electrospun fiber and polymer matrix play a critical role to transfer the load from matrix to the reinforcing agent thus improving the mechanical properties of composite. Herein, different outer wall materials are used to tailor the interface properties of electrospun fibers and to provide the best possible interface between electrospun fibers and epoxy matrix. Figure 3.5 presents a comparison of stress-strain curves of electrospun fiber reinforced composite specimens and neat epoxy specimens. The flexural modulus of PS-PAAm tri-axial hollow fiber reinforced composite slightly increases while the brittleness of the specimens increases significantly which can be noted upon comparing the strains at fracture for PS-PAAm reinforced and neat specimens which are nearly  $7\pm 0.5\%$  and  $14\pm 0.3\%$ , respectively. Moreover, referring to flexural strengths of PS-PAAm tri-axial hollow fiber reinforced and neat specimens, which are respectively  $79\pm 0.5$  MPa and  $75\pm 0.4$  MPa, one can see that PS-PAAm tri-axial hollow fibers increase the load-bearing capacity of the matrix. The PMMA-PAAm tri-axial hollow fiber reinforced composite also shows an increase in flexural modulus and yield strength in comparison to specimens reinforced by PS-PAAm tri-axial hollow fibers. This can be attributed to better interfacial compatibility between the PMMA wall of electrospun fibers and epoxy matrix, which can be further elaborated as follows. As depicted in Figure 3.6, PMMA chains in outer shell of electrospun fibers are partially dissolved thereby interpenetrating into epoxy and hardener mixture, resulting in the entanglement of linear PMMA chains with the cross-linked matrix network and hence the formation of semi interpenetrating polymer network (semi-IPN) structure which lends itself to an improved load transfer between matrix and electrospun fibers [63].

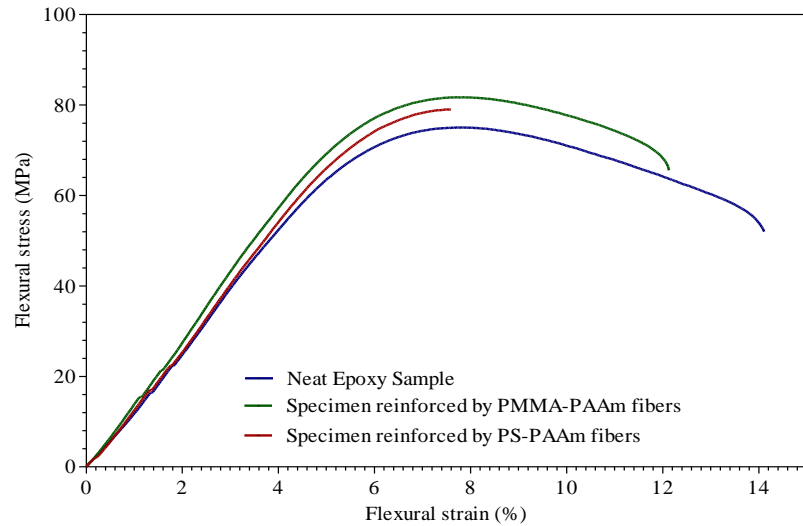


Figure 3.5 Flexural stress-strain curves of samples for neat epoxy and samples reinforced by 0.2 wt.% PS-PAAm and 0.2 wt.% PMMA-PAAm tri-axial hollow fibers. Both fibers are produced with the outer layer solvent of EA and inner layer solvent of water.

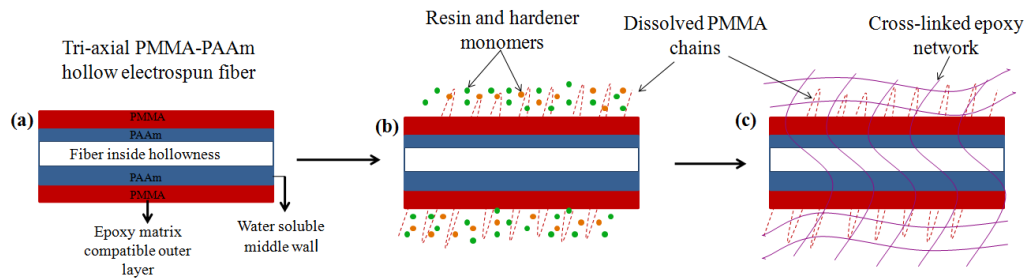


Figure 3.6 Schematic representation of semi-IPN structure formation in PMMA-PAAm tri-axial hollow fiber reinforced composite: (a) PMMA-PAAm tri-axial hollow fiber, (b) partial dissolution of PMMA shell into the resin and hardener mixture and (c) semi-IPN structure.

### 3.3.2.2. The effect of fiber diameter

The diameter of electrospun reinforcing fibers is another critical parameter affecting the mechanical properties of the composite. In Figure 3.7 are provided stress-strain curves for composites reinforced by PMMA-PAAm tri-axial hollow fibers of different diameters while keeping the electrospun fiber content constant for both cases at 0.2 wt.%. PMMA-PAAm tri-axial hollow fibers with an average diameter of 100 nm increase the modulus of composite specimen up to  $1.72 \pm 0.03$  GPa which is significantly higher than the modulus of  $1.44 \pm 0.02$  GPa obtained for specimen reinforced by fibers with an average diameter of 500 nm. Moreover, electrospun fibers with an average

diameter of 100 nm increase flexural strength of specimens up to  $91\pm 0.4$  MPa. This improvement in the flexural properties of composites is attributed to the increase in specific surface area of electrospun fibers due to the decrease in the diameter, which enhances the interactions between the electrospun fibers and the matrix thereby leading to better load transfer between them. On the other hand, finer electrospun fibers shift the failure strain to lower strain levels, which might be attributed to the increase in the number of interface in the composites that can act as crack initiation or stress concentration sites.

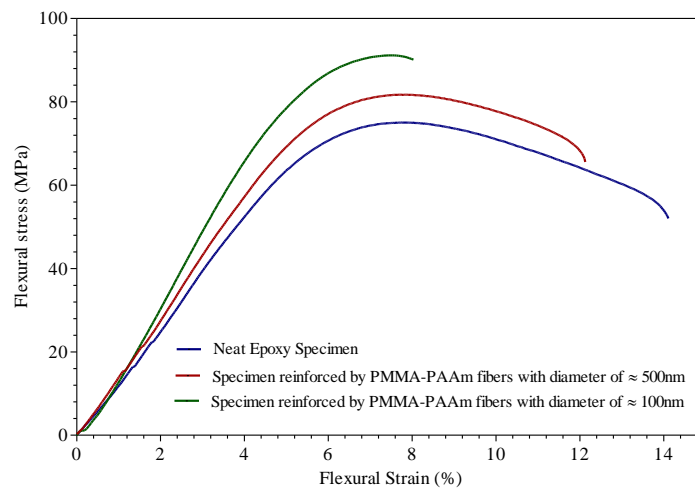


Figure 3.7 Flexural stress-strain curves of neat epoxy sample and samples reinforced by PMMA-PAAm tri-axial hollow fibers with different fiber diameters.

### 3.3.2.3. The effect of fiber content

The effect of electrospun fiber amount on the flexural properties of specimens is also investigated by comparing two different fiber contents of 2 and 0.2 wt.%. Figure 3.8 reveals an increase in flexural modulus of specimens even with low fiber content of 0.2 wt.% whereas raising the fiber content to 2 wt.% further increases the modulus up to  $1.63\pm 0.02$  GPa from the value of  $1.34\pm 0.01$  for neat epoxy specimens. The notable rise in the modulus upon increasing the fiber content is explained by augmenting the accessible interfaces between reinforcing electrospun fibers inside the specimens with epoxy matrix thereby leading to further load transfer to fibers and increasing the modulus. It is also observed that increasing the fiber amount changes the behavior of specimens from ductile to brittle behavior and specimens start to get damaged at lower strain levels, which again can be attributed to the increase in the number of interfaces possibly acting as crack initiation or stress concentration points.

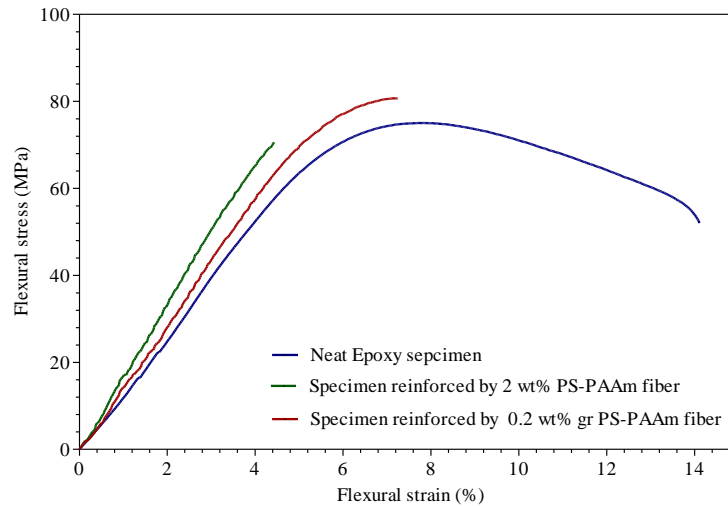


Figure 3.8 Flexural stress-strain curves of neat epoxy specimen and specimens reinforced with 0.2 wt.% and 2 wt.% PS-PAAm tri-axial hollow fiber.

Table 3.2 summarizes flexural strength and flexural modulus of hollow fibers reinforced composites in terms of percentages. The results show that hollow fibers with outer wall of PMMA and the fiber diameter of 100 nm significantly enhance flexural strength and flexural modulus of composite.

Table 3.2 Improvements in the flexural strength and modulus of hollow fibers reinforced composites in %.

Reinforcement	PMMA-PAAm hollow fiber	PS-PAAm hollow fiber	PMMA-PAAm hollow fiber	PS-PAAm hollow fiber
Fiber diameter (nm)	500	500	100	500
Reinforcement amount (wt%)	0.2	0.2	0.2	2
Flexural strength (MPa)	82±0.3	79±0.5	91±0.4	70.5±0.5
Flexural strength improvement (%)	9.3±1	5.3±1.2	21.3±1.2	-5.9±1.2
Flexural modulus (GPa)	1.44±0.02	1.38±0.02	1.72±0.03	1.63±0.02
Flexural modulus improvement (%)	7.4±2.2	2.3±0.7	28.4±3.2	21.6±0.5

### 3.3.3. Fracture surface analysis of hollow fiber reinforced composites

Figure 3.9 gives SEM images for the fracture surfaces of neat epoxy samples and electrospun fiber reinforced composites subjected to 3-point bending tests. In general, the fracture surface of the electrospun fiber reinforced sample looks rougher and more fragmented than that of the neat one. Figure 3.9c exhibits the formation of semi-IPN structure around electrospun fibers, which increase the fiber diameter as well as covers the fiber with thick layer of cross-linked epoxy resin, thus providing higher interfacial interaction and load transfer between the electrospun fibers and epoxy matrix. Figure 3.9d shows the breakage of electrospun fibers at failure area of specimen.

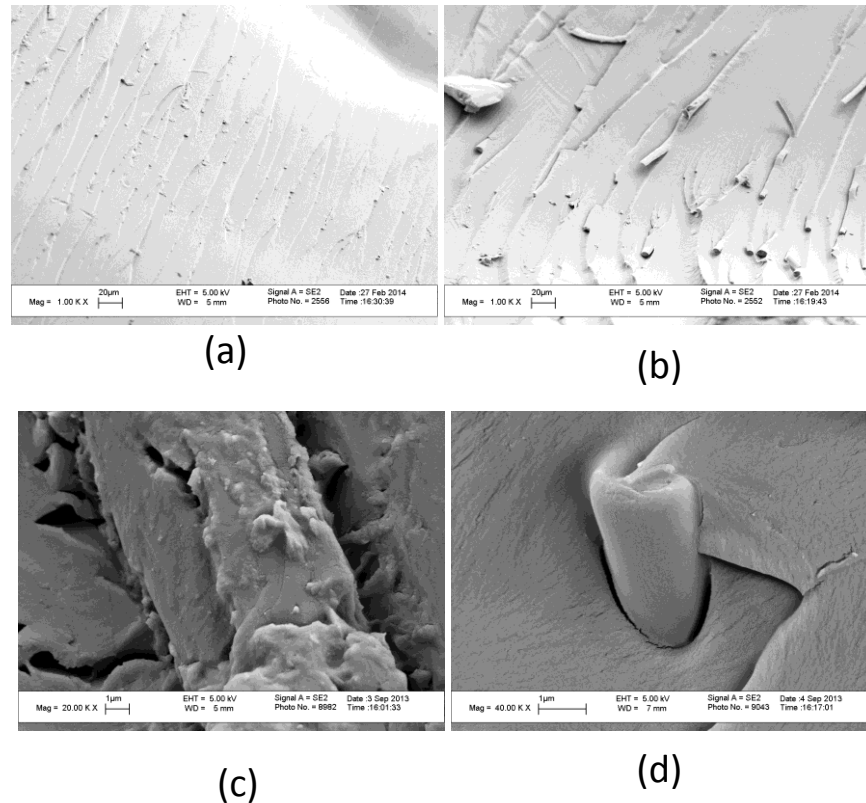


Figure 3.9 SEM images of fracture surface of specimens after 3-point bending tests, (a) Neat epoxy, (b) PMMA/PAAm tri-axial hollow fiber reinforced composite with the outer layer solvent of EA and (c, d) close up view for PMMA/PAAm tri-axial hollow fiber reinforced composite.

### 3.3.4. Laminated glass fiber reinforced composites by hollow fibers

In

Figure 3.10, the flexural properties obtained from 3-point bending test shows minor enhancement in flexural modulus from  $10.8 \pm 0.2$  GPa for conventional glass fiber reinforced specimens up to  $11.5 \pm 0.2$  GPa for samples modified by PMMA-PAAm tri-axial hollow fibers interlayers electrospun with the outer wall solvent of DMF. As can be seen from

Figure 3.10, there are some sudden changes in stress values at higher stress and strain ranges associated with failure of individual reinforcing glass fiber plies. The first sudden drop in the stress value is considered as the breakage of first layer of glass fibers. The presence of PMMA-PAAm tri-axial hollow fibers interlayers improves the breakage strain of first layer of glass fibers by around 12.5 %. Furthermore, the complete failure of electrospun modified samples is shifted to higher strain level by nearly 20 %. The flexural strength of electrospun fiber integrated specimen increases by 14 %. Referring to results in Figure 3.11, one may note that there is no

change in tensile properties between neat and electrospun interlayers integrated glass fiber reinforced epoxy composite specimens. The significant difference between the results of flexural and tensile tests might be attributed to the dissimilarity in the breakage mechanisms for the flexural and the tensile tests. During the flexural test, primary glass fibers are bent perpendicular to the direction of the applied force and in turn damaged leading to formation of cracks, which propagate across the plies of the primary reinforcement. The interlayers between the plies of the primary reinforcement stabilize the crack propagation through arresting cracks thereby giving rise to toughening. However, during tensile test, the direction of applied force is through the plane of matrix and cracks are formed transversely in the plane of plies and not across the plies, hence electrospun interlayers cannot act as efficient crack stabilizer. As well, the tensile strength of the electrospun fibers is significantly inferior to glass fibers. Thus, the contribution of the electrospun interlayer to axial load bearing capacity is negligible in comparison to primary glass fiber reinforcement. The current result of the tensile tests can alternatively be interpreted such that the interlayer does not imperil the tensile properties of composite structure through acting as defects at the interface regions of the composite laminas.

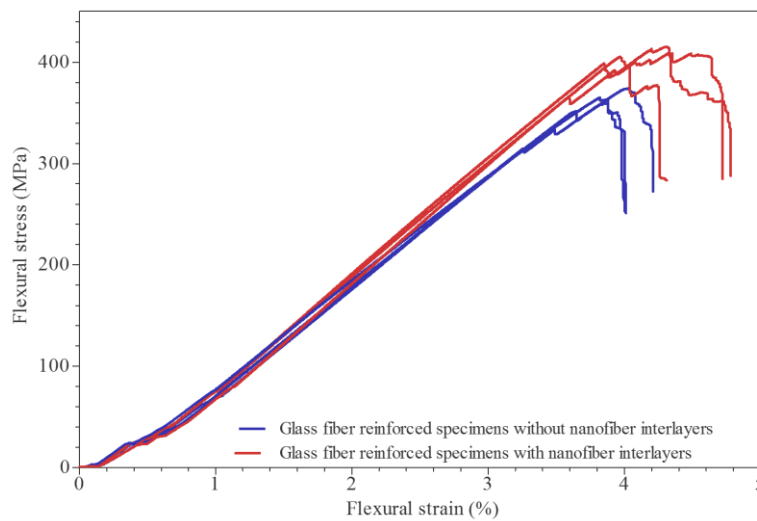


Figure 3.10 Flexural stress-strain curves of glass fiber reinforced epoxy specimen and specimen modified by interlayers of tri-axial hollow fibers of PMMA/PAAm.

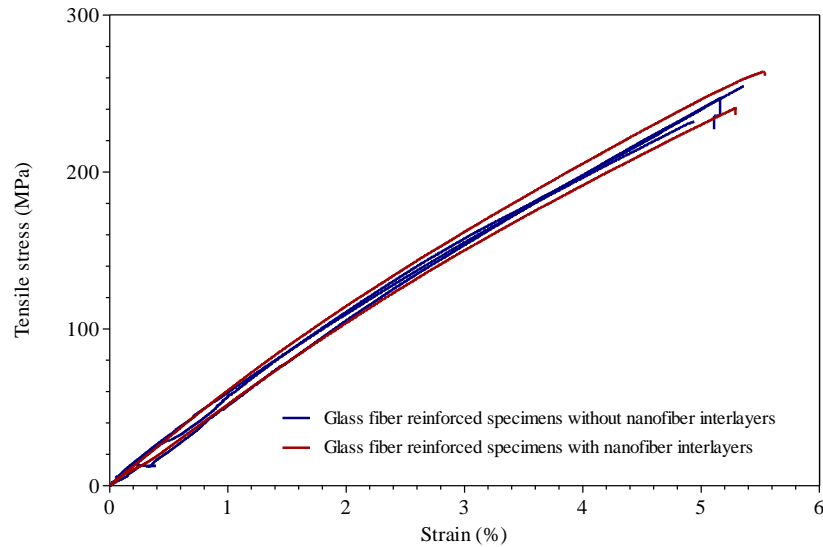


Figure 3.11 Tensile stress vs strain curves of glass fiber reinforced epoxy specimen and specimen modified by interlayers of tri-axial hollow fiber of PMMA/PAAm.

### 3.3.5. Dynamic mechanical properties of glass fiber reinforced composites

DMA analyzes the viscoelasticity of a material by applying a sinusoidal force or displacement and measuring the corresponding response. The storage modulus,  $E'$ , is proportional to the energy stored per cycle (elastic behavior) while the loss modulus,  $E''$ , is associated with the dissipated energy per cycle (viscous behavior) [66]. Tan delta ( $\delta$ ) is a damping term which is defined as the ratio of the loss modulus to the storage modulus, and the temperature corresponding to the  $\tan \delta$  peak is often related to the glass transition temperature ( $T_g$ ). Figure 3.12 shows DMA results of specimens with and without nanofiber interlayers. Referring to the  $\tan \delta$  curves of composites in this figure,  $T_g$  of composite specimen with nanofibers ( $T_g=73^\circ\text{C}$ ) is greater than that of neat composite ( $T_g=66^\circ\text{C}$ ). This increase stems from semi-IPN formed through the entanglement of linear PMMA chains having a  $T_g$  of  $123^\circ\text{C}$  with crosslinked epoxy matrix with lower  $T_g$  [67] since semi-IPN structure may restrict the segmental motion of the matrix leading to higher energy requirement for the glass transition [68]. The increase in  $T_g$  of the composite makes it also suitable for high temperature engineering applications. The significant increase in  $\tan \delta$  peak of nanofiber modified specimen might be attributed to the presence of thermoplastic nanofiber interlayers which experience increasing chain mobility at higher temperature. In addition, the storage modulus of specimen with nanofiber interlayers at glassy region (before  $T_g$ ) is higher than the neat specimen since electrospun fibers provide strong interfacial adhesion between glass fibers and epoxy matrix, which

is also in agreement with the result of flexural tests at room temperature. The storage modulus of specimen laminated with nanofibers in rubbery region (after  $T_g$ ) is lower than that of neat specimen due to the presence of thermoplastic polymeric hollow fibers at the interface of matrix and glass fibers and higher viscous behavior of these hollow fibers than thermoset matrix at elevated temperature.

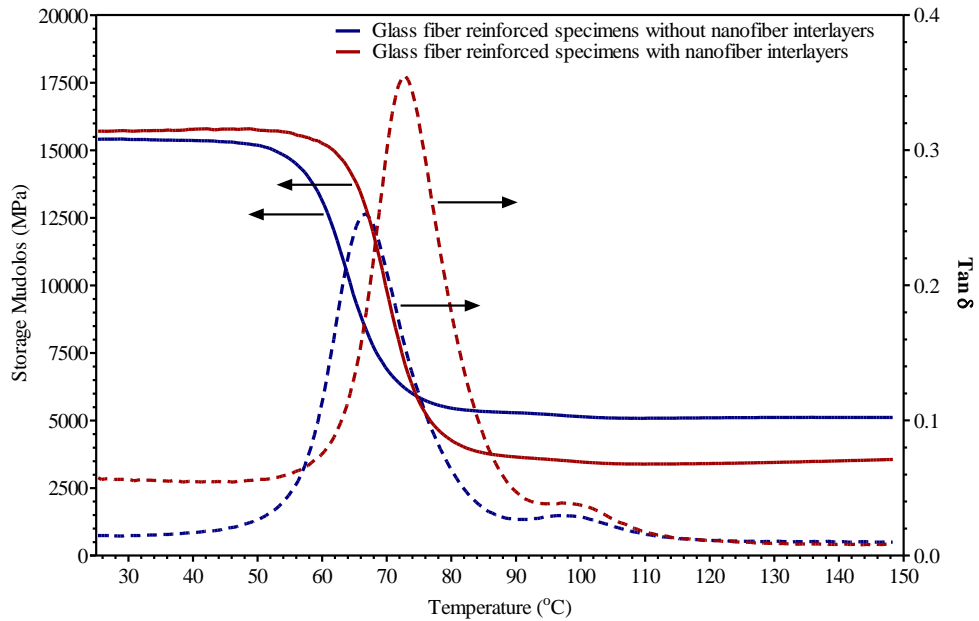


Figure 3.12  $\text{Tan } \delta$  and  $E'$  curves of glass fiber reinforced specimens with and without nanofiber interlayers.

### 3.3.6. Microscopic observation and failure mechanisms

To investigate the failure mechanisms of composites, a fractographic analysis is performed on the cross section of flexural test specimens (bounded by length and the thickness). Figure 3.13 represents SEM images of cross-sectional areas of flexural test specimens after cutting and polishing steps. The cross section corresponds to the right hand side view of Figure 3.2a. Therefore, in the SEM images, the most outer fibers are parallel to the image plane. In these specimens, there are three distinct regions; namely, fibers oriented in a parallel manner to the cross section plane, fibers oriented perpendicularly to cross section plane and matrix rich regions. Figure 3.13a demonstrates the cross section of neat glass fiber reinforced specimen before applying any force or displacement and Figure 3.13b presents a close up view for the boxed region in Figure 3.13a., 3.13c and 3.13d exhibit the cross section of specimens laminated with triaxial hollow fibers before bending. SEM images of both specimens before the application of

flexural force confirm that fibers are satisfactorily wetted by matrix. The failure behaviors of both neat specimen and specimen with triaxial hollow fibers after bending are shown in Figure 3.13e-i. In Figure 3.13e and 3.13f, only the first outer layer (specimen surface at the support side) of the neat specimen is broken down after bending. On the other hand, higher stress is required to break down the layers of specimen laminated with triaxial hollow fibers and after bending, cracks start at both inner (Figure 13h) and outer layers, and the crack initiated at outer layer (Figure 13i) propagates towards inner layers (Figure 13g).

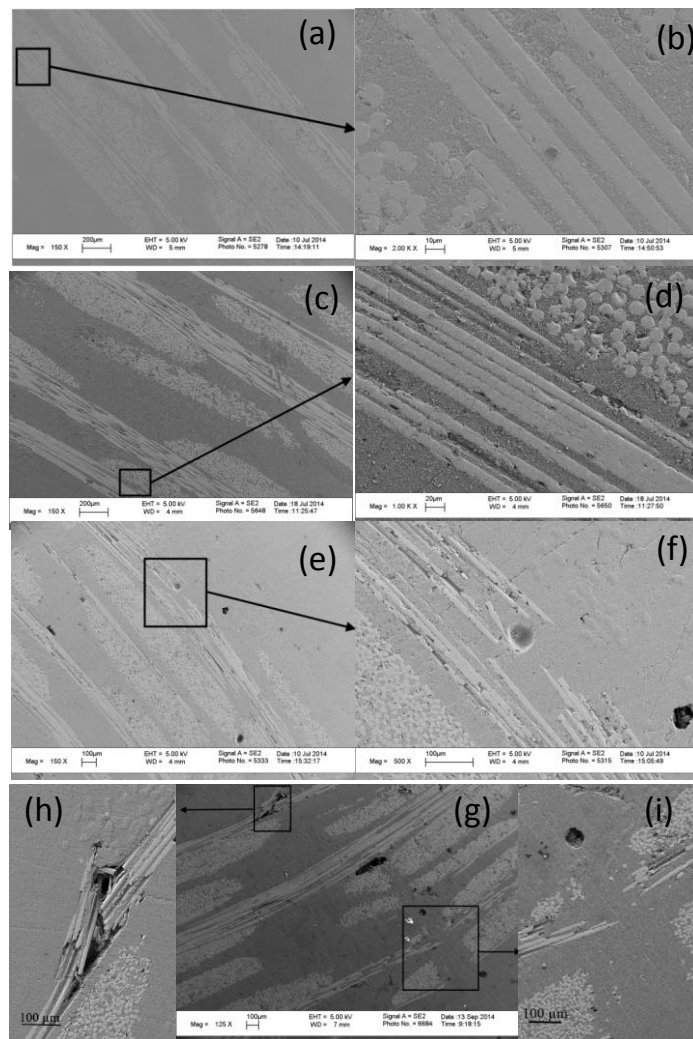


Figure 3.13 SEM images of cross-sectional area of (a, b) glass fiber reinforced epoxy specimen without nanofiber interlayers before applying load, (c, d) glass fiber reinforced epoxy specimen modified by nanofiber interlayers before applying load, (e, f) glass fiber reinforced specimen without nanofiber interlayers after bending, (g, h, i) glass fiber reinforced specimen modified by nanofiber interlayers after bending.

### 3.4. Conclusions

Novel architecture of tri-axial electrospun hollow fibers with controlled diameter and morphology is fabricated by multi axial electrospinning technique. The effect of electrospun fibers with different wall materials, morphology, diameter and fiber content on the mechanical performance of composite specimens is studied. Two different composite production techniques which are casting onto a Teflon mould and vacuum infusion are applied to produce composite structures. Some of the most important findings of the current study might be concisely summarized as;

Electrospun fibers with PMMA outer shell enhance the flexural modulus and strength without affecting the toughness of samples whereas PS outer wall enhance the flexural modulus and strength at the expense of reducing the toughness.

Specimens reinforced by finer electrospun fibers show higher enhancement in flexural modulus at the price of shifting the failure strain to lower strain levels.

The increase in the amount of electrospun fibers augments accessible interfaces between reinforcing electrospun fibers and epoxy matrix in composites, thereby improving load transfer capability and in turn the flexural modulus of the composites. However, the associated increase in the stress concentration points due to the higher number of interfaces degrade the flexural strength as well as strain at breakage.

The utilization of PMMA-PAAm hollow fiber as inter layers of glass fiber laminated composites, enhances the flexural modulus by 6.5 %, flexural strength by 14 %, the onset of first layer of glass fabric failure strain by 12.5 % and final failure strain by 20%. DMA results for glass fiber reinforced specimens laminated with nanofiber interlayers show 7°C increase in  $T_g$  in comparison to neat specimens. Especially, these improvements in conventional glass fiber composites open up new way to produce more reliable and long-lasting composites. Consequently, hollow fiber reinforcement is a promising material for the production of advance composites with ultra lightweight, multi-functionality and an improved structural performance.

The future studies will involve the integration of nanoparticles into the outer layer of multi-walled hollow fibers to further enhance the performance of epoxy composites.

Also, the desired materials can be encapsulated inside hollow the fibers in a single step during electrospinning process which will bring additional functionalities into epoxy composite structures such as vascular self healing.

## **CHAPTER 4. REPEATED SELF-HEALING OF NANO AND MICRON SCALE CRACKS IN EPOXY BASED COMPOSITES BY TRI-AXIAL ELECTROSPUN FIBERS INCLUDING DIFFERENT HEALING AGENTS**

Multi-walled healing fibers with a novel architecture are fabricated through a direct, one-step tri-axial electrospinning process to encapsulate different healing agents inside the fibers with two distinct protective walls. Self healing systems based on ring opening metathesis polymerization (ROMP) and amine-epoxy reaction are redesigned by utilizing these tri-axial fibers. In ROMP, Grubbs' catalyst are integrated in the outer wall of fibers instead of the composite matrix to reduce catalyst amount and prevent its deactivation during composite production. In amine-epoxy healing system, epoxy resin and amine-based curing agent are encapsulated separately by a multi-axial electrospinning. The presence of an extra layer facilitates the encapsulation of amine based healing agents with a high active nature and extends the efficiency and life-time of healing functionality. These new self-healing designs bring repeated self healing ability to preserve the mechanical properties of composite by repairing micron and nano-scale cracks under high loadings.

### **4.1. Introduction**

Embedding reinforcing fibers into the polymeric matrix is the most common way to improve the structural performance (i.e., specific strength and stiffness, among others) of polymeric materials [3]. However, the reinforced polymeric materials (composites in general term) are inherently susceptible to crack initiation and subsequent growth under external loads due to their heterogeneous structure, which unavoidably leads to a gradual degradation in mechanical properties of composites as a function of time [4, 5]. In order to circumvent this issue, it would be a prudent approach to use reinforcing fibers with healing/repairing agent(s) in composite materials [6]. Reinforcing fibers with an healing functionality can improve the mechanical properties of composites, prolong their effective lifetime and expand their capabilities for more advance applications [7]. Inspired by autonomous healing of wounds in living biological systems, scientist and engineers have been in constant search of methods to develop smart materials with self healing capability [8]. One practical approach is based on the delivery of encapsulated liquid

agent into fractured areas whereby the mechanical properties of the damaged polymeric material can be partially or fully restored by repairing micro cracks [69, 70]. In literature, one may uncover several studies with focus of developing better encapsulation techniques which brings about improved self-healing efficiency of polymeric composite [71]. In one of these studies, Motuku et al. [72] demonstrated that the lower impact energy of hollow glass fiber facilitated the rupture of healing fibers and consequently the release of healing agent in micro- and macro-cracks in comparison to copper and aluminum hollow fibers. It should be noted that the presence of these hollow glass fibers in matrix reduces the initial strength of material albeit an increase in damage tolerance and residual strength of composite structure [73]. In addition, filling diminutive hollowness of fibers with a healing agent is not a trivial step in the production of these kinds of self-healing fibers [6, 74, 75]. At this point, core-shell or co-axial electrospinning can be deemed as a promising, versatile, one-step, and efficient technique to encapsulate a broad range of materials in multi-walled nano/micro fibers with a controllable diameter, wall thickness, mechanical properties and surface morphology [76]. In this process, an electric potential difference is created between a collector and a concentric metallic nozzle which host polymeric solution as a shell material in the outer tube and a liquid to be encapsulated as a core material in the inner tube. Due to the electrohydrodynamic forces, both encapsulant and the core fluids are coaxially extruded through the tip of the nozzle in the form of a jet moving towards the collector while undergoing bending instabilities, whipping motions and diameter reduction, and reach at the collector as co-axial electrospun fibers with encapsulated core liquid and with a diameter ranging from several nanometers to micrometers [77]. In the core-shell electrospinning, the outer shell is required to be a polymeric solution with viscoelastic properties, but the core solution can be either viscoelastic or Newtonian liquids [78]. The encapsulation by co-axial electrospinning technique is a physical phenomenon and relies on the physical forces and interactions which eliminate the need for chemically complex and expensive encapsulation methods, and brings a new insight into the design and chemistry of self-healing fibers [79, 80]. Park et al. [81] encapsulated polysiloxane-based healing agents into a poly(vinyl-pyrrolidone) coaxial electrospun beads with the diameters of 2 to 10  $\mu\text{m}$ , which were obtained randomly on electrospun nano-fibers. Moreover, Mitchell et al. [82] obtained beads with the average diameter of 1.97  $\mu\text{m}$  on the nano fibers with the diameter of 235 nm during

coaxial electrospinning of poly(vinyl alcohol) as a shell and epoxy resin as a healing agent.

The critical point in fiber based healing systems is continuous and repetitive release of healing agent into the damaged area, but fibers including beads do not provide this continuity and thus uniformity in fiber structure carries a significant importance to increase self-healing degree. Therefore, Sinha-Ray et al. [76] employed three different techniques (i.e., co-electrospinning, emulsion electrospinning and emulsion solution blowing) to encapsulate healing agents of dicyclopentadiene (DCPD) and isophorone diisocyanate into vascular network like core shell fibers produced by polyacrylonitrile (PAN) in the diameter range of micrometers. The integration of DCPD encapsulated coaxial electrospun PAN fibers into hybrid multi-scale high-strength carbon fiber/epoxy composites as a self healing interlayer restores the toughness of structure due to the self healing functionality [83].

The chemistry of vascular based self-healing composite materials directly affects the stability and life-time of monomer during composite manufacturing process, polymerization kinetics, the delivery of healing agents, mechanical properties of the newly formed polymer as well as its compatibility with matrix [84]. However, there are a limited number of self-healing chemistries to initiate the polymerization in the crack area. Ring opening metathesis polymerization (ROMP) is one of the well-known self-healing systems in which bicyclic monomers such as norbornene derivatives release inside the crack and react with the catalyst that is deposited in the matrix through living polymerization in order to recover the mechanical properties of composite matrix [8, 85-88]. An innovative work in this field was conducted by White et al. [8] who introduced ROMP of DCPD monomers in the presence of Grubbs' catalyst as a healing motif in epoxy matrix. In this approach, crack propagation ruptures micro-capsules containing DCPD monomers and then monomers release inside the crack and react with the pre-dispersed Grubbs' catalyst within matrix and a solid, highly cross-linked polymer, is formed by ROMP reaction.

In spite of exceptional properties of DCPD and Grubbs' catalyst as a healing system such as long shelf-life, low viscosity of healing agent as well as good mechanical properties of the resulting polymer [88], this system suffers from the deactivation of

Grubbs' catalyst upon exposure to air [89] and at high temperature [90], and in the presence of diethylenetriamine which is used as a curing agent of epoxy matrix [91]. As an alternative to DCPD monomer, many efforts have been devoted to the development of self-healing chemistry by using epoxy as a repairing agent which is chemically and physically more compatible to host matrix than DCPD [92, 93]. Epoxy resin is considered as a promising candidate to reduce the cost of self-healing material production and improve self-healing efficiency by increasing the compatibility with the matrix. Yin et. al. [92] produced self-healing woven glass fabric/epoxy composites including epoxy-loaded urea formaldehyde microcapsules fabricated by emulsion polymerization and copper based metal catalysts as a latent hardener embedded in the host matrix. In another work, instead of using a metal catalyst as a hardener, amine solution was filled inside hollow glass bubbles by a vacuum assisted method and these capsules together with microcapsules containing epoxy solution are concurrently integrated into a matrix for the production of self-healing composites [94, 95].

There are only a few published studies on the encapsulation of hardener inside polymeric shells for curing epoxy healing agent thus repairing the damaged area in the matrix.[96, 97] To the authors' knowledge, the encapsulation of epoxy and its hardener by multi-axial electrospinning technique and determination of the self-healing degree of composites including these healing agents have not been reported yet. To this end, in the first part of the present study, DCPD as a healing agent is encapsulated inside electrospun fibers constituting two different polymeric layers with dissimilar hydrophilicity, namely, polyacrylamide (PAAm) as an inner layer and polymethyl methacrylate (PMMA) containing metal catalysts as an outer layer. The low affinity between the inner wall polymer and encapsulated healing agent within the core of fibers limits the interaction of healing agent with its surrounding media and decreases the diffusion rate of healing agent through the wall of fiber hence extending the efficiency and lifetime of healing functionality of fibers. Moreover, the presence of inner layer, PAAm, prevents the direct contact between the catalysts and DCPD healing agent in core part of fiber. The integration of catalyst particles in outer layer of fibers instead of the composite matrix reduces the required amount of this expensive and toxic catalyst, prevents the deactivation of catalyst during the manufacturing process and its service life and more importantly, guarantees the presence of catalyst in the crack area to initiate the polymerization of self-

healing agent released from fibers. In the second part of this work, epoxy resin and amine-based curing agent are encapsulated separately by multi-axial electrospinning and these produced fibers are embedded into composite matrix to measure their self-healing efficiency. The viscosity of epoxy resin inside multi-axial fibers is optimized at different diluent ratios for the effective encapsulation and enhancing self-healing. In addition, the effect of fiber diameter and the type of self-healing agent (DCPD monomer and epoxy resin) on the self-healing properties of the produced composites is investigated by comparing the modulus reduction values by conducting multiple healing cycles.

## **4.2. Experimental**

### **4.2.1. Materials**

Materials used are Methyl methacrylate (SAFC, 98.5%), styrene (SAFC, 99%), glycidyl methacrylate (Aldrich, 97%), Azobisisobutyronitrile (AIBN, Fluka, 98%), acrylamide (Sigma, 99%), N, N dimethyl formamide (DMF, Sigma-Aldrich, 99%), methanol (Sigma-Aldrich, 99.7%), tetrahydrofuran (THF, Merck, 99%), ethyl acetate (EA, Sigma-Aldrich, 99.5%), dicyclopentadiene (DCPD, Merck), Grubbs' catalyst (2nd Generation, Aldrich), acetone (Aldrich, 99.5%), Disperse Red 1 (Fluka), LY 564 resin, and Hardener XB 3403 (Huntsman).

### **4.2.2. Synthesis of Layer Materials**

Polymethyl methacrylate (PMMA), polystyrene (PS) and poly(glycidyl methacrylate-co-styrene) as outer layer material of fibers was synthesized by free radical polymerization of vinyl monomers (30 ml) in the presence of AIBN (1 g) as a radical initiator in the medium of THF (50 ml) at 65°C. Polymerization reaction was carried out for 4 h and then the reaction mixture was precipitated in cold methanol and dried for 12 h in a vacuum oven at 50°C. Polyacrylamide (PAAm) as a hydrophilic polymer and inner layer material was synthesized by dispersion polymerization of acrylamide monomer (30 g) in methanol (100 ml) by using AIBN (1 g) as an initiator at 65°C. Separation of polymer from methanol and unreacted monomer was done by vacuum filtration and washing twice with methanol and drying for 12 h in a vacuum oven at 40°C.

### 4.2.3. Multi-Axial Electrospinning

Tri-axial fibers are produced at ambient room conditions by using a multi-axial electrospinning set-up purchased from Yflow Company with a custom-made tri-axial nozzle. Figure 4.1. shows the schematic representation of multi-axial electrospinning process that can produce double walled electrospun fibers with a healing agent as a core material. All fibers were electrospun with a nozzle to collector distance of 7 cm by tuning the applied voltage in the range of 5 kV to 30 kV. Solutions are loaded independently into the syringes connected to concentric nozzles, and the flow rate of each layer is controlled by separate pumps. The flow rates of solutions for the outer and inner layers and the core are 20  $\mu\text{l}/\text{min}$ , 15  $\mu\text{l}/\text{min}$  and 10  $\mu\text{l}/\text{min}$ , respectively.

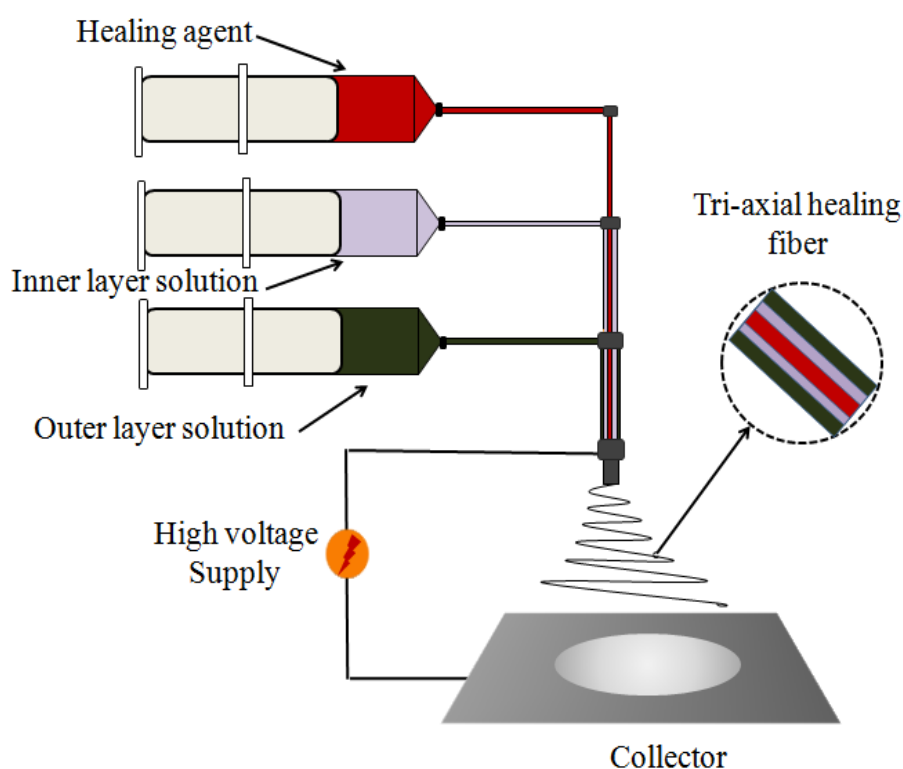


Figure 4.1 A schematic representation for the multi-axial electrospinning set-up.

### 4.2.4. Fabrication of Fiber Reinforced Epoxy Composites

Classical molding technique is utilized to prepare fiber reinforced composites. In this method, 2 wt % multi-axial electrospun hollow fibers and healing fibers with the same hollow fiber content (i.e., excluding the weight of the healing agent) were uniformly laid down into a Teflon mold and then impregnated by the mixture of degassed resin and hardener system. Subsequently, the mold is placed in a vacuum oven to remove entrapped

air bubbles and to cure the resin-hardener mixture at 70°C for 5 days. Electrospun fiber reinforced specimens for three point bending tests have the dimensions of 100x14x3 mm.

#### **4.2.5. Characterization**

The properties of polymers used as layers of electrospun fibers were characterized in detail using Nuclear Magnetic Resonance (NMR) for chemical structure, Gel Permeation Chromatography (GPC) for molecular weight and polydispersity index, Differential Scanning Calorimeter (DSC) for determining glass transition temperature and Thermal Gravimetric Analyzer (TGA) for thermal decomposition in our previous studies [17, 19] and hence were not given here again to avoid redundancy. The functional groups of polymers and fibers were analyzed by Netzsch Fourier Transform Infrared Spectroscopy (FTIR). The surface morphologies of fibers were analyzed by a Leo Supra 35VP Field Emission Scanning Electron Microscope (SEM) and JEOL 2100 Lab6 High Resolution Transmission Electron Microscopy (TEM). Rheological analyses were performed by using a rotational rheometer (Malvern Bohlin CVO). Gel contents of the cured neat specimens were determined by Soxhlet extraction for 24 h using THF. The extracted samples were vacuum dried at 80°C until achieving a constant weight. Three point flexural tests on composite specimens were performed by using ZWICK Proline 100 Universal Test Machine (UTM) with 10 kN load cell using a constant cross-head speed of 1 mm/min.

### **4.3. Results and Discussion**

#### **4.3.1. Fabrication of Multi-Walled Healing Fiber**

In our previous study, we have performed a systematical optimization study to produce tri-axial hollow electrospun fibers with tunable fiber diameters and surface morphologies [17] and demonstrated that the use of solvents with a higher vapor pressure (i.e., THF) resulted in fibers with larger diameters whereas solvents with a lower vapor pressure (i.e., EA and DMF) led to fibers with smaller diameters. In the present study, for self-healing application, healing agent encapsulated tri-axial fibers having different fiber diameters and surface morphologies were fabricated following the systematic in given [17]. This method enables the encapsulation of different types of healing agents within electrospun fibers with different outer wall materials and tailorable interfacial properties

whereby the fabrication of healing fibers with a novel architecture becomes possible. Self-healing mechanisms of tri-axial fibers in composite matrix are investigated by applying two different chemistries: ring opening metathesis polymerization (ROMP) and amine-epoxy reaction.

#### **4.3.2. Fabrication of Self-Healing Multi-Walled Fibers Based on ROMP**

In literature, it was reported that the healing system based on the ring-opening metathesis polymerization (ROMP) of DCPD monomer with a very low viscosity and a low surface energy catalyzed by Grubbs' catalyst repairs damaged areas through restoring the mechanical properties of composite matrix and consequently fulfills requirements expected by an ideal self-healing system [98, 99]. In order to obtain multi-axial fibers with healing functionality, DCPD is encapsulated as a core material inside the tri-axial fibers having different outer layer polymers that are compatible with epoxy matrix, and a hydrophobic middle layer that provides an inert media for DCPD monomer inside the fibers. In literature, metal-based catalytic curing agents (i.e., solid-phase reagents) such as Grubbs' catalyst are commonly mixed with epoxy resin to act as a self-healing agent initiator and promote ring-opening polymerization of encapsulated DCPD [100]. However, Grubbs' catalyst is not cost-effective for the production of a large-scale self-healing composite. Therefore, in the present study, following an alternative approach, catalyst particles were dispersed into the outer layer polymer of electrospun fibers before the electrospinning process in order to minimize the use of catalyst in the composite structure as well as provide a direct contact of catalyst with monomer in the nearest region of the crack. The presence of organic groups in the structure of catalyst makes this organometallic catalyst highly compatible and soluble within several solvents used for the preparation of fibers outer layer. Once the catalyst powder is dissolved in the solvent, it acquires molecular scale thereby being homogeneously distributed in the outer layer of tri-axial fibers. This reduces the catalyst amount used in the preparation of self-healing composite and thus offers a cost effective production. Figure 4.2 exhibits SEM images of as received Grubbs' catalyst at different magnifications.

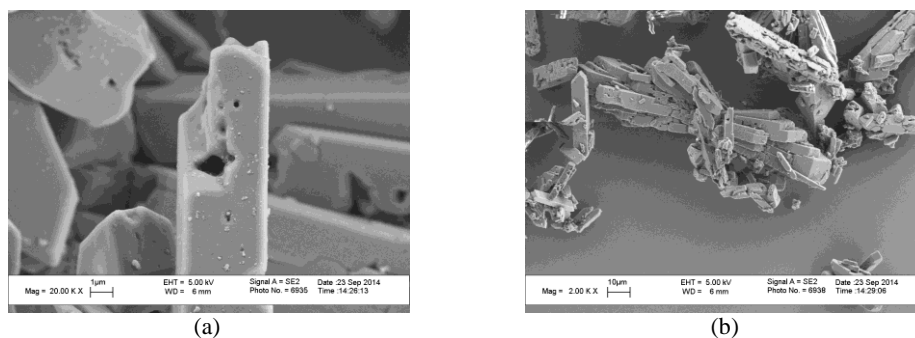


Figure 4.2 (a) and (b) SEM images of as received Grubbs' catalyst at different magnifications.

PMMA, PS and poly(glycidyl methacrylate-co-styrene) are chosen as outer wall polymers of electrospun fibers due to their interfacial compatibility with epoxy matrix. The interfacial interactions between outer wall of electrospun fiber and polymer matrix play a critical role in load transfer from matrix to the fibers and thus improve the mechanical properties of composite [101]. In our previous work, we have shown that the integration of multi-walled hollow fibers with outer layer of PMMA and the diameter of 100 nm into epoxy matrix improves the flexural modulus by 28 %, and flexural strength by 21% [19]. Mechanical improvement in electrospun fiber reinforced epoxy specimens can be explained by the interpenetration of partially dissolved PMMA chains into epoxy and hardener mixture, resulting in the entanglement of linear PMMA chains with the cross-linked matrix network and thus the formation of semi interpenetrating polymer network (semi-IPN) structure which improves load transfer between matrix and electrospun fibers.[19] Therefore, self-healing functionality is selectively added to these electrospun fibers through encapsulating the healing agent therein by adjusting fiber diameter by using different solvents. Figure 4.3a exhibits SEM image of PMMA/PAAm/DCPD tri-axial electrospun fibers with diameters over 2  $\mu\text{m}$  which are produced using PMMA solution in THF as an outer wall and PAAm solution in water as a middle wall. Similarly, SEM images given in Figure 4.3b and 3.3c present PMMA/PAAm/DCPD tri-axial fibers that are fabricated using PMMA solution in EA and DMF as outer wall thereby bring about fibers with diameters of 1  $\mu\text{m}$  and 200 nm, respectively. Healing fibers with larger diameters are expected to contain higher amount of healing agent per unit length of fibers in comparison to that with lower diameter. However, given that the flow rate ratio is kept constant for all experiments, the amount of healing agent in fibers with different diameters is the same per weight unit of fibers. All SEM images in Figure 4.3 reveal that PMMA as the outer wall covers the interior

layer uniformly and continuous fibers without any bead formation are successfully obtained. Furthermore, the solvent type directly affects the surface morphology and porosity of the fibers by due to the thermodynamic instabilities and associated phase separation during the electrospinning process.

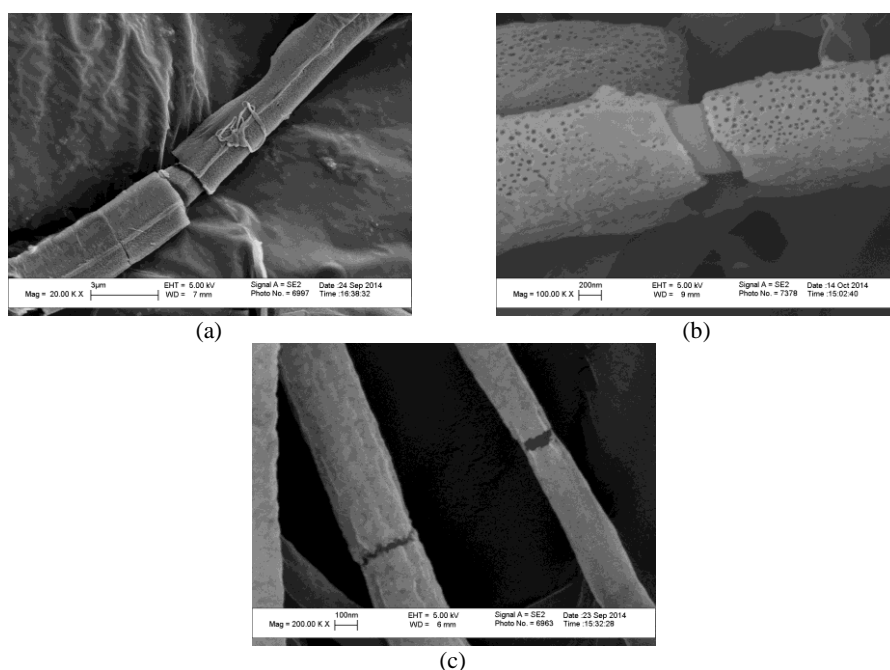


Figure 4.3 SEM images of PMMA/PAAm/DCPD tri-axial healing fibers fabricated utilizing different outer wall solvents (a) THF, (b) EA and (c) DMF.

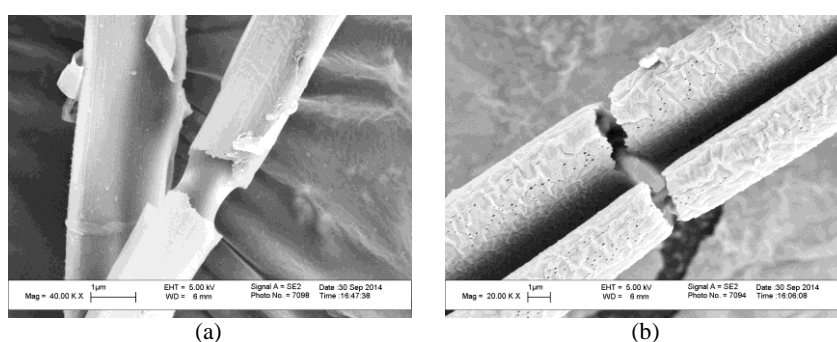


Figure 4.4 SEM images of (a) PS/PAAm/DCPD and (b) poly(glycidyl methacrylate-co-styrene)/PAAm/DCPD tri-axial healing fibers, which are manufactured using EA as an outer wall solvent.

In the course of obtaining an ideal fiber morphology containing DCPD monomer, PS and poly(glycidyl methacrylate-co-styrene) polymers were also used as outer layers of tri-axial fibers. Figure 4.4a exhibits SEM images of PS/PAAm/DCPD tri-axial fibers

and the breakage area of this fiber and middle layer are seen clearly that confirms the formation of multi-layer fiber morphology. Figure 4.4b represents poly(glycidyl methacrylate-co-styrene)/PAAm/DCPD tri-axial fibers fabricated using an outer layer solution prepared in EA and with the diameter of around 1  $\mu\text{m}$ .

To study the self healing efficiency of multi-walled fibers with encapsulated healing agent in a host material, epoxy resin system is reinforced by multi-walled fibers with and without encapsulated healing agent. To ensure that both fiber types have similar influence on the matrix in terms of crack formation due to their presence, their diameters are controlled to be as uniform as possible. Figure 4.5a and 4.5b yield multi-walled hollow fibers of PMMA/PAAm with the outer wall material's solution prepared in DMF and EA, respectively. It is seen that the morphology and diameter of these fibers are very similar to the fibers including DCPD shown in Figure 4.3b and 4.3c, indicating that the encapsulation of DCPD does not affect the fiber structure. To reveal ordered layer formation in fibers, the morphologies of walls with DCPD monomer were analyzed by TEM technique. Figure 4.6a and 4.6b exhibit PMMA/PAAm/DCPD tri-axial healing fibers prepared using the outer layer solvent of DMF. In order to reveal the presence of the healing agent inside the electrospun fibers, DCPD is initially mixed with a specific dye (Disperse Red 1) which hinders the passage of electrons through fibers thereby resulting in the formation of dark regions in the core of the fibers and the bright regions at the edges corresponding to the polymeric shells on the TEM images. Figure 4.6b clearly indicates that the end of the fiber is completely closed by outer layer, which implies that healing agents are completely confined inside fiber structure and only ruptured fibers can release the encapsulated healing agent in the core of the fibers. TEM image of PMMA/PAAm tri-axial hollow fiber prepared by outer layer solvent of EA in Figure 4.6c is an evidence for the presence of two separate walls and empty core of the fiber.

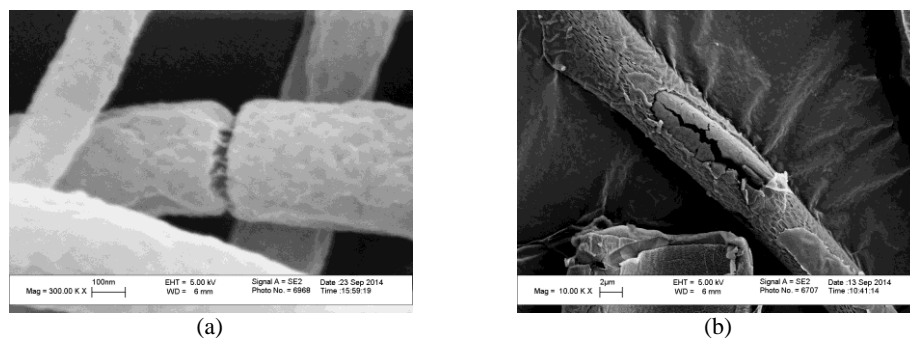


Figure 4.5 SEM images of PMMA/PAAm tri-axial hollow electrospun fibers fabricated using different outer wall solvents of (a) DMF, and (b) EA.

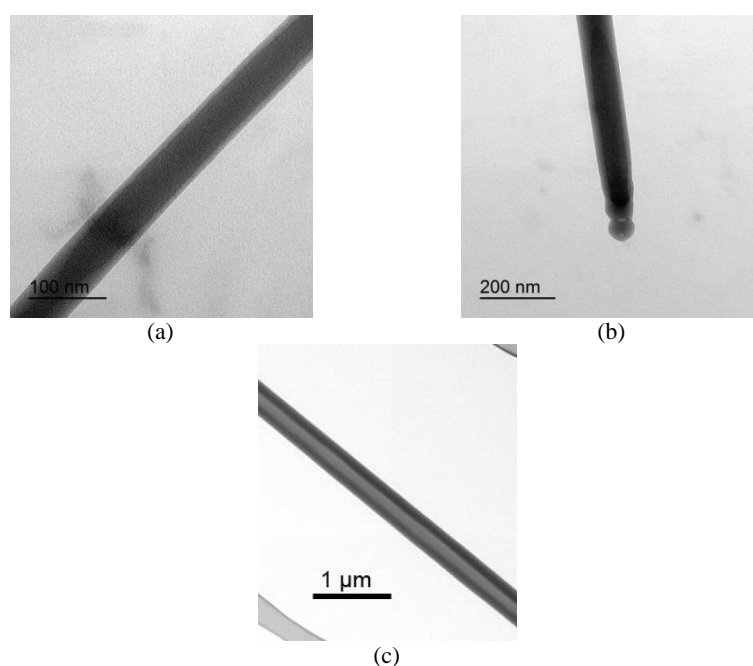


Figure 4.6 TEM images of (a, b) PMMA/PAAm/DCPD tri-axial healing fibers fabricated using DMF as an outer layer solvent, and (c) PMMA/PAAm tri-axial hollow fiber electrospun through using EA as an outer layer solvent.

Figure 4.7a and 4.7b respectively gives images obtained using cathodoluminescence (CL) and coupled secondary electron (SE) for PS/PAAm/DCPD tri-axial healing fibers prepared using DMF as an outer layer solvent. The addition of dye into the healing agent provides an opportunity to have a complete map of healing agent distribution in fibers due to cathodoluminescence effect. In Figure 4.7a, brighter fibers contain self-healing agent whereas darker fibers are empty and do not have any dye in the core of fibers, which confirms the presence of healing agent inside the most of electrospun fibers. The morphology of fibers can be clearly seen in Figure 4.7b.

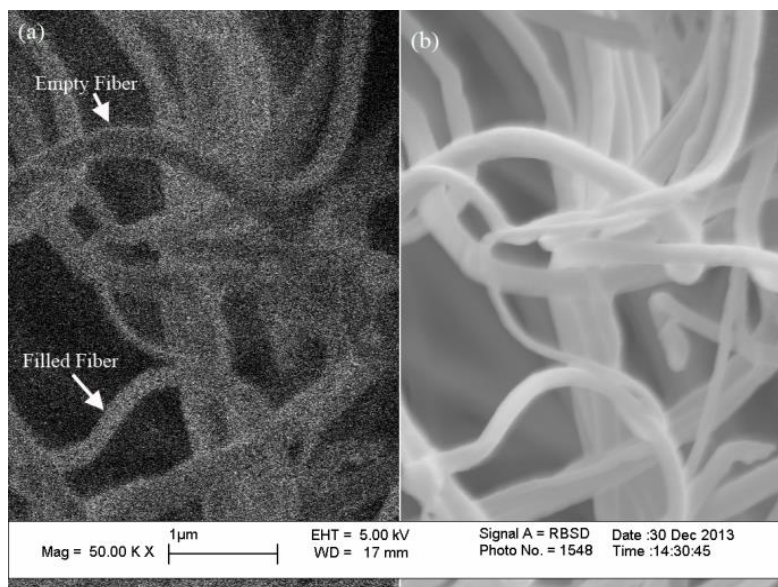


Figure 4.7 (a) Cathodoluminescence and (b) secondary electron coupled SEM images of PS/PAAm/DCPD tri-axial electrospun fibers.

Moreover, FTIR analysis was performed to confirm successful encapsulation of healing agent into the multi-walled fibers through identifying the characteristic peak groups of different wall materials and healing agents. Figure 4.8a shows FTIR spectra of DCPD, PMMA/PAAm tri-axial hollow fiber and PMMA/PAAm/DCPD tri-axial fiber. Liquid DCPD monomer prior to encapsulation gives intense and sharp peaks at  $725\text{ cm}^{-1}$  and  $740\text{ cm}^{-1}$  representing CH=CH bending modes, peak at  $3045\text{ cm}^{-1}$  belonging to C=C stretching vibration, peak at  $2961\text{ cm}^{-1}$  owing to C–H stretching vibrations, and peak at about  $1340\text{ cm}^{-1}$  corresponding to =C–H bending vibration.[102] In the FTIR spectra of electrospun PMMA/PAAm tri-axial hollow fibers in Figure 4.8a, the absorption bands at  $2950\text{ cm}^{-1}$  and  $1745\text{ cm}^{-1}$  belong to C-H and C=O stretchings of PMMA polymer, respectively.[46] The FTIR spectra of PS/PAAm tri-axial hollow fiber and PS/PAAm/DCPD tri-axial fiber in Figure 4.8b show absorption bands at  $3024\text{ cm}^{-1}$  and  $2848\text{ cm}^{-1}$  corresponding to aromatic and aliphatic C-H stretchings of outer wall of PS as well as the peaks at  $1600\text{ cm}^{-1}$  and  $1492\text{ cm}^{-1}$  assigned to aromatic C=C stretchings of this polymer. FTIR spectrum of poly(glycidyl methacrylate-co-styrene) used as an outer wall in Figure 4.8c confirms aromatic peaks of styrene and carbonyl group of glycidyl methacrylate at around  $1700\text{ cm}^{-1}$ , the peak of oxirane group at  $910\text{ cm}^{-1}$  and the peaks of C–O stretching of ester group in the structure of glycidyl methacrylate at  $1140\text{ cm}^{-1}$  and  $1260\text{ cm}^{-1}$ . [103] In addition, asymmetric and symmetric NH stretching of NH<sub>2</sub> at around  $3300\text{ cm}^{-1}$  corresponds to PAAm polymer as a middle wall of all fibers [47]. To

reiterate, the peaks related to outer and middle wall materials and the characteristic peaks of DCPD monomer are observed in three FTIR spectra of electrospun healing tri-axial fibers, which bespeak a successful encapsulation of healing agents in electrospun fibers with different outer wall materials.

#### **4.3.3. Fabrication of Self-Healing Multi-Walled Fibers Based on Amine–Epoxy Reaction**

Due to its reactivity with several curing agents and hardeners at different temperature, excellent adhesion to epoxy matrix, corrosion and chemical resistance, and low curing shrinkage, bisphenol A diglycidyl ether (epoxy resin) can be deemed as versatile healing agent for a wide range of composite materials. However, a direct use of epoxy resin as a healing agent is not practical due to its relatively high viscosity that makes the encapsulation process very hard as well as prevents the flow of the healing agent into the micro-cracks owing to capillarity once the healing fibers or capsules are damaged. To reduce the viscosity and in turn facilitate the encapsulation process, epoxy based healing agent can be diluted in acetone. The excessive addition of acetone into epoxy may reduce the mechanical performance of cured polymer. Hence, it is prudent to keep the amount of acetone used for dilution process at minimum level. In literature, it was reported that mechanical properties of cured epoxy initially diluted using 20 wt.% of acetone is basically remained the same as that of cured virgin epoxy resin, which indicates that the appropriately diluted epoxy resin can be easily encapsulated in electrospinning process [104] and be effectively used as self healing agent. In the present study, for easy encapsulation, the viscosity of epoxy based healing agent is also adjusted using acetone. To this end, the viscosity of epoxy resin and acetone mixtures with different ratios was measured by rotational viscometer. Figure 4.9 exhibits the normalized viscosity of epoxy-acetone mixtures having different ratios with respect to pure epoxy. It is seen that the addition of 20 wt.% acetone into high viscosity epoxy resin causes a dramatic decrease in the viscosity of epoxy; however, further increasing the amount of acetone in the mixture does not change the viscosity much.

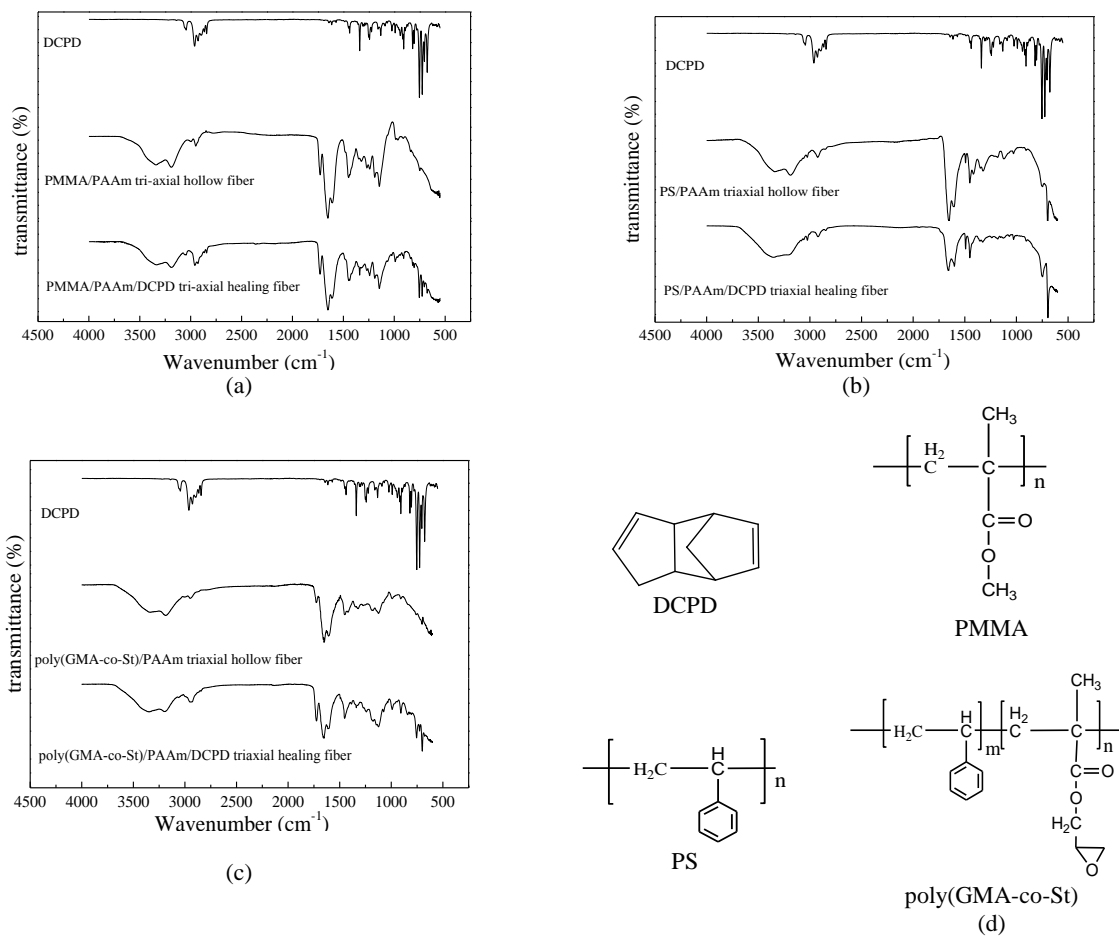


Figure 4.8 FTIR spectra of (a) DCPD, PMMA/PAAm tri-axial hollow fiber and PMMA/PAAm/DCPD tri-axial fiber, (b) DCPD, PS/PAAm tri-axial hollow fiber and PS/PAAm/DCPD tri-axial fiber, (c) DCPD, poly(St-co-GMA)/PAAm tri-axial hollow

fiber and poly(St-co-GMA)/PAAm/DCP tri-axial fiber. (d) the chemical structure of polymers and DCPD.

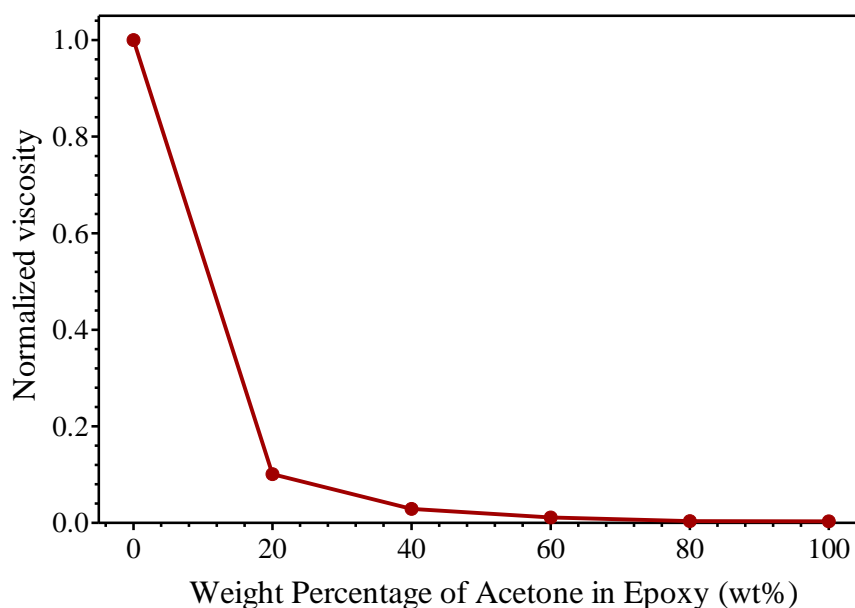


Figure 4.9 The change in the viscosity of epoxy resin as a function of volume percentage of acetone

Figure 4.10 represents SEM images of tri-axial electrospun fibers used as healing reinforcement in epoxy matrix. SEM images of PMMA/PAAm/Hardener tri-axial fibers given in Figure 4.10a and 4.10b show hollowness of fibers after breakage and the release of hardener. Figure 4.10c and 4.1d exhibit the multi-layered structure of PMMA/PAAm/Epoxy tri-axial fibers. In order to start self-healing mechanism in the matrix after the breakage, hardener and epoxy should be encapsulated separately and the fibers should be brittle under high loadings. Figure 4.10e and 4.10f present TEM images of tri-axial fibers of PMMA/PAAm/Hardener and PMMA/PAAm/Epoxy with outer layer solvent of EA in which dark regions in the core of the fibers are due to healing agents while the bright regions at the boundaries correspond to the polymeric shells.

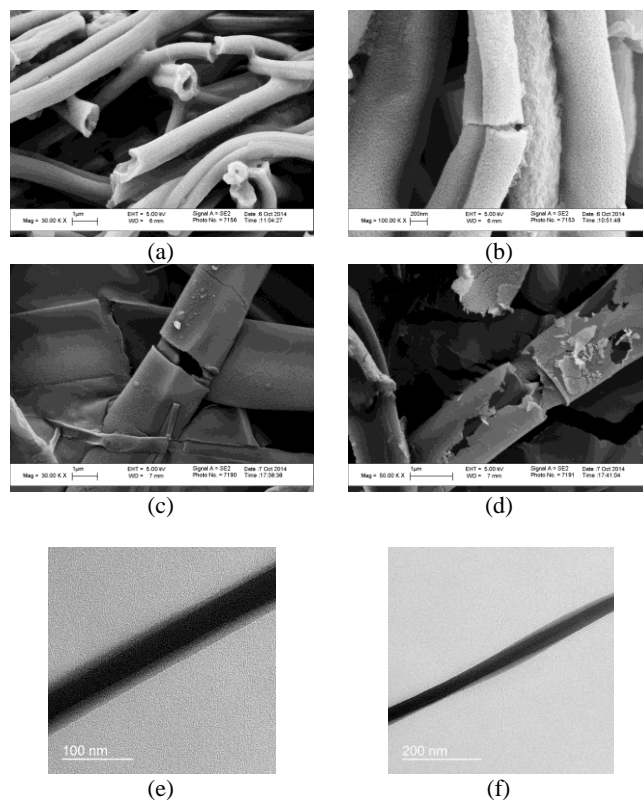


Figure 4.10 (a, b) SEM images and (e) TEM image of PMMA/PAAm/hardener tri-axial fiber with 20 wt% PMMA in EA solution as an outer wall, 20 wt% PAAm in water as a middle wall and hardener as a core material (c, d) SEM images and (f) TEM image of PMMA/PAAm/epoxy tri-axial fiber with 20 wt% PMMA in EA solution as an outer wall, 20 wt% PAAm in water as a middle wall and epoxy-acetone 8:2 mixture as a core material.

FTIR analysis of these tri-axial fibers confirms the presence of encapsulated hardener and epoxy inside the fiber structure. Figure 4.11a shows FTIR spectra of hardener, PMMA/PAAm tri-axial hollow fiber and PMMA/PAAm/hardener tri-axial fiber. In tri-axial fiber containing hardener, the peak at  $1592\text{ cm}^{-1}$  corresponds to N–H bending vibration and strong peak at  $1150\text{ cm}^{-1}$  belongs to C–N stretching that confirms the presence of amine based hardener in the fibers structure [105]. Figure 4.11b exhibits the FTIR spectra of epoxy resin, PMMA/PAAm tri-axial hollow fiber and PMMA/PAAm/epoxy tri-axial fibers. In these spectra, the peaks at  $815\text{ cm}^{-1}$  and  $840\text{ cm}^{-1}$  belonging to oxirane groups verify the presence of epoxy resin in tri-axial fiber structure. After the encapsulation of hardener and epoxy inside tri-axial fiber, the characteristic peaks belonging to PMMA and PAAm are observed in each case and the fingerprints of these polymers are similar to fibers containing DCPD monomer that we discussed in the previous section.

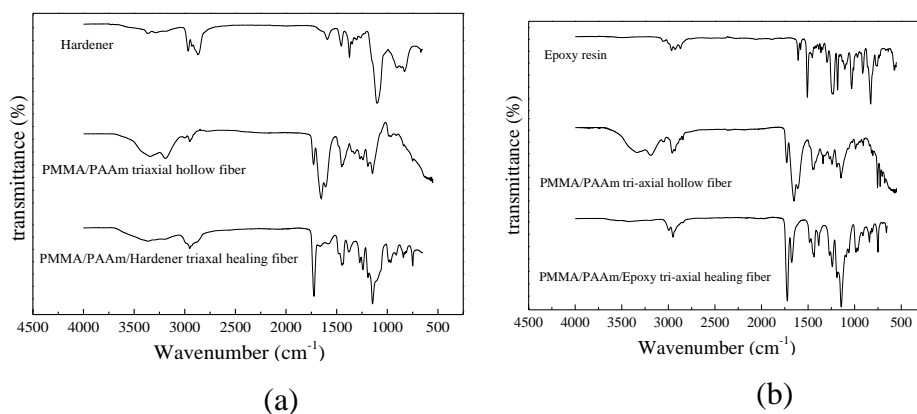


Figure 4.11 FTIR spectra of (a) hardener, PMMA/PAAm tri-axial hollow fiber and PMMA/PAAm/Hardener tri-axial fiber (b) epoxy resin, PMMA/PAAm tri-axial hollow fiber and PMMA/PAAm/epoxy tri-axial fiber

#### 4.3.4. Determination of the Curing State of Matrix

In order to eliminate the possible effect of post-curing on the degree of self-healing and obtain optimum curing time for epoxy specimens, gel content of cured neat epoxy specimens were determined as function of curing time through using soxhlet extraction technique. The value of gel content after extracting uncured oligomers and monomers from structure represents the cross-linking degree of epoxy specimens.[106] In Figure 4.12 is plotted the variation of gel content of neat epoxy specimens as a function of curing time at constant curing temperature of 70°C wherein one can observe that 97% of epoxy and hardener mixture is cured during the first 6 hr of curing process and the percentage of cross-linking gets higher with the increasing curing time. However, after certain time of curing at constant temperature, specimens reach at their ultimate curing state and no notable difference is observed in gel content of specimens after this saturation point. Herein, specimens cured for 5 and 6 days show very similar gel content value which corresponds to complete curing.

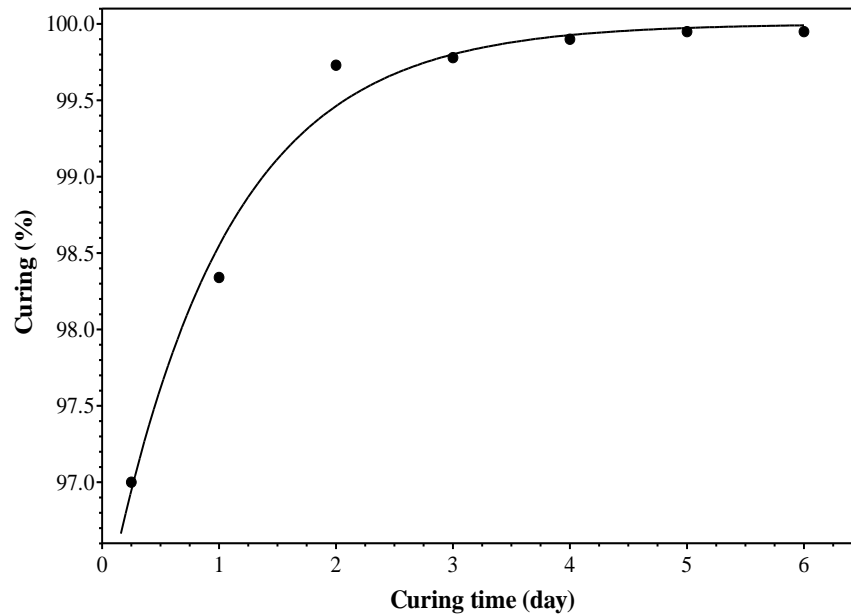


Figure 4.12 The variation of gel content of neat epoxy specimens as a function of curing time at constant curing temperature of 70°C (obtained by soxhlet extraction).

It is explained that after 5 days of curing at temperature of 70°C the specimens reach their maximum curing state and the effect of post curing from self healing data can be eliminated completely.

#### 4.3.5. Evaluation of Self-Healing Efficiency

The usage of tri-axial fiber with epoxy compatible outer layer polymer as a self healing reinforcement in epoxy matrix will expectedly lead to epoxy based composites with enhanced mechanical properties[19]. Therefore, PMMA has been chosen as an outer layer polymer to enhance the interactions between self healing fibers and epoxy matrix. Figure 4.13. introduces stages of designed self-healing process schematically.

In order to perform self healing tests, 3-point bending specimens individually reinforced by PMMA/PAAm hollow tri-axial fibers and Grubbs' catalyst dispersed PMMA/PAAm/DCPD tri-axial fibers as well as the couples of PMMA/PAAm/epoxy and PMMA/PAAm/hardener tri-axial fibers were subjected to repeated bending/healing cycles wherein self-healing composite specimens were subjected to 6 % flexural strain through utilizing corresponding applied stress and then were kept in oven for 24 hr at 70°C for healing reaction. Figure 4.14 exhibits the flexural stress-strain curves of selected specimens reinforced by tri-axial fibers including different healing agents with two

different diameters in each cycle. As seen in stress-strain relations, after the strain of 3 %, samples begin to have a non-linear behavior or yield, which can be attributed to initiation of cracks inside the composite structure. At this stage, there should be a lot of invisible nano- and micro-cracks forming, coalescing and growing inside the structure under the applied stress. In each repeating cycle, flexural modulus decreases gradually since the size and the number of cracks in the matrix of specimens increase. Figure 4.14a demonstrates the flexural stress-strain curves of specimen reinforced by PMMA/PAAm tri-axial hollow fibers with the average fiber diameter of 200 nm while Figure 4.12b shows specimen reinforced by PMMA/PAAm/DCPD tri-axial fibers having DCPD healing agent in the core of fiber and Grubbs' catalyst dispersed in the outer wall with the average fiber diameter of 200 nm. In Figure 4.14b, the reduction of modulus values of specimen reinforced by tri-axial fibers with self-healing functionality in each cycle is lower than the similar specimens reinforced by hollow fibers. This improvement of modulus in the presence of healing fibers indicates that the DCPD monomer and Grubbs's catalyst react by ring opening polymerization to repair the crack area. Also, Table 4.1 tabulates the percentages of reduction in the flexural modulus in comparison to first bending cycle of each specimen. Figure 4.14c and d show the flexural stress-strain curves of specimens reinforced by PMMA/PAAm tri-axial hollow fiber and PMMA/PAAm/DCPD tri-axial healing fibers with the average fiber diameter of 1  $\mu$ m, respectively. Figure 4.14e reveals the repeated healing response of specimen reinforced by both PMMA/PAAm/epoxy and PMMA/PAAm/hardener tri-axial fibers.

In order to demonstrate the healing efficiency of each specimen, their normalized modulus values, defined as the ratio of flexural modulus of the specimen at each bending test cycle to flexural modulus at the first bending test, are compared as a function of healing cycles in Figure 4.14f. All the normalized modulus values for each specimen have decreased with increasing bending/heal cycle number owing to damage accumulation in the structure associated the formation of new cracks as well as the growth or coalescence of old cracks in each bending test cycle. It is clearly seen from Figure 4.14f that the specimens reinforced by PMMA/PAAm/DCPD tri-axial healing fibers with the mean fiber diameter of 200 nm experiences significantly lower reduction in normalized modulus per cycle than that reinforced by tri-axial hollow fibers. This result indicates that the presence of healing fibers inside the structure can trigger the healing

reaction to repair the cracks and recover the mechanical properties of specimens to certain extent. On the other hand, specimens reinforced by PMMA/PAAm hollow fiber and PMMA/PAAm/DCPD healing fibers with average fiber diameter of 1  $\mu\text{m}$  show similar reduction in normalized modulus up to the first healing cycle; however, upon increasing the cycle number, fibers including healing agent start to recover the mechanical properties of matrix and nearly retain normalized modulus of the composite after each bending/heal cycle while modulus values of specimens without healing ability decrease gradually in each cycle. Furthermore, the normalized modulus reduction in the first cycle for specimen reinforced by 1  $\mu\text{m}$  DCPD healing fibers is higher than specimen reinforced by 200 nm healing fiber which is because of higher stress concentrations and in turn denser crack formation in specimens reinforced by larger fibers. However, the reduction in mechanical properties of matrix reinforced by healing fibers having a larger diameter reaches a stable value and subsequently does not change as a function of healing cycle which can be explained by excess amount of healing agent encapsulated inside these kinds of fibers. This is further contributed by the higher amount of DCPD monomer inside larger diameter tri-axial fibers and the release of higher amount of healing agent into the crack area in each healing cycle.

In addition, the recovery for specimen with 200 nm fibers starts at the first cycle, but the reduction in normalized modulus gradually decreases with increasing cycle number since smaller healing fibers trigger the repairing mechanism effectively for nano and sub-micron scale cracks but the encapsulated healing agent is not enough to fill the cracks in micron scale. At this point, DCPD encapsulated tri-axial fibers having larger mean fiber diameter are much proper for healing process of micro cracks and fibers with finer diameter can heal nano-scale cracks efficiently. Moreover, epoxy matrix is concurrently reinforced by PMMA/PAAm/epoxy and PMMA/PAAm/hardener tri-axial fibers with the fiber diameter of 1  $\mu\text{m}$  in order to measure and compare their self-healing efficiency with formerly introduced results. As seen from Figure 4.14f, the healing degree of epoxy based healing system is slightly higher than DCPD based healing system. Epoxy based healing specimen does not fail at the 4th healing cycle whereas DCPD based healing systems prepared with 200 nm and 1  $\mu\text{m}$  completely fail at this cycle. In addition, specimen reinforced by both tri-axial fibers including hardener and epoxy can heal itself until 5th healing cycle. Accordingly the differences in healing cycles with different

healing agents can be attributed to the fact that the epoxy healing system shows higher compatibility with epoxy based matrix while healing material produced by ROMP of DCPD monomer in the presence of Grubbs' catalyst is not compatible with the surrounding matrix like epoxy based system and hence causes the stress concentration leading to the failure of specimens at 4<sup>th</sup> healing cycle. One can see from Table 4.1 that the percentage reduction in the modulus of epoxy-based specimen has leveled off indicating that the self healing process is active, effective, and hence able to preserve the mechanical properties of composite under high loadings.

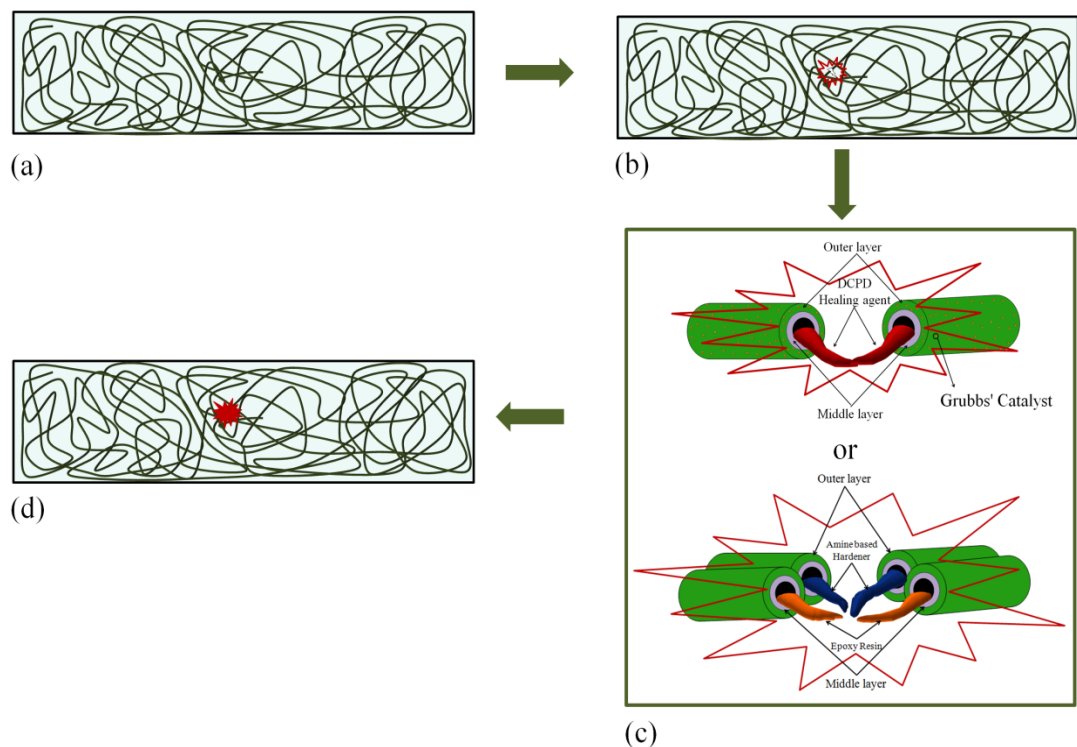


Figure 4.13 Schematic representation of self-healing concept, (a) the incorporation of self healing fibers into a polymer matrix, (b) cracks formation within the matrix due to the external load and consequent rupture of healing fibers, (c) the discharge of healing agent into the crack area followed by its polymerization upon getting in contact with either pre-dispersed catalyst in outer layer of fibers or the hardener released along with the healing epoxy, and (d) healing of crack region.

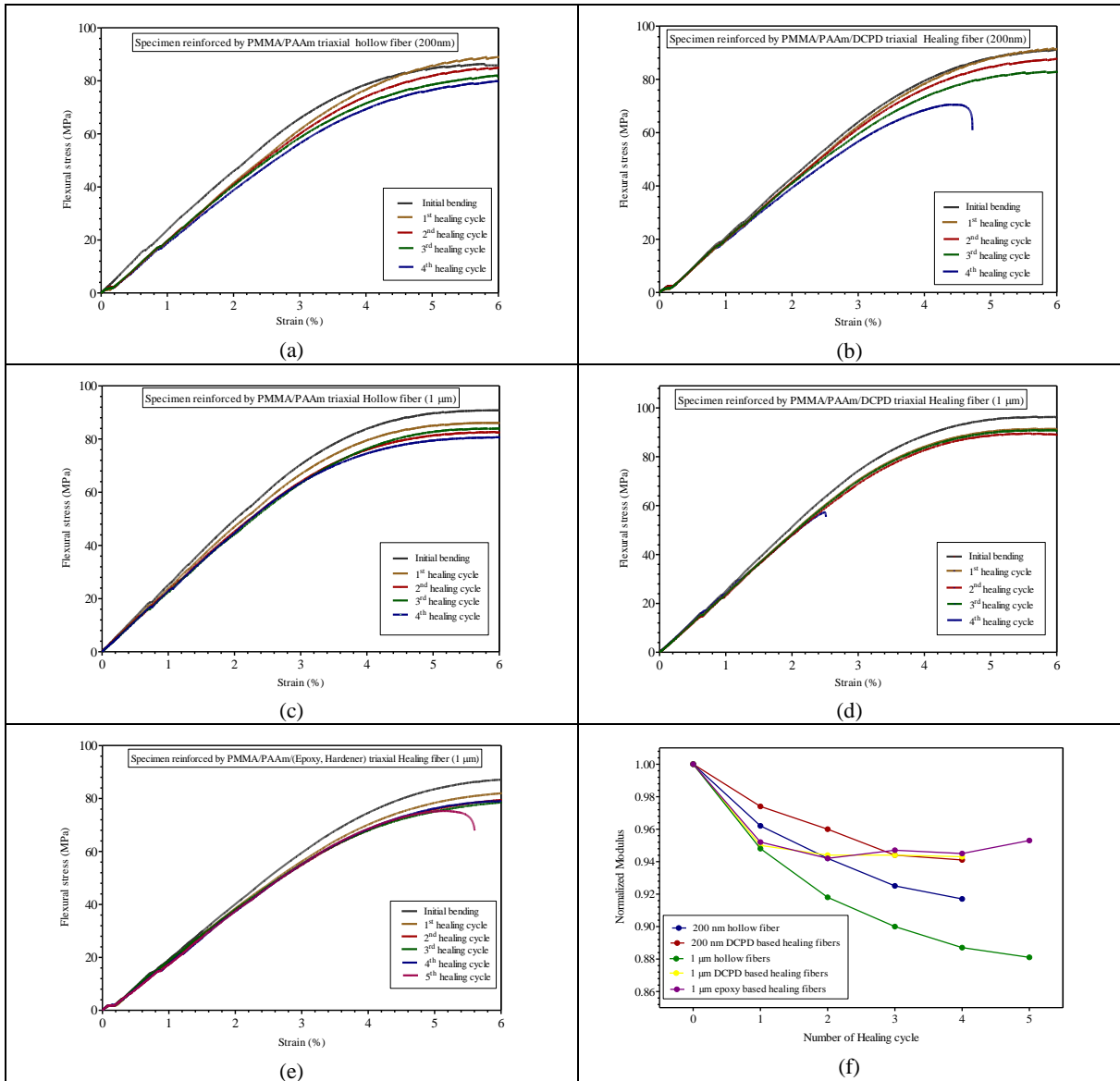


Figure 4.14 Flexural stress-strain curves of specimens reinforced by (a) PMMA/PAAm tri-axial hollow fibers with the average diameter of 200 nm, (b) PMMA/PAAm/DCPD healing fibers with the average diameter of 200 nm, (c) PMMA/PAAm tri-axial hollow fibers with average diameter of 1  $\mu$ m, (d) PMMA/PAAm/DCPD tri-axial healing fibers with the average diameter of 1  $\mu$ m (e) PMMA/PAAm/(hardener, epoxy) tri-axial healing fibers with the average diameter of 1  $\mu$ m and (f) Normalized flexural modulus of composites reinforced by tri-axial hollow and healing fibers with different diameters as a function of healing cycle

Table 4.1 Percent modulus reduction of specimens in each cycle based on initial modulus value.

		200 nm hollow fibers	200 nm DCPD based healing fibers	1 $\mu$ m hollow fibers	1 $\mu$ m DCPD based healing fibers	1 $\mu$ m epoxy and hardener based healing fibers
Modulus reduction (%)	1 <sup>st</sup> cycle	96.2	97.4	94.79	95	95.2
	2 <sup>nd</sup> cycle	94.2	95.95	91.78	94.4	94.2
	3 <sup>rd</sup> cycle	92.5	94.37	89.9	94.4	94.7
	4 <sup>th</sup> cycle	91.7	94.14	88.69	94.3	94.5
	5 <sup>th</sup> cycle	-	-	88.1	-	95.3

#### 4.3.6. Fracture Surface Characterization

Figure 4.15 exhibits SEM images of the fracture surfaces of tri-axial fibers reinforced composites that are obtained at the end of 4<sup>th</sup> healing cycle. Figure 4.15a corresponds to specimen reinforced by PMMA/PAAm hollow fiber with average diameter of 1  $\mu$ m while Figure 4.15b represents the fracture area of specimen with PMMA/PAAm/DCPD tri-axial healing fibers with average diameter of 1  $\mu$ m. The fracture surface of specimen reinforced by hollow tri-axial fibers with the diameter of 1  $\mu$ m looks very fragmented and rough. In addition, Figure 4.15a reveals the severe crack formations induced by repeated bending tests on the specimen reinforced by hollow fibers on the composite structure. On the other hand, Figure 4.15b represents the fracture surface of specimen reinforced by PMMA/PAAm/DCPD tri-axial healing fibers, and it can be seen clearly that new born polyDCPD films are formed by the release of encapsulated healing agent from the ruptured fibers into the cracked area and then reaction with pre-dispersed catalyst particles in outer layer of fibers. Therefore, the smooth surfaces are observed in the cross-sectional area of tri-axial healing fibers because healing agents filled and covered the damaged regions by the initiation of polymerization process. In the absence of healing agent, crack regions in the fracture area are seen clearly in Figure 4.15a. However, in the presence of healing agent, the fracture surface has a smoother appearance due to polymerization of released DCPD monomer thereon as seen in Figure 4.15b. This is the evidence for the efficient healing mechanisms and polymer coverage of crack regions. Figure 4.15c shows specimens reinforced by PMMA/PAAm hollow fiber with average diameter of 200 nm while Figure 4.15d exhibits the fracture area in the specimen with PMMA/PAAm/DCPD tri-axial healing fibers with average diameter of 200 nm. The fracture surface of specimen reinforced by tri-axial electrospun fiber with average fiber diameter of 200 nm in both case of hollow and healing fibers

shows very smoother surface morphology than one of similar specimens reinforced by 1  $\mu\text{m}$  fiber. However, size of the cracks on specimen reinforced by fibers with 200 nm are very small and thus limited amount of healing agents is released into the fracture area or inside the cracks and films of healing polymer occurred by healing process is not distinguishable in the SEM images but healing process has been already confirmed by mechanical tests after repetitive cycles. In addition, Figure 4.15c and 4.15d exhibit very uniform distribution of fibers in the composite structure and nano scale holes on the surface of cracks can be seen clearly.

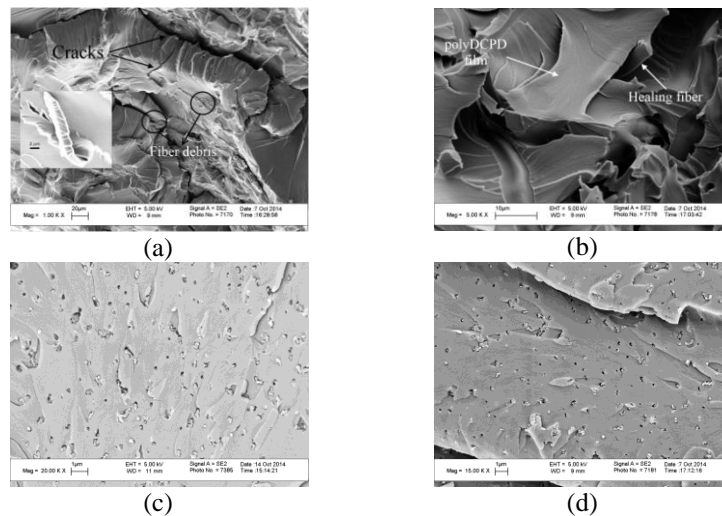


Figure 4.15 SEM images of fracture area of (a) PMMA/PAAm tri-axial hollow fiber reinforced epoxy specimen with the fiber diameter of 1  $\mu\text{m}$ , (b) PMMA/PAAm/DCPD tri-axial healing fiber reinforced epoxy specimen with the fiber diameter of 1  $\mu\text{m}$ , (c) PMMA/PAAm PMMA/PAAm tri-axial hollow fiber reinforced epoxy specimen with the fiber diameter of 200 nm (d) PMMA/PAAm/DCPD tri-axial healing fiber reinforced epoxy specimen with fiber diameter of below 200 nm.

#### 4.4. Conclusions

Novel architecture of electrospun multi-walled healing fibers are utilized in order to encapsulate various healing agents with two different protective walls. For the first design of healing fibers, DCPD as a healing agent is encapsulated inside the electrospun fibers with two different polymeric layers wherein the middle layer encapsulates healing agent due to its low affinity, and outer layer is compatible with epoxy matrix. The dispersion of metal catalysts into outer layer of fibers preserves the activity of catalyst during manufacturing process, reduces the required amount of catalyst in comparison to conventional catalyst dispersion into epoxy matrix, and provides the direct contact between the catalyst and healing monomer in crack region. The presence of an

intermediate layer having low affinity to healing agents facilitate the encapsulation of healing agents with very high active nature such as amine based hardeners into polymeric shells. In the second design of self healing fibers, epoxy resin and amine-based curing agent are separately encapsulated in multi-axial electrospun fibers. The low affinity between the inner wall polymer and encapsulated healing agent within the core of fibers minimizes the environmental effect on healing agents and decreases the diffusion rate of healing agent through the wall of fiber hence extending the efficiency and lifetime of healing functionality of fibers. In addition, the effect of fiber diameter (nano or micron scale) and the type of self-healing agent (DCPD monomer and epoxy resin) on self-healing properties of the produced composites were investigated by comparing mechanical properties. It is shown that healing fibers with larger mean diameter are much more appropriate for healing micro cracks whereas fibers with finer diameter can heal nano-scale cracks more effectively. The healing efficiency of epoxy based healing system is observed to be slightly higher than DCPD based healing system given that epoxy based healing specimen has shown five successful healing cycles while DCPD based healing specimens were broken after the fourth cycle. The reduction in mechanical properties of matrix reinforced by healing fibers reaches a stable value and subsequently does not change as a function of healing cycle while normalized modulus of specimens reinforced by hollow fibers continuously decreases in each cycle. To reiterate, the unique structure of multi-walled electrospun fibers developed in this work has a high potential to create a novel self-healing, smart and responsive materials with enhanced functionalities.

## **CHAPTER 5. ACOUSTIC EMISSION AND FIBER BRAGG GRATING AS A NOVEL TECHNIQUE FOR MEASURING SELF-HEALING EFFICIENCY OF TRI-AXIAL ELECTROSPUN FIBERS/ GLASS FIBER/ EPOXY COMPOSITES**

Tri-axial electrospun fibers with self-healing capability are fabricated through a direct, one-step tri-axial electrospinning process. Tri-axial electrospun fibers with two distinct protective walls are used to encapsulate epoxy resin and its hardener as healing agents in separate cores. The presence of an extra layer between encapsulated liquid healing agent and outer layer of fibers enables the encapsulation of chemically and physically active healing agents, extends the efficiency and life-time of the healing functionality, and provides the capability to enhance the interfacial compatibility between fibers and the matrix. Tri-axial electrospun healing fibers are used to add self-healing capability into solo epoxy matrix and as an interlayer between glass fabric mats in glass fiber reinforced laminated composite. Tri-axial electrospun fiber interlayers with encapsulated healing agent provide self-healing functionality at the interface of glass fibers with epoxy matrix, which is highly prone region to failure in fiber reinforced composites under load. Continuous and uniform morphology of tri-axial fibers provide successful and recurring self-healing ability for both composite types. In addition, various structural health monitoring and non-destructive testing techniques such as incorporation of Fiber Bragg Gratings sensors, and monitoring the acoustic emission, and Poisson's ratio reduction coupled with traditional mechanical testing methods are employed to evaluate the self-healing efficiency of composite structures, which bring a new insight into the evaluation of the healing efficiency of self-healing composites.

### **5.1. Introduction**

Advanced fiber-reinforced polymeric composites (FRPC) have been regarded as unique and promising candidates for a variety of structural applications due to their transcendent specific strength/modulus, physical performances, multi-functionality, design flexibility and relatively easy manufacturability [107]. Albeit with these culminated attributes, FRPCs couldn't unfold their full potential and are still being treated

as marginal due to the poor damage tolerance, delamination strength, impact resistance and low fracture toughness, which facilitate the initiation and the growth of multiple cracks under external loads or extreme environmental conditions [4, 108]. Matrix cracking and failure at the interface of matrix and reinforcing fibers generate stress concentration regions and lead to severe damage mechanisms thereby gradually reducing the stiffness and strength of the composite structures [109-111]. Different approaches have been developed to prevent these problems, namely, improving the interface properties between reinforcing fibers and polymeric matrix [18], and inhibiting the final failure by controlling the crack growth [112], and dispersing modifier particles into the matrix [113]. The integration of self-healing capability into fiber reinforced polymeric composites is one of the cutting edge approaches to augment the reliability and prolong effective lifetime of composite materials for more advanced applications [19]. Several attempts inspired by autonomous wound healing phenomena in biological systems have been made to mimic and integrate this natural process in the development of smart materials with self-healing capability [8]. The delivery of encapsulated reactive liquid agent into fractured area is one of the feasible methods to repair the cracks in the initial stage by restraining the crack propagation and restore the mechanical properties of the damaged materials [69, 70]. Despite several progresses made in the development of self-healing composites, most of the approaches are limited by two main drawbacks. The first one is the reduction in mechanical performance of structure due to the formation of defects during the integration of self-healing agent in the matrix [114]. The other one is the limitation of healing process only for few repairing cycles [115]. In order to address the mentioned limitations and bring new insight to this field, multi-axial electrospun fibers with a self-healing capability can be also considered novel. The electrospun fiber can also act as an interfacial toughening layer to extend the reliability of composites [116]. The effect of electrospun fiber interlayers as a toughening agent were studied and validated extensively by different groups in the literature [18, 117, 118]. The utilization of continuous and self-healing electrospun fibers in the composite structure provides repeated delivery of healing agent into the damage area when compared to the other encapsulation technique such as capsule based micro-encapsulation [19, 119].

Another important issue in self-healing composite production is to create an ability to monitor and characterize the healing performance of composites. Considering the biological systems as an inspiration source for the design and development of the next generation smart, functional and responsive materials, vascular blood network was provided by the integration of multi-walled electrospun fibers containing self-healing agent in the composite structure. Also, a neural system is required to detect damages in the structure and interpret the incoming signals to react with an appropriate response [120].

Different methods and sensors have been developed in recent years to provide structures with structural health monitoring (SHM) capability, which enables in-situ monitoring of structure starting from the fabrication steps until the failure of material [121]. Among these methods, Fiber Bragg Gratings (FBG) sensor based approaches have received particular attention since FBGs can be integrated in the desired regions of composite matrix and hence used to monitor, record and analyze damage states and health of components in the localized or global scale in real time [122]. FBGs have several notable advantages over other sensors such as immunity to electromagnetic interference, high sensitivity, multi-functionality, water and corrosion resistance, real time reading, structural flexibility [123]. Furthermore, due to their rather small size, they can be embedded into composite structures during manufacturing process without endangering the structural integrity [124]. An FBG is a segment of a single-mode optical fiber core with a periodically varying refractive index in the axial (longitudinal) direction [125]. Changes in the physical state of sensors due to the variations in mechanical loading, temperature and environmental conditions cause changes in both refractive index and the grating pitch (spacing between the refractive index) of the FBG sensor [126]. Another successful technique for SHM of fiber reinforced composite structures is acoustic emission which is very sensitive process to locate and monitor the damages in fiber-reinforced polymer composites [127]. In this method, each kind of damage and crack including matrix cracking, interface failure and fiber breakage in the composite structure generates specific acoustic emission signals [128]. In this study, both FBG sensors and acoustic emission methods have been used together to observe self-healing efficiency of composites. Herein, embedding FBG sensors in the composite structure with self healing

functionality is a novel and promising approach to create a neural system in the material since it can be used to monitor the efficacy of the self healing performance [129].

In our previous studies, we conducted a systematical optimization study to produce tri-axial hollow electrospun fibers with tunable fiber diameters and surface morphologies by using different polymers and changing electrospinning processing parameters [17]. In addition, the effect of tri-axial hollow fibers as primary reinforcement and co-reinforcement in the presence of glass fibers were investigated from material selection to processing optimization [18]. Furthermore, tri-walled healing fibers were utilized to encapsulate different healing agents inside the fibers with two distinct protective walls. The presence of an intermediate layer facilitates ease encapsulation of healing agents and extends the efficiency and life-time of the healing functionality and thus preserve the mechanical properties of the composite by repairing micro and nano scale cracks under test condition [19].

In the present work, epoxy resin and amine-based curing agents were encapsulated separately by tri-axial electrospinning inside the core of tri-axial fibers to produce different epoxy based composite structures having self-healing functionality. In the first design, tri-axial electrospun fiber reinforced epoxy composites were fabricated by using classical molding technique in which electrospun fibers act as both reinforcement and healing agent. In the second design, vacuum infusion technique was employed to fabricate glass fiber/tri-axial electrospun fibers/epoxy composite in which tri-axial healing fibers were deposited on the surface of reinforcing glass fabric mat to provide self healing functionality at the interface of reinforcing glass fibers with epoxy matrix and also enhance the composite toughness. To the best of our knowledge, there is no published work focusing on employing various SHM techniques and damage index monitoring such as FBG sensors, acoustic emission, and Poisson's ratio reduction, respectively, coupled with traditional mechanical testing methods to evaluate self-healing efficiency of composite structures. Herein, a systematical research was performed to bring a new insight into the production techniques and monitoring the self-healing efficiency of epoxy based composites. These hierarchical multi-scale designs of composites provide the ability to fabricate self-healing/sensing composite with the extended life-time and reliability.

## **5.2. Experimental**

### **5.2.1. Materials**

Polymethyl methacrylate (PMMA) and polyacrylamide (PAAm) used as outer and middle wall materials of tri-axial fibers, respectively, were synthesized and characterized in details in our previous publications [17, 18]. N, N dimethyl formamide (DMF, Sigma-Aldrich, 99%), deionized water and acetone (Aldrich, 99.5%) were used for the dilution of reagents during electrospinning process. LY 564 resin and hardener XB 3403 (Huntsman) and 0/90 biaxial E-glass stitched fabrics of Metyx company with the average weight of 313 g/m<sup>2</sup> (161 g/m<sup>2</sup> along the 0° direction, and 142 g/m<sup>2</sup> along the 90° direction) are used in composite production process.

### **5.2.2. Tri-Axial Electrospinning**

Tri-axial electrospun fibers were produced at ambient room conditions by using a tri-axial electrospinning set-up purchased from Yflow Company with a custom-made tri-axial nozzle. Figure 5.1 shows the schematic representation of multi-axial electrospinning process. All fibers were electrospun with a nozzle to collector distance of 7 cm by tuning the applied voltage in the range of 5 kV to 30 kV. Solutions are loaded independently into the syringes connected to concentric nozzles, and the flow rate of each layer is controlled by separate pumps. The flow rates of solutions for the outer and inner layers and the core are 20 µl/min, 15 µl/min and 10 µl/min, respectively.

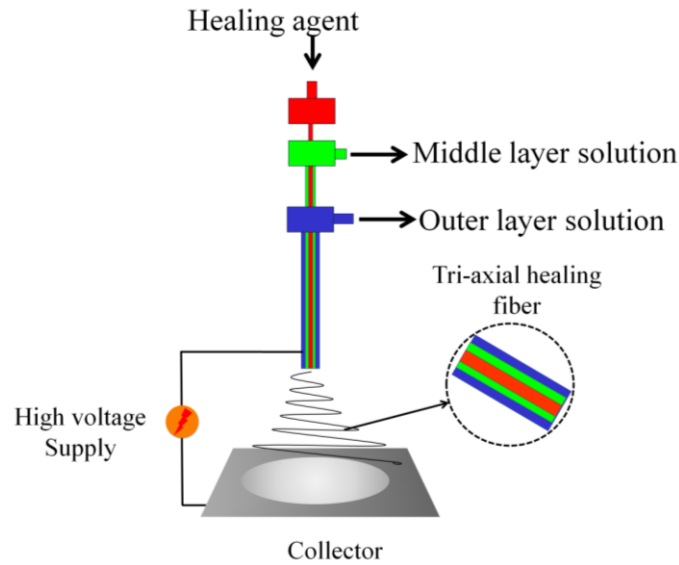


Figure 5.1 A schematic representation for tri-axial electrospinning set-up.

### 5.2.3. Fabrication of Self-healing Fiber Reinforced Epoxy Composites

In the first design, classical molding technique was employed to fabricate composite specimens in which hollow or healing electrospun fibers were used as a primary reinforcement to observe self-healing capability of the structure. Furthermore, self-sensing capabilities were added into two different types of composites by integrating FBG sensors in the structure to sense and monitor the environmental changes and variation in reflective index in FBG sensor. In this method, appropriate amount of electrospun fibers were placed into Teflon mould and uniformly covered on the mold surface and then the FBG sensor was placed in the mold such that it is positioned in the midpoint and above neutral axis of the flexural test specimen in the compression side. After the placement of fibers and FBG sensor, the mixture of degassed resin and hardener system was poured into the mold to produce composite specimen. Subsequently, vacuum was applied to remove the entrapped air bubbles from the resin and then curing was applied at 70 °C for 5 days. The electrospun fiber reinforced molded samples have the length, the width, and the thickness of 100 mm, 14 mm, and 3 mm, respectively, prepared for 3-point bending tests. In the second design, composite laminates with self-healing and self sensing functionalities at the interface of reinforcing glass fibers with epoxy matrix was produced by employing vacuum infusion technique. To this end, tri-axial healing or hollow fibers were initially deposited only on the 0° side of the 90°/0° biaxial E-glass stitched fabrics, which were then stacked to form a laminate of  $[(90^{\circ}/0^{\circ})_3]_S$ . Upon

stacking, the electrospun interlayer on the 0° side is shared with the 90° side of the biaxial fabric. The stacked fabrics were impregnated by the epoxy resin after being degassed by vacuum infusion process to manufacture a composite panel with the dimensions of 40 cm × 30 cm × 0.2 cm. The stacking sequence of the plies together with the placement of interlayer is given in Figure 5.2 The weight fraction of the primary reinforcement is 60 wt % while the weight content of the electrospun fiber is 2 wt %. The volume fractions of glass fiber in the composite laminates were calculated by burning test and found to be about 40 % of overall composites. The manufactured composite panel is cut to prepare flexural and tensile test specimens with the dimensions of 8 cm × 1.5 cm × 0.2 cm and 20 cm × 2.5 cm × 0.2 cm (with the gage length of 15 cm), respectively. To avoid the breakage of tensile specimens at grip locations, both the ends of specimens were tabbed with an aluminum tab having a dimension of 2.5 cm × 2.5 cm × 0.1 cm using two-component, room temperature curing epoxy system (araldite, 2011). Flexural and tensile tests were repeated three times for each specimen.

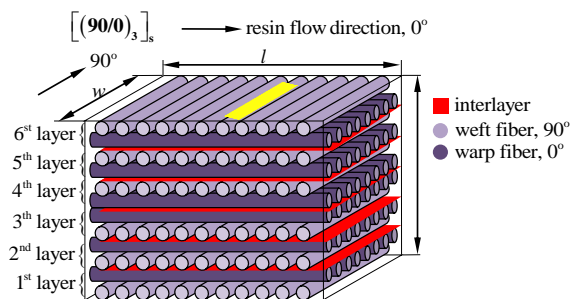


Figure 5.2 Stacking sequence and the placement of the interlayer in composite structure produced by vacuum infusion (the yellow region indicates the cut specimen for flexural and tensile tests) where an FBG sensor with the initial wavelength of 1550 nm was placed between the fifth and sixth layers.

#### 5.2.4. Characterization

The functional groups of polymers and fibers were analyzed by Netzsch Fourier Transform Infrared Spectroscopy (FTIR). Surface morphologies of fibers and fracture surface of composites were analyzed by a Leo Supra 35VP Field Emission Scanning Electron Microscope (SEM). Mechanical tests were conducted by ZWICK Proline 100 Universal Test Machine (UTM) with 10 and 100 kN load cells for 3-point bending and tensile tests, respectively, with a constant cross-head speed of 1 mm min<sup>-1</sup>. 3-point bending and tensile tests were performed in accordance with the ASTM D790-03 and

ASTM D5083-02 standards, respectively. The axial and transverse strains were measured during tensile tests with two clip-on strain gage extensometers (Epsilon 3542 axial extensometer with a fixed gage length of 25 mm and an Epsilon 3575 transverse extensometer with a controllable gage length). In addition, during tensile test, acoustic emission signals were collected by two wideband WD-sensors which were glued by hot melt glue at the end of specimen with 1 cm distance from tabbing of the specimen. A MISTRAS Micro II Digital AE system was used to collect the data from the sensors. In acoustic emission tests, sensitivity threshold was fixed at 60 dB with the sampling rate of 2 MHz. Noesis Software was used for post-processing the data and pattern recognition. The k-means algorithm as a simple and effective method for acoustic emission signal clustering was applied for classifying acoustic emission signal and distinguishing between the different damage mechanisms such as matrix cracking, interfacial debonding and fiber breakage. To investigate the failure mechanisms of manufactured composites, a detailed fractographic analysis was carried out on the cross section along the length of the specimen through the thickness following the procedure detailed in our previous publication [18].

#### **5.2.5. Fiber Bragg Grating Sensors (FBG)**

A fiber Bragg grating sensor includes a periodic modulation of the refractive index in the axial direction of an optical fiber created by a high intensity UV laser. The working principle behind the FBG sensor is based on the detection of changes in the reflective signal from the gratings when it is subjected to physical, thermal, and mechanical fluctuations. The light travelling inside the fiber core scatters in the regions of varying refractive indices. Out-of-phase scattered waves cancel each other while in-phase waves add up constructively to form the reflected spectrum in which the center wavelength is known as Bragg wavelength. According to Bragg conditions, Bragg wavelength can be expressed as  $\lambda_B = 2n_f \Lambda$  in which  $\lambda_B$  is Bragg grating wavelength,  $n_f$  is the effective refractive index of the fiber core and  $\Lambda$  is the grating periodic spacing. Mechanical and thermal deformations are observed by changing the grating spacing and refractive index of FBG sensors. The Bragg wavelength shifts regarding applied strain ( $\Delta\varepsilon$ ) and temperature ( $\Delta T$ ) that can be expressed in the form of  $\Delta\lambda_B = \alpha\Delta\varepsilon + \beta\Delta T$  where  $\alpha$  and  $\beta$  are the relevant strain and temperature sensitivity factors, respectively. Figure 5.3 represents the working principle of FBG sensors. In this study, FBG data were collected at a

sampling rate of 100 Hz with a Micron Optics SM230 interrogator using Micron Optics ENLIGHT software. FBG sensors used in the experiments were 1 mm long with a uniform grating, polyimide coating, and different center wavelengths ranging from 1540 to 1565 nm supplied by Technica SA. Also, these sensors were sewed into inner surface of first layer glass fibers in order to monitor the healing performance of glass fiber reinforced structure.

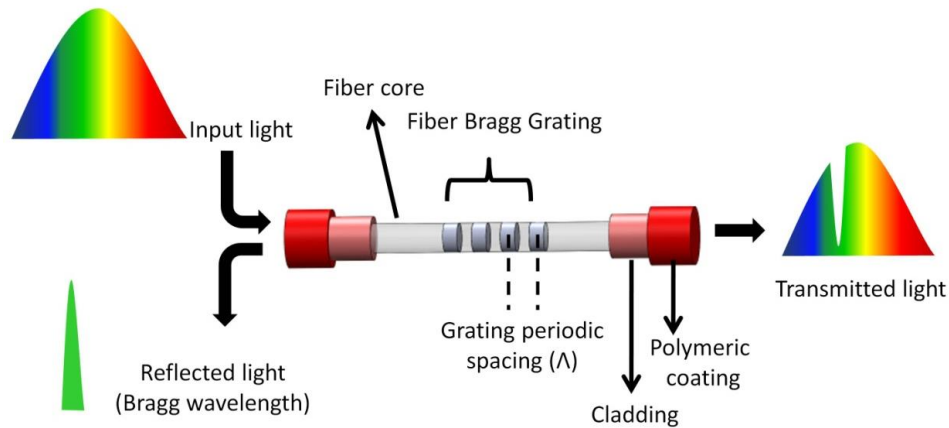


Figure 5.3 Schematic representation of working principle of a FBG.

## 5.3. Results and Discussions

### 5.3.1. Fabrication of Tri-walled Healing Fiber

Both tri-axial hollow and healing fibers were fabricated through tri-axial electrospinning technique to be used as a reinforcing agent. In the healing fibers, two different healing agents, namely hardener and acetone diluted epoxy resin, were separately encapsulated inside the fiber structure. PMMA used as an outer material of fiber shows high compatibility with epoxy matrix and plays a key role in mechanical enhancement of composite by the formation of semi interpenetrating polymer network (semi-IPN) between fibers and epoxy matrix [18]. On the other hand, PAAm chosen as a middle layer material reduces the interaction of healing agents with surrounding environment due to its low affinity between inner material and outer layer polymer [19]. Middle layer in fiber structure brings an advantage for the encapsulation of different healing agents by increasing their efficiency and lifetime.

### 5.3.2. Structural characterization of tri-axial hollow and healing fibers

Figure 5.4 represents SEM and TEM images of tri-axial electrospun healing and hollow fibers used as a reinforcement in epoxy matrix. SEM image of PMMA/PAAm/epoxy tri-axial healing fibers given in Figure 5.4a shows uniform fiber formation. Figure 5.4b exhibits the structure of PMMA/PAAm tri-axial hollow fibers. SEM images bespeak that both healing and hollow fibers have almost the same morphology, which provide the ability to compare the mechanical properties and healing efficiency of epoxy specimens reinforced by these fibers. Figure 5.4c exhibits TEM images of PMMA/PAAm/hardener tri-axial healing fiber in which dark regions in the core of the fiber are due to healing agent while the bright regions at the boundaries correspond to the polymeric shells. Figure 5.4c confirms the complete coverage of healing agent inside the fiber. On the other hand, TEM image of PMMA/PAAm tri-axial hollow fiber in Figure 5.4d reveals the presence of two polymeric walls and hollow core of fiber.

FTIR analysis was performed to confirm successful encapsulation of healing agent into the multi-walled fibers through identifying the characteristic peaks of different wall materials and healing agents. Figure 5.5a shows FTIR spectra of hardener, PMMA/PAAm tri-axial hollow fiber and PMMA/PAAm/hardener tri-axial healing fiber. In the FTIR spectra of electrospun PMMA/PAAm tri-axial hollow fibers shown in Figure 5.5a and 5b, the absorption bands at  $2950\text{ cm}^{-1}$  and  $1745\text{ cm}^{-1}$  belong to C-H and C=O stretchings of PMMA polymer, respectively [46]. For PAAm polymer, asymmetric and symmetric NH stretchings of  $\text{NH}_2$  contribute to the absorption bands at around  $3300\text{ cm}^{-1}$  [17]. In tri-axial fiber containing hardener in Figure 5.5a, the peak at  $1590\text{ cm}^{-1}$  corresponds to N-H bending vibration and strong peak at  $1150\text{ cm}^{-1}$  attributes to C-N stretching which confirms the presence of amine based hardener in the fiber structure [105]. Figure 5.5b exhibits the FTIR spectra of epoxy resin, PMMA/PAAm tri-axial hollow fiber and PMMA/PAAm/epoxy tri-axial fibers. In these spectra, the peaks at  $815\text{ cm}^{-1}$  and  $840\text{ cm}^{-1}$  belonging to oxirane groups verify the presence of epoxy resin in tri-axial fiber structure. Further characterization on encapsulation quality, fiber morphology and other advanced physical-chemical characterizations were discussed in details in our previous publication [19].

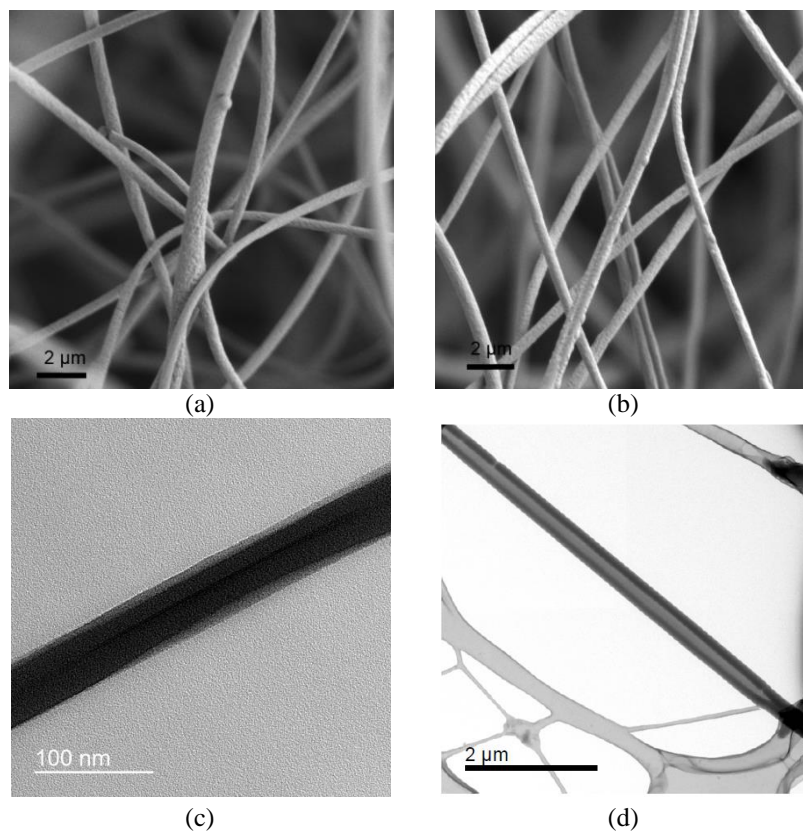


Figure 5.4 SEM images of (a) PMMA/PAAm/epoxy tri-axial healing fibers, (b) PMMA/PAAm tri-axial hollow fiber; TEM images of (c) PMMA/PAAm/hardener tri-axial healing fibers and (d) PMMA/PAAm tri-axial hollow fiber

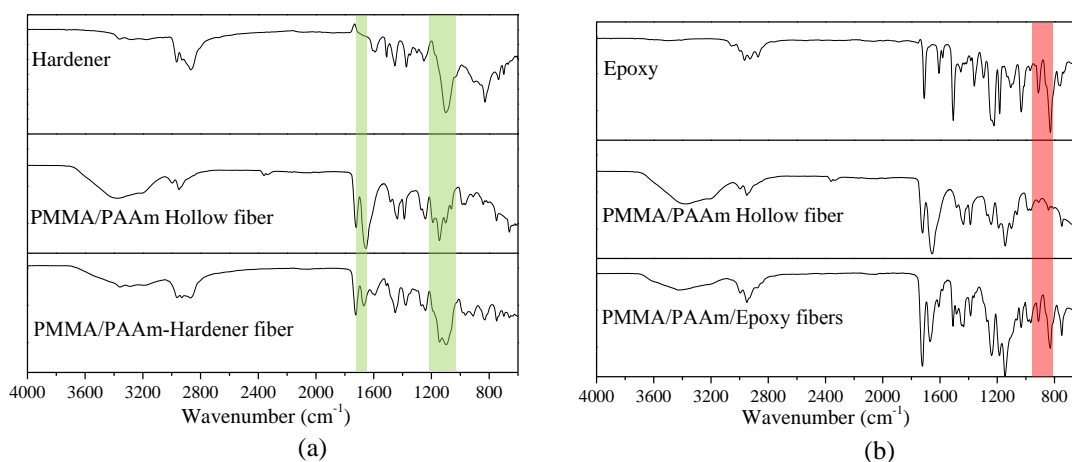


Figure 5.5 FTIR spectra of (a) hardener, PMMA/PAAm tri-axial hollow fiber and PMMA/PAAm/hardener tri-axial fiber and (b) epoxy, PMMA/PAAm tri-axial hollow fiber and PMMA/PAAm/Epoxy tri-axial fiber.

### 5.3.3. Tri-axial self-healing fiber reinforced composite with FBG sensors

In this section, mechanical performance and self-healing functionality of specimens primarily reinforced by PMMA/PAAm hollow tri-axial fibers and PMMA/PAAm/(epoxy, hardener) tri-axial fibers were investigated by various techniques. Both types of specimens were subjected to repeated bending/healing cycles through 3-point bending whereby in each cycle, test discontinued at the flexural strain of 5%. The 5% flexural strain is selected to prevent the creation of non-repairable cracks in each cycle while being able to generate enough nano and micron size cracks in each cycle. During these tests, applied stress, strain and signals from FBGs of each sample were recorded separately and then processed to quantify the healing level of specimens. After each bending/healing cycle, specimens were kept on heating table for 20 h at 70 °C for the completion of healing reaction while relaxing to obtain its original shape for the next test cycle. Figure 5.6a and b exhibit the flexural stress–strain curves of representative specimens reinforced by PMMA/PAAm tri-axial hollow fibers and PMMA/PAAm/(epoxy, hardener) tri-axial healing fibers, respectively. From stress-stain curves of specimens presented in Figure 5.6a and b, it can be concluded that after the strain of 3%, samples started to show non-linear behavior or yield which indicates the initiation of nano- and micro-cracks inside the composite structure under the applied stress. Moreover, for the composite specimen with tri-axial hollow fibers, the stress strain curve of subsequent cycles deviates from the previous cycles notably pointing to the damage accumulation in the specimen. In addition, as seen from stress-stain curves after each test cycle, flexural modulus decreases gradually due to the growth and coalescence of the already formed cracks as well as the creation of new cracks inside the structure. In the stress-stain curves of specimen with self-healing functionality in Figure 5.6b, the reduction in modulus values of self-healing specimen in each cycle is lower than the values of specimen reinforced by hollow fibers presented in Figure 5.6a. This shows that fibers containing healing agent repair the cracked area in specimen structure whereas more severe reduction in mechanical properties of specimen reinforced by hollow fibers is observed. In addition, specimen reinforced by tri-axial self-healing fibers resists the complete fracture one more cycle when compared to the specimens reinforced by tri-axial hollow fiber reinforced specimens. In order to clarify healing efficiency, normalized modulus values for each specimen, defined as the ratio of flexural modulus of the

specimen at each bending test cycle to flexural modulus at the first bending test, are compared as a function of healing cycles in Figure 5.6c. Herein, as the number of bending/healing cycle increases, normalized modulus values for each specimen decreases due to the creation of new cracks and damage accumulation in each test cycle in the structure. As seen in the Figure 5.6c, the specimen reinforced by healing fibers experiences lower reduction in normalized modulus per cycle than the one reinforced by hollow fibers. Figure 5.6c confirms that the presence of healing fibers inside the structure can partially repair the cracks, reduce the damage accumulation in each test cycle, and as a result recover part of the mechanical properties of specimens. Table 5.1 tabulates the percentages of reduction in the flexural modulus in comparison to the first bending cycle of each specimen.

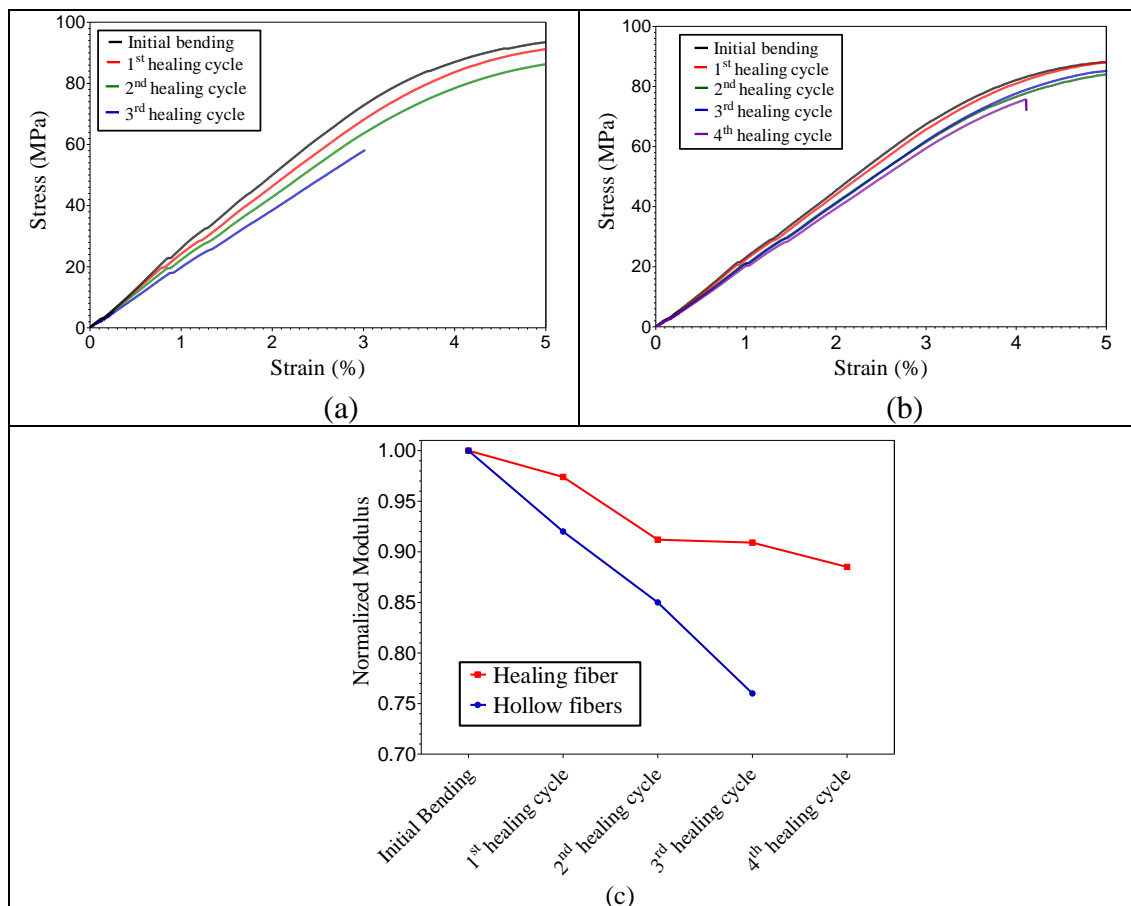


Figure 5.6 Flexural stress–strain curves of specimens reinforced by (a) PMMA/PAAm tri-axial hollow fibers, (b) PMMA/PAAm/(epoxy, hardener) tri-axial healing fibers, and (c) normalized flexural modulus of composites reinforced by tri-axial hollow and healing fibers as a function of healing cycle

Table 5.1 Percent modulus reduction of specimens in each cycle based on initial modulus value

Modulus reduction (%)		Hollow fiber	Healing fiber
	Initial bending		100
1 <sup>st</sup> healing cycle		92	97.4
2 <sup>nd</sup> healing cycle		85	91.2
3 <sup>rd</sup> healing cycle		76	90.9
4 <sup>th</sup> healing cycle		—	88.5

Due being a discrete sensor with a very small gage length, FBG sensors are capable of recording the local variations in the strain fields in their vicinity due to the formation of cracks and damages. Hence, the strain reading of an embedded FBG sensor is affected by the damage state in the composite structure. This future of an embedded FBG sensor can be utilized to investigate the efficacy of self healing of composites such that the repair of cracks in the structure enables the FBG strain reading not to deviate significantly from the one measured on a sound structure. To this end, we have manufactured flexural test specimens reinforced by PMMA/PAAm tri-axial hollow fibers and PMMA/PAAm/(epoxy, hardener) tri-axial healing fibers. Both specimens have an embedded FBG sensor above their neutral axis. Specimens with FBG sensors positioned in the compression side were subjected to 4 cycles of loading up to 5% flexural strain while FBG sensor data are collected during these cycles. After each cycle, specimens were kept in a furnace at 70 °C for 24 hours. The collected FBG data for both specimens were processed and plotted as graph of Bragg's wavelength versus the test time (effectively corresponding to the applied flexural strain) although not shown here for brevity. Upon examining the variation of wavelength shift or equivalently strain acquired during each loading cycle, it was observed that the FBG sensor embedded in a specimen reinforced by PMMA/PAAm tri-axial hollow fibers yields different strain level where the strain of each cycle deviates from the previous one notably. On the other hand, the FBG of the specimen reinforced by PMMA/PAAm/(epoxy, hardener) tri-axial healing fibers gives rather close strain level after each cycle. To be able to concisely present and quantify the FBG data of each healing cycle, the shift in the Bragg wavelength between the initial cycle and subsequent healing cycles were computed for each data point and then divided by the corresponding shifted Bragg wavelength and the total number of data point such that  $\alpha = \sum_{j=1}^{j=N} (\lambda_{i,j} / \lambda_{h,j} - 1) / N$ . Here,  $\alpha$  is referred to as the damage indicator,  $\lambda_{i,j}$  and  $\lambda_{h,j}$  are the Bragg wavelengths of each data point "j" for initial bending cycle, and subsequent healing cycles, and N is the total number of data points.

Figure 5.7 shows  $\alpha$  vs healing cycle for each healing test for specimens reinforced by PMMA/PAAm tri-axial hollow and PMMA/PAAm/(epoxy, hardener) tri-axial healing fibers. In this figure,  $\alpha$  values of specimen reinforced by PMMA/PAAm tri-axial hollow fibers drastically increase in each cycle whereas those of the specimen reinforced by PMMA/PAAm/(hardener, epoxy) tri-axial healing fibers change slightly. This indicates that the self-healing process repairs most of the cracks formed during the flexural loading whereby the strain state of the composite specimen is recovered to that of initially undamaged structure to a certain extent. To elaborate the discussion further, the FBG strain reading is significantly affected by the formation of cracks in the composites which alters the distribution of strain field since the FBG is a discrete local sensor. Hence, the strain measured by embedded local sensor with a rather small gage length can be significantly different in the presence of damage in the structure. One would clearly expect that if there was not any crack in the specimen, or those formed was repaired after each cycle, the measured strains in each cycle should be nearly identical. Thus, the FBG aided method for the determination of the healing efficiency is a novel approach and shown to be effectively used for accurate, fast and real-time measurements of healing functionality in smart self-healing materials.

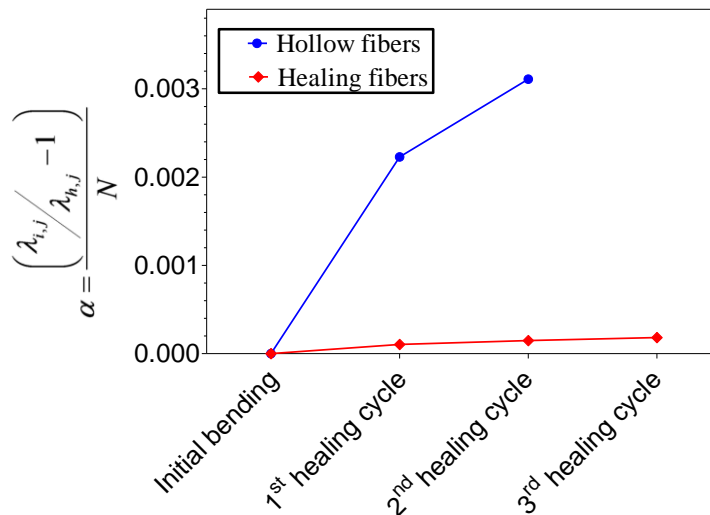


Figure 5.7 The variation of damage indicator as a function of healing cycles.

### 5.3.4. Fracture surface characterization

The morphology of fracture surfaces was examined to understand self-healing efficiency and mechanism in the crack regions. Figure 5.8 exhibits SEM images of fracture surfaces of hollow fiber and tri-axial self-healing fiber reinforced composites obtained at the end of healing cycles. The fracture surface of specimen reinforced by hollow tri-axial fibers looks very fragmented and rough as seen in Figure 5.8a and b. On the other hand, Figure 5.8c and d represent the fracture surface of specimen reinforced by PMMA/PAAm/(epoxy, hardener) tri-axial healing fibers. It can be seen clearly that new born epoxy films are formed by the release of encapsulated healing agent from the ruptured fibers into the cracked area and then reacts with the released hardener. Therefore, the smooth surfaces are observed in the cross-sectional area of tri-axial healing fibers because healing agents filled and covered the damaged regions by curing epoxy at the damaged regions.

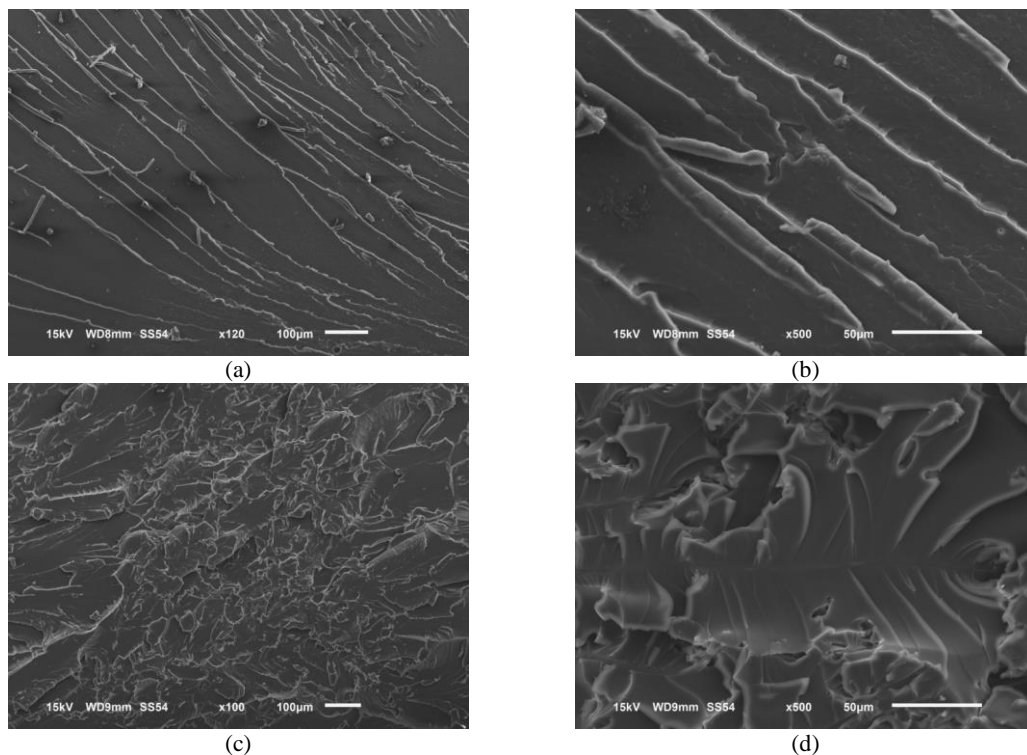


Figure 5.8 SEM images of fracture areas of (a, b) PMMA/PAAm tri-axial hollow fiber reinforced epoxy specimen, (c, d) PMMA/PAAm/(epoxy, hardener) tri-axial healing fibers reinforced epoxy specimen

### 5.3.5. Self-healing of epoxy/glass fibers interfaces

#### 5.3.5.1. Evaluation of self-healing by Flexural test and FBG sensors

Multi-functional tri-axial healing fibers were deposited onto the surface of glass fabric mats to act as an interface modifier agent. These fibers are capable of release a curable resin into the interface of polymeric matrix and glass fabric in the path of a propagating crack as well as enhance the interlaminar strength of structure [18, 19]. The stacking sequence of plies together with the placement of interlayer is given in Figure 5.2. In addition, an FBG was sewed into inner surface of first layer glass fibers in order to monitor the curing, healing and performance of glass fiber reinforced structure since as stated previously FBG sensors lend themselves to monitoring the variation of strain field due to the formation and repair of cracks in their vicinity. Herein, 3-point bending specimens reinforced by hollow or healing fibers were subjected to repeated bending/healing cycles and these specimens were subjected to 3% flexural strain. After each cycle, composite specimens were kept in oven for 24 h at 70 °C to trigger the healing reaction. In order to measure healing efficiency, normalized modulus values for each specimen were compared as a function of healing cycles in Figure 5.9a. All normalized modulus values were decreased by increasing bending/healing cycle number due to damage accumulation in the structure associated with the matrix cracking, primary reinforcing fiber-matrix delamination, and fiber breakage in each bending test cycle. It is clearly seen from Figure 5.9a that the specimens having PMMA/PAAm/(epoxy, hardener) healing fiber interlayers experience significantly lower reduction in normalized modulus per cycle than hollow fiber reinforced specimens. This result indicates that the presence of healing fibers as an interlayer in the glass fiber reinforced structure can trigger the healing reaction to repair the cracks, and repair the glass fiber and epoxy deboning at the interface, and recovers the mechanical properties of specimens to a certain extent. In Figure 5.9a, after initial bending, normalized modulus values for two specimens reinforced by hollow and healing fibers decrease. However, the reduction in normalized modulus for specimens having healing functionality are comparably less than hollow fiber reinforced specimens, and self-healing specimen shows a plateau behavior by increasing the healing cycle up to 4<sup>th</sup> healing cycle, and its normalized modulus values are almost in same range between 2<sup>nd</sup> and 4<sup>th</sup> healing cycle. After 4<sup>th</sup> cycle, normalized modulus of this specimen starts to decrease linearly until 6<sup>th</sup> cycle due to the depletion of

healing material in the cracked regions. However, after 6<sup>th</sup> healing cycle, self-healing activities are observed again in the healing specimens due to the creation of cracks in different regions of specimens and the rupture of new healing fibers. On the other hand, specimens reinforced by hollow fibers show almost linear reduction of normalized modulus until the end of the healing cycles.

During 3-point bending test of specimens, signals received from FBGs were recorded and internal behavior of specimens was monitored by these sensitive sensors. Figure 5.9c exhibits the signals recorded from specimen having self-healing functionality. In the initial bending cycles, Bragg wavelength increases linearly since the FBG sensors were placed in the tension side of the specimen. In the subsequent cycles, damage induced in composite structures hinder the applied flexural load to be transferred to the FBG sensor region and in turn, FBG sensors start reading strain levels much smaller than that in the initial cycle. After the initiation of self-healing mechanism upon the release of healing agent, FBG sensor in composite with self healing ability partially regains its sensitivity due to the repair of damage in its vicinity. The recovery efficiency decreases as healing cycles increases owing to the accumulation of damage and depletion of healing agent inside the healing fibers in the sensor region. On the other hand, in Bragg wavelength vs. duration of test graphs of the specimen reinforced by hollow fibers as seen in Figure 5.9b, except the first cycle, FBG sensor losses its strain sensitivity, and similar behavior is detected in each cycle due to the lack of healing agent. This FBG monitoring process confirms the healing functionality of self-healing fibers at the interface of glass fiber and epoxy matrix, which is a novel effective and non-destructive technique for the evaluation of self-healing efficiency.

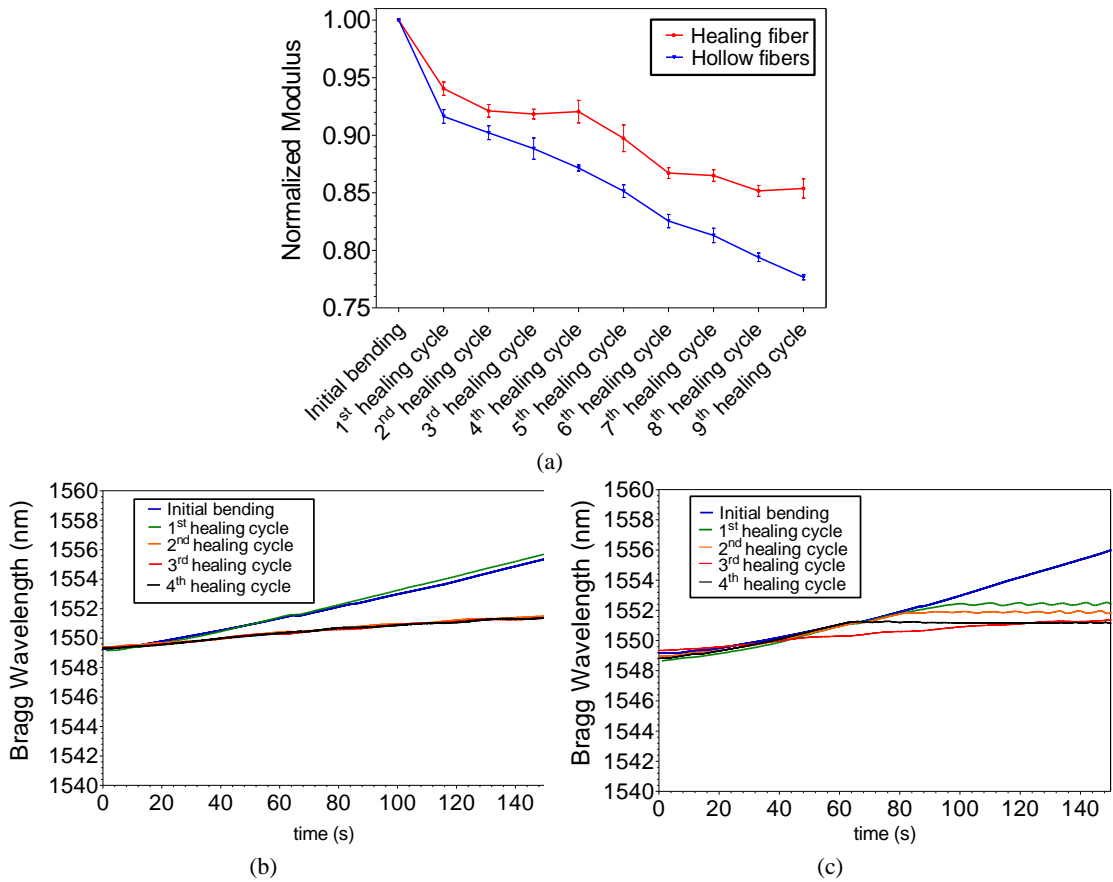


Figure 5.9 (a) Normalized flexural modulus of glass fiber reinforced composites as a function of healing cycle and, Bragg wavelength vs. test duration graph for (b) PMMA/PAAM tri-axial hollow fibers reinforced composites and (c) PMMA/PAAM/(epoxy, hardener) tri-axial healing fibers

### 5.3.5.2. Evaluation of self-healing by tensile test, Poisson's ratio and acoustic emission

Self-healing performance of glass fiber/epoxy composite co-reinforced by hollow and healing tri-axial fibers as interlayer was also investigated under tensile loading condition with the aim of showing that tension induced damages can also be healed through the proposed healing mechanism. In order to perform self-healing tests in tensile mode, self-healing composite specimens with hollow and healing tri-axial fibers were subjected to repeated tensile/healing cycles wherein the specimens were subjected to 200 MPa stress and then were kept in oven for 24 h at 70 °C for healing reaction. Figure 5.10a exhibits the normalized tensile modulus of specimens as a function of

tensile/healing cycles. For both specimens, normalized tensile modulus values decrease with increasing tensile/healing cycle due to the damage induced stiffness degradation, a well-known phenomenon for composite materials under cyclic loading. However, specimens with PMMA/PAAm/(epoxy, hardener) healing fibers experience lower reduction in normalized modulus per cycle than hollow fiber reinforced specimen. This confirms the effective activation of self healing mechanism through the applied tensile loading on the specimens. In order to enhance our understanding on damage initiation and propagation under tensile load and the role of self-healing on damage repair, axial strain ( $\epsilon_x$ ) and transverse strain ( $\epsilon_y$ ) were monitored by axial and transversal extensometers simultaneously during the tensile test whereby Poisson's ratio  $\nu_{xy} = -\epsilon_y/\epsilon_x$  was computed and then plotted as a function of axial strain as seen in Figure 5.10b and c. At the initial stage, Poisson's ratio increases rapidly for all specimens by increasing the axial strain, and reaches a maximum point, which will be hereafter referred to as the maximum Poisson's ratio due to the fact that the lateral strain increases nonlinearly as a function of applied axial strain [113, 130]. For the initial tensile cycle in both hollow and healing fiber reinforced specimens, Poisson's ratio initially increases and then reaches a plateau around the value of 0.14 which indicates that both specimens have similar initial mechanical performance and behavior. For hollow fiber reinforced specimen, thereafter, it decreases notably in each cycle. The decreasing trend in Poisson's ratio is associated with the reduction in the rate of the increase of the lateral strain due to the transverse cracking. Knowing that transverse crack will reduce the transfer of axial stress to the lateral direction and hence, the specimen should experience a progressively smaller increase in the lateral strain with applied load as the test continues. On increasing the test cycles, the applied axial strain can create further transverse cracks and damage in composite materials, and hence Poisson's ratio follows a dissimilar path to the previous cycles. As the cycle number increases, the Poisson's ratio gets smaller maximum values. This is attributed to the fact that, on the formation and accumulation of transverse cracks, the axial strain cannot be transferred in the lateral direction and, therefore, the lateral strain for a given axial strain decreases with respect to the previous cycle. The difference among the corresponding paths of Poisson's ratio for initial and subsequent cycles increases more notably in specimen reinforced by hollow fiber than that reinforced by self healing fibers. For hollow fiber reinforced composite, the decreasing trend of the Poisson's ratio after the maximum of each cycle is much bigger than that for self healing fiber reinforced

composite specimen. In addition, the Poisson's ratio of the specimen without healing functionality fluctuates signaling the formation and accumulation of cracks in the structure. These observations prove repair of cracks or damage formed in composite after each cycle and hence self-healing capability of the developed method. It is prudent to state that the Poisson's ratio monitoring can be used as an effective and novel damage index for studying the effectiveness of self healing process.

In addition, acoustic emission technique was employed during tensile test to quantify the different damage modes and evaluate self-healing efficiency at the interface of reinforcing fibers and polymeric matrix. Sensors at the surface of specimens record the generated acoustic signals from all parts of specimen. Various acoustic signals generated during mechanical tests can be post-processed by different techniques such as pattern recognition and clustering to determine the specific damage modes [131]. For the identification of matrix cracking, interface failure and fiber breakage, acoustic signals were clustered by applying K-means algorithm. As it is seen in Figure 5.10d and e, three distanced clusters are distinguished in each test cycle. The first cluster in the range of 50-150 Hz corresponds to matrix cracking, the second cluster between 150-400 Hz represents the signals generated due to interface phenomena and the third cluster in the range of 400-520 Hz is associated with fiber breakage in the composite structure [132]. In Figure 5.10d and e, in the initial tensile test and 1<sup>st</sup> healing cycles, similar acoustic emission clustering patterns are seen for both specimens reinforced with healing fibers and hollow fibers and these signals are mostly located at matrix cracking region. On the other hand, in 2<sup>nd</sup> healing and subsequent healing cycles, specimen without healing capability showed several crack formations and interface failure in its structure (Figure 5.10d) whereas the number of acoustic hits for specimen with healing capability is comparably much lower. In addition, in the 4<sup>th</sup> healing cycle, more severe fracture mechanism is activated in the specimen without healing capability. However, specimens having healing fibers repair the interface damages and prevent the accumulation of cracks and extend the life-time of composite structure.

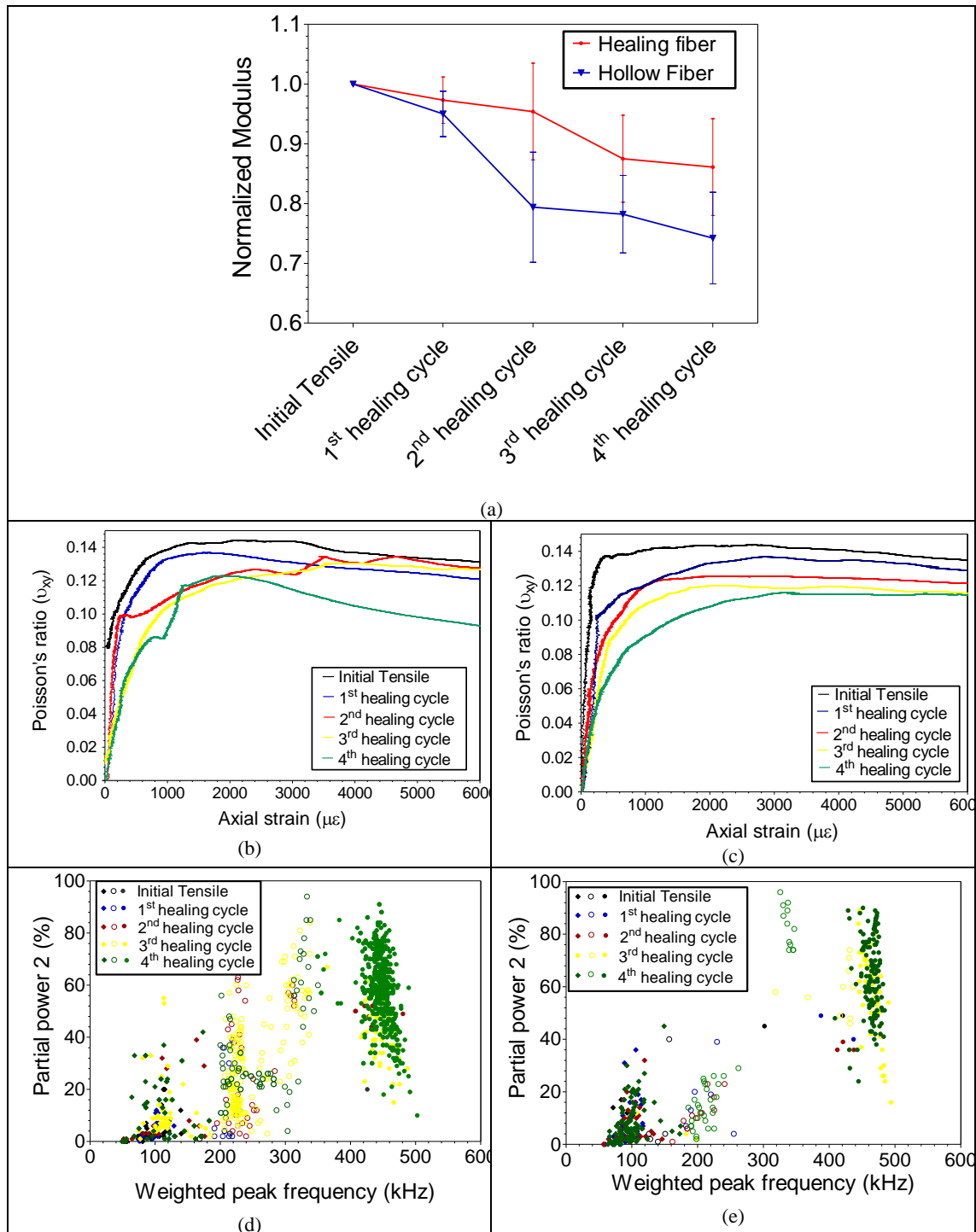


Figure 5.10 (a) Normalized tensile modulus of glass fiber reinforced composites as a function of healing cycle, (b-c). Poisson's ratio vs. axial strain graphs for PMMA/PAAm tri-axial hollow fibers and PMMA/PAAm/(epoxy, hardener) tri-axial healing fibers reinforced composites, respectively, (d-e) acoustic emission clustering patterns for PMMA/PAAm tri-axial hollow fibers and PMMA/PAAm/(epoxy, hardener) tri-axial healing fibers reinforced composites, respectively, where in these scatter-plots, each data point represents an acoustic signal.

### 5.3.6. Fracture surface characterization

A fractographic analysis was performed on the cross section of flexural test specimens (bounded by length and the thickness) to scrutinize the effect of hollow and healing tri-axial fiber on the healing efficiency of composites. Fig 11 presents SEM images of cross-sectional areas of flexural test specimens after cutting and polishing steps. Fig. 11a exhibits the cross section of specimen reinforced by hollow fiber after last healing experiment and complete delamination is seen at the interface of glass fiber and matrix. On the other hand, in Fig 11b, repairing the interface between glass fiber and matrix is observed clearly. Herein, healing agent leaks into the crack region and heals this region by initiation of polymerization after curing process. Therefore, SEM analysis supports self-healing composite production by the integration of tri-axial electrospun fibers.

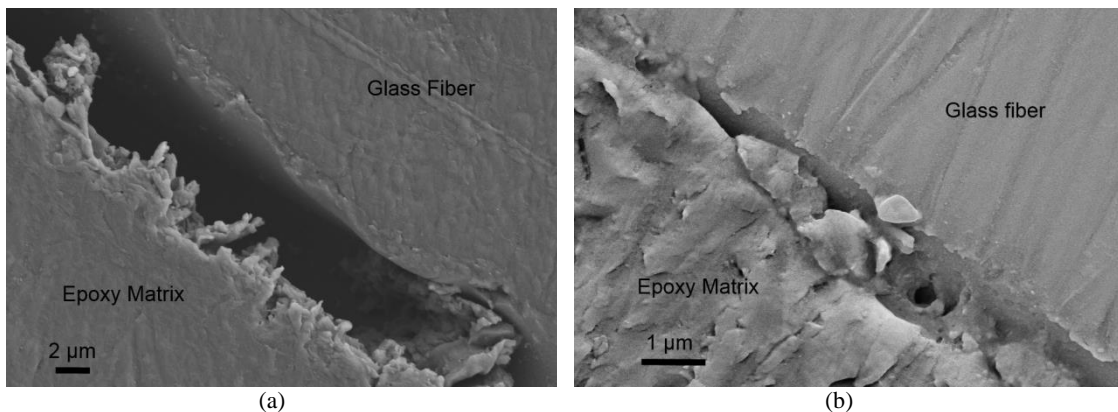


Figure 5.11 SEM images of cross-sectional areas of (a) PMMA/PAAm tri-axial hollow fibers reinforced composite and (b) PMMA/PAAm/(epoxy, hardener) tri-axial healing fibers reinforced composite.

### 5.4. Conclusions

Tri-axial electrospun fibers are utilized to encapsulate the epoxy resin and its hardener as healing agents into the core of the fibers. The presence of two distinct protective walls enables the control of interfacial interaction between outer layer of fibers with epoxy matrix and thus preserving the mechanical properties of composite compared to virgin structure. In addition, utilization of a polymeric middle layer with low affinity to encapsulated liquids minimizes the environmental effect on healing agents, and extends the efficiency and lifetime of healing functionality of the fibers. Two different composite

production techniques are employed to fabricate self-healing epoxy based composite structures. In the first method, tri-axial electrospun fiber reinforced epoxy composites were fabricated by using classical molding technique in which electrospun fibers act as both reinforcement and healing agent. In the second method, vacuum infusion technique was employed to fabricate glass fiber/tri-axial electrospun fibers/epoxy composite in which tri-axial healing fibers provide self-healing functionality at the interface of the glass fibers with epoxy matrix and enhance the composite toughness. Traditional mechanical testing methods and different SHM techniques such as FBG sensors, acoustic emission, and Poisson's ratio reduction are employed to analyze the health and damage states of components in the localized and global scale in real time. Successful and recurring self-healing ability of composite structures and healing functionality of fibers at the interface of glass fiber with the epoxy matrix are confirmed through different characterization techniques. To reiterate, the integration of multi-functional tri-axial electrospun fibers into composite structures as well as utilization of SHM techniques to evaluate the performance of self-healing materials which is developed in this work, can be a stepping-stone for future developments of multi-functional self-healing materials.

## **CHAPTER 6. NANO-ENGINEERED DESIGN AND MANUFACTURING OF HIGH-PERFORMANCE EPOXY MATRIX COMPOSITES WITH CARBON FIBER/SELECTIVELY INTEGRATED GRAPHENE AS MULTI-SCALE REINFORCEMENTS**

Three different architectural designs are developed for manufacturing advanced multi-scale reinforced epoxy based composites in which graphene sheets and carbon fibers are utilized as nano- and micro-scale reinforcements, respectively. In the first design, electrospraying technique as an efficient and up-scalable method is employed for the selective deposition of graphene sheets onto the surface of carbon fabric mats. Controlled and uniform dispersion of graphene sheets on the surface of carbon fabric mats enhances the interfacial strength between the epoxy matrix and carbon fibers and increases the efficiency of load transfer between matrix and reinforcing fibers. In the second design, graphene sheets are directly dispersed into the hardener-epoxy mixture to produce carbon fiber/epoxy composites with graphene reinforced matrix. In the third design, the combination of the first and the second arrangements is employed to obtain a multi-scale hybrid composite with superior mechanical properties. The effect of graphene sheets as an interface modifier and as a matrix reinforcement as well as the synergetic effect due to the combination of both arrangements are investigated in details by conducting various physical-chemical characterization techniques. Graphene/carbon fiber/epoxy composites in all three different arrangements of graphene sheets show enhancement in in-plane and out of plane mechanical performances. In the hybrid composite structure in which graphene sheets are used as both interface modifier and matrix reinforcing agent, remarkable improvements are observed in the work of fracture by about 55% and the flexural strength by about 51% as well as notable enhancement on other mechanical properties.

### **6.1. Introduction**

Multi-scale reinforced polymeric composite materials with superior mechanical and physical properties as well as multi-functionality play a key role in rapid technological development in recent years [133, 134]. Fiber-reinforced thermoset composites having favorable strength-to-weight and stiffness-to-weight ratios have

emerged as high-performance structural materials in applications such as wind turbines [135], construction [136], aeronautics [137], and aerospace [138]. However, most of the fiber-reinforced composites suffer from poor damage tolerance, impact resistance, delamination strength, and low fracture toughness, which have put serious restrictions on the wider usage of composites in engineering applications and the state-of-the-art load bearing structures [19, 139, 140]. The performance of fiber-reinforced composites is particularly affected by the properties of the constituent materials and the strength of fiber–matrix interfaces which influence the efficiency of load transfer from the matrix to the reinforcements [9, 10]. In order to address these issues and achieve the desired performance, there have been several attempts for the enhancement of composite properties which are categorized into two parts: improvement of matrix properties and interface modification [11]. One of the main methods for the improvement of the matrix dominant property is based on the dispersion of modifier particles into the matrix of fiber reinforced structures. These modifier particles are divided into two categories which are soft thermoplastic or rubber particles [141] and rigid reinforcing particles [142]. The incorporation of soft particles into epoxy matrix leads to several processing limitations [143] and also the reduction in strength, modulus, stiffness and glass transition temperature ( $T_g$ ) of matrix [144, 145]. On the other hand, the integration of rigid fillers into the matrix provides promising modification possibility by improving toughness, stiffness, modulus and  $T_g$  values of composites [146]. Nevertheless, it was reported in the literature that the soft particles provide higher toughening in comparison to rigid particles [147]. When compared to the changes in the matrix dominant properties, the addition of both soft and rigid particles rarely influences the fiber-dominated mechanical properties of composites [148].

The mechanical properties and the performance of fiber reinforced composite structures are also affected by interfacial bondings between fiber and matrix in which weak interfacial strength undermines shear stress transfer to fibers thus limiting the performance and the efficiency of composite structures. There are different types of fiber surface modification techniques such as polymeric coating [149], thermal treatment [150], chemical oxidation [151], plasma treatment [152] and increasing the surface roughness of carbon fibers [153] in order to create better chemical and physical interactions between fiber reinforcement and the polymer matrix. Recently, the

integration of reinforcing nanoparticles onto the surface of primary reinforcing fibers has emerged as an alternative technique to enhance the interfacial interaction between the constituents [154] and several methods have been developed for the deposition of nanoparticles on the surface of reinforcement micro-fibers [155]. Chemical vapor deposition (CVD) is one of the methods that has been applied to grow carbon nanotubes on the surface of carbon fibers to achieve higher interlaminar strength and toughness in multi-layered composites [154]. However, the CVD process is time-consuming and energy demanding and, in turn, expensive in pilot-scale production owing to harsh processing conditions and high processing temperature. The processing conditions cause the removal of fiber sizing material applied onto fibers during manufacturing hence deteriorating the original mechanical performance of fibers [156]. Furthermore, electrophoresis is another technique for the deposition of electro-active nanoparticles onto the carbon fiber surface by applying DC potential between the carbon fibers and the counter electrode [156]. However, this method is limited for certain types of nanoparticles which mostly are carbon-based nanoparticles [157]. In another deposition technique, carbon fibers are directly coated by a sizing solution containing nano-particles [51, 158]. Herein, the viscosity of sizing solution changes by the addition of nanoparticles and also this technique requires further energy and time-consuming drying steps. In addition, sizing material coated on carbon fiber hinders the direct contact between matrix and nanoparticles. The interactions of carbon nanotube with the matrix are extensively studied to improve the characteristic properties of fiber reinforced composites. Graphene has also started receiving attention as modifier/reinforcement in polymers and polymeric composites due to being one of the strongest materials ever measured with a theoretical Young's modulus of 1060 GPa and an ultimate strength of 130 GPa [12, 13]. In addition, high specific surface area of graphene sheets results in stronger interfacial interactions and better load transfer between polymeric matrix and reinforcement particles which make them suitable candidate for nanocomposite fabrication [14]. It is known that nanocomposites reinforced by graphene-based materials even at very low loadings have shown great influence on mechanical performance, thermal, electrical conductivity, and flame retardancy in comparison of unmodified polymers [15, 16]. One of the main methods for the improvement of the matrix dominant property is based on the dispersion of modifier particles into the matrix of fiber reinforced structures. The integration of rigid fillers into the matrix provides promising modification possibility by improving

toughness, stiffness, modulus and  $T_g$  values of composites [146]. On the other hand, the mechanical properties and the performance of fiber reinforced composite structures are also affected by interfacial bondings between fiber and matrix in which weak interfacial strength undermines shear stress transfer to fibers thus limiting the performance and the efficiency of composite structures.

In the present work, electro spraying (or electrohydrodynamic spraying) technology is used for the deposition of thermally exfoliated graphene oxide (TEGO) sheets on the surface of carbon fibers for the modification of carbon fibers /epoxy matrix interface without damaging the original properties of carbon fibers. To the best of our knowledge, there is no published work for the deposition of graphene sheets on the surface of carbon fiber by electro spraying process. This technique is fast, efficient, cost-effective and easily up-scalable process since it is possible to control the amount of nanoparticles precisely, coating rate, the position of coating and final dispersion state of deposited reinforcing particles. TEGO as nano reinforcement was selectively dispersed into epoxy/carbon fiber composite with three different arrangements. In the first arrangement, TEGO was dispersed onto the surface of reinforcing carbon fibers via electro spraying to enhance interfacial interaction between fiber and matrix. In the second arrangement, hardener containing TEGO was prepared by sonication process and then mixed with epoxy resin. The final mixture is used to impregnate the stack of dry carbon fiber through the vacuum infusion process thereby producing carbon fiber reinforced composites. In the last arrangement, the combination of the first and the second arrangements was employed to obtain a multi-scale hybrid composite with superior mechanical properties. In this hybrid design, the failure behavior of carbon fiber reinforced epoxy matrix composites structures is improved by multi-scale mechanisms where traditional continuous carbon fiber reinforces the composite structure in micron-scale while nanoparticles reinforce the matrix and carbon fiber-matrix interface in nanoscale.

## **6.2. Experimental**

### **6.2.1. Materials**

Materials used are N, N dimethyl formamide (DMF, Sigma-Aldrich, 99%), Thermally exfoliated graphene oxide (TEGO) Grade-2 (purchased from Nanografen Co.),

Araldite LY 564 resin, Hardener XB 3403, uniaxial carbon fabrics of Metyx company with the average weight of 310 g/m<sup>2</sup> (300 g/m<sup>2</sup> 800 Tex 12K along 0° direction, and 10 g/m<sup>2</sup> 68 Tex E-Glass along 90° direction).

### **6.2.2. Selective dispersion of TEGO as matrix and interface reinforcing agents**

Two different approaches were employed to integrate TEGO sheets into a composite structure. In the first approach as schematically represented in Figure 6.1a, TEGO sheets were exfoliated and dispersed into low viscosity hardener liquid by using probe sonicator (Qsonica, Q700) for 10 min at room temperature, and then bath sonication (Sonorex Digital 10P, Bandelin GmbH, Germany) was applied for complete exfoliation and stabilization of the TEGO-containing hardener for 24 hr at 40°C.

In the second approach, 0.1 wt% TEGO sheets were directly dispersed in DMF by means of probe and bath sonication to obtain well-dispersed electrocoat solutions for the coating process. Then, the prepared suspension was loaded into electrocoat syringe and subsequently sprayed onto both surfaces of dry carbon fiber ply under an electrical voltage of 15 kV, solution flow rate of 100 µl/min and spraying distance of 15 cm (Figure 6.1b). In order to spray TEGO sheets on the entire surface area of carbon fabric/ply, electrocoat system was mounted on a homemade fully automated two axis router system with variable movement speed in both x- and y-directions so that spraying can be performed at any desired locations.

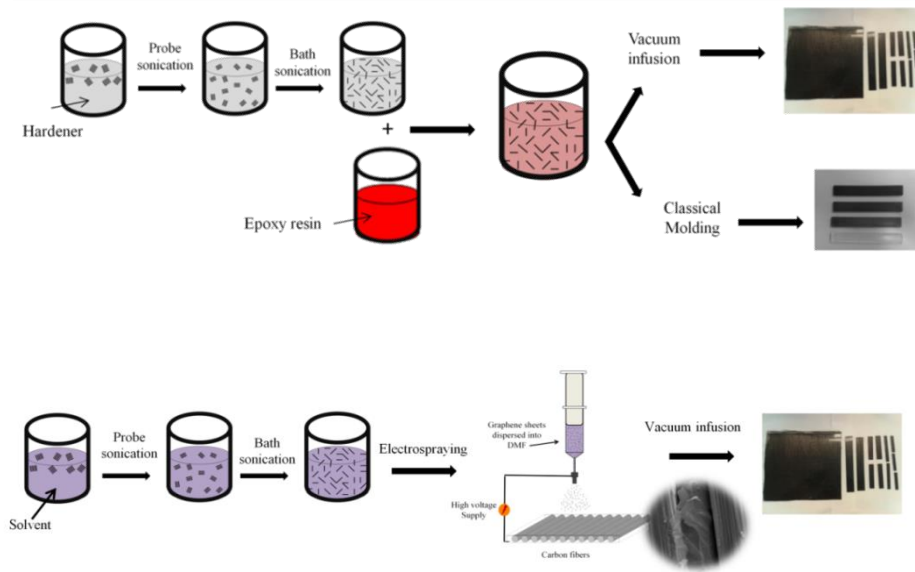


Figure 6.1 Schematic representation of (a) dispersion of TEGO sheets into the epoxy matrix to obtain nano-reinforced matrix and (b) dispersion of TEGO sheets as an interface reinforcement agent by electrospaying process.

### 6.2.3. Fabrication of Multi-scale reinforced epoxy composites

As the first step, the classical molding technique was employed to fabricate TEGO reinforced composite samples to find the optimum concentration of dispersed TEGO sheets into the epoxy matrix. To this end, mixtures of degassed resin and hardener system with different TEGO sheet concentrations were poured into Teflon molds, vacuumed in a vacuum oven to remove the entrapped air bubbles from the resin, cured at 75°C for 24 h, and then post cured at 90°C for 24 h. The molded samples were processed into three-point bending test specimens with the length, width, and the thickness of 100 mm, 14 mm, and 3 mm, respectively.

As the second step, composite laminates with three different multi-scale reinforcement architectures were produced to scrutinize how the method of integrating TEGO sheets into carbon fiber reinforced epoxy matrix composite affects the mechanical properties of manufactured composites. To this end, in the first design, TEGO sheets were electrospayed onto both surfaces of unidirectional dry carbon fiber plies as an interface modifier. Subsequently, electrospayed carbon fiber plies are stacked into a  $[90^{\circ}/0^{\circ}]_5$  configuration and then impregnated by a degassed neat epoxy resin-hardener system as shown in Figure 6.2. The TEGO weight percentage in this composite laminate is about

to be 0.01 wt%. In the second design, TEGO sheets were dispersed directly into epoxy and hardener mixture to act as a matrix reinforcement agent. Neat carbon fiber plies with  $[90^\circ/0^\circ]_S$  stacking sequence were also impregnated by this TEGO integrated resin system after degassing. The weight percentage of TEGO in the epoxy-hardener mixture is 0.05 and the total weight percentage of TEGO in the manufactured carbon fiber reinforced composite is 0.01 wt%. The third design is the combination of the first and the second approach such that both TEGO deposited carbon fiber plies with the same stacking sequence as before and TEGO containing epoxy-hardener mixtures were used to fabricate composite laminates. The total weight percent of TEGO in this combination is 0.02 wt%. In each design, stacked carbon fiber plies (neat or TEGO deposited) were impregnated by degassed resin using vacuum infusion method. The dimension of the manufactured composite laminates is  $40\text{ cm} \times 35\text{ cm} \times 0.12\text{ cm}$ .

The volume fractions of carbon fiber in the composite laminates were calculated by burning test to be nearly 70 % of overall composites. The composite panels were cut to the size of flexural, tensile, DMA and impact test specimens: namely,  $8\text{ cm} \times 1.5\text{ cm} \times 0.12\text{ cm}$ ,  $20\text{ cm} \times 2.5\text{ cm} \times 0.12\text{ cm}$  (with the gage length of 15 cm),  $6.5\text{ cm} \times 1\text{ cm} \times 0.12\text{ cm}$  and  $6\text{ cm} \times 1\text{ cm} \times 0.12\text{ cm}$ , respectively. To avoid the breakage of tensile specimens at grip locations, aluminum tabs with a dimension of  $3\text{ cm} \times 2.5\text{ cm} \times 0.1\text{ cm}$  were bonded to the both ends of specimens by using two-component room temperature curing epoxy system (Araldite, 2011).

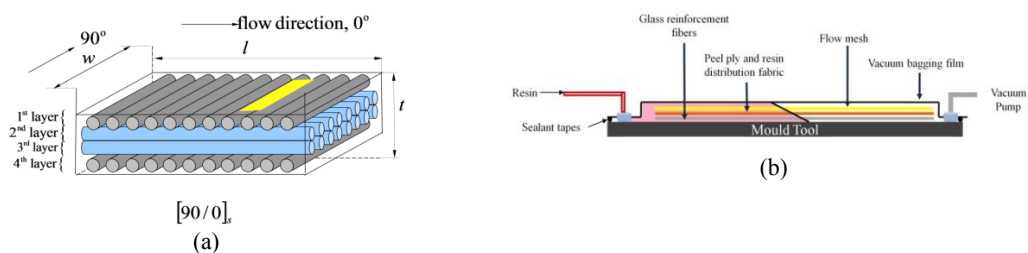


Figure 6.2 Schematic representation of composite manufacturing by vacuum infusion, (a) stacking sequence where the yellow region indicates the cut specimen for mechanical tests, and (b) the vacuum infusion system.

#### 6.2.4. Characterization

The morphologies of TEGO before and after dispersion and of carbon fibers with and without graphene deposition were analyzed by a Leo Supra 35VP Field Emission Scanning Electron Microscope (SEM) and the cross-sectional area of specimens after

breakage was analyzed by a JEOL JSM 6010 Scanning Electron Microscope (SEM). Raman spectroscopy was used to analyze the structural changes of graphene layers and carbon fibers by using a Renishaw inVia Reflex Raman microscopy system with the laser wavelength of 532 nm at room temperature in the range of 100–3500  $\text{cm}^{-1}$ . X-ray photoelectron spectroscopy (XPS) measurements were conducted by using a Physical Electronics Quantum 2000 Scanning ESCA Microprobe. The mechanical tests were conducted by ZWICK Proline 100 Universal Test Machine (UTM) with 10 and 100 kN load cells for 3-point bending and tensile tests, respectively, with a constant cross-head speed of 2 mm/min. The three-point bending and tensile tests on the relevant specimens were performed in accordance with ASTM D790-03 and ASTM D5083-02 standards, respectively. The axial and transverse strains were measured during tensile tests with two clip-on strain gage extensometers (Epsilon, Tech. Corp.). To scrutinize the failure mechanisms of manufactured composites, a detailed fractographic analysis was carried out on the cross section along the length of the specimen through thickness following the detailed procedure given in our previous publication [18]. Charpy impact tests of the composites were performed on an instrumented CEAST Resil Impactor apparatus at a speed of 2.9  $\text{m s}^{-1}$  by using a pendulum with nominal energies of 4 J. The measurements were conducted according to ASTM D256 method by using rectangular unnotched specimens.

### **6.3. Results and discussion**

#### **6.3.1. Morphologies and properties of TEGO**

The surface chemistry of graphene significantly influences its dispersion in the epoxy matrix hence affecting the amount of improvement to be achieved in the mechanical performance of composites. Specifically, carbon/oxygen ratio of graphene and the viscosity of hardener-epoxy mixture are two important parameters which directly affect the dispersion behavior of graphene sheets. In order to prevent aggregations of graphene sheets and reduce the defects in the matrix, TEGO is preferred as a reinforcing agent in the present work since thermal treatment removes most of oxygen groups from the surface of the graphene oxide, increases exfoliation ratio and changes the hydrophilic nature of graphene oxide [159]. The oxygen content of TEGO determined through XPS analysis is about 6% (provided by the manufacturer) and this oxygen amount is sufficient

to provide proper interactions between TEGO and amine-based hardener or solvents.[160] SEM micrographs in Figure 6.3a and 5.3b reveal the layered structure and worm-like appearance of as received TEGO sheets before applying any sonication. However, after the sonication, the complete dispersion and layer separation of TEGO in the DMF can be seen clearly in Figure 6.3c. In addition, as received TEGO sheets have a density of 0.022 g/ml and average layer number of 25 (provided by the manufacturer).

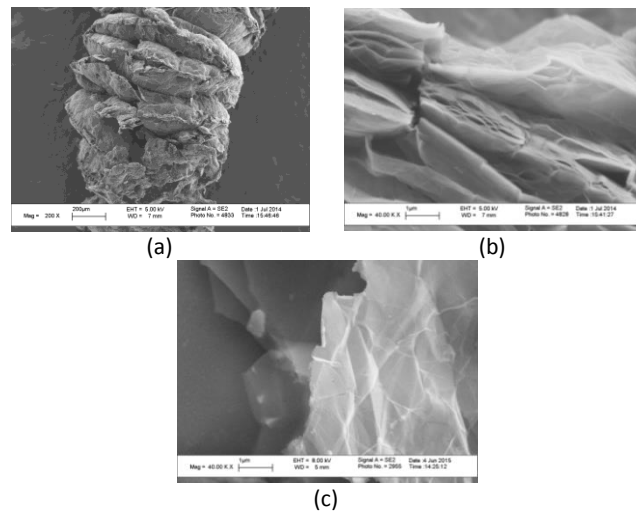


Figure 6.3 SEM micrographs of (a, b) as received TEGO particles at different magnifications and (c) TEGO sheets after the dispersion into DMF by sonication.

### 6.3.2. TEGO as a primary reinforcement

#### 6.3.2.1. Mechanical performance of epoxy/TEGO Nanocomposites

In the initial step of composite production, the optimum amount of TEGO in the epoxy matrix was determined by applying classical molding technique. Figure 6.4a shows flexural stress-strain curves for the neat specimen and TEGO reinforced epoxy specimens with three different TEGO concentrations of 0.0125 wt%, 0.025 wt% and 0.05 wt%. Figure 6.4b and 5.4c exhibit changes in flexural modulus and strength of epoxy/TEGO nanocomposites as a function of TEGO concentration. In both flexural modulus and strength values, a gradual increase is observed until the 0.025 wt% TEGO and the maximum mechanical performance is reached at the concentration of 0.05 wt% TEGO. In addition, 0.05 wt% of TEGO is the highest concentration for homogeneous dispersion and complete exfoliation during the sonication process. Otherwise, the presence of unexfoliated particles in composite structure creates stress concentration sites, which degrade the mechanical performance of the structure.

Table 2.1 gives the improvement percentages of flexural modulus and strength of TEGO reinforced epoxy specimens. The highest increase in flexural modulus is 85% and the highest increase in flexural strength is 64 %, which are achieved by the addition of 0.05 wt% TEGO. Considering the limitation in dispersibility of TEGO in hardener due to the notable increase in its surface area after being exfoliated, and the corresponding highest mechanical performance achieved, 0.05 wt% was chosen to be maximum achievable TEGO concentration that can be uniformly and properly dispersed in epoxy matrix and deemed to be optimum concentration as a co-reinforcement together with carbon fibers in multi-scale composite systems.

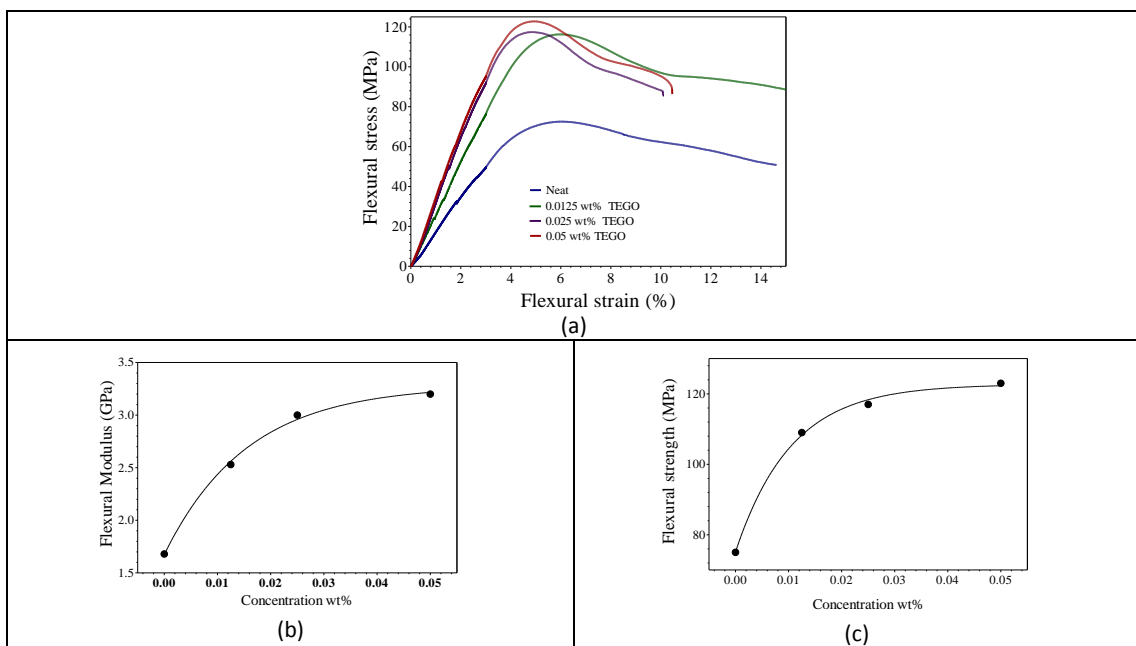


Figure 6.4 (a) Flexural stress–strain curves of neat and TEGO/epoxy composite specimens with different TEGO contents, (b) flexural modulus improvement and (c) flexural strength improvement graphs as a function of TEGO content.

Table 6.1 Flexural strength and modulus values and their improvement percentages of neat and TEGO/epoxy composites.

	Neat	0.0125 wt%	0.025 wt%	0.05 wt%
Flexural Strength (MPa)	75±2	109±5	117±3	123±2
Flexural Strength improvement (%)	----	45	56	64
Flexural Modulus (GPa)	1.68±0.08	2.53±0.3	3±0.1	3.1±0.1
Flexural Modulus improvement (%)	----	51	78	85

### **6.3.2.2. Fracture surface analysis of neat specimen and TEGO/Epoxy composite**

Examining the morphology of fracture surfaces helps understand the dispersion behavior of TEGO sheets and the failure mechanisms in the crack regions. Figure 6.5 exhibits SEM images for the fracture surfaces of the neat specimen and 0.05 wt% TEGO/epoxy composite after 3-point bending tests. The fracture surface of the neat specimen presented in Figure 6.5a and 5.5b at different magnifications is flat and smooth which is the characteristic of brittle fracture behavior and points to the low fracture toughness of the neat specimen. In contrast, the fracture surface of composite reinforced by 0.05 wt% TEGO is significantly rougher than that of the neat specimen as seen in Figure 6.5c and 5.5d. The increase in the roughness of fracture surface associated with the creation of additional surfaces due to the crack deflection, tilting and twisting during fracture is common for particle reinforced composites. [161] The creation of rough surfaces can facilitate the dissipation of energy during the breakage of composites, which bespeaks the reinforcement effect of TEGO sheets in the epoxy matrix. Here, the toughness increases since TEGO sheets are tightly held to the resin by strong interfacial bonding between TEGO and epoxy matrix. Furthermore, uniform roughness is observed in Figure 6.5c and 5.5d, which indicates homogeneous dispersion and complete exfoliation of TEGO sheets in the matrix without any noticeable aggregations.

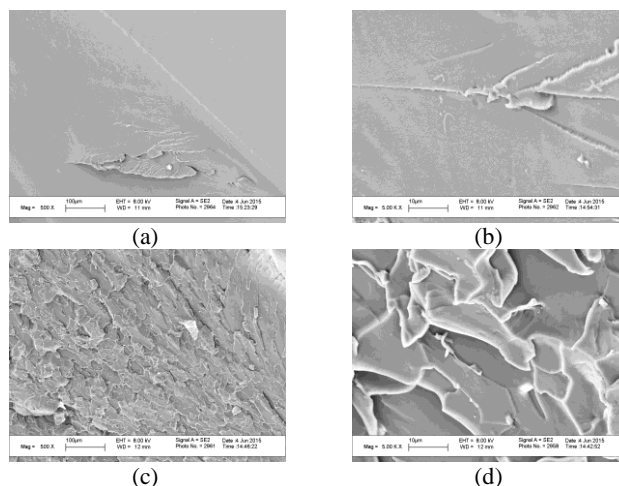


Figure 6.5 SEM images of the fracture surface of specimens after three-point bending tests (a, b) neat epoxy, and (c, d) 0.05 wt% TEGO/epoxy composite.

### 6.3.3. Modification Carbon Fiber-Epoxy Matrix Interface by Electro spray Deposition of TEGO

Electrospraying method is employed for the deposition of TEGO sheets onto the surface of carbon fabric mats. This method is a solvent based technology in which TEGO sheets are initially dispersed into a suitable solvent and then atomized by means of electrical forces. In the electro spraying process, high electric field force is applied between the nozzle and the carbon fiber mat thus breaking up the initial droplet formed at the tip of the nozzle into fine electrically charged droplets [162]. The electric field between the nozzle and the target provides a guided path for these fine droplets thereby leading to uniform, homogeneous, and target localized coverage of carbon fiber mat by nano-reinforcing particles. At this point, the crucial parameter is the preparation of TEGO suspension solutions in which TEGO sheets are fully exfoliated and can be stable in suitable time scale. The complete exfoliation and stable suspensions are just achieved by multi-step and extensive sonication processes. Figure 6.6a and 5.6b reveal smooth surface and parallel superficial grooves of as-received carbon fabric mat at different magnifications while Figure 6.6c and 5.6d show very thin and transparent graphene layer formation on the surface of carbon fibers after TEGO dispersion. In addition, Figure 6.6e provides a low magnification image for carbon fabric surface after electro spraying treatment wherein one can see that TEGO sheets cover the fabric surface discretely and uniformly. It is noted that electro spraying process does not damage the consistency of fibers since carbon fibers still preserve original surface morphology after solution spraying. Extremely thin graphene layers (with a very large surface area to volume ratio)

have strong tendency to attach on active surfaces due to attractive interfacial forces (i.e., van der Waals forces, electrostatic interactions and dangling bonds, among others).[163] These interactions are strong enough to deform graphene sheets in an out-of-plane direction whereby graphene sheets can conform onto the surface geometry of carbon fiber as seen in Fig. 6c and 6d, and to prevent graphene sheets from falling off the surfaces of carbon fiber strands during the handling and processing. The presence of graphene sheets on the surface of carbon fibers enhances the interfacial strength between fibers and polymeric matrix by increasing the surface roughness and surface energy as well as providing chemical and hydrogen bonding between matrix and reinforcement due to the presence of oxygen functional groups on the surface of TEGO sheets and carbon fibers.

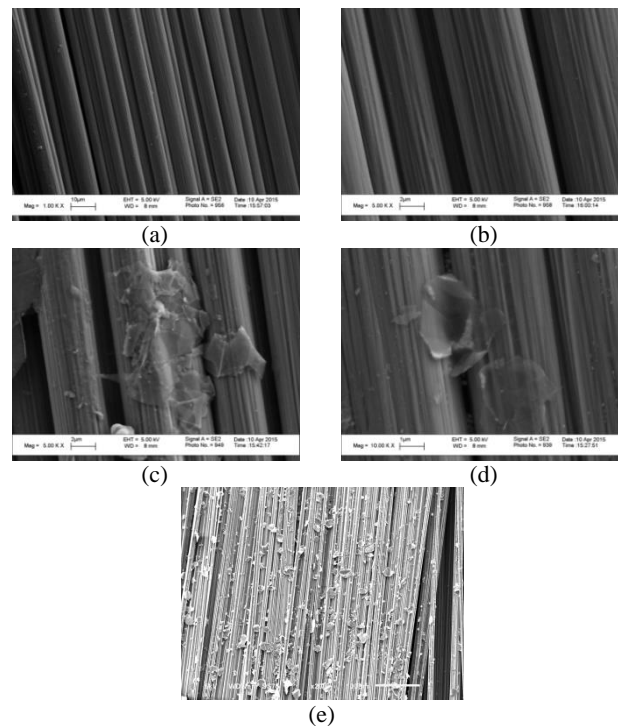


Figure 6.6 SEM images of carbon fabric mat (a, b) as-received, (c, d) after electro spraying of TEGO sheets and (e) low magnification image of carbon fabric with electro sprayed TEGO.

In order to evaluate the effect of electro spraying process on the structural changes and surface chemistry of the carbon fibers, RAMAN and XPS analysis were performed on untreated and electro sprayed fibers. Figure 6.7 presents the Raman spectra of as received carbon fiber, TEGO sheets, and TEGO sprayed carbon fibers. Carbon fiber exhibits two main characteristic Raman peaks which are D peak at  $\sim 1353\text{ cm}^{-1}$  corresponding to disordered carbon structure and G peak at  $\sim 1584\text{ cm}^{-1}$  attributed to graphitized carbon and in-plane vibrations of  $sp^2$  bonded carbon atoms [164]. On the other

hand, pristine TEGO has D, G and 2D peaks, which lie at around  $1348\text{ cm}^{-1}$ ,  $1575\text{ cm}^{-1}$ , and  $2720\text{ cm}^{-1}$ , respectively. After the deposition of TEGO sheets on the surface of carbon fibers, the characteristic peaks of graphene become dominant and 2D band appears at  $2721\text{ cm}^{-1}$  whose intensity directly depends on the number of graphene layers [165]. This observation indicates that carbon fiber surface is covered by graphene sheets. It is known from literature that the ratio of D and G peak intensities ( $I_D/I_G$ ) gives defect concentration in carbonic structure, and higher  $I_D/I_G$  stands for the higher  $sp^3/sp^2$  ratio in carbonic structure [164]. Table 6.2 compares the intensities of Raman peaks and  $I_D/I_G$  ratios of pristine TEGO, pristine carbon fiber and TEGO sprayed carbon fiber. Low  $I_D/I_G$  ratio for TEGO sheets confirms that TEGO sheets are mostly in graphitic structure and carbon atoms mainly are in  $sp^2$  type bond geometry, which is responsible for high conductivity of TEGO sheets. On the other hand, neat carbon fiber has higher  $I_D/I_G$  ratio about 0.96 indicating the dominance of  $sp^3$  bonds. After the coverage of TEGO sheets on carbon fiber mats,  $I_D/I_G$  ratio significantly decreases since Raman peaks of graphene become prominent. Furthermore,  $I_G/I_{2D}$  ratio directly depends on the number of graphene layers and indicates the coating thickness. After the appearance of 2D peak in Raman spectra of TEGO coated carbon fibers,  $I_G/I_{2D}$  ratio is about 1.84 which is lower than the ratio of pristine TEGO about 1.99. This indicates that graphene layers are dispersed on the carbon fiber mat under electric field during electrospraying process thereby covering the surface of carbon fibers, but graphene sheets still preserve its multi-layer structure. Consequently, Raman spectroscopy analysis proves TEGO coating on carbon fiber surface since Raman signals are directly collected from the specimen surface.

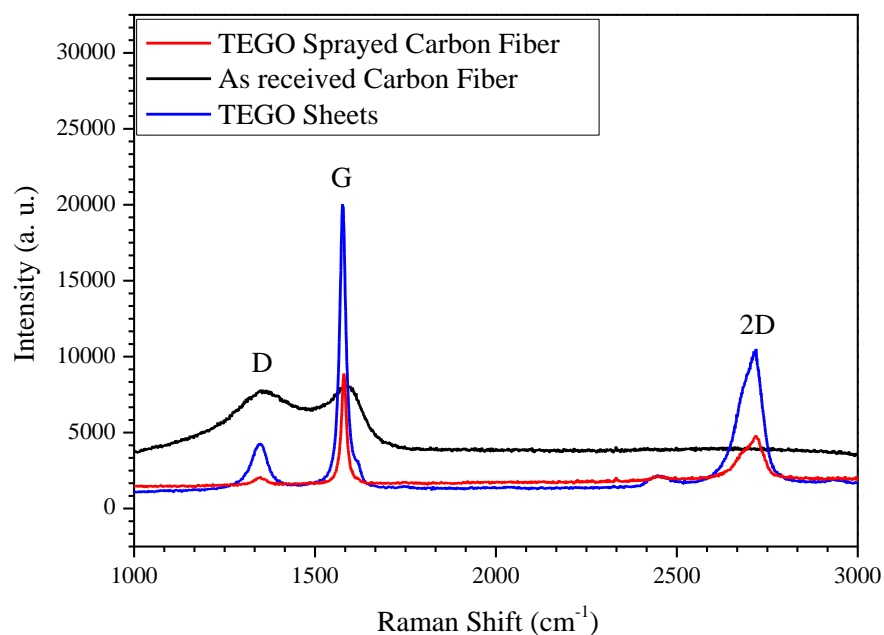


Figure 6.7 Raman spectra of as received carbon fiber, TEGO sheets, and TEGO sprayed carbon fiber

XPS is a quantitative surface analysis technique that is used to evaluate the elemental composition and functional groups of as received carbon fiber, TEGO sheets, and TEGO sprayed carbon fibers. In order to determine oxygen-containing functional groups, C1s and O1s signals were analyzed at binding energies of  $\sim 286$  and  $\sim 532$  eV, respectively, and functional groups were assigned based on the characteristic binding energy of each element.<sup>[166]</sup> The intensities of C1s and O1s peaks for each material were compared in the XPS survey scan spectra as seen in Figure 6.8 C/O ratios and types of functional groups with their atomic percentage calculated from XPS results are presented in

Table 6.3. C/O ratios of as received carbon fiber, TEGO and TEGO sprayed carbon fiber are 3.6, 14.8 and 5.0, respectively. The changes in C/O ratio indicate that the deposition of TEGO sheets on carbon fiber surface changes the elemental composition and thus the carbon content on the surface of carbon fiber increases. In

Table 6.3, the C1s envelope of TEGO sheets has mainly  $sp^2$  carbon bonds about 77.3 at.% because of a hexagonal ring of six carbon atoms in TEGO structure. The C1s peaks of carbon fibers contain C-C bonds at 284.8 eV, C-O bond at 286.4 and O=C-O bond at 289 eV with the atomic weight percentages of 41, 34.4 and 3, respectively and no  $sp^2$  hybridized carbon atoms (C-C) are detected on the surface of carbon fibers. After the electro spraying of TEGO sheets on carbon fiber surface,  $sp^2$  carbon atoms appear in the structure with the atomic weight percentage of 4.0. The deconvoluted O1s XPS spectrum of TEGO sprayed carbon fiber exhibits C=O bonds at 531 eV due to the coverage of TEGO sheets. XPS analysis also confirms the coating of TEGO sheets on carbon fiber mats quantitatively.

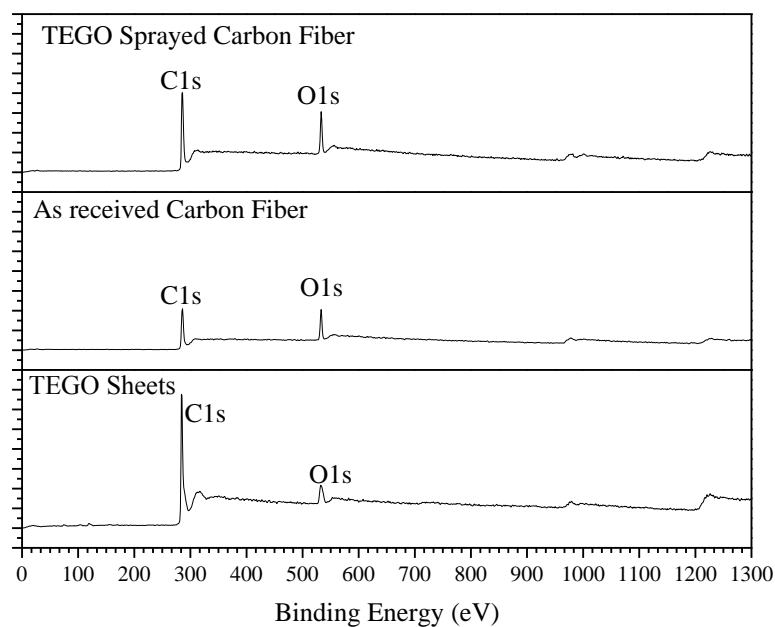


Figure 6.8 XPS survey scan spectra of as received carbon fiber, TEGO, and TEGO sprayed carbon fiber

Table 6.2 The intensities and peak positions of D and G bands, and ID/IG ratios of pristine carbon fiber, TEGO sprayed carbon fiber and TEGO sheets

	D band intensity (a. u.)	G band intensity (a. u.)	I <sub>D</sub> /I <sub>G</sub>	2D band Peak intensity (a. u.)	I <sub>G</sub> /I <sub>2D</sub>
As received Carbon Fiber	7763	8073	0.96	—	—
TEGO sprayed Carbon Fiber	2016	8840	0.22	4808	1.84
TEGO sheets	4193	19821	0.21	9968	1.99

Table 6.3 XPS spectra results of C1s and O1s for TEGO, carbon fiber, and TEGO sprayed carbon fiber

Sample	XPS C1s Spectra			XPS O1s Spectra			C/O ratio
	Peak Attribution	Binding Energy (eV)	Atomic %	Peak Attribution	Binding Energy (eV)	Atomic %	
TEGO Sprayed carbon fiber	C-C	284.8	48.5	C-O	532.9	15.3	5.0
	C-O	286.4	28.4	C=O	531.0	1.4	
	O=C-O	288.9	1.4				
	C-C sp <sup>2</sup>	284.1	4.0				
As received carbon fiber	C-C	284.8	41.0	C-O	532.8	21.7	3.6
	C-O	286.4	34.4				
	O=C-O	289.0	3.0				
TEGO	C-C	284.8	3.1	C-O	532.4	4.3	14.8
	C-O	286.3	3.1	C=O	530.6	1.6	
	O=C-O	288.9	4.25				
	C-C sp <sup>2</sup>	284.1	77.3				
	C=O	287.8	1.0				

#### 6.3.4. Mechanical performance of multi-scale reinforced composites

Four different composite samples were designed and fabricated through vacuum infusion technique: (1) conventional epoxy/carbon fiber composites without any TEGO sheets as a reinforcement (CFRP), (2) epoxy/carbon fiber composite with 0.01 wt% TEGO as an interface reinforcement (CFRP/INT), (3) epoxy/carbon fiber composite with 0.01 wt% TEGO as a matrix reinforcement (CFRP/MTX) and, (4) epoxy/carbon fiber composite fabricated by the addition of both 0.01 wt% TEGO as an interface

reinforcement and 0.01 wt% TEGO as an matrix reinforcement (CFRP/INT+MTX). The performances of these four arrangements were evaluated by in- and out-of-plane mechanical tests and impact tests to determine the ideal multi-scale reinforcement configuration.

#### **6.3.4.1. Flexural properties**

Flexural properties are key parameters for the evaluation of mechanical performance and understanding the interactions between matrix and fiber at the interface in composite materials. The representative flexural stress vs. strain curves obtained from 3-point bending tests for four different specimens are shown in Figure 6.9a. Three different flexural properties were obtained from these tests: that is to say, flexural modulus (FM) as a parameter for the tendency of the composite material to bend, flexural strength (FS) as a factor indicating the resistance of materials against the fracture, and the work of fracture (WOF) scaling the energy dissipated in the course of fracture of the specimen. The flexural test results show that FM, FS and WOF values of the multi-scale epoxy composites reinforced by any arrangement of nano-reinforcements are notably higher than those of conventional carbon fiber/epoxy composite signifying the efficacy of engineered nano-integration. In comparison of the results of CFRP, FM, FS and WOF values of interface modified CFRP (CFRP/INT) specimens produced by electrospraying of TEGO sheets on carbon fiber mats increase about 18.5 %, 16.2 %, and 31 %, respectively. TEGO sheets used as an interface modifier have matrix compatible functional groups that enhance the interfacial properties and subsequently improve the interfacial bonding strength thereby leading to more effective load distribution among phases, and also inhibition of micro cracks at the interface. In the case of matrix modified CFRP specimens fabricated by direct mixing of TEGO sheets in epoxy-harder mixture (CFRP/MTX), FM, FS and WOF are improved by about 15 %, 20.5 %, and 22.3 %, respectively. The CFRP/MTX specimens have notably lower WOF improvement percentage than CFRP/INT specimens, which stems from different fracture mechanisms between these two composite arrangements. Namely, in the CFRP/INT specimens, fracture occurs at higher strain values as seen in Figure 6.9a and fiber breakage becomes dominant during failure mechanism. On the other hand, as for CFRP/MTX specimens, the presence of TEGO sheets in the matrix increases the matrix modulus whereby the matrix carries higher loads with respect to the matrix of CFRP/INT specimens in

accordance with the rule of the mixture in composite materials. As a result, the higher amount of cracks occurs in matrix and failure occurs at lower strain values as can be seen in Figure 6.9a, and Figure 6.10b-c. During 3-point bending tests, matrix cracking dissipates less energy compared to carbon fiber breakage that explains the difference between WOF values of these two types of composites. As for the composites with multi-scale and multi-arrangement reinforcements (CFRP/INT+MTX) in which both matrix and interface of composite structure are modified by TEGO sheets, due to synergic effect of two different TEGO arrangements, FM, FS and WOF are enhanced by 31.1 %, 51.2 %, and 55 %, respectively. In CFRP/INT+MTX specimens, compared to CFRP/MTX specimens, the higher portion of applied load is transferred to fibers due to the modified interface, and so, both matrix cracking and fiber failure contribute to the failure of structure because of enhanced interface properties and more efficient load transfer from matrix to the reinforcing fibers. Therefore, TEGO sheets acting as a reinforcing agent in both matrix and fiber structure in multi-scale composite design increase WOF values due to the higher energy dissipation.

#### **6.3.4.2. Tensile properties**

The effect of TEGO on tensile properties of composites produced by different arrangements was investigated by applying an axial load by UTM. Fig .9b exhibits the representative tensile stress and strain curves of four carbon fiber epoxy composites with different nano-reinforcement configurations. As can be obviously observed in Figure 6.9b, for any nano-reinforcement configurations, tensile modulus (TM) and tensile strength (TS) of nano-reinforced multi-scale epoxy composites are higher than those of conventional carbon fiber/epoxy composites. TM and TS values of CFRP/INT specimens are enhanced by about 15.5% and 9.6%, respectively because of improved interfacial bonding strength in the presence of interface modifier particles. On the other hand, TM and TS of CFRP/MTX specimens are improved by about 20.3% and 17.4%, respectively due to the contribution of TEGO sheets to load distribution and their ability to enhance the matrix properties. In CFRPs, the main load carrying constituent along the tensile direction is carbon fibers. Therefore, expectedly, the improvement in the tensile properties due to the interface modification by TEGO is not as notable as that in flexural properties since the TEGO does not improve the tensile properties of carbon fiber properties. As in the case of the matrix modification, since the TEGO significantly

modifies the matrix properties in a volumetric manner recalling Figure 6.4, the improvement is observed regardless of loading direction, namely, flexural and tensile. In composites with the multi-scale and multi-arrangement of nano-reinforcements (CFRP/INT+MTX), the improvement in TM and TS are about 20.3 % and 19.4 %. These values are rather close to those obtained for CFRP/MTX specimens given that in the tensile mode, the volumetric matrix properties are dominant over interface properties between the matrix and the carbon fiber.

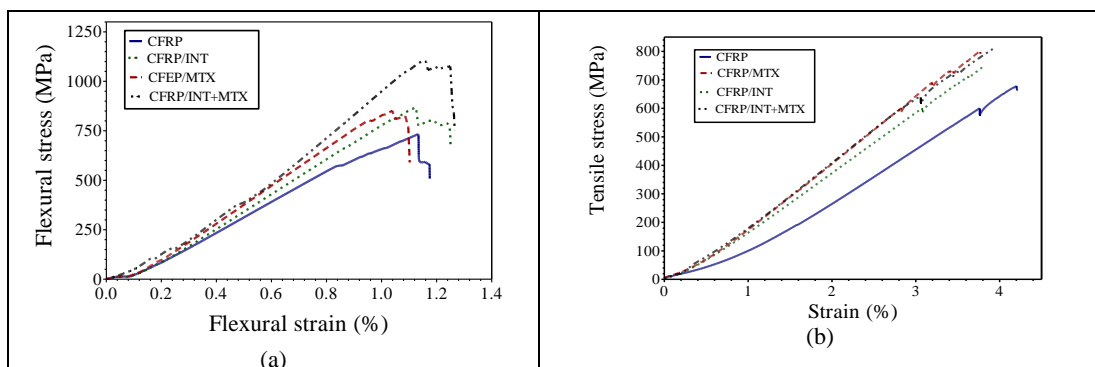
During tensile tests, axial strain ( $\epsilon_x$ ) and transverse strain ( $\epsilon_y$ ) were monitored by axial and transversal extensometers simultaneously wherefrom Poisson's ratio,  $\nu_{xy} = -\epsilon_y/\epsilon_x$  corresponding to a contraction in y-direction when an extension is applied in x-direction, is computed  $\nu = -\frac{\epsilon_y}{\epsilon_x}$  and then plotted as a function of axial strain in Figure 6.9c. Poisson's ratio increases rapidly for all specimens with the rise in the axial strain and then reach a plateau. This initial rise in the Poisson's ratio is due to the fact that lateral strain increases nonlinearly as a function of applied axial strain. As seen from Figure 6.9c, each composite configuration acquires different plateau behavior. One may observe that in the region where the Poisson's ratio is of an increasing trend, for a given axial strain value, Poisson's ratios of the nano-integrated composite specimens are smaller than the Poisson's ratio of the neat specimen. This bespeaks that the stiffness of the nano-integrated composites increases thereby reducing the lateral deformation. The comparison of the results of nano-integrated composite specimens indicates that the matrix reinforcement with the graphene is more effective in increasing the stiffness of the composite structure. Moreover, the results of Poisson's ratio are in agreement with the outcomes of other mechanical tests where the specimens with TEGO as both matrix reinforcement and interface modifier have higher mechanical performance due to strong interfacial bonding between nano-reinforced matrix, and surface modified carbon fibers, enabling improved load transfer across the composites.

#### **6.3.4.3. Charpy impact test**

Charpy impact test is used to determine the impact strength or energy absorbed during the fracture of specimens under high strain rates. The improvement in the impact strength of CFRP/INT, CFRP/MTX, and CFRP/INT+MTX specimens are about 16.6%, 25.3%, and 29.9%, respectively, compared to unmodified CFRP specimens. The fact that

the CFRP/MTX composite specimens yield higher impact strength than CFRP/INT specimens and also the negligible difference in the impact strengths of CFRP/MTX and CFRP/INT+MTX specimens are evidence for matrix toughening effect of graphene sheets. Expectedly, CFRP/INT specimens do not have as much increase in the impact strength as two others since nano graphene as interface modifier is more effective for load transfer between carbon fibers and matrix and do not contribute to the toughness of the composites at high strain rates. For all composites, the summary of the results of mechanical tests and achieved percent improvements in mechanical properties with respect to neat CFRP composites is given in

Table 6.4 and Figure 6.9d, respectively. As can be clearly seen in Figure 6.9d, the integration of TEGO sheets in any arrangements as matrix reinforcement or a carbon fiber epoxy matrix interface modifier widen the mechanical performance window of the composite structure. In addition, specimens with TEGO sheets as an interface modifier show higher FS and WOF values compared to the specimens with TEGO used as a matrix reinforcing agent. On the other hand, specimens with TEGO as matrix reinforcement show greater FM, TS, TM and impact strength (IMP) values compared to the interface modified specimens. Furthermore, the synergic effect of TEGO integration as matrix reinforcement and interface modifier results in a wider window of the mechanical performance of composite structure and superior performance in all mechanical tests.



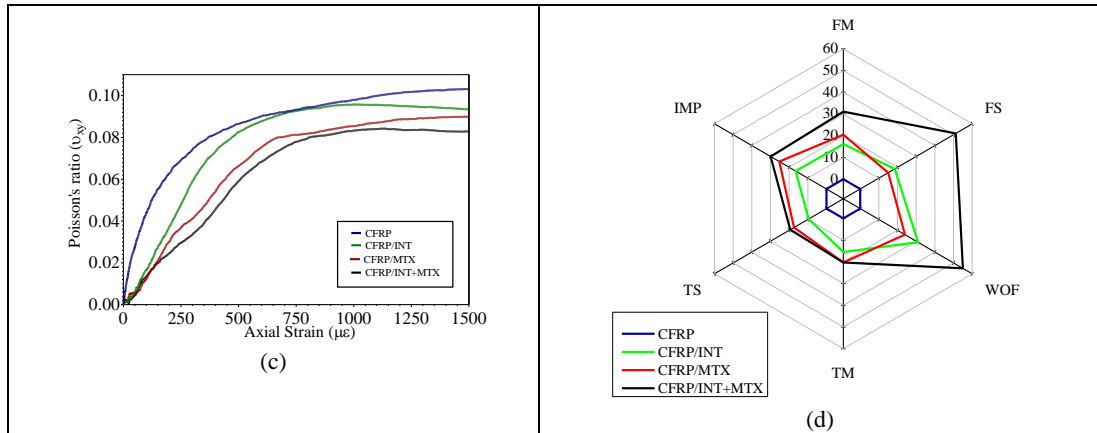


Figure 6.9 (a) Flexural stress-strain curves, (b) tensile stress-strain curves (c) Poisson's ratio versus axial strain of carbon fiber-reinforced epoxy specimens with different TEGO arrangements and (d) the window of percentage improvement in mechanical performance with respect to the properties of CFRP.

Table 6.4 Summary of mechanical properties of carbon fiber reinforced specimens

	CFRP	CFRP/INT	CFRP/MTX	CFRP/INT+MTX
Flexural Strength (MPa)	730±19	865±28	853±22	1104±30
Flexural Strength improvement (%)	----	18.5	15	51.2
Flexural Modulus (GPa)	74.2±3	86.2±2	89.4±1	97.3±5
Flexural Modulus improvement (%)	----	16.2	20.5	31.1
WOF (kJ/m <sup>2</sup> )	18.0±0.6	23.5±0.4	22.3±0.2	27.9±0.8
WOF improvement (%)	----	31	24	55
Tensile Strength (MPa)	670.8±32	735.5±28	787.9±31	800.9±14
Tensile Strength improvement (%)	----	9.6	17.4	19.4
Tensile Modulus (GPa)	18.7±0.5	21.6±0.2	22.5±0.5	22.5±0.3
Tensile Modulus improvement (%)	----	15.5	20.3	20.3
Impact Strength (kJ/m <sup>2</sup> )	89.3	104.1	111.9	116.0
Impact Strength improvement (%)	----	16.6	25.3	29.9

### 6.3.5. Microscopic observation and failure mechanisms

A fractographic analysis was performed on the cross section of flexural test specimens (bounded by length and the thickness) to scrutinize the effect of different nano-reinforcement configurations on the failure mechanisms of composites. Figure 6.10 represents SEM images of cross-sectional areas of flexural test specimens after cutting

and polishing steps. The cross sections correspond to the right-hand side view shown in Figure 6.2a. In these specimens, there are two different orientation of fiber reinforcement; fibers oriented in a parallel manner to the cross section plane at outer layers and fibers oriented perpendicularly to cross section plane in the middle of specimens. Figure 6.10a shows the cross section of neat glass CFRP specimen after the breakage under flexural load. It can be seen that the first layer of fibers directly subjected to the applied load is completely broken down and the delamination of first and second layers of fibers is observed in the fractographic analysis. This delamination in the neat CFRP composite specimen confirms the relatively weak interfacial interaction between reinforcing fibers and epoxy matrix, which triggers the separation of carbon fibers from matrix under the applied flexural load. Figure 6.10b exhibits the cross section of CFRP/INT specimen in which the outer layer of fibers is crushed and broken down under the applied load while delamination does not occur, and the first and the second layers are well connected to each other after the failure. The absence of delamination in CFRP/INT specimen indicates superior interfacial bonding between carbon fibers and epoxy matrix due to the modification of interface by electrospayed TEGO sheets. The failure behavior of CFRP/MTX is presented in Figure 6.10c wherein fractures occur in the form of matrix cracking, and fiber breakage does not take place in the first layer of fibers, unlike other specimens. The failure in the form of matrix cracking in CFRP/MTX specimen is due to the increase in elastic modulus of the matrix, which enables the matrix to bear the higher load in comparison to specimens with neat epoxy as matrix whereby the higher amount of cracks occurs in the matrix. Figure 6.10d shows the fractured cross section of a CFRP/INT+MTX specimen after flexural failure where one can see fiber breakage of the first layer as well as some matrix cracking. In addition, a few minor delaminations are observed albeit the higher flexural load imposed on this family of the specimen for fracture as seen Figure 6.9a. The higher flexural load required for the fracture of CFRP/INT+MTX specimen under 3-point bending test deteriorates the interfacial bonding between carbon fibers and matrix thereby leading to partial delamination in the structure. These fractographic analyses provide an important insight as to the nature of the failure of specimens and the effect of TEGO sheets on interfacial interactions and load distribution between polymeric matrix and reinforcing components in each composite structure.

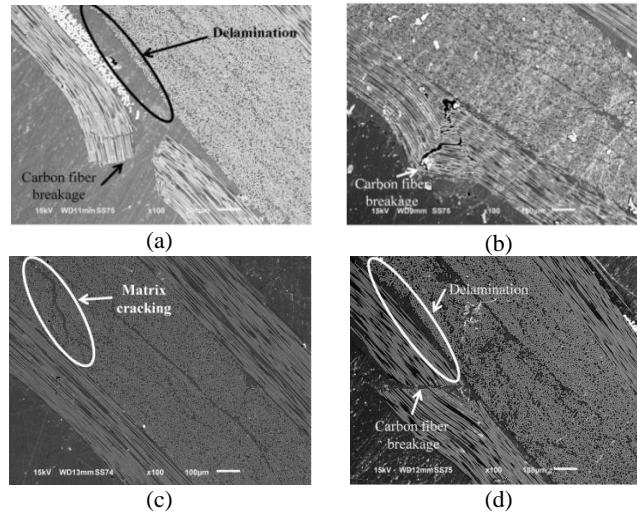


Figure 6.10 SEM images of cross-sectional area of specimens after flexural failure (a) CFRP, (b) CFRP/INT, (c) CFRP/MTX, and (d) CFRP/INT+MTX.

#### 6.4. Conclusions

Electrospraying, which is a fast, efficient and easily up-scalable process, is employed for the deposition of graphene sheets onto carbon fabric mats to strengthen the interfacial interactions between carbon fiber reinforcement and epoxy matrix. The integration of graphene sheets on carbon fiber interface enhances the efficiency of load transfer from matrix to reinforcing fibers whereby the mechanical performance of composite structure notably improves due to the stronger interfacial strength. In addition, the results of XPS and Raman spectroscopy analyses confirm that the deposition of graphene layers via electrospraying technique does not affect the chemical structure and properties of carbon fibers adversely, and the carbon fabric mat preserves its structural consistency during composite manufacturing steps.

In order to obtain high mechanical performance with optimum graphene concentration, the effect of graphene sheets as a primary reinforcement on the properties of the epoxy matrix was initially investigated in details by three-point bending tests. The flexural strength and modulus of graphene-reinforced epoxy composites with a low concentration of 0.05 wt% TEGO produced by using classical molding technique are improved about 64 % and 85 %, respectively. Well-dispersed and stable TEGO containing epoxy hardener was prepared by sonication technique to prevent the agglomeration of graphene sheets in an epoxy matrix and structural defect formation. Then, a formulated mixture of graphene and epoxy was infused into the  $[0/90]_s$  stack

using vacuum infusion to produce carbon fiber reinforced epoxy composites. The integration of graphene into the carbon fiber reinforced composite in the form of matrix reinforcement leads to appreciable enhancement in the mechanical performance of manufactured composite structures. Furthermore, the utilization of graphene sheets as both interface modifier and matrix reinforcement shows a synergistic effect thereby resulting in excellent improvements in the mechanical performance of the hybrid composite structure. Namely, when compared to unmodified composite structure, flexural strength, modulus and work of fracture are enhanced by about 51.2 %, 31.1 %, and 55 %, respectively while tensile strength, modulus, and impact strength are augmented by about 19.4 %, 20.3 %, and 29.9 %, respectively. The detailed fractographic analyses were performed to establish an understanding on different fracture mechanisms involved in the failure of specimens under flexural loads and the effect of selective TEGO dispersion on composite performance and especially the interfacial interactions between carbon fibers and epoxy matrix. This novel architectural design involving multi-scale reinforced epoxy composite structures and nano-scale modified carbon fiber epoxy interface provides a readily scalable process for industrial applications and can be further explored for the development of lighter advanced structural composites. We consider our conclusions to be a stepping-stone for our future work for multi-scale composite structures that will focus on the dynamical-mechanical and electrical-thermal properties of these developed hybrid structures in the next report. The findings of this study are believed to contribute to the state of the art significantly given that the notable improvements are achieved in the presence of already strong carbon fiber reinforcements.

## **CHAPTER 7. TAILORING VISCOELASTIC RESPONSE, SELF-HEATING AND DEICING PROPERTIES OF HIGH-PERFORMANCE CARBON FIBER REINFORCED EPOXY COMPOSITES WITH SELECTIVELY DISPERSED GRAPHENE AS INTERFACE AND MATRIX REINFORCEMENTS**

Three different architectural designs of multi-scale reinforced epoxy based composites with carbon fiber as micro-scale and graphene as nano-scale reinforcement are fabricated through vacuum infusion technique. In the first design, electrospraying technique was employed to deposit graphene sheets on the surface of carbon fibers as an interface modifier, in the second design, graphene sheets are incorporated into the epoxy resin to improve the matrix properties, and in the last design, the combination of the first and second designs are used to achieve a composite structure with superior mechanical and physical properties. In the first part of this study, dynamical mechanical testing techniques are applied to investigate the viscoelastic behavior of composite structures at different temperatures, frequencies and graphene configurations. In addition, activation energy for glass transition and a master curve for each composite are calculated by using Arrhenius equation and Williams–Landel–Ferry (WLF) time-temperature superposition principle, respectively. In the second part, the effect of graphene and its configuration on the electrical conductivity, thermal diffusivity and electro-thermal performance of composites are studied in details. The in-plane electrical conductivity of composite structure with graphene as both interface modifier and matrix reinforcement showed a significant electrical conductivity enhancement of 240% compared to a specimen without any nano-filler. In addition, Joule heating stem from the passage of electrical current through conductive composite are employed to add self-heating and de-icing capabilities to the composite structure. The results indicate that carbon fiber reinforced composites gain multi-functionality and preserve its mechanical integrity and enhance their performance at service conditions when graphene is used as both an interface modifier and a matrix reinforcement in the structure.

## 7.1. Introduction

Fiber-reinforced polymeric composites with superior strength and stiffness to weight ratio, relatively ease manufacturing process, and multi-functionality are promising candidate in design and development of structural and functional materials for aerospace, aeronautics, energy and automobile industries [1]. However, growing demand of industries for materials with higher mechanical and physical and chemical properties causes new trends towards nanocomposite production. Nanocomposites brings advantages in mechanical integrity and physical properties of polymeric structures due to their high mechanical performance and density reduction [2]. However, there are several restrictions in the fabrication of nanocomposites which are complex processing, poor dispersion of nano-phase in polymeric matrix, and re-agglomeration of nanoparticles. In the recent years, various nano-reinforcements have been utilized in order to exploit potential of fiber reinforced composites and extent their capabilities [18, 113].

One of the distinct properties of polymeric composites is their viscoelastic behavior, which renders their structural applications under dynamic loads. On the other hand, viscoelastic properties of polymeric structures are very sensitive to the presence of nano-particles in the composite structure and thus detailed investigations are required to get a comprehensive understanding of the effect [167]. Damping behavior is another crucial parameters to monitor the dynamical-mechanical behavior of fiber-reinforced composites [168]. Major damping sources in fiber reinforced polymeric composites are viscoelastic damping coming from nature of constituent materials, damping at the interface of reinforcing fibers with matrix, and damping related to the damages [169]. Dynamic mechanical analysis (DMA) is a very useful tool to analyze the mechanical and viscoelastic behavior of polymeric materials and detect any kinds of transitions and relaxation processes in the composite structure in the wide range of temperatures and frequencies under periodic stress [170]. In addition, DMA tests are very informative about interfacial properties of reinforcing fibers in the chosen polymeric matrix [18].

Additionally, most of the fiber-reinforced composites that have been developed upto now are electrically and thermally insulator and this limits their utilization in potential applications. Herein, the incorporation of conductive nano-particles into the matrix enhances the electrical and thermal conductivities [171-173]. One of the

phenomena in electrically conductive structures is Joule heating or Ohmic heating based on the passage of electric current through conductive structure that releases heat due to the electrical resistance [174]. At this point, this phenomenon provides a convenient and effective way to add different functionalities into the polymeric composite structures.

Today one of the main problems in aerospace and wind turbine blades structures is icing of polymeric composite in service conditions [175]. Icing alters the shape, dynamic behavior and weight of structure and thus performance of whole structure. Ohmic-heating provides an active, easy, controllable and efficient method to add anti-icing capability into the polymeric structures. Electrical heating melts a thin layer of ice on the surface of structure and then ice starts to detach from the composite surface. In addition, heating by electrical current provides an ability to program the system to act in a timely manner or work based on the response of integrated sensors. This active controllability decreases the required energy and the degradation risk of composite because of overheating. Furthermore, uniform distribution of heat assisted by nanoparticles prevents the thermal degradation of composite coming from local heating which is a common phenomenon in the conventional active and passive anti-icing methods [176].

In our previous study [113], three different architectural designs of advanced multi-scale reinforced epoxy based composites were developed in which graphene sheets and carbon fibers were utilized as nano- and micro-scale reinforcements, respectively. In the first design, electrospraying technique was employed for the selective deposition of graphene sheets onto the surface of carbon fabric mats as an efficient and up-scalable method to enhance the interfacial strength between epoxy matrix and carbon fibers and thus increase the efficiency of load transfer between matrix and reinforcing fibers (encoded as CFRP/INT). In the second design, graphene sheets were dispersed directly into the hardener-epoxy mixture and graphene reinforced carbon fiber/epoxy composites were fabricated through vacuum infusion process (CFRP/MTX). In the third design, the combination of the first and the second arrangements were employed to manufacture a multi-scale hybrid composite with nano-reinforced matrix and improved interfacial strength between carbon fibers and epoxy matrix to achieve superior mechanical properties (CFRP/INT+MTX). Moreover, a specimen without any nano-scale reinforcement was manufactured to make a comparison in the mechanical performance

of nano-material reinforced composite (CFRP). Graphene/carbon fiber/epoxy composites in these three different arrangements of graphene sheets showed enhancement in in-plane and out-of plane mechanical performances. Especially hybrid composite structure of CFRP/INT+MTX in which graphene sheets were used as both interface modifier and matrix reinforcing agent, showed remarkable improvements on mechanical performance due to the synergetic effect.

In aforementioned structures, carbon fibers and graphene sheets are thermally and electrically conductive reinforcements that can create electrical and thermal conduction paths as well as provide selective and uniform distribution of heat through the composite parts. This type of polymeric composite with improved electrical and thermal conductivity can be utilized for electric heating materials or devices. Also, these materials do not suffer from corrosion, heavy weight and expensive manufacturing processes over metallic competitors [174].

Significant efforts are being made to extend the capabilities and reliabilities of fiber reinforced composites towards advanced applications by integrating nano- and micro-reinforcing agents and modifying their microstructure [113, 156]. However, most of these studies are using static testing techniques to investigate the microstructure effect on the mechanical performance of composite structures. This work addresses these issues by providing a detailed investigation about viscoelastic behavior of epoxy matrix composites with carbon fiber/selectively integrated graphene as multi-scale reinforcements by dynamic mechanical tests. The effects of temperature, frequency and graphene configuration on dynamical responses, damping behavior and viscoelastic activation energy were studied by using dynamical mechanical testing technique. The time–temperature superposition approach was used to predict the mechanical performance of polymeric samples outside the experimental time scales. To the best of our knowledge, there is no comprehensive work focusing on electrical and thermal conductivities, self-heating and deicing capabilities of multi-scale reinforced composite structures at the same time. In the present study, a systematical research was performed to bring a new insight into the design and fabrication hierarchical multi-scale and multi-functional structural materials. These hierarchical multi-scale designs of composites provide the ability to fabricate, mechanically high performance and electrically conductive structures with self-heating and deicing capabilities for advance applications.

## **7.2. Experimental**

### **7.2.1. Materials**

Materials used are N, N dimethyl formamide (DMF, Sigma-Aldrich, 99%), deionized water, thermally exfoliated graphene oxide (TEGO)-Grade 2 received from Nanografen Co. Araldite LY 564 resin, Hardener XB 3403 Uniaxial carbon fabrics of Metyx company with the average weight of 310 g/m<sup>2</sup> (300 g/m<sup>2</sup> 800 Tex 12K along the (0°) direction, and 10 g/m<sup>2</sup> 68 Tex E-Glass along the (90°) direction) and SPI Flash-Dry Silver Paint.

### **7.2.2. Fabrication of Multi-scale Reinforced Epoxy Composites**

In our previous study, composite laminates with three different multi-scale reinforcement architectures were developed by the integration of graphene as matrix and interface reinforcements in different configurations and their mechanical performances were investigated [18, 113]. In the first design, TEGO as an interface modifier was deposited on both two sides of unidirectional dry carbon fiber plies by electrospraying process. The weight percentage of TEGO in CFRP/INT specimens was adjusted as 0.01 wt%. In the second design, CFRP/MTX specimens were fabricated by the dispersion of TEGO sheets directly into epoxy and hardener mixture acting as a matrix reinforcement agent and then untreated carbon fiber plies were impregnated by using this TEGO integrated resin system. The weight percentage of TEGO in CFRP/MTX specimens was about 0.01 wt%. The third design was the combination of the first and the second approaches in which TEGO was used as both matrix reinforcement and interface modifier, which named as CFRP/INT+MTX. The total weight percent of TEGO in this combination was approximately 0.02 wt%. In all these specimens, carbon fiber plies were stacked into a [90°/0°]<sub>s</sub> configuration and then impregnated by a degassed epoxy resin-hardener system using vacuum infusion method. In the present work, these three composites were produced by following aforementioned production conditions to examine their viscoelastic response, self-heating and de-icing properties.

### 7.2.3. Dynamic Mechanical Analyses (DMA)

Dynamic Mechanical Analyzer (Netzsch DMA 242 C) was used to analyze the mechanical properties of composite specimens as a function of temperature, and frequency. Three-point bending mode was applied at frequencies of 1.0, 2.0, 5.0, 10.0 and 20.0 HZ with a heating rate of 3 °C per min in the temperature range of 30 to 150 °C.

### 7.2.4. Electrical Conductivity Measurements

In order to measure the in-plane electrical conductivity, specimens were cut into the desire dimensions and electrodes were prepared by applying silver paste to the two ends of specimen to provide uniform electrical current as shown in **Figure 7.1**. The electrical conductivity ( $\sigma$ ) was calculated by using  $\sigma=L/RA$  formula where R is the electrical resistance, A is the cross sectional area of specimen, and L is the length of the specimen. The R values were calculated for each specimen based on Ohm's role ( $R=V/I$ ) by applying different currents provided by a DC power supply (GPC-3060D, GW Instek) in the range of 0-1.4 A and reading the voltage values received from a Brymen 857a digital multimeter.

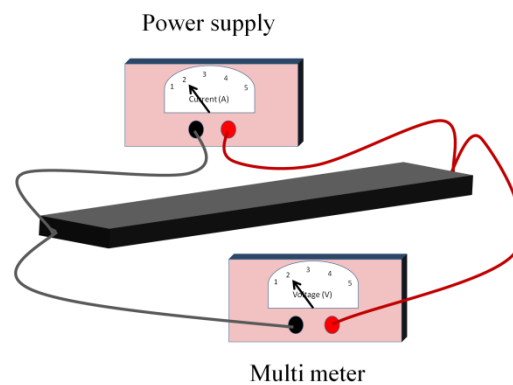


Figure 7.1 Schematic representation of electrical conductivity measurement set-up

### 7.2.5. Thermal diffusivity analysis by pulse thermography

The pulse thermography experiments were performed using PTvis 6000 module of edevis complete package (Edevis GmbH, Stuttgart, Germany) on 10 cm x 10 cm\*0.127 cm composite laminates. The system consists of a thermal camera, a Xenon flash lamp (6 kJ of optical energy), a control unit, a computer, and processing software

(DisplayIMG 6). The camera used for surveillance of pulse thermography experiments was FLIR System ATS X6580 SC equipped with a sensitive MWIR 640 x 512 sensor (1,5 – 5  $\mu\text{m}$ ) with capability to obtain images with maximum frame rate of 355 Hz at 640 x 512 Pixel. The thermal sensitivity of this camera is below 20mK. In the pulse thermography experiments, surface of specimens were excited by a pulse from a Xenon flash lamp then absorbed light transferred into heat and disturbed the thermal equilibrium of the sample. During these experiment thermography camera registers the temperature changes in the sample. Of special interest of this study is the evaluation of the time dependent thermal distribution within the composite specimens with different TEGO sheets configurations.

#### **7.2.6. Self-heating and Anti-Icing characterization**

Self-heating or Ohmic heating of specimens were examined by applying a constant current of 1 A at both ends of specimens in which silver past were applied previously. A FLIR SC300-Series thermal camera was used to observe the thermal profiles created due to Joule heating on composite specimens. Anti-icing experiments were conducted under the relevant sections by applying a constant current across the specimens at  $-35\text{ }^{\circ}\text{C}$  and dropping 20  $\mu\text{l}$  water on the surface of specimens.

### **7.3. Results and discussions**

#### **7.3.1. Dynamic mechanical analysis (DMA)**

DMA is a sensitive, powerful and versatile method to investigate the temperature dependency, and viscoelastic behavior of polymer based materials by measuring their stiffness and damping characteristics [177]. This technique applies a periodic stress to the sample and monitors the sample responses (including in- and out of phase responses). In-phase response is correlated to storage modulus ( $E'$ ) while out of phase responses are index of loss modulus ( $E''$ ). The ratio of these two parameters is defined as mechanical loss factor ( $\tan \delta$ ) in which a relation between the in-phase (elastic) and the out-of-phase (viscous) phase could be determined [178].

### 7.3.2. Dynamical-mechanical behavior of specimens under temperature sweep

Dynamical-mechanical properties of composites are strongly linked to type of matrix and reinforcement, matrix and reinforcement interaction and reinforcement content and orientations [179-181]. Figure 7.2 exhibits the storage modulus ( $E'$ ) and  $\tan \delta$  curves *vs* temperature for CFRP, CFRP/MTX, CFRP/INT and CFRP/INT+MTX specimens obtained at the frequency of 1 Hz. It can clearly be seen in Figure 7.2 that storage modulus which is an index of stiffness and load bearing capability of structure, at glassy region, temperature is lower than glass transition temperature ( $T_g$ ), shows different values for each specimen depending on TEGO sheets configuration. For CFRP/INT specimen in which nano-scale reinforcements were integrated at the interface of reinforcing carbon fibers with epoxy matrix a partial improvement on  $E'$  value at glassy state was observed compared to  $E'$  value of CFRP specimen. Furthermore, CFRP/MTX specimen in which TEGO sheets were dispersed into the polymeric matrix showed even higher  $E'$  value at glassy state when compared to CFRP and CFRP/INT specimens. The integration of TEGO sheets as both interface modifier and matrix reinforcement agent in the CFRP/INT+MTX specimen activates a synergetic effect leading to a significant increase in the  $E'$  value at glassy state compared to other specimens. However,  $E'$  after  $T_g$  and at the rubbery state showed different behavior compared to glassy state behavior of specimens. Similar  $E'$  value at rubbery state for both CFRP and CFRP/INT specimens reveal the negligible effect of interface of carbon fibers and polymeric matrix on  $E'$  values above  $T_g$  region. On the other hand, both specimens of CFRP/MTX and CFRP/INT+MTX in which TEGO sheets were incorporated into polymeric matrix showed similar  $E'$  values at rubbery state which is higher than  $E'$  at rubbery state for CFRP and CFRP/INT specimens. Thus, it can be conclude that at rubbery region matrix dominant properties control the composite behavior where integrating TEGO sheets enhances the storage modulus at rubbery regions by restricting the mobility of the polymeric chains [182].

Term  $\tan \delta$ , as an index of damping behavior of specimen, defined as the ratio of the loss modulus to the storage modulus. The peak of  $\tan \delta$  *vs* temperature graph is often related to the glass transition temperature.  $T_g$  is a very critical parameter for polymer based composite to determine maximum service temperature in their final application condition [66]. In Figure 7.2, it is clearly seen that incorporation of TEGO sheets in any

configurations do not change the  $T_g$  value. Furthermore, height of  $\tan\delta$  peak which is considered as an index of damping behavior of composites is different for each configuration of TEGO in specimens [183]. As it can be seen for CFRP and CFRP/INT specimens' height of  $\tan\delta$  peak and consequently damping behavior is higher compared to matrix modified CFRP/MTX and CFRP/INT+MTX specimens. These lower damping values for matrix modified specimens reveal that matrix properties play a critical role on damping behavior of composite structure compared to interface properties of carbon fiber with matrix.

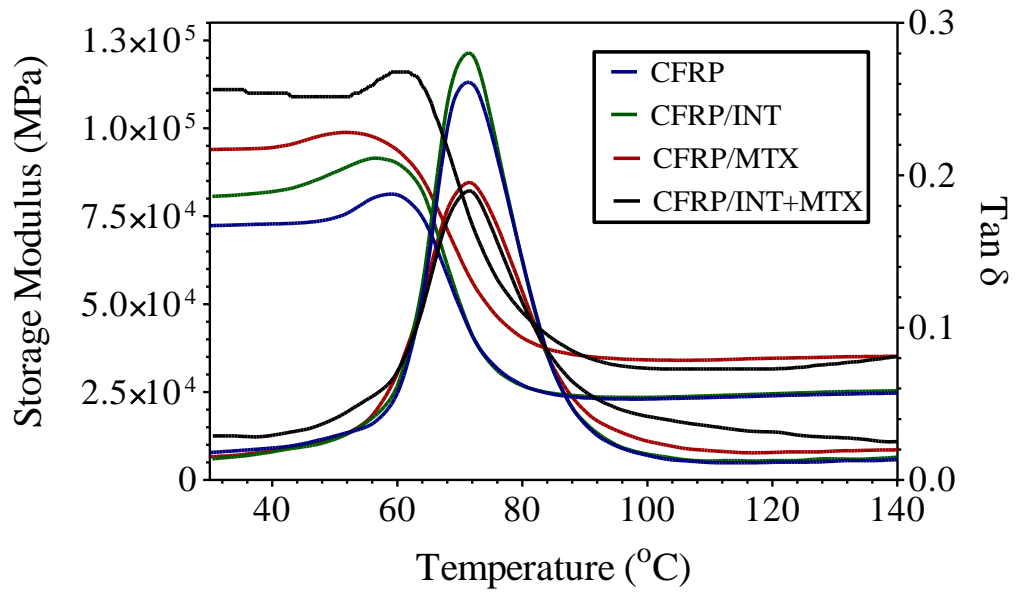


Figure 7.2 Temperature sweep of  $\tan\delta$  and  $E'$  curves of CFRP, CFRP/INT, CFRP/MTX and CFRP/INT+MTX at frequency of 1 Hz.

### 7.3.3. Frequency dependency of dynamical-mechanical properties and viscoelastic activation energy

Frequency of applied load is one of the main parameters influencing the response of polymeric structures in dynamical-mechanical analyzes. A common trend in polymeric materials is to shift  $\tan\delta$  curves to higher temperatures by increasing the test frequency [184]. **Figure 7.3a-3d** represent the  $\tan\delta$  curves for different composite specimens at heating rate of 3 °C/min at five different frequencies of 1, 2, 5, 10, and 20 Hz. In **Figure 7.3a-3d** it is seen that increasing the test frequency shifts the  $T_g$  in all the specimens to higher temperatures. However, availability of information on  $T_g$  at different frequency for polymeric systems enable us to apply Arrhenius equation on system behavior and

evaluate the activation energy of glass transition or viscoelastic activation energy [66]. The glass transition activation energy is a key factor in prediction of creep behavior and lifetime of polymeric structures in working conditions [185, 186]. Arrhenius equation for predict temperature and frequency relation DMA test are used repeatedly in different publications as Eq (1) [66, 187, 188]:

$$(1)$$

wherein  $\omega$  is the test frequency,  $\omega_0$  is pre-exponential factor, T is temperature, R is universal gas constant, and  $\Delta H$  is the activation energy. The ratio of test frequencies in different experiments is related to  $T_g$  by Eq (2) [66]:

$$\frac{\omega_1}{\omega_2} = \frac{\omega_i \exp\left(-\frac{\Delta H}{RT}\right) \exp\left(-\frac{\Delta H}{RT_{g1}}\right)}{\exp\left(-\frac{\Delta H}{RT_{g2}}\right)} \quad (2)$$

which can be converted to temperature shift factor,  $aT$  by Eq(3) [189]:

$$\log\left(\frac{\omega_1}{\omega_2}\right) = \log a_i = \frac{\Delta H}{R} \left(\frac{1}{T_{g2}} - \frac{1}{T_{g1}}\right) \quad (3)$$

Thus, the activation energy of glass transition,  $\Delta H$ , can be calculated from the slope of  $\ln(\omega)$  vs.  $1/T_g$  graph using Eq (4) [167, 186, 190]:

$$\Delta H = R \frac{(\ln \omega_1 - \ln \omega_2)}{\left(\frac{1}{T_{g2}} - \frac{1}{T_{g1}}\right)} = -R \frac{d(\ln \omega)}{d\left(\frac{1}{T_g}\right)} \quad (4)$$

**Figure 7.3e** represents the graph of  $\ln(\omega)$  vs.  $1000/T_g$  for four composite specimens. Table 7.1 summarizes the slopes of each line calculated by applying least square regression method,  $R^2$  values and activation energy (calculated by Eq (4)) obtained from Fig. 3e. The activation energy for neat CFRP specimen was about 346.7 kJ/mol but the addition of TEGO as an interface modifier slightly increased the activation energy upto 351.3 kJ/mol. An increase in activation energy of CFRP/INT specimen stems from the enhancement of interfacial interactions between carbon fiber and matrix, and thus the restrictions in the movement of polymeric chains at the interface. Moreover, the

dispersion of TEGO sheets into the epoxy matrix increased the activation energy upto 391.9 kJ/mol due to much more interactions of polymeric chains with TEGO sheets in the whole composite. In addition, the highest activation energy was obtained as 394.7 kJ/mol belonging to CFRP/INT+MTX specimen due to higher TEGO content in the structure. Higher activation energies obtained for TEGO modified composites provide higher stability at elevated temperatures.

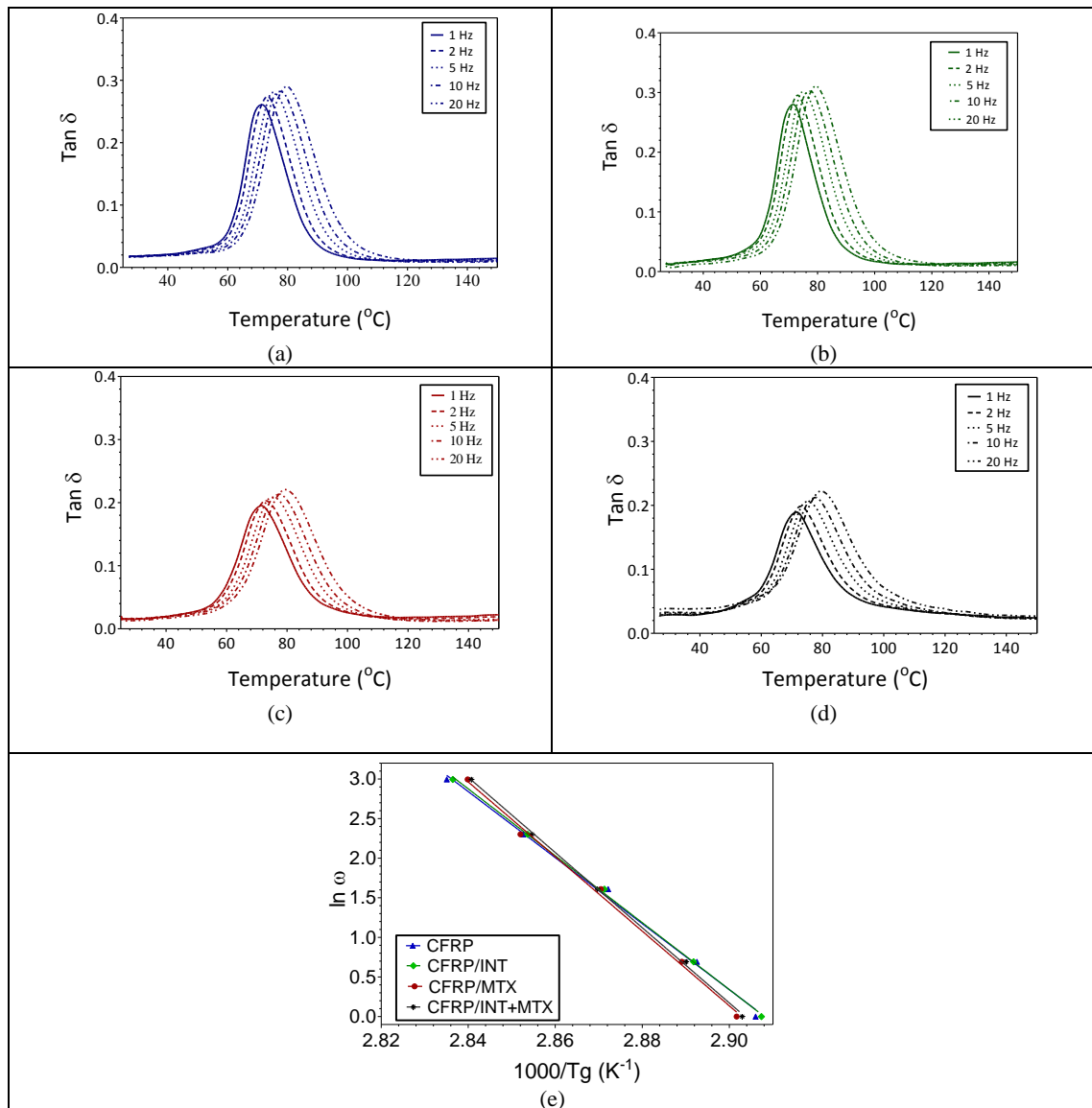


Figure 7.3  $\tan \delta$  vs temperature curves depending on different frequencies in the range of 1 to 20 Hz for (a) CFRP, (b) CFRP/INT, (c) CFRP/MTX, (d) CFRP/MTX+INT specimens, and (e) the graph of  $\ln(\omega)$  vs.  $1000/T_g$

Table 7.2 Slopes of  $\ln\omega$  vs.  $1000/T_g$  graphs, R<sup>2</sup> values, and activation energies ( $\Delta H$ ) of composite specimens

	Slope	R <sup>2</sup>	$\Delta H$ (kJ/mol)
CFRP	-41.70±1.6	0.996	346.7
CFRP/INT	-42.25±0.7	0.999	351.3
CFRP/MTX	-47.14±1.7	0.996	391.9
CFRP/INT+MTX	-47.47±0.7	0.999	394.7

#### 7.3.4. Master curves by time–temperature superposition

The time–temperature superposition approach provides a tool to predict the mechanical performance of polymeric composites out of experimental time scales [191]. The data presented in master curves can be used to estimate long-term behavior of materials such as creep (low frequency data) or material behavior in the exposure to an impact load (higher frequencies)[192, 193]. Herein, master curves were constructed for  $\tan\delta$  at different frequencies and temperature ranges by using Williams–Landel–Ferry or WLF model in which shift factor is described by Eq (5) [194, 195]:

$$\log a_t = \frac{-C_1(T - T_o)}{C_2 + (T - T_o)} \quad (5)$$

where  $C_1$  and  $C_2$  are material-dependent constants. It is generally accepted that WLF equation are valid for temperature above  $T_g$  [188]. However, in this study, WLF equation was applied for whole temperature ranges of DMA test in order to investigate the deviation of specimens' behavior with different TEGO configurations at different temperature ranges. **Figure 7.4** exhibits  $\tan\delta$  master curves at different reference temperatures and frequencies. One can see that for CFRP and CFRP/INT specimens having no TEGO sheets in the matrix, the peak frequencies of  $\tan\delta$  curves changed nonlinearly by increasing the reference temperature upto  $T_g$  ( $\sim 75$  °C). On the other hand, taking the reference temperatures upper than  $T_g$  resulted in graphs with linear change on the peak frequencies of  $\tan\delta$ . In another words, in CFRP and CFRP/INT specimens for temperatures lower than  $T_g$ , the peak frequencies of  $\tan\delta$  shift nonlinearly towards lower frequencies due to the deviation of materials behavior from WLF model while these changes are linear at reference temperatures higher than  $T_g$ . In addition, in CFRP/MTX and CFRP/INT+MTX specimens, the peak frequencies of  $\tan\delta$  in all the temperature ranges changed linearly without any significant deviation from linear behavior. This phenomenon can be explained by the alteration on chain mobility of polymeric matrix

because of the presence of graphene sheets being effective in all reference temperature ranges.

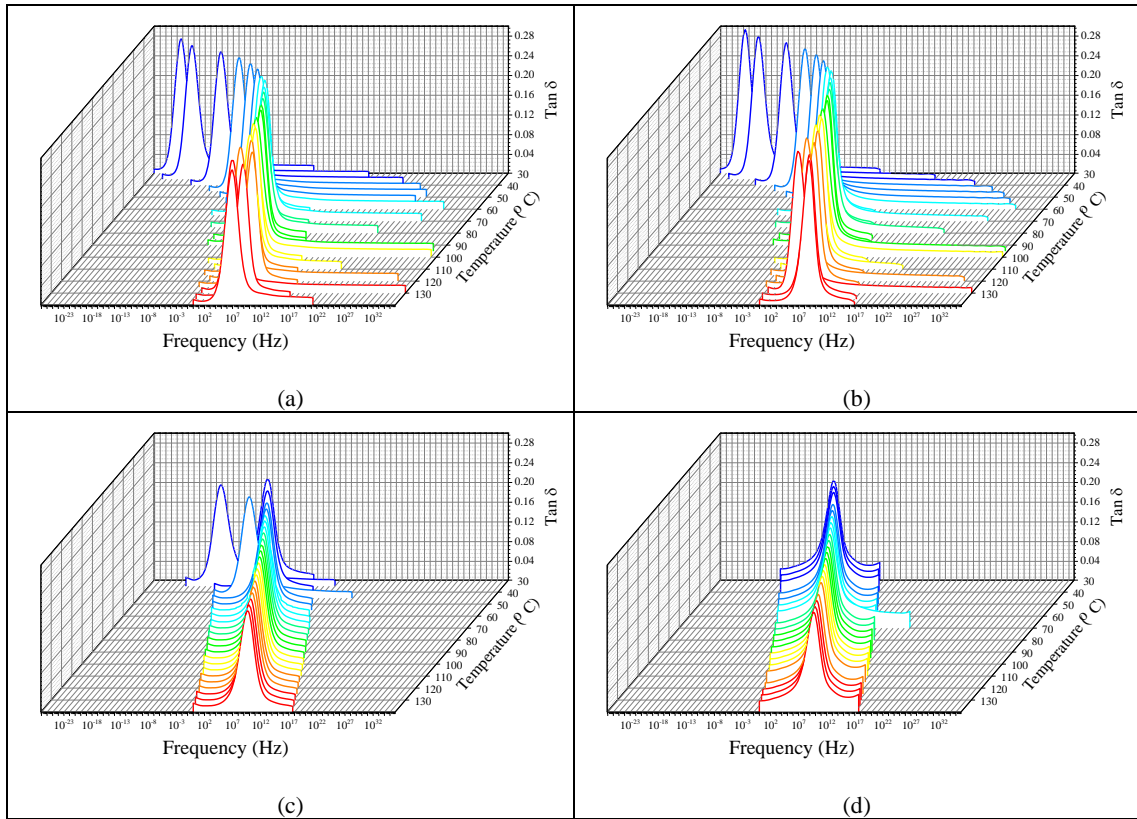


Figure 7.4  $\text{Tan}\delta$  vs frequency master curves of (a) CFRP, (b) CRFP/INT, (c) CFRP/MTX and (d) CFRP/MTX+INT at different reference temperatures

### 7.3.5. Electrical Conductivity

DC electrical conductivities (in-plane) of multi-scale reinforced composites were measured by applying various electrical currents and reading the induced voltage of the specimens. **Figure 7.5a** exhibits the current-voltage (I-V) curves of CFRP, CFRP/INT, CFRP/MTX and CFRP/INT+MTX. In all the specimens, voltage increased linearly by increasing the electric current. However, the slopes of these lines are different in each configuration of TEGO sheets. **Figure 7.5b** represents the changes in the electrical conductivities of specimens regarding TEGO configuration in composite structure. The results showed that the electrical conductivity of neat CFRP specimen was about  $30 \text{ S}\cdot\text{cm}^{-1}$  whereas the composite conductivity decreased down to  $16.8 \text{ S}\cdot\text{cm}^{-1}$  by the deposition of conductive TEGO sheets on carbon fiber surface. Similar tendency was also observed in the literature but there is not enough explanation about the decrease in electrical

conductivity by using conductive materials as interface modifier [156]. In neat composite, main electron pathway happens in carbon fibers. In the present study, TEGO as an interface modifier increases the surface-to-volume ratio of carbon fibers but starts to entrap electrons coming from carbon fibers and this results in an increase in electron surface scattering and thus the reduction in electrical conductivity [196-198]. On the other hand, the incorporation of TEGO sheets into polymeric matrix increased the electrical conductivity upto  $47.6 \text{ S.cm}^{-1}$  due to the creation of new conduction pathways through epoxy matrix by TEGO sheets in addition to carbon fibers having main electron conduction routes. Furthermore, there is a sudden increase in electrical conductivity of CFRP/INT+MTX specimen as  $102 \text{ S.cm}^{-1}$  due to co-presence of electrical conduction paths of carbon fibers and TEGO network in the matrix and also proper connection of these two electrical conduction paths by TEGO sheets at the interface of carbon fibers.

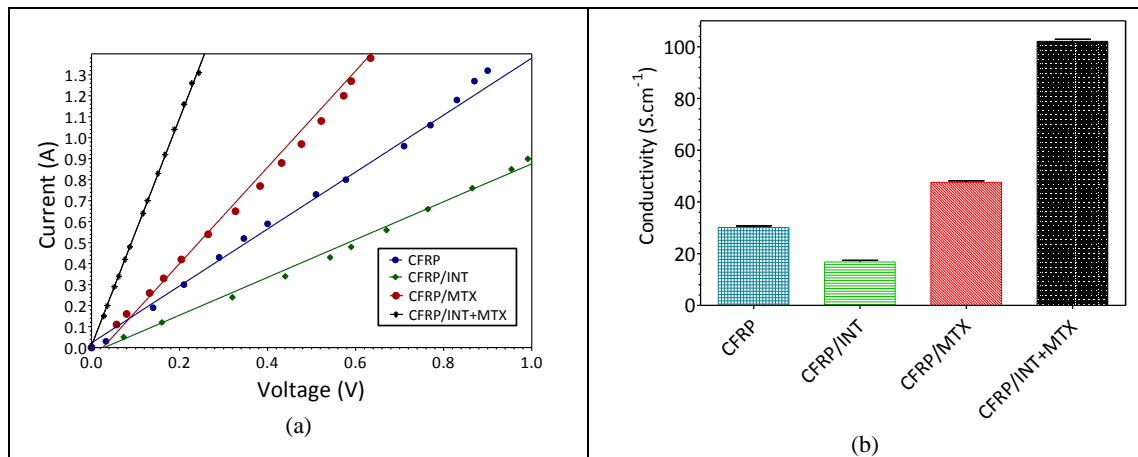


Figure 7.5 (a) I-V curves and (b) electrical conductivity value vs specimen type

### 7.3.6. Self- heating performance

One of the phenomena in a conductive structure is Joule heating or Ohmic heating. Based on this phenomenon, the passage of electrical current through any conductive structure would release heat [199]. Benefiting from this phenomenon, conductive composite structures can be used as electrical resistors, which convert electrical energy into thermal energy [174, 200]. Herein, a constant current of 1 A was applied on the composite specimens and generated temperature profiles were monitored by a thermal camera. Figure 7.6 shows the temperature profiles of each specimen at their steady state forms. Figure 7.6a and 7.6b exhibit the temperature profiles for CFRP and CFRP/INT specimens in which very intense heating were observed at the edges and especially in the

connection areas of specimens to power supply due to the low electrical and thermal conductivities of specimens. On the other hand, in Figure 7.6a and 6b, temperature is much lower at the middle of CFRP and CFRP/INT specimens. This extreme difference between edge and middle temperatures of specimens can restrict their utilization in electrical heating based devices since more thermal degradation occurs at the edges by applying current whereas the middle of specimens would not reach the desired temperature. Furthermore, in the CFRP/MTX specimen, in Figure 7.6c, the presence of TEGO sheets in the matrix increases the electrical conductivity of specimen and thus lower amount of heat generation is observed under the constant current compared to the aforementioned specimens. In addition, CFRP/MTX specimen shows more uniform temperature distribution on its surface as seen in Figure 7.6c due to an increase in thermal conductivity of structure in the presence of TEGO sheets. On the other hand, in Figure 7.6d, electrical conductivity of CFRP/INT+MTX specimen increases significantly which causes much lower heat generation. Also, thermal camera image showed much uniform temperature distribution for CFRP/INT+MTX specimen.

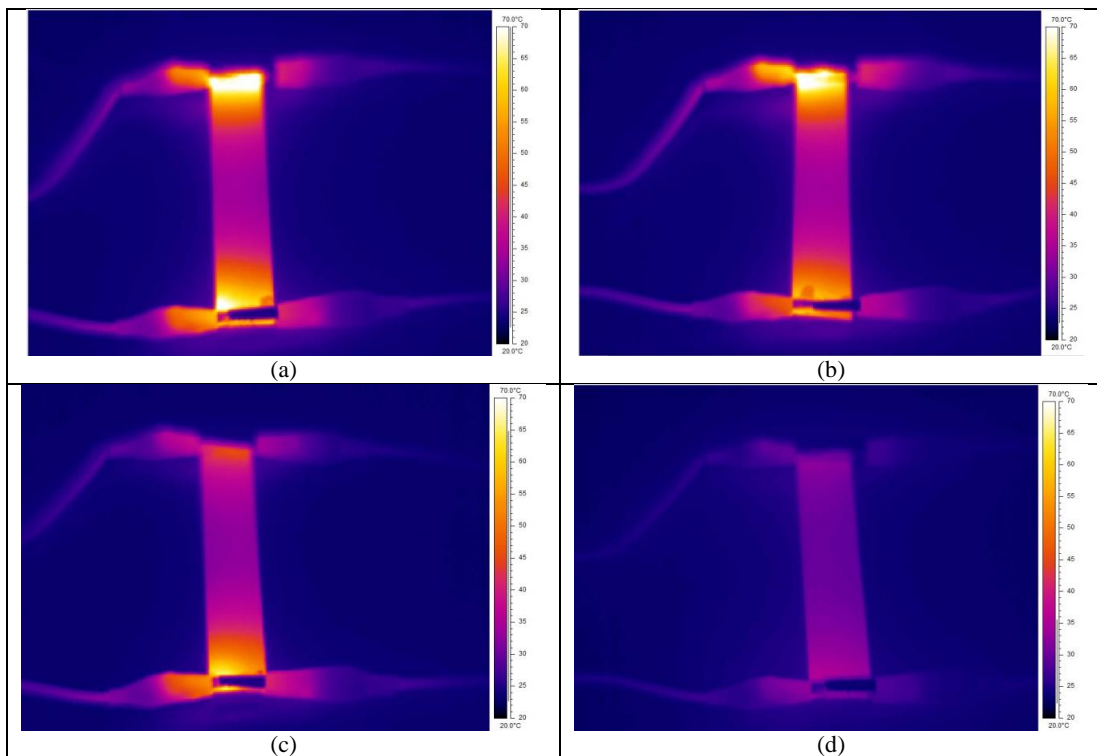


Figure 7.6 Thermograms of (a) CFRP, (b) CFRP/INT, (c) CFRP/MTX, and (d) CFRP/INT+MTX under constant current of 1 A.

### 7.3.7. Thermal-Diffusivity Characteristics of Composite Specimens

The extremely short test duration and high detection sensitivity make pulse thermography a suitable non-contact test method to characterize the thermal properties of composite specimens. In this method, thermal equilibrium of specimen was disturbed by the deposition of a short pulse of energy by a powerful xenon flash lamp at the front surface of specimen. The temperature decay on the surface of specimen was registered by a thermal camera as a function of time. Temperature decay data can be used to extract information on test specimen properties (e.g. thickness, and thermal properties) [201]. Thermal diffusivity as an index of heat propagation speed through conduction in any material is defined by Eq (6) [202]:

$$D = \frac{k}{\rho C_p} \quad (6)$$

where  $k$  is thermal conductivity,  $C_p$  is specific heat capacity and  $\rho$  is density. In composite materials, thermal diffusivity is directly related to the material microstructure and constituent material properties and its orientation. Figure 7.7 exhibits the temperature-time curves for specimens having different TEGO sheets configurations. Each curve consists of two separate parts namely: initial linear decrease of temperature by time in a log-log plot and latter is the thermal equilibrium when heat reaches the back of specimen. In these curves, the crossing point between these two linear regimes is defined as  $\tau_c$  related to the time which is required for heat to cross the entire sample with thickness of  $L$ . The crossing time ( $\tau_c$ ) can be used to calculate the heat diffusivity ( $D$ ) based on Parker *et al.* Theory by using Eq (7) [203, 204]:

$$D = \frac{L^2}{\tau_c} \quad (7)$$

Table 7.3 summarizes specimen thickness,  $\tau_c$  and thermal diffusivity values calculated by using pulse thermography. In CFRP specimen, thermal diffusivity was calculated as  $5.98 \text{ mm}^2 \text{ s}^{-1}$ . In the CFRP/INT specimen, the speed of heat conduction of specimen increases while the heat capacity of specimen remained unchanged resulted in a jump in thermal diffusivity of specimen to  $6.31 \text{ mm}^2 \text{ s}^{-1}$  due to the presence of TEGO sheets on the surface of carbon fibers providing higher surface area for thermally

conductive carbon fibers. On the other hand, the incorporation of TEGO sheets into the polymeric matrix of CFRP/MTX specimen increased the thermal conductivity and decreased the heat capacity of structure by restricting the movement of polymer chains leading to an increase in thermal diffusivity to  $6.20 \text{ mm}^2 \text{ s}^{-1}$  [205, 206]. Furthermore, thermal diffusivity of CFRP/INT+MTX specimen increased upto  $6.61 \text{ mm}^2 \text{ s}^{-1}$  and had higher thermal conductivity compared to the other samples due to the synergistic effect of TEGO sheets available at the interface and in the matrix of composite structures.

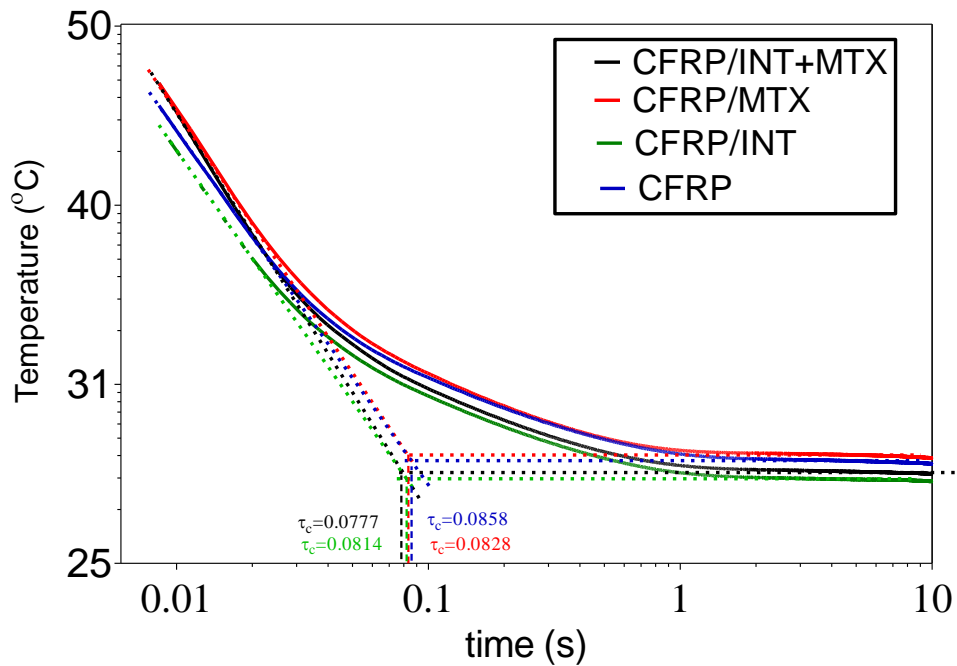


Figure 7.7 Surface temperature decay curves calculated for composite specimens regarding different TEGO sheets configurations.

Table 7.3 Sample thickness, crossing time ( $\tau_c$ ) and calculated Thermal diffusivity

	Sample thickness (mm)	$\tau_c$ (s)	D ( $\text{mm}^2 \text{ s}^{-1}$ )
CFRP	$1.27 \pm 0.02$	0.0858	5.98
CFRP/INT	$1.27 \pm 0.03$	0.0814	6.31
CFRP/MTX	$1.27 \pm 0.03$	0.0828	6.20
CFRP/INT+MTX	$1.27 \pm 0.03$	0.0777	6.61

### 7.3.8. Self-heating Application in De-icing

In order to investigate the deicing capability of specimens,  $20 \mu\text{l}$  water droplet was placed in the middle of composite specimen surface and water droplet was frozen at temperature of  $-35 \text{ }^\circ\text{C}$  by using a set-up shown in Figure 7.8a. The deicing time were measured for CFRP, CFRP/INT and CFRP/MTX specimens by applying the current of 3

A to the drop of droplet from surface of specimen. However, for CFRP/INT+MTX specimen having the highest conductivity value, the heat generated under constant current of 3 A is not enough for the initiation of deicing process. Therefore, higher current of 4 A was applied to CFRP/INT+MTX specimen. In CFRP/INT+MTX specimen, it is feasible to increase the current up to 4 A without degrading the specimen which is not applicable for other specimens. The deicing performance of specimens in Figure 7.8b reveals that CFRP and CFRP/INT show almost similar deicing behavior. On the other hand, the ice drop time of CFRP/MTX decreases. Noting the lower generation of heat in CFRP/MTX specimen at constant current compared to CFRP and CFRP/INT, lower drop time stems from higher thermal conductivity of specimen which facilitates the heat distribution all over the specimen. In addition, in CFRP/INT+MTX specimen, the capability to apply higher current on the specimens results in notable less drop time and consequently better de-icing performance among other specimens.

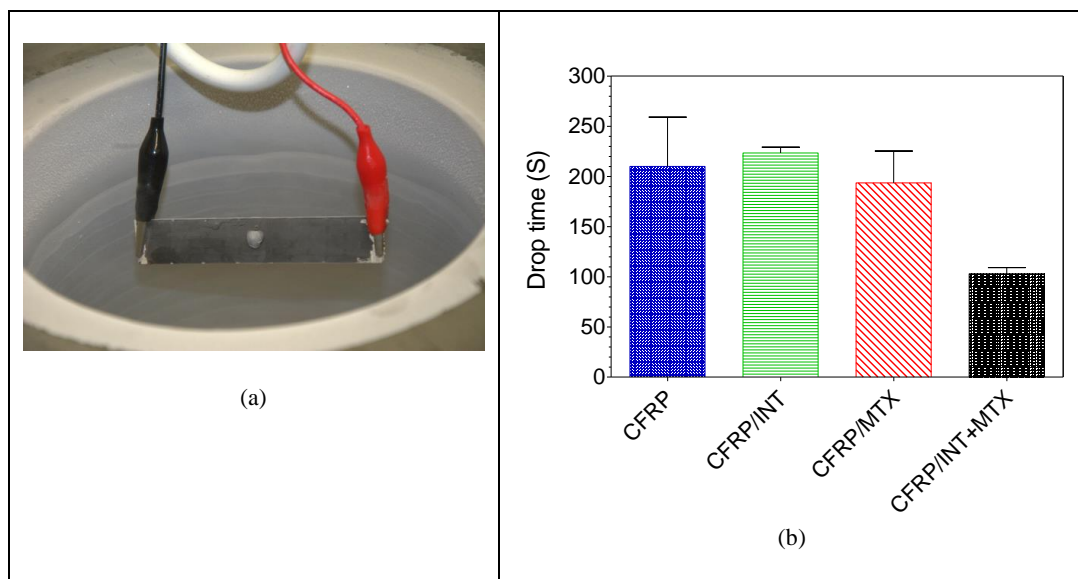


Figure 7.8 (a) The setup of de-icing experiment, and (b) Ice drop time of CFRP, CFRP/INT, CFRP/MTX under constant current of 3 A, and CFRP/INT+MTX under constant current of 4 A.

#### 7.4. Conclusions

Multi-layer graphene oxide sheets with superior mechanical performance, electrical and thermal conductivities were integrated with three different configurations into carbon fiber reinforced epoxy composites. In the first design, graphene was used as an interface modifier between carbon fiber and the matrix, in the second design, graphene

was used as a matrix reinforcement and the third design was the combination of the first and second designs. Dynamical-mechanical behavior of specimens under temperature sweep showed that damping behavior of fiber reinforced structures was strongly linked to the matrix properties rather than the interface of reinforcing fibers and the matrix. In addition, glass transition activation energy and master curves for each specimen were calculated to understand the graphene sheets effect on composite performance under various dynamic loads and temperature ranges. When graphene was used as both an interface modifier and a matrix reinforcement in the composite structure, electrical conductivity of this newly design composite showed 240% enhancement. Also, the thermal diffusivity of this composite measured through monitoring the surface temperature by pulse thermography technique had higher values than the other specimens. This facilitated the heat transfer inside the structure and thus more uniform temperate profile can be achieved in carbon fiber reinforced composites by dispersing graphene selectively. In addition, composites gained de-icing functionality by introducing self-heating capability based on Joule heating. It was observed that CFRP/INT+MTX specimens possess a significant higher de-icing performance over other specimens. Consequently, multi-scale carbon fiber reinforced composites by the integration of graphene as nanofiller will bring new direction in the composite applications to develop and fabricate more reliable, multi-functional and long-lasting materials.

## CHAPTER 8. CONCLUSIONS

This study was conducted in six major sections. The findings for each step can be summarized as follows:

### i. Direct fabrication of multi-walled hollow electrospun fibers with controllable structure and surface properties

In this part of study, multi-walled electrospun fibers with controllable hollowness and different polymeric layers were fabricated by a single step process. The inner and outer diameters of fibers and surface morphologies are controlled by changing the solvent type, applied voltage, polymer concentration, and polymer type. The system and process parameters of tri-axial electrospinning were optimized to fabricate an ideal multi-walled hollow fiber structure.

### ii. Multi-walled hollow nanofibers as reinforcing agents in nanocomposites

The effect of electrospun fibers with different wall materials, morphology, diameter, and fiber content on the mechanical performance of composite specimens is studied. Two different composite production techniques, which are casting onto a Teflon mould and vacuum infusion, are applied to produce composite structures. The utilization of PMMA-PAAm hollow fiber as inter layers of glass fiber laminated composites, enhances the flexural modulus by 6.5 %, flexural strength by 14 %, the onset of first layer of glass fabric failure strain by 12.5 % and final failure strain by 20%. DMA results for glass fiber reinforced specimens laminated with nanofiber interlayers show 7°C increase in  $T_g$  in comparison to neat specimens.

### iii. Repeated Self-healing of Nano and Micron Scale Cracks in Epoxy based Composites

Electrospun multi-walled healing fibers are utilized in order to encapsulate various healing agents with two different protective walls. For the first design of healing fibers, DCPD as a healing agent is encapsulated inside the electrospun fibers with two different polymeric layers wherein the middle layer encapsulates healing agent due to its low affinity, and outer layer is compatible with epoxy matrix. The effect of fiber diameter (nano or micron scale) and the type of self-healing agent (DCPD monomer and epoxy

resin) on self-healing properties of the produced composites were investigated by comparing mechanical properties. It is shown that healing fibers with larger mean diameter are much more appropriate for healing micro cracks whereas fibers with finer diameter can heal nano-scale cracks more effectively. The unique structure of multi-walled electrospun fibers developed in this work has a high potential to create a novel self-healing, smart and responsive materials with enhanced functionalities.

#### iv. Acoustic emission and Fiber Bragg grating as a novel technique for measuring self-healing efficiency

Two different composite production techniques are employed to fabricate self-healing epoxy based composite structures. In the first method, tri-axial electrospun fiber reinforced epoxy composites were fabricated by using classical molding technique in which electrospun fibers act as both reinforcement and healing agent. In the second method, vacuum infusion technique was employed to fabricate glass fiber/tri-axial electrospun fibers/epoxy composite in which tri-axial healing fibers provide self-healing functionality at the interface of the glass fibers with epoxy matrix and enhance the composite toughness. Traditional mechanical testing methods and different SHM techniques such as FBG sensors, acoustic emission, and Poisson's ratio reduction are employed to analyze the health and damage states of components in the localized and global scale in real time. Successful and recurring self-healing ability of composite structures and healing functionality of fibers at the interface of glass fiber with the epoxy matrix are confirmed through different characterization techniques.

#### v. High-Performance Epoxy Matrix Composites with Carbon Fiber/Selectively Integrated Graphene as Multi-Scale Reinforcements

Three different architectural designs are developed for manufacturing advanced multi-scale reinforced epoxy based composites in which graphene sheets and carbon fibers are utilized as nano- and micro-scale reinforcements, respectively. In the first design, graphene sheets are used as interface modifier between the carbon fiber and the matrix; in the second design, graphene sheets are used as matrix reinforcement and third design is combination of the first and the second designs. The integration of graphene sheets on carbon fiber interface enhances the efficiency of load transfer from matrix to reinforcing fibers. The integration of graphene into the carbon fiber reinforced composite

in the form of matrix reinforcement leads to appreciable enhancement in the mechanical performance of manufactured composite structures. Furthermore, the utilization of graphene sheets as both interface modifier and matrix reinforcement shows a synergetic effect thereby resulting in excellent improvements in the mechanical performance of the hybrid composite structure. Namely, when compared to unmodified composite structure, flexural strength, modulus and work of fracture are enhanced by about 51.2 %, 31.1 %, and 55 %, respectively while tensile strength, modulus, and impact strength are augmented by about 19.4 %, 20.3 %, and 29.9 %, respectively.

vi. Viscoelastic Response, Self-heating and Deicing properties of Carbon Fiber/Selectively Integrated Graphene/epoxy composites

Graphene sheets with superior mechanical performance, electrical and thermal conductivities are integrated with different configurations into carbon fibers reinforced composites. Dynamical-mechanical behavior of specimens under temperature sweep showed that damping behavior of fiber reinforced structures are strongly linked to the matrix properties rather than interface of reinforcing fibers and the matrix. In addition, activation energy of the glass transition as well as master curves for each specimen types were calculated under various dynamic loads and temperature ranges. The electrical conductivity of composites was increased up to 240% compared to unmodified specimen. Self-heating performance and thermal diffusivity of specimens were measured by monitoring the surface temperature and pulse thermography techniques. The electrical conductivity and self-heating capability of specimens were employed to develop composites with de-icing functionalities.

## REFERENCES:

- [1] E.J. Siochi, J.S. Harrison, Structural nanocomposites for aerospace applications, *MRS Bulletin* 40(10) (2015) 829-835.
- [2] J. Seyyed Monfared Zanjani, B. Saner Okan, Y. Menciloglu, Manufacturing of multilayer graphene oxide/poly(ethylene terephthalate) nanocomposites with tunable crystallinity, chain orientations and thermal transitions, *Materials Chemistry and Physics*.
- [3] A. Zucchelli, M.L. Focarete, C. Gualandi, S. Ramakrishna, Electrospun nanofibers for enhancing structural performance of composite materials, *Polym Advan Technol* 22(3) (2011) 339-349.
- [4] B.C. Ray, D. Rathore, Environmental Damage and Degradation of FRP Composites: A Review Report, *Polym Composite* 36(3) (2015) 410-423.
- [5] Y.-K. Song, C.-M. Chung, Repeatable self-healing of a microcapsule-type protective coating, *Polymer Chemistry* 4(18) (2013) 4940-4947.
- [6] J.W.C. Pang, I.P. Bond, A hollow fibre reinforced polymer composite encompassing self-healing and enhanced damage visibility, *Compos Sci Technol* 65(11-12) (2005) 1791-1799.
- [7] G. Williams, R. Trask, I. Bond, A self-healing carbon fibre reinforced polymer for aerospace applications, *Compos Part a-Appl S* 38(6) (2007) 1525-1532.
- [8] S.R. White, N.R. Sottos, P.H. Geubelle, J.S. Moore, M.R. Kessler, S.R. Sriram, E.N. Brown, S. Viswanathan, Autonomic healing of polymer composites, *Nature* 409(6822) (2001) 794-7.
- [9] A. Gopinath, M.S. Kumar, A. Elayaperumal, Experimental Investigations on Mechanical Properties Of Jute Fiber Reinforced Composites with Polyester and Epoxy Resin Matrices, *Procedia Engineering* 97(0) (2014) 2052-2063.
- [10] J. Gassan, A study of fibre and interface parameters affecting the fatigue behaviour of natural fibre composites, *Composites Part A: Applied Science and Manufacturing* 33(3) (2002) 369-374.
- [11] A. Warriar, A. Godara, O. Rochez, L. Mezzo, F. Luizi, L. Gorbatikh, S.V. Lomov, A.W. VanVuure, I. Verpoest, The effect of adding carbon nanotubes to glass/epoxy composites in the fibre sizing and/or the matrix, *Composites Part A: Applied Science and Manufacturing* 41(4) (2010) 532-538.
- [12] C. Lee, X. Wei, J.W. Kysar, J. Hone, Measurement of the Elastic Properties and Intrinsic Strength of Monolayer Graphene, *Science* 321(5887) (2008) 385-388.
- [13] L.S. Schadler, S.C. Giannaris, P.M. Ajayan, Load transfer in carbon nanotube epoxy composites, *Applied Physics Letters* 73(26) (1998) 3842-3844.

- [14] Ramanathan T, A.A. Abdala, Stankovich S, D.A. Dikin, M. Herrera Alonso, R.D. Piner, D.H. Adamson, H.C. Schniepp, Chen X, R.S. Ruoff, S.T. Nguyen, I.A. Aksay, R.K. Prud'Homme, L.C. Brinson, Functionalized graphene sheets for polymer nanocomposites, *Nat Nano* 3(6) (2008) 327-331.
- [15] H. Kim, A.A. Abdala, C.W. Macosko, Graphene/Polymer Nanocomposites, *Macromolecules* 43(16) (2010) 6515-6530.
- [16] Y.T. Park, Y. Qian, C. Chan, T. Suh, M.G. Nejhad, C.W. Macosko, A. Stein, Epoxy Toughening with Low Graphene Loading, *Advanced Functional Materials* 25(4) (2015) 575-585.
- [17] J. Seyyed Monfared Zanjani, B. Saner Okan, I. Letofsky-Papst, M. Yildiz, Y.Z. Menciloglu, Rational design and direct fabrication of multi-walled hollow electrospun fibers with controllable structure and surface properties, *European Polymer Journal* 62(0) (2015) 66-76.
- [18] J.S.M. Zanjani, B. Saner Okan, Y.Z. Menciloglu, M. Yildiz, Design and fabrication of multi-walled hollow nanofibers by triaxial electrospinning as reinforcing agents in nanocomposites, *Journal of Reinforced Plastics and Composites* 34(16) (2015) 1273-1286.
- [19] J.S. Monfared Zanjani, B.S. Okan, I. Letofsky-Papst, Y. Menciloglu, M. Yildiz, Repeated self-healing of nano and micro scale cracks in epoxy based composites by tri-axial electrospun fibers including different healing agents, *RSC Adv.* 5(89) (2015) 73133-73145.
- [20] G.F.J. Müller, M. Stürzel, R. Mülhaupt, Core/Shell and Hollow Ultra High Molecular Weight Polyethylene Nanofibers and Nanoporous Polyethylene Prepared by Mesoscopic Shape Replication Catalysis, *Advanced Functional Materials* 24(19) (2014) 2860-2864.
- [21] Y. Hong, X. Chen, X. Jing, H. Fan, Z. Gu, X. Zhang, Fabrication and Drug Delivery of Ultrathin Mesoporous Bioactive Glass Hollow Fibers, *Advanced Functional Materials* 20(9) (2010) 1503-1510.
- [22] K.-L. Ou, C.-S. Chen, L.-H. Lin, J.-C. Lu, Y.-C. Shu, W.-C. Tseng, J.-C. Yang, S.-Y. Lee, C.-C. Chen, Membranes of epitaxial-like packed, super aligned electrospun micron hollow poly(l-lactic acid) (PLLA) fibers, *European Polymer Journal* 47(5) (2011) 882-892.
- [23] L. Niu, C.-L. Zhao, J. Kang, S. Jin, J. Guo, H. Wei, A chemical vapor sensor based on Rayleigh scattering effect in simplified hollow-core photonic crystal fibers, *Opt. Commun.* 313(15) (2014) 243-247.
- [24] M. Bognitzki, H. Hou, M. Ishaque, T. Frese, M. Hellwig, C. Schwarte, A. Schaper, J.H. Wendorff, A. Greiner, Polymer, Metal, and Hybrid Nano- and Mesotubes by Coating Degradable Polymer Template Fibers (TUFT Process), *Adv. Mater. (Weinheim, Ger.)* 12(9) (2000) 637-640.

- [25] Y. Qiu, J. Yu, Synthesis of titanium dioxide nanotubes from electrospun fiber templates, *Solid State Communications* 148(11-12) (2008) 556-558.
- [26] Z. Huang, Y. Chen, W. Zhou, H. Nie, Y. Hu, Preparation of silica hollow fibers by surface-initiated atom transfer radical polymerization from electrospun fiber templates, *Materials Letters* 63(21) (2009) 1803-1806.
- [27] P. Liu, Y. Zhu, J. Ma, S. Yang, J. Gong, J. Xu, Preparation of continuous porous alumina nanofibers with hollow structure by single capillary electrospinning, *Colloids Surf., A* 436 (2013) 489-494.
- [28] D. Li, Y. Xia, Direct Fabrication of Composite and Ceramic Hollow Nanofibers by Electrospinning, *Nano Letters* 4(5) (2004) 933-938.
- [29] D. Li, J.T. McCann, Y. Xia, Use of electrospinning to directly fabricate hollow nanofibers with functionalized inner and outer surfaces, *Small* 1(1) (2005) 83-6.
- [30] E. Zussman, A.L. Yarin, A.V. Bazilevsky, R. Avrahami, M. Feldman, Electrospun Polyaniline/Poly(methyl methacrylate)-Derived Turbostratic Carbon Micro-/Nanotubes, *Advanced Materials* 18(3) (2006) 348-353.
- [31] Y. Dror, W. Salalha, R. Avrahami, E. Zussman, A.L. Yarin, R. Dersch, A. Greiner, J.H. Wendorff, One-step production of polymeric microtubes by co-electrospinning, *Small* 3(6) (2007) 1064-73.
- [32] E. Ozden-Yenigun, E. Simsek, Y.Z. Menciloglu, C. Atilgan, Molecular basis for solvent dependent morphologies observed on electrosprayed surfaces, *Physical Chemistry Chemical Physics* 15 (2013) 17862-17872.
- [33] V. Kalra, J.H. Lee, J.H. Park, M. Marquez, Y.L. Joo, Confined Assembly of Asymmetric Block-Copolymer Nanofibers via Multiaxial Jet Electrospinning, *Small* 5(20) (2009) 2323-2332.
- [34] H. Chen, N. Wang, J. Di, Y. Zhao, Y. Song, L. Jiang, Nanowire-in-Microtube Structured Core/Shell Fibers via Multifluidic Coaxial Electrospinning, *Langmuir* 26(13) (2010) 11291-11296.
- [35] W. Liu, C. Ni, D.B. Chase, J.F. Rabolt, Preparation of Multilayer Biodegradable Nanofibers by Triaxial Electrospinning, *ACS Macro Letters* 2(6) (2013) 466-468.
- [36] D. Han, A.J. Steckl, Triaxial electrospun nanofiber membranes for controlled dual release of functional molecules, *ACS applied materials & interfaces* 5(16) (2013) 8241-5.
- [37] C.M. Hansen, *Hansen Solubility Parameters: A User's Handbook*, CRC Press LLC2000.
- [38] Z. Kurban, A. Lovell, S.M. Bennington, D.W.K. Jenkins, K.R. Ryan, M.O. Jones, N.T. Skipper, W.I.F. David, A Solution Selection Model for Coaxial Electrospinning and Its Application to Nanostructured Hydrogen Storage Materials, *The Journal of Physical Chemistry C* 114(49) (2010) 21201-21213.

- [39] C.J. Luo, E. Stride, M. Edirisinghe, Mapping the Influence of Solubility and Dielectric Constant on Electrospinning Polycaprolactone Solutions, *Macromolecules* 45(11) (2012) 4669-4680.
- [40] Q. Zhou, M. Bao, H. Yuan, S. Zhao, W. Dong, Y. Zhang, Implication of stable jet length in electrospinning for collecting well-aligned ultrafine PLLA fibers, *Polymer* 54(25) (2013) 6867–6876.
- [41] C.J. Luo, M. Nangrejo, M. Edirisinghe, A novel method of selecting solvents for polymer electrospinning, *Polymer* 51(7) (2010) 1654-1662.
- [42] S. Megelski, J.S. Stephens, D.B. Chase, J.F. Rabolt, Micro- and Nanostructured Surface Morphology on Electrospun Polymer Fibers, *Macromolecules* 35(22) (2002) 8456-8466.
- [43] A. Rahmat, N. Tofighi, M.S. Shadloo, M. Yildiz, Numerical simulation of wall bounded and electrically excited Rayleigh–Taylor instability using incompressible smoothed particle hydrodynamics, *Colloids and Surfaces A: Physicochemical and Engineering Aspects* In Press, Corrected Proof — Note to users (2014).
- [44] T.J. Sill, H.A. von Recum, Electrospinning: Applications in drug delivery and tissue engineering, *Biomaterials* 29(13) (2008) 1989-2006.
- [45] J.T. McCann, D. Lia, Y. Xia, Electrospinning of nanofibers with core-sheath, hollow, or porous structures, *Journal of Materials Chemistry* 15 (2005) 735-738.
- [46] K. Kaniappan, S. Latha, Certain Investigations on the Formulation and Characterization of Polystyrene / Poly(methyl methacrylate) Blends, *International Journal of ChemTech Research* 3(2) (2011) 708-717.
- [47] R. Murugan, S. Mohan, A. Bigotto, FTIR and Polarised Raman Spectra of Acrylamide and Polyacrylamide, *Journal of the Korean Physical Society* 32(4) (1998) 505-512.
- [48] T. Kashiwagi, A. Inaba, J.E. Brown, K. Hatada, T. Kitayama, E. Masuda, Effects of weak linkages on the thermal and oxidative degradation of poly(methyl methacrylates), *Macromolecules* 19(8) (1986) 2160-2168.
- [49] M. Ferriol, A. Gentilhomme, M. Cochez, N. Oget, J.L. Mieloszynski, Thermal degradation of poly(methyl methacrylate) (PMMA): modelling of DTG and TG curves, *Polymer Degradation and Stability* 79(2) (2003) 271-281.
- [50] A. Saeidi, A.A. Katbab, E. Vasheghani-Farahani, F. Afshar, Formulation design, optimization, characterization and swelling behaviour of a cationic superabsorbent based on a copolymer of [3-(methacryloylamino)propyl]trimethylammonium chloride and acrylamide, *Polymer International* 53(1) (2004) 92-100.
- [51] A. Godara, L. Gorbatikh, G. Kalinka, A. Warriar, O. Rochez, L. Mezzo, F. Luizi, A.W. van Vuure, S.V. Lomov, I. Verpoest, Interfacial shear strength of a glass fiber/epoxy bonding in composites modified with carbon nanotubes, *Compos Sci Technol* 70(9) (2010) 1346-1352.

- [52] G. Lubineau, A. Rahaman, A review of strategies for improving the degradation properties of laminated continuous-fiber/epoxy composites with carbon-based nanoreinforcements, *Carbon* 50(7) (2012) 2377-2395.
- [53] E. Ozden-Yenigun, Y.Z. Menceloglu, M. Papila, MWCNTs/P(St-co-GMA) composite nanofibers of engineered interface chemistry for epoxy matrix nanocomposites, *ACS Appl Mater Interfaces* 4(2) (2012) 777-84.
- [54] B. De Schoenmaker, S. Van der Heijden, I. De Baere, W. Van Paepegem, K. De Clerck, Effect of electrospun polyamide 6 nanofibres on the mechanical properties of a glass fibre/epoxy composite, *Polymer Testing* 32(8) (2013) 1495-1501.
- [55] E. Ozden, Y.Z. Menceloglu, M. Papila, Engineering chemistry of electrospun nanofibers and interfaces in nanocomposites for superior mechanical properties, *ACS Appl Mater Interfaces* 2(7) (2010) 1788-93.
- [56] Y.A. Dzenis, D.H. Reneker, Delamination resistant composites prepared by small diameter fiber reinforcement at ply interfaces, Google Patents, 2001.
- [57] G. Li, P. Li, C. Zhang, Y. Yu, H. Liu, S. Zhang, X. Jia, X. Yang, Z. Xue, S. Ryu, Inhomogeneous toughening of carbon fiber/epoxy composite using electrospun polysulfone nanofibrous membranes by in situ phase separation, *Compos Sci Technol* 68 (2008) 987-994.
- [58] S. Sihn, R.Y. Kim, W. Huh, K.-H. Lee, A.K. Roy, Improvement of damage resistance in laminated composites with electrospun nano-interlayers, *Compos Sci Technol* 68 (2008) 673-683.
- [59] J. Zhang, T. Lin, X.G. Wang, Electrospun nanofibre toughened carbon/epoxy composites: Effects of polyetherketone cardo (PEK-C) nanofibre diameter and interlayer thickness, *Compos Sci Technol* 70(11) (2010) 1660-1666.
- [60] K. Bilge, E. Ozden-Yenigun, E. Simsek, Y.Z. Menceloglu, M. Papila, Structural composites hybridized with epoxy compatible polymer/MWCNT nanofibrous interlayers, *Compos Sci Technol* 72(14) (2012) 1639-1645.
- [61] K. Bilge, S. Venkataraman, Y.Z. Menceloglu, M. Papila, Global and local nanofibrous interlayer toughened composites for higher in-plane strength, *Compos Part a-Appl S* 58 (2014) 73-76.
- [62] Y. Gao, S. Sagi, L. Zhang, Y. Liao, D.M. Cowles, Y. Sun, H. Fong, Electrospun nano-scaled glass fiber reinforcement of bis-GMA/TEGDMA dental composites, *Journal of Applied Polymer Science* 110(4) (2008) 2063-2070.
- [63] S. Lin, Q. Cai, J. Ji, G. Sui, Y. Yu, X. Yang, Q. Ma, Y. Wei, X. Deng, Electrospun nanofiber reinforced and toughened composites through in situ nano-interface formation, *Compos Sci Technol* 68(15-16) (2008) 3322-3329.
- [64] J.S. Monfared Zanjani, B.S. Okan, M. Yildiz, Y. Menceloglu, Fabrication and Morphological Investigation of Multi-walled Electrospun Polymeric Nanofibers, *MRS Proceedings* 1621 (2014) 119-126.

- [65] Ö. Demircan, S. Ashibe, T. Kosui, A. Nakai, Mechanical properties of biaxial weft-knitted and cross-ply thermoplastic composites, *Journal of Thermoplastic Composite Materials* (2014) 0892705713519119.
- [66] W.K. Goertzen, M.R. Kessler, Dynamic mechanical analysis of carbon/epoxy composites for structural pipeline repair, *Composites Part B: Engineering* 38(1) (2007) 1-9.
- [67] I.M. Kalogeras, W. Brostow, Glass transition temperatures in binary polymer blends, *Journal of Polymer Science Part B: Polymer Physics* 47(1) (2009) 80-95.
- [68] K.M.Z. Hossain, I. Ahmed, A.J. Parsons, C.A. Scotchford, G.S. Walker, W. Thielemans, C.D. Rudd, Physico-chemical and mechanical properties of nanocomposites prepared using cellulose nanowhiskers and poly(lactic acid), *J Mater Sci* 47(6) (2012) 2675-2686.
- [69] C. Dry, Procedures developed for self-repair of polymer matrix composite materials, *Compos Struct* 35(3) (1996) 263-269.
- [70] D.G. Shchukin, Container-based multifunctional self-healing polymer coatings, *Polymer Chemistry* 4(18) (2013) 4871-4877.
- [71] J.A. Syrett, C.R. Becer, D.M. Haddleton, Self-healing and self-mendable polymers, *Polymer Chemistry* 1(7) (2010) 978-987.
- [72] M. Motuku, U.K. Vaidya, G.M. Janowski, Parametric studies on self-repairing approaches for resin infused composites subjected to low velocity impact, *Smart Mater Struct* 8(5) (1999) 623-638.
- [73] R.S. Trask, G.J. Williams, I.P. Bond, Bioinspired self-healing of advanced composite structures using hollow glass fibres, *Journal of the Royal Society, Interface / the Royal Society* 4(13) (2007) 363-71.
- [74] S.M. Bleay, C.B. Loader, V.J. Hawyes, L. Humberstone, P.T. Curtis, A smart repair system for polymer matrix composites, *Compos Part a-Appl S* 32(12) (2001) 1767-1776.
- [75] D.Y. Wu, S. Meure, D. Solomon, Self-healing polymeric materials: A review of recent developments, *Prog Polym Sci* 33(5) (2008) 479-522.
- [76] S. Sinha-Ray, D.D. Pelot, Z.P. Zhou, A. Rahman, X.F. Wu, A.L. Yarin, Encapsulation of self-healing materials by coelectrospinning, emulsion electrospinning, solution blowing and intercalation, *Journal of Materials Chemistry* 22(18) (2012) 9138-9146.
- [77] X. Xia, X. Wang, H.M. Zhou, X. Niu, L.G. Xue, X.W. Zhang, Q.F. Wei, The effects of electrospinning parameters on coaxial Sn/C nanofibers: Morphology and lithium storage performance, *Electrochim Acta* 121(0) (2014) 345-351.
- [78] Z. Sun, E. Zussman, A.L. Yarin, J.H. Wendorff, A. Greiner, Compound Core-Shell Polymer Nanofibers by Co-Electrospinning, *Advanced Materials* 15(22) (2003) 1929-1932.

- [79] X.-F. Wu, A.L. Yarin, Recent progress in interfacial toughening and damage self-healing of polymer composites based on electrospun and solution-blown nanofibers: An overview, *Journal of Applied Polymer Science* 130(4) (2013) 2225-2237.
- [80] M.W. Lee, S. An, C. Lee, M. Liou, A.L. Yarin, S.S. Yoon, Hybrid Self-Healing Matrix Using Core–Shell Nanofibers and Capsuleless Microdroplets, *ACS applied materials & interfaces* 6(13) (2014) 10461-10468.
- [81] J.H. Park, P.V. Braun, Coaxial electrospinning of self-healing coatings, *Adv Mater* 22(4) (2010) 496-9.
- [82] T.J. Mitchell, M.W. Keller, Coaxial electrospun encapsulation of epoxy for use in self-healing materials, *Polymer International* 62(6) (2013) 860-866.
- [83] X.F. Wu, A. Rahman, Z.P. Zhou, D.D. Pelot, S. Sinha-Ray, B. Chen, S. Payne, A.L. Yarin, Electrospinning core-shell nanofibers for interfacial toughening and self-healing of carbon-fiber/epoxy composites, *Journal of Applied Polymer Science* 129(3) (2013) 1383-1393.
- [84] S. Neuser, V. Michaud, Effect of aging on the performance of solvent-based self-healing materials, *Polymer Chemistry* 4(18) (2013) 4993-4999.
- [85] J.D. Rule, E.N. Brown, N.R. Sottos, S.R. White, J.S. Moore, Wax-protected catalyst microspheres for efficient self-healing materials, *Advanced Materials* 17(2) (2005) 205-+.
- [86] A.S. Jones, J.D. Rule, J.S. Moore, S.R. White, N.R. Sottos, Catalyst morphology and dissolution kinetics of self-healing polymers, *Chem Mater* 18(5) (2006) 1312-1317.
- [87] M. Majchrzak, P.J. Hine, E. Khosravi, An autonomous self-healing system based on ROMP of norbornene dicarboximide monomers, *Polymer* 53(23) (2012) 5251-5257.
- [88] T.C. Mauldin, J.D. Rule, N.R. Sottos, S.R. White, J.S. Moore, Self-healing kinetics and the stereoisomers of dicyclopentadiene, *Journal of the Royal Society, Interface / the Royal Society* 4(13) (2007) 389-93.
- [89] D.F. Taber, K.J. Frankowski, Grubbs' catalyst in paraffin: an air-stable preparation for alkene metathesis, *The Journal of organic chemistry* 68(15) (2003) 6047-8.
- [90] L. Guadagno, P. Longo, M. Raimondo, C. Naddeo, A. Mariconda, A. Sorrentino, V. Vittoria, G. Iannuzzo, S. Russo, Cure Behavior and Mechanical Properties of Structural Self-Healing Epoxy Resins, *J Polym Sci Pol Phys* 48(23) (2010) 2413-2423.
- [91] B. Alcaide, P. Almendros, J.M. Alonso, Ruthenium-catalyzed chemoselective N-allyl cleavage: novel Grubbs carbene mediated deprotection of allylic amines, *Chemistry* 9(23) (2003) 5793-9.
- [92] Y. Tao, Z. Lin, R. Min Zhi, Z. Ming Qiu, Self-healing woven glass fabric/epoxy composites with the healant consisting of micro-encapsulated epoxy and latent curing agent, *Smart Materials and Structures* 17(1) (2008) 015019.

- [93] K.S. Toohey, C.J. Hansen, J.A. Lewis, S.R. White, N.R. Sottos, Delivery of Two-Part Self-Healing Chemistry via Microvascular Networks, *Advanced Functional Materials* 19(9) (2009) 1399-1405.
- [94] Z. He, Y. Jinglei, Development of self-healing polymers via amine–epoxy chemistry: I. Properties of healing agent carriers and the modelling of a two-part self-healing system, *Smart Materials and Structures* 23(6) (2014) 065003.
- [95] H. Zhang, P. Wang, J. Yang, Self-healing epoxy via epoxy–amine chemistry in dual hollow glass bubbles, *Compos Sci Technol* 94(0) (2014) 23-29.
- [96] D.A. McIlroy, B.J. Blaiszik, M.M. Caruso, S.R. White, J.S. Moore, N.R. Sottos, Microencapsulation of a Reactive Liquid-Phase Amine for Self-Healing Epoxy Composites, *Macromolecules* 43(4) (2010) 1855-1859.
- [97] S. Khoee, Z. Kachoei, Design and development of novel reactive amine nanocontainers for a self-healing epoxy adhesive: self-repairing investigation using the lap shear test, *RSC Advances* 5(27) (2015) 21023-21032.
- [98] M.R. Kessler, S.R. White, Self-activated healing of delamination damage in woven composites, *Compos Part a-Appl S* 32(5) (2001) 683-699.
- [99] G.O. Wilson, M.M. Caruso, N.T. Reimer, S.R. White, N.R. Sottos, J.S. Moore, Evaluation of ruthenium catalysts for ring-opening metathesis polymerization-based self-healing applications, *Chem Mater* 20(10) (2008) 3288-3297.
- [100] L. Guadagno, P. Longo, M. Raimondo, C. Naddeo, A. Mariconda, V. Vittoria, G. Iannuzzo, S. Russo, Use of Hoveyda–Grubbs’ second generation catalyst in self-healing epoxy mixtures, *Composites Part B: Engineering* 42(2) (2011) 296-301.
- [101] M.M. Demir, N. Horzum, A. Tasdemirci, K. Turan, M. Guden, Mechanical interlocking between porous electrospun polystyrene fibers and an epoxy matrix, *ACS Appl Mater Interfaces* 6(24) (2014) 21901-5.
- [102] J.Y. Shieh, H.J. Hwang, S.P. Yang, C.S. Wang, Synthesis and properties of a cyanate ester containing dicyclopentadiene(II), *J Polym Sci Pol Chem* 43(3) (2005) 671-681.
- [103] S.Ü. Çelik, A. Bozkurt, Preparation and proton conductivity of acid-doped 5-aminotetrazole functional poly(glycidyl methacrylate), *European Polymer Journal* 44(1) (2008) 213-218.
- [104] L. Yuan, G. Liang, J. Xie, L. Li, J. Guo, Preparation and characterization of poly(urea-formaldehyde) microcapsules filled with epoxy resins, *Polymer* 47 (2006) 5338–5349.
- [105] C. Liu, R. Bai, Q. San Ly, Selective removal of copper and lead ions by diethylenetriamine-functionalized adsorbent: behaviors and mechanisms, *Water research* 42(6-7) (2008) 1511-22.

- [106] M.A. Khan, N. Haque, A.A. Kafi, M.N. Alam, M.Z. Abedin, Jute reinforced polymer composite by gamma radiation: Effect of surface treatment with UV radiation, *Polym-Plast Technol* 45(5) (2006) 607-613.
- [107] M.S. Islam, Y. Deng, L. Tong, S.N. Faisal, A.K. Roy, A.I. Minett, V.G. Gomes, Grafting carbon nanotubes directly onto carbon fibers for superior mechanical stability: Towards next generation aerospace composites and energy storage applications, *Carbon* 96 (2016) 701-710.
- [108] L. Mishnaevsky, H. Zhou, H. Yi, R. Peng, H. Wang, G. Dai, L. Gui, X. Zhang, Microscale damage mechanisms and degradation of fiber-reinforced composites for wind energy applications: results of Danish–Chinese collaborative investigations, *Journal of Composite Materials* 48(24) (2014) 2977-2991.
- [109] J.R. Xiao, B.A. Gama, J.W. Gillespie, Progressive damage and delamination in plain weave S-2 glass/SC-15 composites under quasi-static punch-shear loading, *Compos Struct* 78(2) (2007) 182-196.
- [110] P. Maimí, P.P. Camanho, J.A. Mayugo, A. Turon, Matrix cracking and delamination in laminated composites. Part I: Ply constitutive law, first ply failure and onset of delamination, *Mechanics of Materials* 43(4) (2011) 169-185.
- [111] O. Al-Khudairi, H. Hadavinia, A. Waggott, E. Lewis, C. Little, Characterising mode I/mode II fatigue delamination growth in unidirectional fibre reinforced polymer laminates, *Materials & Design* 66, Part A(0) (2015) 93-102.
- [112] C. Canturri, E.S. Greenhalgh, S.T. Pinho, The relationship between mixed-mode II/III delamination and delamination migration in composite laminates, *Compos Sci Technol* 105 (2014) 102-109.
- [113] J.S. Monfared Zanjani, B.S. Okan, Y.Z. Menciloglu, M. Yildiz, Nano-engineered design and manufacturing of high-performance epoxy matrix composites with carbon fiber/selectively integrated graphene as multi-scale reinforcements, *RSC Advances* 6(12) (2016) 9495-9506.
- [114] R.S. Trask, G.J. Williams, I.P. Bond, Bioinspired self-healing of advanced composite structures using hollow glass fibres, *Journal of The Royal Society Interface* 4(13) (2007) 363-371.
- [115] K.S. Toohy, N.R. Sottos, J.A. Lewis, J.S. Moore, S.R. White, Self-healing materials with microvascular networks, *Nat Mater* 6(8) (2007) 581-585.
- [116] S. Sinha-Ray, D.D. Pelot, Z.P. Zhou, A. Rahman, X.-F. Wub, A.L. Yarin, Encapsulation of self-healing materials by coelectrospinning, emulsion electrospinning, solution blowing and intercalation, *Journal of Materials Chemistry* 22 (2012) 9138-9146.
- [117] L. Daelemans, S. van der Heijden, I. De Baere, H. Rahier, W. Van Paepegem, K. De Clerck, Using aligned nanofibres for identifying the toughening micromechanisms in nanofibre interleaved laminates, *Compos Sci Technol* 124 (2016) 17-26.

- [118] N.H. Nash, T.M. Young, W.F. Stanley, The influence of a thermoplastic toughening interlayer and hydrothermal conditioning on the Mode-II interlaminar fracture toughness of Carbon/Benzoxazine composites, *Composites Part A: Applied Science and Manufacturing* 81 (2016) 111-120.
- [119] M.W. Lee, S. An, H.S. Jo, S.S. Yoon, A.L. Yarin, Self-Healing Nanofiber-Reinforced Polymer Composites. 1. Tensile Testing and Recovery of Mechanical Properties, *ACS applied materials & interfaces* 7(35) (2015) 19546-19554.
- [120] P.J. Schubel, R.J. Crossley, E.K.G. Boateng, J.R. Hutchinson, Review of structural health and cure monitoring techniques for large wind turbine blades, *Renewable Energy* 51 (2013) 113-123.
- [121] B. Kamsu-Foguem, Knowledge-based support in Non-Destructive Testing for health monitoring of aircraft structures, *Advanced Engineering Informatics* 26(4) (2012) 859-869.
- [122] C.J. Keulen, E. Akay, F.F. Melemez, E.S. Kocaman, A. Deniz, C. Yilmaz, T. Boz, M. Yildiz, H.S. Turkmen, A. Suleman, Prediction of fatigue response of composite structures by monitoring the strain energy release rate with embedded fiber Bragg gratings, *Journal of Intelligent Material Systems and Structures* 27(1) (2016) 17-27.
- [123] C.J. Keulen, M. Yildiz, A. Suleman, Multiplexed FBG and Etched Fiber Sensors for Process and Health Monitoring of 2-&3-D RTM Components, *Journal of Reinforced Plastics and Composites* (2011).
- [124] M. Yildiz, N.G. Ozdemir, G. Bektas, C.J. Keulen, T. Boz, E.F. Sengun, C. Ozturk, Y.Z. Menciloglu, A. Suleman, An Experimental Study on the Process Monitoring of Resin Transfer Molded Composite Structures Using Fiber Optic Sensors, *Journal of Manufacturing Science and Engineering* 134(4) (2012) 044502-044502.
- [125] A. Othonos, K. Kalli, *Fiber Bragg gratings: fundamentals and applications in telecommunications and sensing*, Artech House 1999.
- [126] M. Majumder, T.K. Gangopadhyay, A.K. Chakraborty, K. Dasgupta, D.K. Bhattacharya, Fibre Bragg gratings in structural health monitoring—Present status and applications, *Sensors and Actuators A: Physical* 147(1) (2008) 150-164.
- [127] S. Masmoudi, A. El Mahi, S. Turki, Fatigue behaviour and structural health monitoring by acoustic emission of E-glass/epoxy laminates with piezoelectric implant, *Applied Acoustics* (2015).
- [128] M.G.R. Sause, T. Müller, A. Horoschenkoff, S. Horn, Quantification of failure mechanisms in mode-I loading of fiber reinforced plastics utilizing acoustic emission analysis, *Compos Sci Technol* 72(2) (2012) 167-174.
- [129] J.S. Leng, D. Winter, R.A. Barnes, G.C. Mays, G.F. Fernando, *Structural health monitoring of smart civil structures using fibre optic sensors*, 2005, pp. 42-48.

- [130] C. Yilmaz, C. Akalin, E.S. Kocaman, A. Suleman, M. Yildiz, Monitoring Poisson's ratio of glass fiber reinforced composites as damage index using biaxial Fiber Bragg Grating sensors, *Polymer Testing* 53 (2016) 98-107.
- [131] K. Mohamed Bak, K. Kalaiichelvan, A. Jothilingam, S. RajendraBoopathy, Acoustic emission characterization of failure modes of single-lap joints in glass/epoxy specimens, *Journal of Composite Materials* 50(1) (2016) 3-23.
- [132] M. Kempf, O. Skrabala, V. Altstädt, Acoustic emission analysis for characterisation of damage mechanisms in fibre reinforced thermosetting polyurethane and epoxy, *Composites Part B: Engineering* 56 (2014) 477-483.
- [133] M.-Y. Lyu, T. Choi, Research trends in polymer materials for use in lightweight vehicles, *Int. J. Precis. Eng. Manuf.* 16(1) (2015) 213-220.
- [134] G. Mittal, V. Dhand, K.Y. Rhee, S.-J. Park, W.R. Lee, A review on carbon nanotubes and graphene as fillers in reinforced polymer nanocomposites, *Journal of Industrial and Engineering Chemistry* 21(0) (2015) 11-25.
- [135] C. Kong, J. Bang, Y. Sugiyama, Structural investigation of composite wind turbine blade considering various load cases and fatigue life, *Energy* 30(11-12) (2005) 2101-2114.
- [136] T.C. Triantafillou, N. Plevris, Strengthening of RC beams with epoxy-bonded fibre-composite materials, *Materials and Structures* 25(4) (1992) 201-211.
- [137] E.C. Botelho, R.A. Silva, L.C. Pardini, M.C. Rezende, A review on the development and properties of continuous fiber/epoxy/aluminum hybrid composites for aircraft structures, *Materials Research* 9 (2006) 247-256.
- [138] A. Toldy, B. Szolnoki, G. Marosi, Flame retardancy of fibre-reinforced epoxy resin composites for aerospace applications, *Polymer Degradation and Stability* 96(3) (2011) 371-376.
- [139] P.J. Hine, M. Bonner, I.M. Ward, Y. Swolfs, I. Verpoest, A. Mierzwa, Hybrid carbon fibre/nylon 12 single polymer composites, *Composites Part A: Applied Science and Manufacturing* 65(0) (2014) 19-26.
- [140] G.W. Beckermann, K.L. Pickering, Mode I and Mode II interlaminar fracture toughness of composite laminates interleaved with electrospun nanofibre veils, *Composites Part A: Applied Science and Manufacturing* 72(0) (2015) 11-21.
- [141] X. Tian, Y. Geng, D. Yin, B. Zhang, Y. Zhang, Studies on the properties of a thermosetting epoxy modified with chain-extended ureas containing hydroxyl-terminated polybutadiene, *Polymer Testing* 30(1) (2011) 16-22.
- [142] S. Deng, J. Zhang, L. Ye, J. Wu, Toughening epoxies with halloysite nanotubes, *Polymer* 49(23) (2008) 5119-5127.

- [143] M. Rico, J. López, B. Montero, R. Bellas, Phase separation and morphology development in a thermoplastic-modified toughened epoxy, *European Polymer Journal* 48(10) (2012) 1660-1673.
- [144] P.P. Vijayan, M.G. Harikrishnan, D. Puglia, P.P. Vijayan, J.M. Kenny, S. Thomas, Solvent Uptake of Liquid Rubber Toughened Epoxy/Clay Nanocomposites, *Advances in Polymer Technology* (2015) n/a-n/a.
- [145] S. Zavareh, G. Samandari, Polyethylene glycol as an epoxy modifier with extremely high toughening effect: Formation of nanoblend morphology, *Polymer Engineering & Science* 54(8) (2014) 1833-1838.
- [146] L.-C. Tang, Y.-J. Wan, K. Peng, Y.-B. Pei, L.-B. Wu, L.-M. Chen, L.-J. Shu, J.-X. Jiang, G.-Q. Lai, Fracture toughness and electrical conductivity of epoxy composites filled with carbon nanotubes and spherical particles, *Composites Part A: Applied Science and Manufacturing* 45(0) (2013) 95-101.
- [147] H.-Y. Liu, G.-T. Wang, Y.-W. Mai, Y. Zeng, On fracture toughness of nano-particle modified epoxy, *Composites Part B: Engineering* 42(8) (2011) 2170-2175.
- [148] X. Jia, J. Zhu, W. Li, X. Chen, X. Yang, Compressive and tensile response of CFRP cylinders induced by multi-walled carbon nanotubes, *Compos Sci Technol* 110(0) (2015) 35-44.
- [149] J.D.H. Hughes, The carbon fibre/epoxy interface—A review, *Compos Sci Technol* 41(1) (1991) 13-45.
- [150] Z. Dai, B. Zhang, F. Shi, M. Li, Z. Zhang, Y. Gu, Effect of heat treatment on carbon fiber surface properties and fibers/epoxy interfacial adhesion, *Applied Surface Science* 257(20) (2011) 8457-8461.
- [151] E. Fitzer, K.H. Geigl, W. Hüttner, R. Weiss, Chemical interactions between the carbon fibre surface and epoxy resins, *Carbon* 18(6) (1980) 389-393.
- [152] M.A. Montes-Morán, R.J. Young, Raman spectroscopy study of HM carbon fibres: effect of plasma treatment on the interfacial properties of single fibre/epoxy composites, *Carbon* 40(6) (2002) 845-855.
- [153] W. Song, A. Gu, G. Liang, L. Yuan, Effect of the surface roughness on interfacial properties of carbon fibers reinforced epoxy resin composites, *Applied Surface Science* 257(9) (2011) 4069-4074.
- [154] V.P. Veedu, A. Cao, X. Li, K. Ma, C. Soldano, S. Kar, P.M. Ajayan, M.N. Ghasemi-Nejhad, Multifunctional composites using reinforced laminae with carbon-nanotube forests, *Nat Mater* 5(6) (2006) 457-462.
- [155] Y. Wang, Z. Xu, L. Chen, Y. Jiao, X. Wu, Multi-scale hybrid composites-based carbon nanotubes, *Polym Composite* 32(2) (2011) 159-167.

- [156] E. Bekyarova, E.T. Thostenson, A. Yu, H. Kim, J. Gao, J. Tang, H.T. Hahn, T.W. Chou, M.E. Itkis, R.C. Haddon, Multiscale Carbon Nanotube–Carbon Fiber Reinforcement for Advanced Epoxy Composites, *Langmuir* 23(7) (2007) 3970-3974.
- [157] Y. Wang, I. Zhitomirsky, Electrophoretic Deposition of Manganese Dioxide–Multiwalled Carbon Nanotube Composites for Electrochemical Supercapacitors, *Langmuir* 25(17) (2009) 9684-9689.
- [158] B. Yu, Z. Jiang, X.-Z. Tang, C.Y. Yue, J. Yang, Enhanced interphase between epoxy matrix and carbon fiber with carbon nanotube-modified silane coating, *Compos Sci Technol* 99(0) (2014) 131-140.
- [159] B. Saner, F. Okyay, Y. Yürüm, Utilization of multiple graphene layers in fuel cells. 1. An improved technique for the exfoliation of graphene-based nanosheets from graphite, *Fuel* 89(8) (2010) 1903-1910.
- [160] J.I. Paredes, S. Villar-Rodil, A. Martínez-Alonso, J.M.D. Tascón, Graphene Oxide Dispersions in Organic Solvents, *Langmuir* 24(19) (2008) 10560-10564.
- [161] A.J. Kinloch, A.C. Taylor, The mechanical properties and fracture behaviour of epoxy-inorganic micro- and nano-composites, *J Mater Sci* 41(11) (2006) 3271-3297.
- [162] L. Haghighi Poudeh, B. Saner Okan, J. Seyyed Monfared Zanjani, M. Yildiz, Y.Z. Menceloglu, Design and Fabrication of Hollow and Filled Graphene-based Polymeric Spheres via Core-Shell Electrospinning, *RSC Advances* (2015).
- [163] X. Liu, N.G. Boddeti, M.R. Szpunar, L. Wang, M.A. Rodriguez, R. Long, J. Xiao, M.L. Dunn, J.S. Bunch, Observation of Pull-In Instability in Graphene Membranes under Interfacial Forces, *Nano Letters* 13(5) (2013) 2309-2313.
- [164] A. Ferrari, J. Meyer, V. Scardaci, C. Casiraghi, M. Lazzeri, F. Mauri, S. Piscanec, D. Jiang, K. Novoselov, S. Roth, Raman spectrum of graphene and graphene layers, *Physical review letters* 97(18) (2006) 187401.
- [165] E. Steven, W.R. Saleh, V. Lebedev, S.F.A. Acquah, V. Laukhin, R.G. Alamo, J.S. Brooks, Carbon nanotubes on a spider silk scaffold, *Nat Commun* 4 (2013).
- [166] B.S. Okan, A. Yürüm, N. Gorgülü, S.A. Gürsel, Y. Yürüm, Polypyrrole Coated Thermally Exfoliated Graphite Nanoplatelets and the Effect of Oxygen Surface Groups on the Interaction of Platinum Catalysts with Graphene-Based Nanocomposites, *Industrial & Engineering Chemistry Research* 50(22) (2011) 12562-12571.
- [167] J.S. Im, E. Jeong, S.J. In, Y.-S. Lee, The impact of fluorinated MWCNT additives on the enhanced dynamic mechanical properties of e-beam-cured epoxy, *Composites Science and Technology* 70(5) (2010) 763-768.
- [168] N.A. Bakar, C.Y. Chee, L.C. Abdullah, C.T. Ratnam, N.A. Ibrahim, Thermal and dynamic mechanical properties of grafted kenaf filled poly (vinyl chloride)/ethylene vinyl acetate composites, *Materials & Design* 65 (2015) 204-211.

- [169] R. Chandra, S.P. Singh, K. Gupta, Damping studies in fiber-reinforced composites – a review, *Composite Structures* 46(1) (1999) 41-51.
- [170] D. Ray, B.K. Sarkar, S. Das, A.K. Rana, Dynamic mechanical and thermal analysis of vinyl ester-resin-matrix composites reinforced with untreated and alkali-treated jute fibres, *Composites Science and Technology* 62(7–8) (2002) 911-917.
- [171] B. Willocq, R.K. Bose, F. Khelifa, S.J. Garcia, P. Dubois, J.M. Raquez, Healing by the Joule effect of electrically conductive poly(ester-urethane)/carbon nanotube nanocomposites, *Journal of Materials Chemistry A* 4(11) (2016) 4089-4097.
- [172] R. Dermanaki Farahani, M. Gagne, J.E. Klemberg-Sapieha, D. Therriault, Electrically Conductive Silver Nanoparticles-Filled Nanocomposite Materials as Surface Coatings of Composite Structures *Advanced Engineering Materials* (2016) n/a-n/a.
- [173] I.U. Hwang, H.N. Yu, S.S. Kim, D.G. Lee, J.D. Suh, S.H. Lee, B.K. Ahn, S.H. Kim, T.W. Lim, Bipolar plate made of carbon fiber epoxy composite for polymer electrolyte membrane fuel cells, *Journal of Power Sources* 184(1) (2008) 90-94.
- [174] J.-E. An, Y.G. Jeong, Structure and electric heating performance of graphene/epoxy composite films, *European Polymer Journal* 49(6) (2013) 1322-1330.
- [175] A.-R.O. Raji, T. Varadhachary, K. Nan, T. Wang, J. Lin, Y. Ji, B. Genorio, Y. Zhu, C. Kittrell, J.M. Tour, Composites of Graphene Nanoribbon Stacks and Epoxy for Joule Heating and Deicing of Surfaces, *ACS Applied Materials & Interfaces* 8(5) (2016) 3551-3556.
- [176] M. Mohseni, A. Amirfazli, A novel electro-thermal anti-icing system for fiber-reinforced polymer composite airfoils, *Cold Regions Science and Technology* 87 (2013) 47-58.
- [177] X. Lv, Z. Huang, C. Huang, M. Shi, G. Gao, Q. Gao, Damping properties and the morphology analysis of the polyurethane/epoxy continuous gradient IPN materials, *Composites Part B: Engineering* 88 (2016) 139-149.
- [178] A.K. Saha, S. Das, D. Bhatta, B.C. Mitra, Study of jute fiber reinforced polyester composites by dynamic mechanical analysis, *Journal of Applied Polymer Science* 71(9) (1999) 1505-1513.
- [179] H. Chen, O. Jacobs, W. Wu, G. Rüdiger, B. Schädel, Effect of dispersion method on tribological properties of carbon nanotube reinforced epoxy resin composites, *Polymer Testing* 26(3) (2007) 351-360.
- [180] P.C. Ma, J.-K. Kim, B.Z. Tang, Effects of silane functionalization on the properties of carbon nanotube/epoxy nanocomposites, *Composites Science and Technology* 67(14) (2007) 2965-2972.
- [181] V.S. Sreenivasan, N. Rajini, A. Alavudeen, V. Arumugaprabu, Dynamic mechanical and thermo-gravimetric analysis of *Sansevieria cylindrica*/polyester composite: Effect of fiber length, fiber loading and chemical treatment, *Composites Part B: Engineering* 69 (2015) 76-86.

- [182] T. Brocks, M.O.H. Cioffi, H.J.C. Voorwald, Effect of fiber surface on flexural strength in carbon fabric reinforced epoxy composites, *Applied Surface Science* 274 (2013) 210-216.
- [183] B. Li, W. Yao, H. Shao, B. Huang, A. He, Composition-properties relationship in epoxidized trans-1,4-polyisoprene obtained by heterogeneous method, *Polymer Science Series A* 57(5) (2015) 581-585.
- [184] W. Stark, Investigation of the curing behaviour of carbon fibre epoxy prepreg by Dynamic Mechanical Analysis DMA, *Polymer Testing* 32(2) (2013) 231-239.
- [185] L.C.O. Silva, G.G. Silva, P.M. Ajayan, B.G. Soares, Long-term behavior of epoxy/graphene-based composites determined by dynamic mechanical analysis, *Journal of Materials Science* 50(19) (2015) 6407-6419.
- [186] W.K. Goertzen, M.R. Kessler, Creep behavior of carbon fiber/epoxy matrix composites, *Materials Science and Engineering: A* 421(1-2) (2006) 217-225.
- [187] H.F. Brinson, L.C. Brinson, *Time and Temperature Behavior of Polymers, Polymer Engineering Science and Viscoelasticity: An Introduction*, Springer US, Boston, MA, 2015, pp. 231-285.
- [188] R. Li, Time-temperature superposition method for glass transition temperature of plastic materials, *Materials Science and Engineering: A* 278(1-2) (2000) 36-45.
- [189] G. Li, P. Lee-Sullivan, R.W. Thring, Determination of Activation Energy for Glass Transition of an Epoxy Adhesive Using Dynamic Mechanical Analysis, *Journal of Thermal Analysis and Calorimetry* 60(2) 377-390.
- [190] M.W. Keller, B.D. Jellison, T. Ellison, Moisture effects on the thermal and creep performance of carbon fiber/epoxy composites for structural pipeline repair, *Composites Part B: Engineering* 45(1) (2013) 1173-1180.
- [191] J. Diani, P. Gilormini, J.S. Arrieta, Direct experimental evidence of time-temperature superposition at finite strain for an amorphous polymer network, *Polymer* 58 (2015) 107-112.
- [192] V.S. Chevali, D.R. Dean, G.M. Janowski, Flexural creep behavior of discontinuous thermoplastic composites: Non-linear viscoelastic modeling and time-temperature-stress superposition, *Composites Part A: Applied Science and Manufacturing* 40(6-7) (2009) 870-877.
- [193] T.K. Vaidyanathan, J. Vaidyanathan, Z. Cherian, Extended creep behavior of dental composites using time-temperature superposition principle, *Dental Materials* 19(1) (2003) 46-53.
- [194] M.L. Williams, R.F. Landel, J.D. Ferry, The Temperature Dependence of Relaxation Mechanisms in Amorphous Polymers and Other Glass-forming Liquids, *Journal of the American Chemical Society* 77(14) (1955) 3701-3707.

- [195] A. Montazeri, K. Pourshamsian, M. Riazian, Viscoelastic properties and determination of free volume fraction of multi-walled carbon nanotube/epoxy composite using dynamic mechanical thermal analysis, *Materials & Design* 36 (2012) 408-414.
- [196] Q. Huang, C.M. Lilley, M. Bode, Surface scattering effect on the electrical resistivity of single crystalline silver nanowires self-assembled on vicinal Si (001), *Applied Physics Letters* 95(10) (2009) 103112.
- [197] V. Timoshevskii, Y. Ke, H. Guo, D. Gall, The influence of surface roughness on electrical conductance of thin Cu films: An ab initio study, *Journal of Applied Physics* 103(11) (2008) 113705.
- [198] U. Jacob, J. Vancea, H. Hoffmann, Surface-roughness contributions to the electrical resistivity of polycrystalline metal films, *Physical Review B* 41(17) (1990) 11852-11857.
- [199] Y. Song, Y. Pan, Q. Zheng, X.-S. Yi, The electric self-heating behavior of graphite-filled high-density polyethylene composites, *Journal of Polymer Science Part B: Polymer Physics* 38(13) (2000) 1756-1763.
- [200] S. Isaji, Y. Bin, M. Matsuo, Electrical conductivity and self-temperature-control heating properties of carbon nanotubes filled polyethylene films, *Polymer* 50(4) (2009) 1046-1053.
- [201] F. Mercuri, U. Zammit, N. Orazi, S. Paoloni, M. Marinelli, F. Scudieri, Active infrared thermography applied to the investigation of art and historic artefacts, *Journal of Thermal Analysis and Calorimetry* 104(2) (2011) 475-485.
- [202] H.-B. Shim, M.-K. Seo, S.-J. Park, Thermal conductivity and mechanical properties of various cross-section types carbon fiber-reinforced composites, *Journal of Materials Science* 37(9) (2002) 1881-1885.
- [203] W.J. Parker, R.J. Jenkins, C.P. Butler, G.L. Abbott, Flash Method of Determining Thermal Diffusivity, Heat Capacity, and Thermal Conductivity, *Journal of Applied Physics* 32(9) (1961) 1679-1684.
- [204] F. Scudieri, F. Mercuri, R. Volterri, Non-invasive Analysis of Artistic Heritage and Archaeological Findings by Time Resolved IR Thermography, *Journal of Thermal Analysis and Calorimetry* 66(1) 307-314.
- [205] M. Abdalla, D. Dean, P. Robinson, E. Nyairo, Cure behavior of epoxy/MWCNT nanocomposites: The effect of nanotube surface modification, *Polymer* 49(15) (2008) 3310-3317.
- [206] S. Ganguli, A.K. Roy, D.P. Anderson, Improved thermal conductivity for chemically functionalized exfoliated graphite/epoxy composites, *Carbon* 46(5) (2008) 806-817.